

Functional Elements for Quantum-Dot-Based Integrated Quantum Photonics

Présentée le 6 mars 2020

à la Faculté des sciences de base
Laboratoire de physique des nanostructures
Programme doctoral en physique

pour l'obtention du grade de Docteur ès Sciences

par

Antoine Maxime DELGOFFE

Acceptée sur proposition du jury

Prof. P. Ricci, président du jury
Prof. E. Kapon, Prof. N. Grandjean, directeurs de thèse
Prof. M. Felici, rapporteur
Prof. O. Hess, rapporteur
Prof. A. Fontcuberta i Morral, rapporteuse

Remerciements

Une thèse, c'est un travail de quatre ans, au fil duquel on grandit un peu mais probablement pas assez pour y arriver tout seul. Le soutien de nombreuses personnes a été nécessaire, et je tiens ici à les en remercier.

Tout d'abord et naturellement, le professeur Eli Kapon pour m'avoir accueilli au sein du Laboratoire de Physique des Nanostructures pour me former à l'une de mes passions, l'Optique. J'ai eu le privilège d'y réaliser mes travaux pratiques, mon projet de master et poursuivre avec cette thèse de doctorat. En contact avec sa rigueur, son esprit scientifique et son souci du détail, j'ai eu l'occasion d'apprendre et gagner en autonomie au niveau de l'enseignement, de la gestion de projet et des méthodologies de recherche, de rédaction et de présentation. Des ingrédients essentiels pour débiter une carrière qui je l'espère sera enrichissante et fructueuse.

Je souhaite aussi remercier le professeur Nicolas Grandjean pour la co-supervision de ce long travail et la gentillesse de m'avoir accueilli au sein du LASPE pour les derniers mois de rédaction.

Aux docteurs Benjamin Dwir et Alok Rudra pour leur accompagnement et qui sont des mines de savoir scientifique et général.

Bien entendu, je remercie les membres du jury : les professeurs Anna Fontcuberta i Morral, Marco Felici, Ortwin Hess, pour avoir donné de leur temps pour parcourir ce manuscrit et pour leurs commentaires constructifs et questions pertinentes lors de l'épreuve de la défense.

Au personnel des salles blanches de l'institut de Physique, en particulier Nicolas Leiser, Damien et Yoan Trolliet ainsi que Jonathan Delaloye, pour leur travail et leur authenticité.

A notre secrétaire du LPN, Gabriella Fuchs, pour sa positivité.

A mes collègues de bureau et compatriotes français : Clément Jarlov, Bruno Rigal et Pascal Gallo avec qui j'ai fait mes premiers pas au LPN.

A Alexey Lyasota, Mikhail Lazarev et les docteurs Irina Kulkova & Alessio Miranda qui ont aussi contribué aux efforts du LPN lors de mon séjour.

A nos visiteurs de passage du Danemark : Jacob Rosenkrantz de Lasson, Kristoffer Joanesarson, le docteur Yi Yu qui a partagé aussi mon bureau plus d'un an, et le professeur Jesper Mørk.

A Marc-André Dupertuis, pour son émerveillement contagieux pour l'optique quantique transmis lors de ses cours.

Aux étudiants de passage au LPN, pour un petit projet d'été : Achraf Kabbabi et Monika Zimmermann ; pour un travail de semestre : Sven Borghardt, Manuel Deckart, Martha Benthem, Fabien Gremion, Fingal Persoud, Giulio Terrasanta ; ou encore pour un travail de diplôme : Yichen Ma et Thomas Produit.

Aux deux ou trois générations d'étudiants que j'ai pu encadrer en cours de Physique Générale ou en Optique. L'échange a été réciproque, j'ai aussi pas mal appris à leur contact.

A l'Ecole Polytechnique Fédérale de Lausanne pour m'avoir donné l'opportunité d'y effectuer l'intégralité de mon cursus universitaire, Bachelor, Master et Ph. D., neuf années dans un cadre international privilégié au bord du Léman.

Remerciements

Et à ce petit pays qu'est la Suisse, où j'espère planter durablement mes attaches pour rester auprès de certaines personnes, qui présente un cadre idyllique de lacs, montagnes et forêts où il fait bon faire des randonnées et naviguer à la voile.

Aussi à mes deux bienveillants thérapeutes, qui m'ont accompagné en partie dans la traversée d'une période loin d'être facile, et qui je le souhaite, se reconnaîtront s'ils ont un jour l'occasion de lire ce paragraphe.

A mes amis proches mais à celles et ceux avec qui j'ai partagé les bancs des auditoriums lors du Bachelor & Master, ou rencontrés lors de mon engagement associatif à l'Agepoly puis PolyJapan.

En particulier, je voudrais remercier trois précieux amis avec qui le partage intellectuel est un plaisir toujours renouvelé et qui ont franchement aidés à traverser les années de thèse avec un peu plus de légèreté. Sébastien Basterrechea pour sa passion commune pour le Japon, son goût surprenant pour les mathématiques ainsi que ses traits d'esprit. Samy Adjani, pour son indéfectible soutien et les franches rigolades quant à l'absurdité des choses. Et Bruno Rigal pour sa joie de vivre, son optimisme et sa vivacité d'esprit.

A mes amis de mes années en France, en particulier Clément et Antoine, que je n'ai plus tellement l'occasion de voir car ainsi vont les choses, mais que je n'oublie pas puisqu'ils ont fait à mes côtés un bout du chemin qui m'a amené jusqu'ici.

Enfin, à mes grand-parents. A mes parents Michèle et Christian, sans qui évidemment je ne serais pas là, pour l'éducation qui m'a été transmise, pour avoir entretenu ma curiosité dès le plus jeune âge, suscité une vocation scientifique, et enfin donné les moyens de poursuivre mes études aussi loin. A ma sœur Camille et mon beau-frère Michael, mon frère Clément et ma belle-sœur Sophie et mes deux neveux Arthur et Victor. A mes oncles et tantes, cousins et cousines, à mon parrain Bernard et Frédo, et ma marraine ainsi que leurs proches.

Bien évidemment, la liste serait autrement plus longue si elle se voulait exhaustive, ainsi à toutes celles et ceux que j'ai omis de nommer,

Un grand et sincère merci pour avoir été simplement présent à un moment ou un autre.

"Per aspera ad astra"

"Par des sentiers ardues jusqu'aux étoiles"

Abstract

Single photons are very promising candidates to carry quantum information. They are robust to decoherence and bridge the gap of long distances in an instant. They possess a variety of degree of freedoms suitable for entanglement. Quantum Integrated Photonics (QIP) aims at harnessing quantum-states of light on tiny chips, from their generation to their processing and eventual detection. Within this context, this thesis explores functional QIP elements resulting from the monolithic integration of semiconductor quantum dots (QDs) in tailored photonic crystal complexes of coupled cavities and waveguides. Quantum dots present atom-like optical and electronic properties, which make them ideal for a deterministic, on-demand generation of single photons. Such QD-based devices can be expected to provide solutions for applications of QIPs in quantum computing, quantum communication and quantum metrology.

In this field, a recurrent challenge is the difficulty to reproducibly fabricate structures in which more than one quantum emitter are positioned by design. The technology of pyramidal, site-controlled QDs has reached a point of maturity where it is now possible to reproducibly fabricate microscopic photonic circuits in which an arbitrary number of interacting quantum emitters can be embedded to precision better than 50nm. This thesis exploits this technology for making further progress towards functional QIP devices. The work relies on the systematic investigation of two types of structures. Reference structures with dense arrays of QDs are used to observe the optical mode structures of novel photonic crystal (PhC) structures. In parallel, identical structures with only a few QDs for selective excitation of modes, and eventually coupling to single modes, are studied. The use of a spatially-resolved micro-photoluminescence spectroscopy lifts ambiguities on the contributions of different dots to specific mode excitation. The observations are further consolidated by the quantitative comparison to 2D FDM numerical simulations in which the dispersion of the refractive index is accounted for.

First, we investigate the generic cavity structure of a defect-potential PhC cavity in which modes are confined by a local mismatch in the photon dispersion. This is achieved by the precise transverse shifts of selected holes in a PhC defect waveguide, which is interpreted as tailoring of the waveguide mode effective refractive index. The photonic confinement is observed to occur at the various photonic band-edges, with the peculiar polarization signatures. The lowest-energy confined modes display quality factors and mode volumes on par with more conventional $L_{n=3}$ cavities. The selective excitation of few modes and weak coupling to a single mode are demonstrated with integrated site-controlled QDs. A Purcell enhancement of ~ 8 and strong co-polarization effect are achieved with the help of thermal tuning.

Next, the concept of the defect-potential is expanded to realize a tilted-potential PhC cavity that supports Airy-Bloch photonic modes. This is done by the staggered shifts of holes from 0 to s_{\max} along the waveguide cavity. These modes have a characteristic “head” component where the field is strongest, and a delocalized oscillating “tail” component. This makes them suitable to locally interact and extract single photons from site-controlled QDs and transport them to remote locations. The location of the head is related to the quasi linear energy-position dispersion of the tilted-potential structure. This feature provides means for constructing an efficient wavelength-multiplexed single-photon injector. Relative robustness to Anderson localization is also observed, and selective excitation of several modes with properly positioned QDs is demonstrated. Weak coupling of a QD to a single mode is achieved by thermal tuning, showing co-polarization effect and Purcell enhancement.

Finally, returning to the general goal of fabricating a functional monolithic photonic circuit, a model structures containing several functional elements is fabricated and tested. It consists of two PhC waveguides side-coupled to a center $L_{n=3}$ cavity, with four ports connected to the outside world by means of suspended nanobeams and grating couplers. Five QDs are embedded in specific positions; four can act as on-chip single photon sources while

the fifth, embedded in the center cavity, could be used for photon processing functions. The optical mode structure of this model system is investigated, and the optical channels where the center cavity is coupled to both waveguides are revealed. The quasi-resonant excitation of a QD via its p-shell is demonstrated using a pump laser beam that is injected into the waveguides through the grating coupler. The p-shell and s-shell of the QDs are shown to be connected to two different optical channels. These results also give interesting insights towards possible future on-chip laser integration for QD optical pumping.

The results of this thesis consolidate the assets of the site-controlled pyramidal QD technology towards the realization of functional elements for quantum integrated photonics circuits. Interesting outlooks involve remote QD-QD radiative coupling, collective effects and on-chip entanglement sharing. Efforts should be focused on improving the dipole oscillator strengths to enhance the coupling interactions and attain strong coupling. To study non-classical effects with more than one QD, the development of a mean to tune individually the various emitters cannot be avoided.

Keywords

Nanotechnology, nanophotonics, nanostructures, quantum information science, quantum integrated photonics, photonic confinement, III-V semiconductors, heterostructures, excitons, quantum dots, photonic crystals, waveguides, tailored-potential, cavity QED, Jaynes-Cummings model, Purcell effect, disorder, Anderson localization, single photons, MOCVD, micro-photoluminescence

Acronyms

AFM: Atomic Force **M**icroscope

AM: Alignment **M**ark

BS: Beam-**S**plitter

CROW: Coupled **R**esonators **O**ptical **W**aveguide

CM: Cavity **M**ode

DOLP: Degree **O**f Linear **P**olarization

LDOS: Local **D**ensity **O**f **S**tates

EBL: Electron Beam **L**ithography

InGaAs: Indium **G**allium **A**rsenide

HBT: Hanbury-**B**rown & **T**wiss

(B)HF: (**B**uffered) **H**ydro**F**luoric

HOM: Hong-**O**u-**M**andel

ICP: Inductively Coupled **P**lasma

MIBK:IPA: Methyl Isobutyl **K**etone: Iso**P**ropyl **A**lcohol

MO-CVD/VPE: Metal**O**rganic-**C**hemical **V**apour **D**eposition / **V**apour **P**hase **E**pitaxy

(A)PD: (**A**valanche) **P**hoto**D**iode

PECVD: Plasma **E**nhanced **C**hemical **V**apor **D**eposition

PhC: **P**hotonic **C**rystal

PIC: **P**hotonic **I**ntegrated **C**hip

PNR: Photon-**N**umber **R**esolving

(TR) μ PL: (**T**ime-**R**esolved) **m**icro**P**hoto**L**uminescence

PMMA: Poly(**M**ethyl **M**eth**A**crylate)

(SK)QD: (**S**transki-**K**rastanov) **Q**uantum **D**ot

QIP: Quantum **I**ntegrated **P**hotonics

QM: Quantum **M**echanics

Acronyms

QW: Quantum Well

QWR: Quantum WiRe

RIE: Reactive Ion Etching

S/T-EM: Scanning/Transmission Electron Microscope

SNSPD: Superconducting Nanowires Single-Photon Detector

TE-/TM-Ga/In: TriEthyl-/TriMethyl-Gallium/Indium

US: UltraSound

WG: WaveGuide

Table of contents

Remerciements.....	i
Abstract.....	iii
Keywords.....	iv
Acronyms	v
Table of contents.....	vii
Chapter 1	Introduction..... 1
1.1	Quantum-enabled technologies 1
1.1.1	Quantum information science 1
1.1.2	Quantum integrated photonics 3
1.2	Solid-state quantum emitters: semiconductor quantum dots..... 6
1.2.1	Quantum-confined electrons..... 6
1.2.2	Semiconductor quantum dots 7
1.2.3	Types of semiconductor quantum dots..... 13
1.3	Photonic crystal structures..... 15
1.3.1	Photonics bands and bandgaps 15
1.3.2	Photonic confinement in photonic crystal structures..... 16
1.4	Quantum dots in photonic crystals..... 18
1.4.1	Radiative transitions in photonicallly-modified environments 18
1.4.2	Technological challenges..... 23
1.5	Scope and aim of this thesis 24
Chapter 2	Numerical and experimental methods 26
2.1	Design of the photonic crystal structures..... 26
2.1.1	Constraints of QD embedding..... 26
2.1.2	Solving numerically Maxwell's equations..... 27
2.1.3	Effects of refractive index dispersion 30
2.1.4	Tailored-potential PhC cavities 32
2.2	Embedding pyramidal site-controlled QDs in PhC structures 34
2.2.1	Substrate preparation for QD growth 34
2.2.2	Growth and characterization of pyramidal site-controlled QDs..... 36
2.2.3	Optical characterization of QDs arrays..... 37
2.2.4	Photonic crystal structure fabrication..... 38
2.3	Micro-photoluminescence (μ PL) spectroscopy..... 40

Table of contents

2.3.1	Micro-PL setup.....	40
2.3.2	Spatial imaging of PL spectra	42
2.3.3	Time-resolved PL spectroscopy.....	44
2.4	Conclusion of chapter and perspectives.....	45
Chapter 3	Defect-potential photonic crystal cavity.....	47
3.1	Defect-potential cavity : concept and computed mode structure	47
3.1.1	Concept.....	47
3.1.2	Optical mode structure of a defect-potential cavity	48
3.1.3	Binding energies of the defect modes.....	53
3.1.4	Effects of disorder.....	54
3.2	Fabrication of defect-potential cavities.....	58
3.3	Observation of defect modes	59
3.3.1	Defect mode spectra.....	59
3.3.2	Defect modes Q-factors	64
3.3.3	Experimental binding energies	65
3.4	Integration with single site-controlled QDs	67
3.4.1	Selective excitation of the V-polarized $\#0M(0)$ defect mode.....	67
3.4.2	Weak coupling of a site-controlled QD with the V-polarized $\#0M(0)$ defect mode.....	69
3.4.3	Selective excitation of the H-polarized $\#0\Gamma(1)$ defect mode	73
3.4.4	Weak coupling of a site-controlled QD with the H-polarized $\#0\Gamma(1)$ defect mode	74
3.5	Conclusion of chapter and perspectives.....	76
Chapter 4	Tilted-potential photonic crystal cavity	77
4.1	Tilted-potential photonic crystal cavity: concept.....	77
4.1.1	From defect-potential to tilted-potential PhC cavities	77
4.1.2	Analytic solutions.....	78
4.1.3	Structure parameters.....	79
4.2	Tilted-potential photonic crystal cavity: computed mode structure.....	80
4.2.1	Optical mode structure	80
4.2.2	Extraction of a figure of merit: dE/dx , sensitivity to parameters	84
4.2.3	Effects of disorder.....	85
4.3	Fabrication of tilted-potential photonic crystal cavities	89
4.4	Observed optical mode properties	90
4.4.1	Optical mode spectra	90
4.4.2	Airy-Bloch modes Q -factors	94
4.4.3	Experimental energy-position slopes dE/dx	95
4.5	Integration with single site-controlled QDs	96
4.5.1	Selective excitation of Airy-Bloch modes.....	96
4.5.2	Weak coupling of a single site-controlled QD with an Airy-Bloch mode.....	99

4.6	Conclusion of chapter and perspectives.....	103
Chapter 5	Towards a functional integrated QD-PhC device.....	105
5.1	Typical functional devices and their experimental model.....	105
5.1.1	Example of functional integrated QD-PhC devices.....	105
5.1.2	Experimental model.....	107
5.2	Fabrication of the model structure.....	118
5.3	Observation of the optical mode structure.....	119
5.4	Quasi-resonant pumping of integrated single site-controlled QDs.....	122
5.4.1	Strategy of excitation.....	122
5.4.2	Quasi-resonant excitations.....	124
5.5	Conclusion of chapter and perspectives.....	129
Chapter 6	Conclusions of thesis and outlooks.....	131
6.1	Conclusions of thesis.....	131
6.2	Future directions.....	133
Appendix A	137
Appendix B	139
Appendix C	143
Contributions	147
Bibliography	149
Publications and conferences	165
Curriculum-Vitae	167

Chapter 1 Introduction

The beginning of the 20th century witnessed the birth of the foundations of Quantum Mechanics (QM) by the brightest scientific minds. It rapidly became one of the most successful theories of modern physics, with supporting experiments and predictions to never seen before levels of precision.

QM explains physical processes at nanometric scales in terms of probabilities for observing specific outcomes. The physical systems are represented by states in a complex Hilbert space, and their time evolution is governed by the system Hamiltonian accounting for the relevant physical interactions. Its application to atomic and sub-atomic systems led to the *first quantum revolution*, which enabled, to cite a few, applications such as lasers, semiconductor electronics, and magnetic resonance imaging technologies, with their large impact we know today.

Currently, at the beginning of the 21st century, a *second quantum revolution* is happening. Concepts of QM are being further exploited towards building artificial quantum systems, typically at the nanoscale, that can simulate many of the non-classical effects known in natural quantum systems such as atoms and molecules. This has led to the emergence of a new field, Quantum Information Science, in which these quantum technologies are elaborated and used in new applications (see **Fig. 1:1**). One of these nanotechnologies is quantum nano-photonics, in which quantum mechanical states of light are generated and employed towards applications in quantum computing, communications and sensing.

In parallel, integrated photonics, the analog of integrated electronics for light processing, has been developed in the last 50 years to meet the ever-growing demands in data bandwidths and to complement the attributes of electronics. This has led to the realization of compact on-chip photonic devices and circuits for processing classical light, especially for applications in optical communications and sensors. Applying integrated photonics concepts to the manipulation of quantum states of light, such as single photons, is at the focus of current research and is expected to lead to a new generation of quantum integrated photonics (QIP) for handling quantum light.

The effort in this thesis work has been focused on this vision, attempting to produce and analyze novel QIP chips combining site-controlled quantum dots (QDs) and photonic crystal (PhC) nanostructures. The basic features of these concepts and technologies are briefly reviewed in this chapter.

1.1 Quantum-enabled technologies

Several quantum-enabled technologies, belonging to the field of quantum information science are presented in this section. In particular, the choice of quantum integrated photonics is motivated.

1.1.1 Quantum information science

The fundamental properties and assets a quantum state have, boil down to five ingredients:

- **Superposition:** the possibility of a single object to be described simultaneously in a variety of states (sometimes orthogonal), the most popular depiction is the paradox of Schrödinger's cat thought experiment. It is key to the generation of probabilistic outcomes.
- **Coherence:** the ability of the various wave components to have a constant relative phase between them. It is key to the realization of visible interference effects; without coherence, quantum effects are smeared out.
- **Entanglement:** the ability to describe several objects as a single entity that is not separable as combinations of the individual objects. The objects have perfectly correlated behaviors. It is key to non-locality.

- Tunneling: the ability of a wavefunction to penetrate an energy barrier, which in a classical framework is forbidden. It is key to delocalization, or connectivity.
- No-cloning: no unitary process can make a perfect copy of an unknown arbitrary quantum-state without altering the original quantum state. A quantum state can be destroyed in order to be transferred somewhere else, but a copy cannot co-exist independently of the original object. It is key to secure encryption.

Focusing on the sub-field of Quantum Information Science, several physical platforms have been developed in order to employ these quantum concepts towards simulation, communication and metrology (see Fig. 1:1).

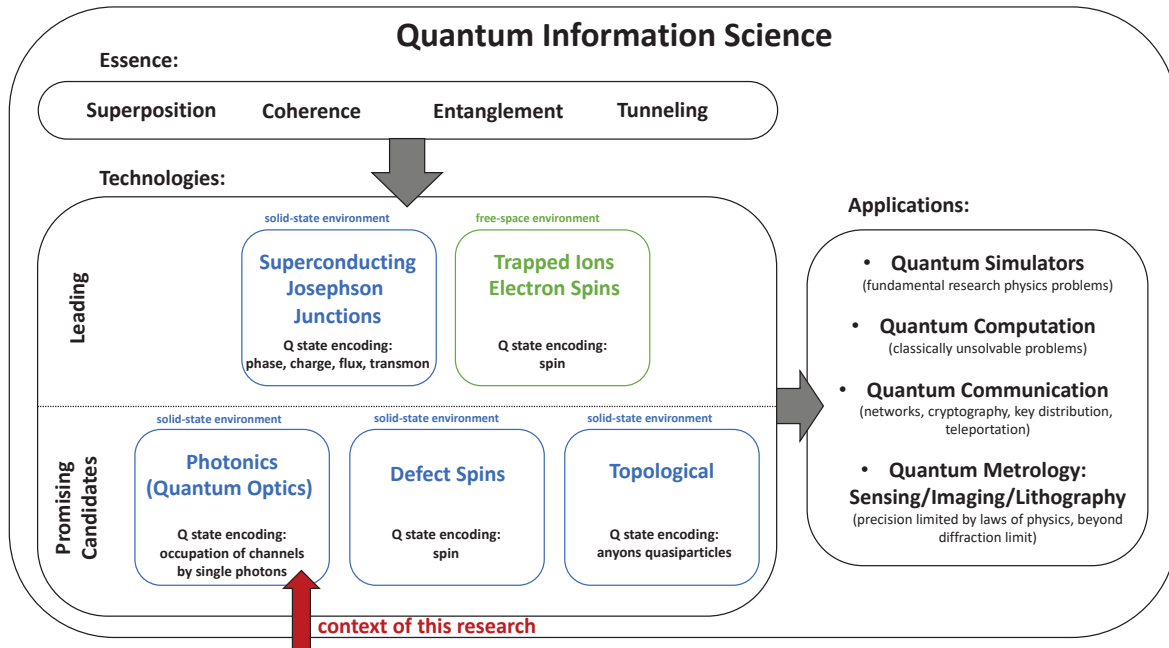


Fig. 1:1 – Major quantum concepts, platforms and applications under research and development. The context of the work presented in this thesis is indicated.

The leading technologies for defining and manipulating quantum states are superconducting Josephson junction circuits [1], [2] and ion traps [3], [4]. In the former, currents and magnetic fluxes in superconductors are used to encode quantum bits (qubits), whereas in the latter electron spins of ions trapped in magnetic fields carry the qubit information. The other promising candidates are photonic circuits [5], [6], silicon CMOS circuits [7]–[9] and topological circuits [10], [11]. In the first case, qubits are encoded by the occupation of optical channels with indistinguishable single photons. In the second case, quantum information is held by the states of defect spins defined in silicon by the application of electric fields using gate electrodes. In the third case, it is encoded by the states of multiple quasiparticles (anyons).

These physical platforms are being investigated for applications in several emerging quantum technologies.

In quantum simulators, the physics of a quantum system that is difficult to manipulate conventionally can be probed by mapping the objects to the coupled qubits of an analog system. The physical interaction is encoded through a tailored Hamiltonian. This allows to naturally address fundamental issues, by reproducing phase transitions between states of matter arising in the many-body problem [12]. To simulate the mechanisms of photosynthesis [13] and try to understand why it is so efficient. Or to compute dissociation energies of chemical bonds [14] to eventually develop new drugs.

In quantum computers, qubits are used instead of classical bits to perform massive parallel processing efficiently thanks to superposition, entanglement and large Hilbert spaces. A series of one or two qubits logical gates are applied onto arrays of coupled qubits to control the probabilities of outcomes. Qubits are eventually projected onto classical bits. For specific problems, this dramatically reduces the simulation time compared to a classical

digital computer. Quantum computers are the focus of influent actors such as IBM, Google, Rigetti, Microsoft, IonQ and D-Wave. A chip with several qubits is already accessible through a remote Cloud service [15].

In quantum communication, perfect secrecy sharing of encrypted data between users is ensured by the laws of QM and the no-cloning theorem. Quantum networks are making an appearance, with first commercial applications of quantum-key distribution through local fiber networks available [16], [17], eventually extended in between cities and countries with free-space space-born links [18]–[20]. These rely on developments in quantum teleportation of quantum states [21], quantum memories and repeaters [22], [23] by entanglement swapping. It may lead one day to the appearance of a Quantum Internet [24].

Among the branches of quantum metrology [25], [26], highly sensitive devices can be developed for enhanced diagnosis or navigation purposes. Color centers of nano-diamonds [27] and atomic vapor cells [28] can sense weak local magnetic fields. Cold atoms matter-waves [29] can detect fractions of rotation in Sagnac gyroscopes. Fibers based on Raman [30] can detect small gradients of temperature over distances. Gravitational-waves detectors are based on squeezed-states interferometry [31]. In terms of imaging, quantum ghost imaging [32], [33] uses the perfect correlation of entangled pairs of photons to make images in noisy environment with an improved signal-to-noise ratio (SNR). Quantum telescopes [34], [35] could enhance the sharpness of images by gain amplification of imperfectly cloned photons and computation of centroids. Similarly, quantum lithography techniques using entangled NO-ON states [36] can imprint features beating the diffraction limit.

Overall, the understanding of quantum mechanics will also allow better energy management, with extremely efficient processes, involving only a few quanta, for all-optical switching [37] and energy harvesting [38]. The playground is seemingly endless.

1.1.2 Quantum integrated photonics

This thesis narrows down on the use of quantum optics within the field of quantum information science and technology [39]. Indeed, photons do not interact with each other in most circumstances, they travel fast and possess several degrees of freedom: wavelength, spin and orbital angular momenta. Besides advantages in applications that these features offer, the field of quantum photonics has also become a testbed for quantum information science experiments.

Photonic quantum states can be encoded with either deterministic streams of single photons or clusters of N entangled photons. The generation of pairs ($N=2$) correlated in either frequency or polarization is ensured by cascaded or non-linear emission processes. These occur typically in atomic cascades [40], [41], and in crystals with the $\chi^{(2)}$ -based spontaneous parametric down conversion (SPDC) and $\chi^{(3)}$ -based spontaneous four-waves mixing (SFWM). Barium Boron Oxide (BBO) [42], Periodically-Poled Lithium Niobate (PPLN) [43] or Potassium Titanyl Phosphate (PPKTP) [44] are the materials of choice for such applications. If only one photon is required for the process, the detection of one of the two, the idler, heralds the presence of the other, the signal. Alternatively, single photons are naturally produced by atom-like transitions [45]–[50] that involve the de-excitation or recombination of only a few charge carriers at a time.

Photons wavepackets can then be manipulated to encode quantum information through time-bin entanglement [51], frequency-bin entanglement [52], polarization-entanglement [42], orbital angular momentum entanglement [53] or path-entanglement [54]–[58]. In particular, path-entanglement relies on the use of beam-splitters (BS) to split an input stream of single photons in several output spatial modes, and elements to modify the relative phases of the photons occupying these spatial modes. This is done, for instance, with a Hanbury-Brown-Twiss (HBT) setup [59], using a balanced 50/50 neutral beam-splitter, an adjustable delay line and detectors to evaluate the photon statistics with the $g^{(2)}$ correlation function. If the two arms are equivalent, true single photon emission is certified by an anti-bunching behavior. Successive single photons can be synchronized by two analogous methods. The first consists in having the early photon travel a longer distance. The second consists in slowing down the early photon by altering the properties of the medium in which it propagates. By doing so, two single photons can be recombined by spatial overlap on a BS. In normal circumstances photons do not interact; however, if they are

indistinguishable, a non-linearity can manifest thanks to quantum interferences. The probabilities of exiting in independent outputs mutually then cancel out. Only the highly correlated outcomes remain where both single photons are paired together in one output or the other. This effect is known as the Hong-Ou-Mandel effect (HOM) [60].

Integrated electronics benefited from the compactness of micro- and nano-fabrication techniques. They provide means for a denser integration of components, the creation of more efficient and complex novel devices while also keeping the prices down, thanks to streamlined manufacturing processes. It appeared logical to expect that Quantum Photonics would benefit from the development of integrated chips as well. Furthermore, tiny chips are easier to isolate from interactions with the environment, in order to preserve quantum coherence. Quantum Integrated Photonics (QIP) was thus born. Borrowing from the knowledge of condensed matter-light interactions, QIP also provides solutions for enhanced physical mechanisms such as optical absorption and spontaneous and stimulated emissions.

As an illustration, let us specifically consider the case of a HOM and HBT quantum photonic device (see **Fig. 1:2**), with which it is possible to analyze the characteristics of single photon states. Such a device can be split into two main parts: the part where the photons are processed during their propagation, and the part where the outcomes of the manipulation are detected. Three versions of these devices and the related single photon sources, with increasing level of compactness and integration, are illustrated in **Fig. 1:2**.

In **Fig. 1:2(a)**, the device is realized at the macroscopic scale, using free-space or fiber optics. The generation of polarization-entangled pairs of photons can be realized with the pumping of a SPDC BBO crystal mentioned earlier. For the processing stage, the use of a simple $\lambda/2$ -plate can correct for the polarization of the second photon so that the two are indistinguishable. A movable corner-cube can ensure the synchronized recombination of the two photons over a balanced 50/50 non-polarizing BS. Due to the quantum interferences within the HOM, the two indistinguishable photons exit together in either the path towards detector A or the path towards detectors B & C. A second balanced 50/50 non-polarizing BS can reverse the HOM effect and split the two photons. Detector A, B and C click whenever a photon hits them, but detector A [61] can ensure that two photons were detected at once, while detectors B and C can be more conventional Boolean single-photon avalanche photodiodes (SPADs). Naturally, detector A can be replaced by a combination of a beam-splitter and two SPADs such as B and C [62]. The coincidence counts on the three detectors provide the information on the quality of the single photon stream statistics via the measured $g^{(2)}$ function [63], [64] and the fidelity of the wave-packets via the visibility of the HOM dip [65]–[70].

Fig. 1:2(b) illustrates a possible integration on a chip at the mesoscopic scale, considering state-of-the-art advances. For the stage of generation of single photons, SPDC and SFWM sources can be integrated, using, respectively, PPLN [71] and Si micro-rings [72]. A possible solution to fight the probabilistic photon generation is to combine and switch the fluxes or spatially multiplex non-linear sources to generate a deterministic single photon stream [73]. Currently, these sources require several dozens of milli-Watts of power and are pumped by external commercial lasers or laser diodes. The integration of on-chip lasers is a challenging issue. Lasers on silicon are still a subject of ongoing research [74], due to a non-trivial hybrid integration of III-V-based components with Si substrates [75]. For the processing part, however, many reliable components in the CMOS-compatible silicon platform have originally been developed for optical interconnects and classical photonic integrated chips operating at telecommunication wavelengths. The beam-splitters can be realized with low-loss passive ridge waveguides that can be fabricated with silica on silicon [76], even directly written in silica with a laser [77]. A tunable delay can be implemented by the cascading of ring resonators wavelength-tuned with heaters [78]. Detection is often based on NbN or NbTiN superconducting nanowires single-photon detectors (SNSPDs) which now can be fabricated on top of the waveguides [79].

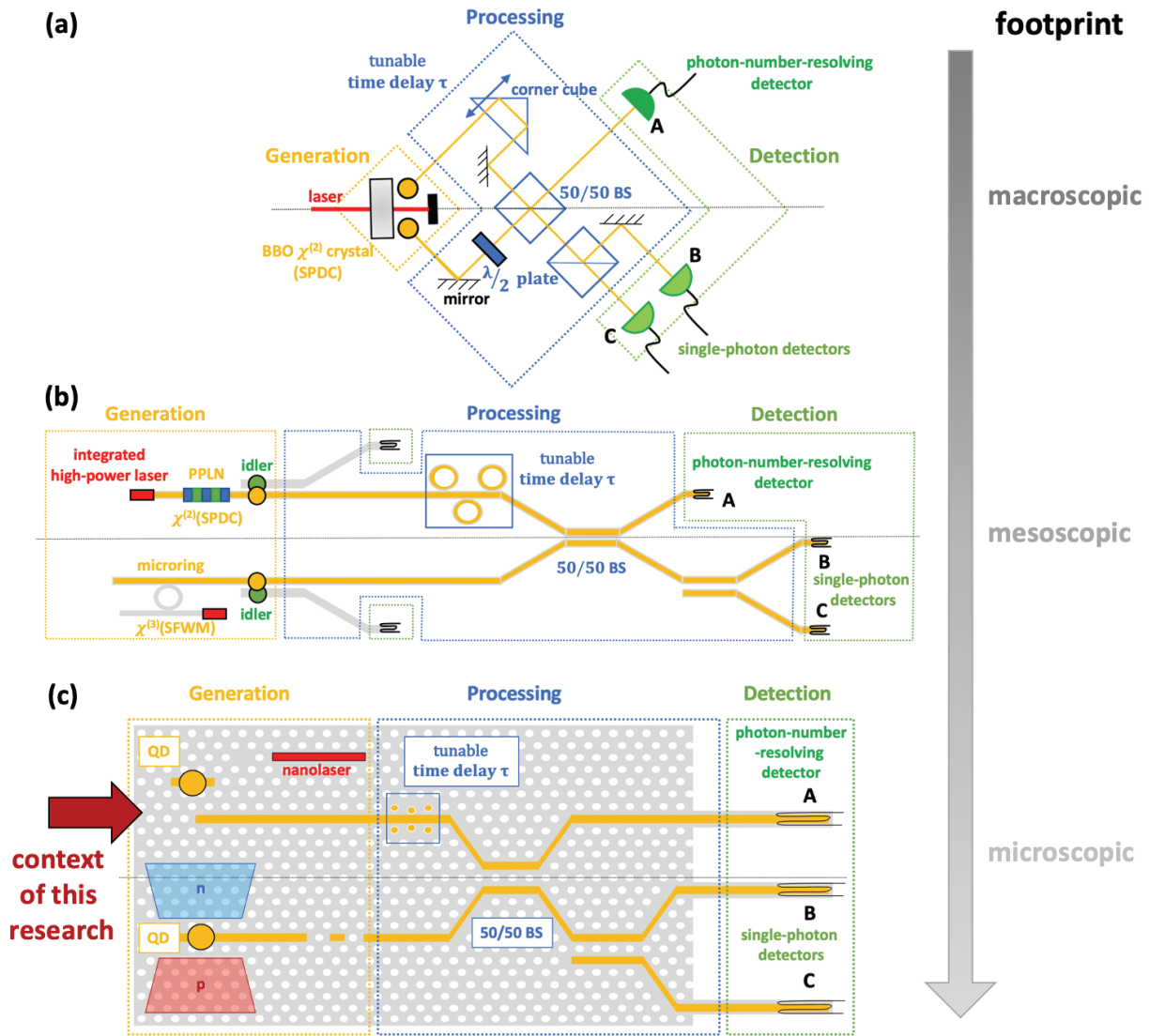


Fig. 1:2 – Schematics of possible realization of a Hong-Ou-Mandel + Hanbury-Brown-Twiss quantum devices at three different scales: (a) macroscopic ($\sim 10^{-1}$ - 10^1 m), (b) mesoscopic ($\sim 10^{-4}$ - 10^{-1} m) and (c) microscopic ($\sim 10^{-5}$ - 10^{-4} m). This device can be useful for assessing the quality of single photon generation. The three regions of generation of single photons (blue dot-line), their processing (yellow dot-line) and their detection (green dot-line) are highlighted. Several elements of already existing technologies are shown.

Finally, **Fig. 1:2(c)** illustrates a possible on-chip integration at the microscopic scale. Here research has been focused on the promising tracks of quantum dot (QD) emitters interfaced to GaAs photonic crystals (PhC) circuits [80], [81]. The quasi-deterministic generation of indistinguishable single photons by QDs is nearly perfect [82]. By themselves, QDs emit in all directions of space. Placing these emitters in regular ridge waveguides would be rather inefficient. PhC structures provide a medium in which the optical density of states is engineered to ensure an anisotropic and frequency-selective confinement of light. In these structures the electric fields can be squeezed into tiny volumes of space producing strong vacuum fluctuations. The resulting Quantum Electrodynamics (QED) light-matter interaction of the quantum emitters' dipole with these electric fields enhances the spontaneous emission in specific directions of space, so that the extracted bright flux of photons can be funneled into specific optical channels [83], [84]. Currently, the generation of single photons is achieved by resonant pulsed excitation with an external laser; the integration of an on-chip means of optical pumping has not been solved yet. Electrically injected QD diodes have been reported [85]–[87], but integration in PhC structures is challenging due to the problem of achieving good optical confinement with doping and metallic contacts. Single photons can be further purified by narrow resonant-tunneling coupling. Time delays could theoretically be implemented with adjustable PhC slow-

light [88] sections to synchronize the emission of two spatially multiplexed QDs. As of today, state-of-the-art fabrication cannot prevent Anderson localization [89]–[94] and important propagation losses [95]–[97] near the photonic band-edges. A balanced beam-splitting operation can be realized with evanescently coupled PhC waveguides or suspended beams [98]. Detection here also can also rely on nanowire SNSPDs [79], [99], [100]. Currently, the most advanced implementations of such QIP circuits rely on hybrid schemes, merging technical solutions at various scales or with different materials [101]. Recent examples consist in QD-based single photon diodes butt-coupled [102], [103] to a waveguide-chip. However, to date a true integrated solution in a monolithic platform is yet to be seen.

Moving towards this goal is the focus of this thesis.

1.2 Solid-state quantum emitters: semiconductor quantum dots

In this section, we detail how semiconductor QDs can trap charge carriers by quantum confinement in a reduced volume in space, and efficiently lead them to recombine to generate single photons. The mechanisms that are detrimental to the purity of the single photon emission are explained. The various fabrication techniques to integrate semiconductor QDs are mentioned.

1.2.1 Quantum-confined electrons

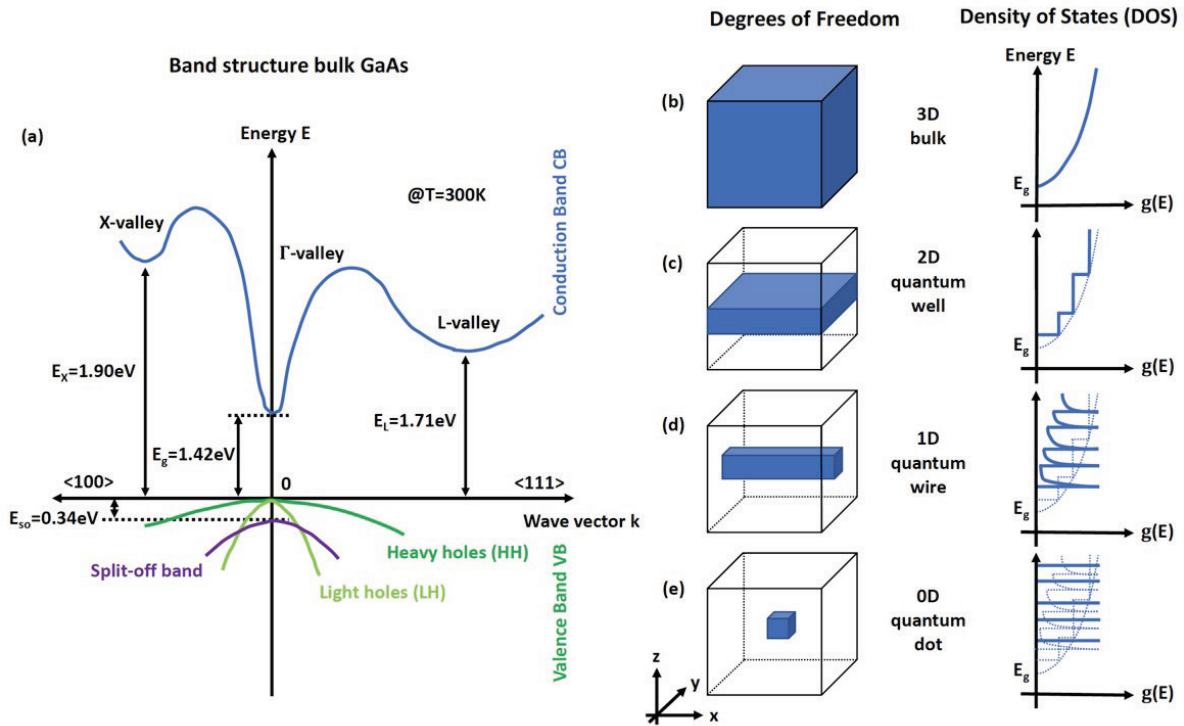


Fig. 1:3 – (a) Conduction band and valence bands bandgap in bulk GaAs at T=300K. (b-e) Degrees of freedom of motion and density of states for electrons with reduction of dimensionality. (a) is adapted from [104].

A solid-state crystal is a periodic arrangement in space of atoms surrounded by electrons. The periodic ordering gives electrons the ability to delocalize and propagate freely across the crystal. Solving the stationary Schrödinger's equation for electrons in the periodic potential of these atoms:

$$\mathcal{H}\phi(\mathbf{r}) = \left(-\frac{\hbar^2}{2m_0} \nabla^2 + V(\mathbf{r}) \right) \phi(\mathbf{r}) = E \cdot \phi(\mathbf{r}), \quad (\text{Eq. 1:1})$$

yields the electronic bands structure of the system. It specifies at which eigen-energies the electrons can propagate as a function of the direction, specified by a wavevector \mathbf{k} . The corresponding eigen-vectors, or wavefunctions, indicate the spatial distributions of the electrons.

In the particular case of semiconductors, bandgaps of typically few electron-volts (eVs) in energy appear between conduction and valence bands, forbidding the propagation of electrons over the full irreducible Brillouin-Zone. Such materials are insulators with interesting optical properties, especially if the bandgap is direct over the Γ ($\mathbf{k}=\mathbf{0}$) point. A schematized band structure of bulk Gallium Arsenide (GaAs), a III-V material well-known for the for producing efficient infrared lasers, is presented in **Fig. 1:3(a)**. In this case, by the use of excess energy, e.g., in the form of a photon, electrons of the valence bands can be promoted to the conduction band, leaving behind an absence of electrons, a hole, in the valence band. After a certain lifetime, possibly involving intermediate processes, the two charge carriers may recombine radiatively and generate a photon with energy given by the energy difference between the recombining states. In the bulk, hot electrons with kinetic energy are free to diffuse in the 3 dimensions of space, making recombination processes quite inefficient. Therefore, reducing the degrees of freedom by quantum confinement in one or more directions gives a means for increasing the control over the motion of the charge carriers, and can lead to increase recombination efficiency. This is one reason why efficient semiconductor lasers are based on quantum wells [105], and efficient photovoltaic cells are based on nanowires (quantum wires) [106]. With the deprivation of degrees of freedom, the density of available states $g(E)$ in a band is altered. As shown in **Fig. 1:3(b-e)**, for bulk $g(E) \propto (E-E_g)^{1/2}$, for a quantum well $g(E) \propto \sum \theta(E - E_i)$ where θ denotes the Heaviside distribution, for quantum wires $g(E) \propto \sum (E - E_i)^{-1}$ and for quantum dots (quantum boxes) $g(E) \propto \sum \delta(E - E_i)$ where δ indicates a Dirac function. Due to the discrete energy spectrum, quantum dots are sometimes referred to as “artificial atoms”. The same arguments hold also for holes in the valence bands, except that their energy axis points downwards in the corresponding diagrams.

1.2.2 Semiconductor quantum dots

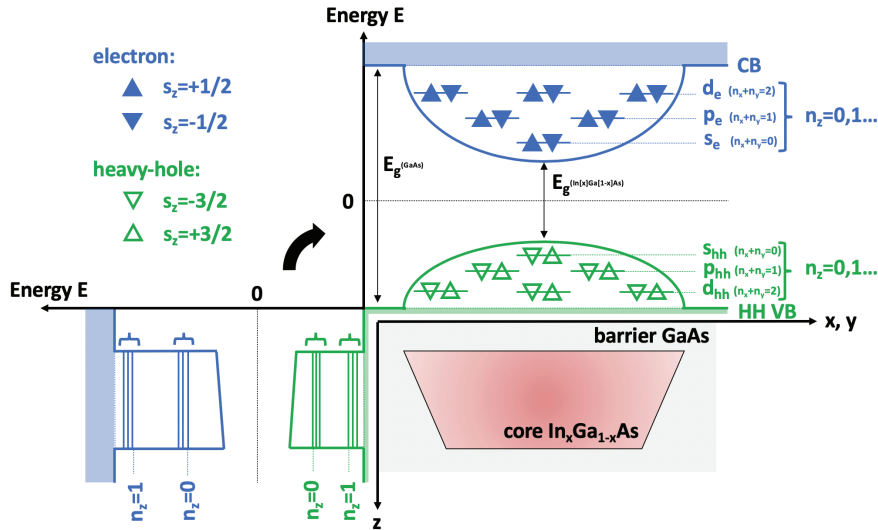


Fig. 1:4 – Schematic illustration of the confinement of electrons and heavy-holes by an $\text{In}_x\text{Ga}_{1-x}\text{As}/\text{GaAs}$ QD. Quantum confinement along the height z with n_z principal quantum number. Parabolic confinement along the base $x-y$ direction, with depiction of s, p, d shells and their maximum occupation.

The QDs covered in this thesis are thin ($<10\text{nm}$) and rather wide in the wafer plane ($\sim 20\text{-}30\text{nm}$). The confinement is thus anisotropic, very strong across the thickness (z -direction) and more relaxed with an approximately parabolic confinement potential in the (x, y) plane. The effect of quantum confinement in typical $\text{InGaAs}/\text{GaAs}$ QDs is schematized in **Fig. 1:4**. The number of levels and shells depicted is arbitrary and may vary from QD to QD depending on the core/barrier materials, potential depth, geometry, and size. From this point on, we focus on heavy-holes because the degeneracy of heavy- and light-holes is lifted by the vertical confinement and strain built up by

the lattice mismatch of core and barrier materials [107], [108]. The eigen-energies of the confined states can be approximated by [109]:

$$E_{n_x, n_y, n_z} = \pm \left(\frac{E_g^{\text{In}[x]\text{Ga}[1-x]\text{As}}}{2} + \hbar\omega_i(n_x + n_y + 1) + \frac{\hbar^2}{2m_i^*} \left(\frac{\pi n_z}{L_z} \right)^2 \right) [\text{eV}], \quad i = e, hh \quad (\text{Eq. 1:2})$$

where the integers n_x, n_y, n_z are the quantum numbers related to the respective real space directions. The first term represents the bandgap of the bulk semiconductor. The second term stems from the quantization of the harmonic oscillator potential produced by the parabolic confinement. The last term is associated with the strong vertical confinement. Concretely, the quantum well-like confinement along z yields discretized bands that are further split in shells labelled as s, p, d, ..., by analogy to the terminology for atoms. Due to Pauli's principle, which states that no two fermions can be in the same quantum state, the occupancies of the shells are limited. The s-shell can accommodate 2 electrons (holes), the p-shell 4 of them, while the d-shell up to 6. An electron (a heavy-hole) occupying a shell is further characterized by its spin, with a characteristic projected value of $s_z = \pm 1/2$ ($= \pm 3/2$) and orbital angular momentum $L_z = |n_x - n_y|$ [109], resulting in total angular momentum projection of $J_z = S_z + L_z = \pm 1/2$ ($\pm 3/2$) in the particular case of the s-shell electrons (heavy holes).

The associated eigen-vectors, i.e. wavefunctions, of the confined electrons (heavy-holes) can be expressed as:

$$|\phi_i(\mathbf{r})\rangle = |F_i(\mathbf{r})\rangle |u_i(\mathbf{k} = \mathbf{0}, \mathbf{r})\rangle |s_{z,i}\rangle, \quad i = e, hh \quad (\text{Eq. 1:3})$$

The left term is the envelope function, the center term corresponds to the Bloch crystal term evaluated at the Γ point, and the last term is associated with the spin state.

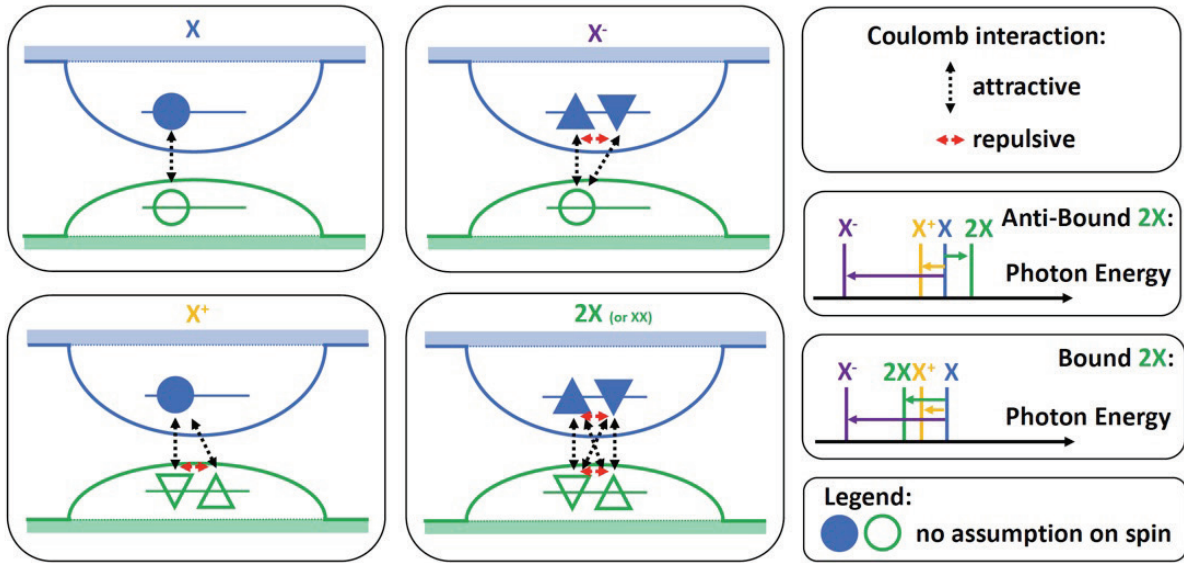


Fig. 1:5 – Schematic of the approximation of a QD as a 2-Levels System (2-LS) when considering only the s_e & s_{hh} shells and their transitions. Depictions of the four lowest energy transitions: X (exciton), X⁻ (negatively charged exciton, or negative trion), X⁺ (positive trion), 2X (bi-exciton, also denoted XX). Arrows represent Coulomb correlations.

Radiative recombination followed by emission of a photon from a QD can occur when at least two charge carriers (an electron and a hole) are trapped by the dot, see **Fig. 1:5**. Coulomb interaction between the charge carriers, however, modifies the emission energy of the resulting charge complexes. For a single pair of trapped electron and hole, a neutral exciton (X) is formed, with a finite binding energy that red shifts the energy of the emitted photon with respect to the photon energy corresponding to an unbound e-h pair. An electron in excess to the X forms the negatively charged exciton (X⁻), also called negative trion. A hole in excess to the X, forms the positive trion (X⁺). Eventually, with a second pair of trapped electron and hole, a double exciton or bi-exciton is

formed (2X). Other species involving a lifted degeneracy of the heavy-hole and light-hole valence bands are described in [110]. The binding energies can be estimated by the Coulomb interaction:

$$V_{i,j}^C = \langle \phi_i(\mathbf{r}_i), \phi_j(\mathbf{r}_j) \left| \frac{q_i q_j}{4\pi\epsilon_0\epsilon_r |\mathbf{r}_i - \mathbf{r}_j|} \right| \phi_i(\mathbf{r}_i), \phi_j(\mathbf{r}_j) \rangle [eV], \quad i, j = e, hh \quad (\text{Eq. 1:4})$$

between the trapped charge carriers. It is attractive (negative potential energy) for opposite signs of charges, and repulsive (positive) for same signs. The energies of the four excitonic species can be written as follows:

$$E_X = E_e - E_{hh} - V_{e,hh}^C [eV], \quad (\text{Eq. 1:5})$$

$$E_{X-} = E_X + (E_e - V_{e,hh}^C + V_{e,e}^C) = E_X + E_{X,X-}^{bind},$$

$$E_{X+} = E_X + (-E_{hh} - V_{e,hh}^C + V_{hh,hh}^C) = E_X + E_{X,X+}^{bind},$$

$$E_{2X} = E_X + (E_X - 2V_{e,hh}^C + V_{e,e}^C + V_{hh,hh}^C) = E_X + E_{X,2X}^{bind},$$

where E_e and E_{hh} are evaluated with (Eq. 1:2). The additional term, the binding energy, is either negative, in which case a species is bound to the neutral exciton, or positive, and thus it is anti-bound [111]. A typical spectral configuration encountered in the pyramidal site-controlled QDs considered in this thesis is illustrated in **Fig. 1:5**. Identification of the spectral lines [110] can be done with a combination of numerical **k.p** modeling based on TEM observations, and power-dependent, polarization-resolved micro-photoluminescence measurements.

The recombination of an electron and a heavy-hole, in addition to energy conservation, follows restrictive physical selection rules, which dictate the optical properties. The momentum matrix element of such a process is stated by the following formula [80]:

$$\mathbf{P} = \langle \phi_{hh} | \mathbf{p} | \phi_e \rangle = \langle F_{hh}(\mathbf{r}) | F_e(\mathbf{r}) \rangle \langle u_{hh}(\mathbf{0}, \mathbf{r}) | \mathbf{p} | u_e(\mathbf{0}, \mathbf{r}) \rangle \langle s_{z,hh} | s_{z,e} \rangle, \quad (\text{Eq. 1:6})$$

which is non-zero (conservation of momentum) if:

- i. the envelope wavefunctions F have the same parity.
- ii. the Bloch terms have opposite parity (the action of operator \mathbf{p} reverses the parity of the bra or ket on which it is applied)
- iii. the total angular momentum is conserved, the sum of the two spins must be compatible with the possible helicities of the photons.

In accordance with point ii., the Bloch terms of electrons are known to have an s parity (sphere-like) while holes have a p parity (donut-like, with a node). Based on these, the ket of the confined charge carriers are rewritten as [80]:

$$|\uparrow\rangle = |u_e^s\rangle |\Delta\rangle, \quad (\text{Eq. 1:7})$$

$$|\downarrow\rangle = |u_e^s\rangle |\nabla\rangle,$$

$$|\uparrow\rangle = \frac{-1}{\sqrt{2}} \cdot (|u_{hh}^x\rangle + i|u_{hh}^y\rangle)|\Delta\rangle,$$

$$|\downarrow\rangle = \frac{-1}{\sqrt{2}} \cdot (|u_{hh}^x\rangle + i|u_{hh}^y\rangle)|\nabla\rangle,$$

where, as in Fig. 1:4, the blue triangle pointing upwards(downwards) for the electrons have a spin $s_z = +1/2(-1/2)$ and the green triangles of the heavy-holes have $s_z = +3/2(-3/2)$. With such considerations, the optical transition rate due to recombination of the neutral exciton state $|\downarrow\uparrow\rangle$ to empty ground is described by the matrix element:

$$P = \langle g|p|\downarrow\uparrow\rangle = -\langle F_{hh}(\mathbf{r})|F_e(\mathbf{r})\rangle \langle u_{hh}^x|p_x|u_e^s\rangle \cdot \frac{1}{\sqrt{2}} \cdot (\mathbf{e}_x + i \cdot \mathbf{e}_y), \quad (\text{Eq. 1:8})$$

with the last term representing left-handed circular polarization. In fact, for a highly symmetric QD (rotation symmetry), the other transitions $|\uparrow\downarrow\rangle$; $|\uparrow\downarrow\uparrow\rangle$; $|\downarrow\uparrow\downarrow\rangle$; $|\downarrow\uparrow\uparrow\rangle$; $|\uparrow\downarrow\downarrow\rangle$; $|\uparrow\downarrow\uparrow\downarrow\rangle$ are predicted to be circularly polarized. However, in reality, QDs are more often than not anisotropic; the broken symmetry favors more one dipole than the other, but instead of becoming elliptic the polarization ends up linear along x or y [112].

Fig. 1:6 depicts one such situation and details the quantum states along the recombination paths in a QD with fully occupied s-shells. The recombination of a pair of electron and heavy-hole and emission of a photon puts the QD system into superposition states of the neutral excitons. The structural asymmetry lifts the degeneracy of the two neutral excitons, sometimes called X and Y, with a discrepancy in energy named the fine structure splitting (FSS), typically on the order of few to hundreds μeV s. These intermediate exciton states are labelled as bright, for their ability to emit photons while conserving angular momentum. Before decay to the ground state, if the thermal energy $k_B T$ is greater than an activation energy E_a , the trapped electrons can undergo a spin flip, which temporarily turns off such transition. The modified states are known as dark states. They do not exist for the 2X, X, X^+ because the charge carriers can always recombine radiatively. If harnessed, this ability is useful for quantum-state engineering [113].

The emission of entangled photon pairs requires a vanishing FSS. In this case, the polarizations become circular (right-handed and left-handed) as predicted by (Eq. 1:8) [80]. Indistinguishable photons from a cascaded emission require equal photon energies of X and 2X. Simultaneous two-photon emission can also be realized through the virtual “leapfrog” mechanism [114] that requires pumping at $[(E_{X^x} + E_{X^y})/2 + (E_{2X^x} + E_{2X^y})/2]/2$.

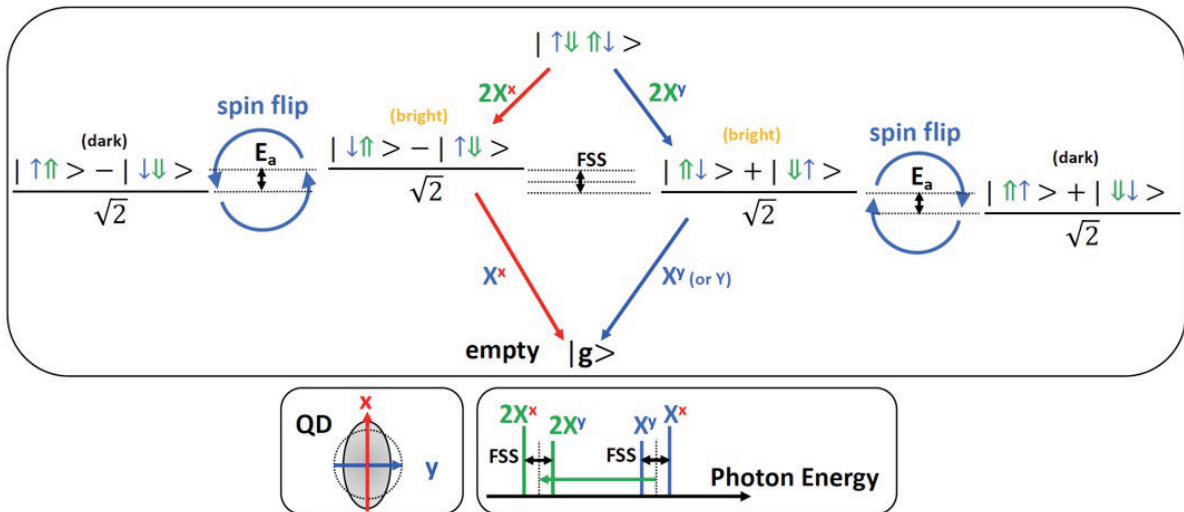


Fig. 1:6 - Depiction of the radiative cascade 2X-X and optical properties in the general case of a slightly asymmetric QD with non-degenerate 2X and X states. The arrows show paths of allowed radiative recombination in which a single photon is emitted.

Similar complex cascaded processes involving the other excitonic species and higher order states of the higher shells also exist.

The oscillator strength of a dipole transition is given by the following formula [80]:

$$f = \frac{2|\mathbf{P}|^2}{(\hbar\omega_0)m_0} = \frac{E_P}{(\hbar\omega_0)} |\langle F_{hh}(\mathbf{r}) | F_e(\mathbf{r}) \rangle|^2 \text{ [adim.]}, \quad (\text{Eq. 1:9})$$

$$E_P = \frac{2|\langle u_{hh}^x | p_x | u_e^x \rangle|^2}{m_0} = \frac{2|\langle u_{hh}^y | p_y | u_e^y \rangle|^2}{m_0} \text{ [eV]},$$

with E_P known as the Kane energy ($\sim 22\text{eV}$ for GaAs) which is a characteristic of the bulk crystal material. The only parameter susceptible to be modified is the term involving the overlap of the envelope wavefunctions of the electrons and holes. It can be adjusted by altering the QDs confinement potentials.

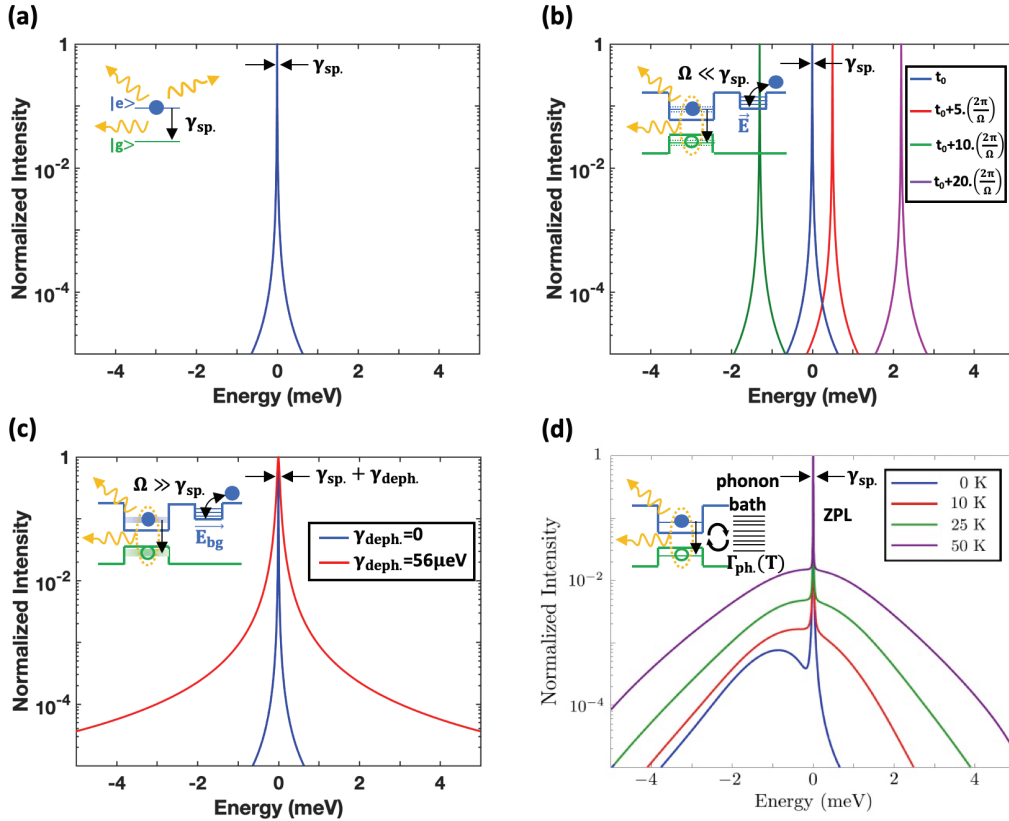


Fig. 1:7 – Schematics of four broadening mechanisms of a QD linewidth. (a) Intrinsic broadening, (b) spectral wandering, (c) pure dephasing, (d) phonon broadening. Reprinted and adapted with permission from [80] for (d).

Ideally, the spectral linewidth of the emitted photon is limited by the finite lifetime of the transition. This is a direct manifestation of the Wiener-Khinchin theorem [115]: the full-width at half maximum (FWHM) of the Fourier-transform limited Lorentzian lineshape corresponds to the spontaneous emission rate $\hbar\gamma_{QD} = \frac{\hbar}{T_2} = \hbar\gamma_{sp.} = \frac{\hbar}{2\tau_{sp.}} = \frac{\hbar}{2T_1}$ (see **Fig. 1:7(a)**), with T_2 the coherence time and $\tau_{sp.}=T_1$ the intrinsic radiative lifetime. In a real QD system, several mechanisms can yield modification and broadening of this spectral linewidth. **(b)** Charged impurities trapped nearby an excited QD will exert a Coulomb interaction on the confined carriers. If the exerted electric field fluctuates slowly over time with respect to the spontaneous emission rate, the field affects the QD quasi

statically with a background. As a direct consequence, the emission line will switch to different energies over a series of emission events, typically across differences of dozens of μeV s to possibly a few meV s. This is known as spectral wandering.

(c) If the electric field of the charged impurities fluctuates faster than the spontaneous emission rate, the QD energy levels broaden due to the averaging of the spectral wandering effect. This effect is known as pure dephasing, because it impacts the phase coherence. The line-shape is effectively broadened into a wider distribution which FWHM is $\hbar\gamma_{QD} = \hbar\gamma_{sp.} + \hbar\gamma_{deph.} = \frac{\hbar}{2\tau_{sp.}} + \frac{\hbar}{T_2^*}$, where T_2^* is the pure-dephasing time. Pure dephasing can be quenched by stabilization of the charged environment, for instance by placing the QD in a p-i-n junction in reverse bias, whereby a static stronger electric field arises and the medium gets depleted of free carriers [116].

As was mentioned before, the QD is situated in a solid-state environment, and thus it can interact with it by means of phonons, quanta of the crystal lattice vibrations. The effect of the phonon bath is depicted in **Fig. 1:7(d)**, based on [80]. The effect of phonon exchange results in spectral tails, manifest even at $T=0\text{K}$. The effect is asymmetric and energy and temperature dependent. At low temperature, the lower energy tail is prominent; the hotter QD transfers heat to the colder lattice in the form of phonons, and the resulting photons have a lower energy. At higher temperature, it becomes more likely for the QD to absorb phonons from the lattice and emit photons of larger energies. The center part of the spectrum is not altered because the phonon density vanishes due to conservation of energy; hence it is denoted the zero-phonon line (ZPL). The most obvious way to curb the effect of phonons is to decrease the lattice temperature, thus measurements are usually carried at cryogenic temperatures of 4-10K reached by conventional liquid helium cooling. Reducing the temperature also plays in favor of radiative recombination efficiency, whereas high thermal energy $k_B T$ can trigger the thermo-ejection of the charge carriers and the dissociation of excitons [117]. The Auger auto-ionization mechanism [117] is also thought to be responsible for the blinking of QD emission.

Any broadening effect outside of the intrinsic radiative lifetime T_1 broadening (Fourier-transform limited $T_2=2T_1$, $T_2^*=0$) deteriorates the purity of single photon emission because it produces a broader spectral content. But it also facilitates interaction between two different QDs by increasing spectral overlap. Pure dephasing and acoustic phonons also provide more opportunities for a QD to couple to a cavity mode detuned in energy [118], [119].

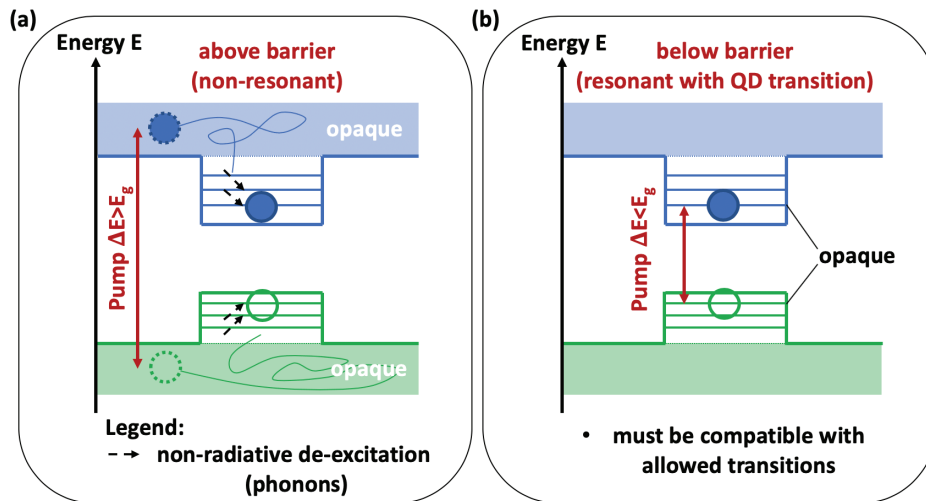


Fig. 1:8 – Schematic of photoexcitation of a QD, left: above barrier, right: below barrier.

Excitation of electron-hole pairs in QDs is typically accomplished via optical pumping or electrical injection of charge carriers. In optical pumping, the QD can be excited with photons of energy either larger (above barrier) or smaller (below barrier) than the bandgap in the barriers of the QD (see **Fig. 1:8**).

(a) In the former case, free photo-generated carriers are created in the region of the barrier material and diffuse around until some of them are eventually captured by the QD, relax to lower energy states via phonon emission, and recombine. (b) In the case of below-barrier excitation, electrons and holes are created directly inside the QD. This process is less efficient, because the low density of states inside the QD reduces the rate of absorption of the pump light. However, this process avoids the “sea” of free charge carriers generated in the bulk material, thus tremendously reducing the possibility of broadening of the QD emission lines by pure dephasing. Such below-barrier excitation is termed “resonant” when the pumping photons have the same energy as that of the QD ground states transition, and “quasi-resonant” when the excited electron-hole pairs populated the excited (e.g., p-states) of the QD. Technically, below-barrier photoexcitation is more difficult to implement because of the need to filter out the intense pumping laser beam in order to efficiently detect the QD photoluminescence signal.

Electrical pumping provides a way to excite the QD quasi-resonantly, avoiding population of the barriers by electron-hole plasma. However, it requires fabricating electrical contacts and doping of the QD barriers, which can also detrimentally affect the quality of the emission spectrum.

1.2.3 Types of semiconductor quantum dots

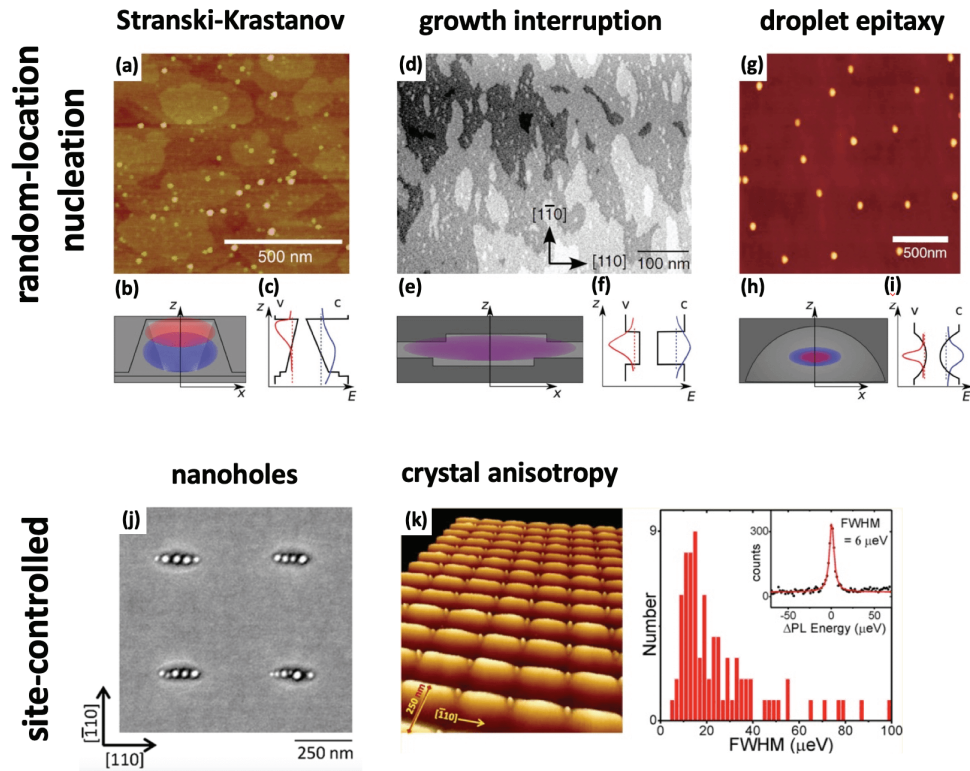


Fig. 1:9 – Fabrication techniques of semiconductor QDs, AFM images. Upper panel: self-assembled dots fabricated by (a) Stranski-Krastanov technique, (d) epitaxial growth interruption, (g) droplet epitaxy; (b-c, e-f, h-i) illustrate the corresponding geometries, potential landscape and carriers wavefunctions; lower panel: site-controlled dots achieved by substrate patterning with (j) nanoholes, (k) ridges and nanoholes relying on crystal anisotropy. The histogram associated with (k) shows a skewed distribution of homogeneously broadened linewidths with a maximum below 20 μeV, extracted from above barrier excitation; (inset) minimum linewidth of 6 μeV limited by pure dephasing. Reprinted with permission from [80] for (a-h), from [120] for (j,k). Copyright 2013 American Chemical Society.

Fig. 1:9 reviews the various types of semiconductor QDs that can be encountered in the literature. We identify essentially two groups, self-assembled QDs that nucleate at random locations, and site-controlled QDs. These can be grown either by Molecular Beam Epitaxy (MBE) [121] or Metal-Organic Chemical Vapor Phase Epitaxy (MOVPE, alternatively named Metal-Organic Chemical Vapor Deposition, MOCVD) [122].

(a-c) illustrate the Stranski-Krastanov (SK) QDs, including the geometry, the resulting potential landscape and the associated confined electron and hole wavefunctions [80]. They form typically with two binary alloys, when depositing for instance InAs on top of a GaAs substrate. As a result of the large lattice mismatch between the two crystals, strain builds up and is eventually relaxed by plastic-deformation, in the form of tiny islands. Adjusting the thickness and composition provides control over the density of the produced SKQDs across few orders of magnitudes. SKQDs are perhaps the most common and well-established type of epitaxial QDs, in large part thanks to a relative ease of fabrication that also provides high-quality optical properties: narrow linewidths and large oscillator strengths. However, they intrinsically suffer from important shortcomings, namely, a very large inhomogeneous broadening of more than 30-50meVs [123] due to the large variety of shapes and dimensions (~ 1 -10nm heights, ~ 10 -100nm widths), and the lack of control over symmetries impact polarization. These QDs grow on a wetting layer [124]–[127] that plays an important role in the carrier feeding mechanisms.

(d-f) illustrate QDs created by an epitaxial growth interruption process of a semiconductor QW layer [128]. The roughness of heterostructure interfaces creates thickness fluctuations, which produce local traps that can bind the excitons of an otherwise 2D quantum well. In such case the lateral confinement is very weak, with broad (~ 100 s nm) but largely overlapping electron and hole wavefunctions acting in favor of large oscillator strengths and efficient recombination. Naturally, there is a complete lack of control over QD symmetry and thus of polarization.

(g-i) illustrate QDs generated by droplet epitaxy [129]. This technique was developed more recently and consists in the evaporation of droplets of group III metals onto a substrate, on top of which group V atoms are deposited and induce crystallization. Controlling the flux and annealing conditions controls the diffusion of the species and produce various nanostructure geometries, ranging from quantum dots to quantum rings, double quantum rings and even nanoholes [130]. Droplet QDs can produce dome-shaped energy potentials that confine very tightly the carriers wavefunctions with elevated in-plane rotational symmetry, which is an asset for polarization control. Narrow linewidths down to 35 μ eV have also been reported [131].

For completeness, we also mention the colloidal semiconductors QDs [132], which are fabricated by nucleation in liquid phases. They are made by perfectly symmetrical quasi-spherical shells of different compositions, e.g., CdSe. Such QD material can be deposited as “inks” on top of surfaces.

At very low surface densities, typically $\sim 10\mu\text{m}^{-2}$, single QDs made as described above can be identified, and then isolated spectrally [133] or by the fabrication of structures around them [134]. Integrated photonic structures incorporating a “single” self-assembled QD can thus be fabricated [135]. However, since there is no correlation between the position of different dots, it is very challenging to place more than one QD in a single photonic structure of specific size, and thus scaling to several-QD systems is severely compromised. Hence the need for techniques offering control over the positions of the QD emitters.

(j) illustrates one such technique. Patterning a substrate with nanoholes etched through a mask induces nucleation to occur preferentially inside them [120]. However, experiments show that the number of dots per nanohole may vary across the substrate, and in particular some holes may be void of QDs, which compromises the deterministic site control nature of the approach.

(k) Lithographically structured substrates, in which various crystalline facets are exposed by etching surface relief patterns, can provide a solution by controlling the surface fluxes of the growth precursors [120]. Using MBE and such structured (100) substrates, QDs grow along the [110] direction in which B-steps are arsenic-terminated, but not along $\bar{1}10$ where A-steps are gallium-terminated. Single QDs can be grown with the proper combination of parameters: in this case, the distance between the A-steps-oriented ridges in which B-steps nanoholes are etched, and the thickness of the buffer layer. The histogram included in (k) illustrates state-of-the-art homogeneous broadening of linewidths of QDs prepared in this way. Linewidths as narrow as 6 μ eV, limited by pure dephasing, are achieved with the growth of a high-purity, thick buffer layer. Record Fourier-transform-limited linewidths ($\leq 1\mu$ eV) can be achieved by resonance fluorescence (RF) and carrier depletion of the barrier with an external electric-field [136], [137] to effectively cancel pure dephasing effects.

The growth of pyramidal site-controlled QDs, discussed in this thesis, relies on MOVPE on (111)B GaAs substrates patterned with inverted pyramids [138], [139]. The QDs form at the sharp tip of the pyramids due to the balance of growth rate anisotropy and capillarity [140], [141]. These mechanisms and relation with the surface patterns ensure site-control of regular QD arrays.

Even when grown in dense arrays, site-controlled pyramidal QDs can be isolated by etching mesas [142], [143] to study the properties of single QDs. Narrow emission linewidths, as narrow as 20 μ eV [144] have been demonstrated, limited by a spectrometer's resolution. In addition, record low inhomogeneous broadening of 1.4meV has been reported [142], owing to the high control on sizes of the template pyramids. This pyramid size controls, in turn, the QD growth rates and eventually the emission energies [145]. Growth of pyramidal QDs on mixed-size arrays, to generate spectrally isolated emission energies [143], was also reported. Emission of single photons from such QDs [146] was demonstrated. An elevated symmetry of these QDs regularly produces low FSS ≤ 20 s μ eV [147], which is mandatory for generating polarization-entangled pairs through the use of the 2X-X radiative cascade [148] (see Fig. 1:6). The electrical injection into pyramidal QDs grown in large GaAs/AlGaAs pyramids has also been demonstrated [85], [149]. More details of the pyramidal site-controlled QDs will be presented in Chapter 2 sections 2.2.2-2.2.3.

1.3 Photonic crystal structures

Photonic crystals (PhCs) [150] are dielectric structures in which the refractive index varies periodically in one or more directions [151]. With proper configuration and periodicity, they can be designed to completely block propagation of electromagnetic propagation in all directions, which makes them useful in realizing tight optical confinement with unique features.

1.3.1 Photonics bands and bandgaps

For photons, a structure in which the dielectric constant is modulated periodically, with a pitch on the order of the wavelength, is analogous to a semiconductor material with periodic arrangement of atoms for electrons. A structure of photonic bands then manifests, and a photonic energy bandgap can be created. Outside the bandgap, light can propagate freely through the structure, while inside it, propagation is dramatically impeded as a consequence of destructive interferences from the many coherent reflections that result. This effect can be created in 1D, by alternating sheets of materials with different dielectric constants, as is the case in a Distributed Bragg Reflector (DBR); in 2D, for instance with air columns in a dielectric medium or the complementary opposite case; or even in 3D, with the illustrious wood-pile or stacked opals structures [152]. These features can be derived from Maxwell's equations for the electric E and magnetic H fields, that can be cast in the form of an eigen-problem with the following Master equation [151]:

$$\nabla \times (\nabla \times \frac{1}{\epsilon_r(\mathbf{r})} \nabla \times \mathbf{H}(\mathbf{r})) = \left(\frac{\omega}{c}\right)^2 \cdot \mathbf{H}(\mathbf{r}), \quad (\text{Eq. 1:10})$$

$$\mathbf{E}(\mathbf{r}) = \frac{i}{\omega \epsilon_0 \epsilon_r(\mathbf{r})} \cdot \nabla \times \mathbf{H}(\mathbf{r}) \text{ [V/m]}.$$

By analogy to the quantum Hamiltonian for electrons, the operator in **(Eq. 1:10)** acts on the magnetic (electric) field and includes the spatially varying potential landscape represented by the dielectric function. Allowed frequencies of light are specified as the possible eigen-values of the problem. The dispersion of the frequencies as a function of the wavevector \mathbf{k} forms the photonic band structure of the system. For infinite periodic dielectric structures, Bloch's theorem allows writing the solutions as a product of a periodic (Bloch) term and an envelope function:

$$\mathbf{E}(\mathbf{r}, \omega) = \xi_{\mathbf{k}}(\mathbf{r}, \omega) \cdot e^{i\mathbf{k} \cdot \mathbf{r}}. \quad (\text{Eq. 1:11})$$

A PhC structure will not necessarily exhibit a photonic bandgap for all polarization states of light. This is illustrated in **Fig. 1:10(a)**, for the case of a 2D PhC having a triangular lattice (pitch a) of air holes (radius r) in the plane (x, y) and infinite translation along z . Depending on the choice of the ratio radius to pitch r/a , a full photonic bandgap, covering the entire span of the irreducible Brillouin-Zone, may open either for Transverse Electric (TE, in red) or Transverse Magnetic (TM, in violet) modes, not always simultaneously for both (yellow).

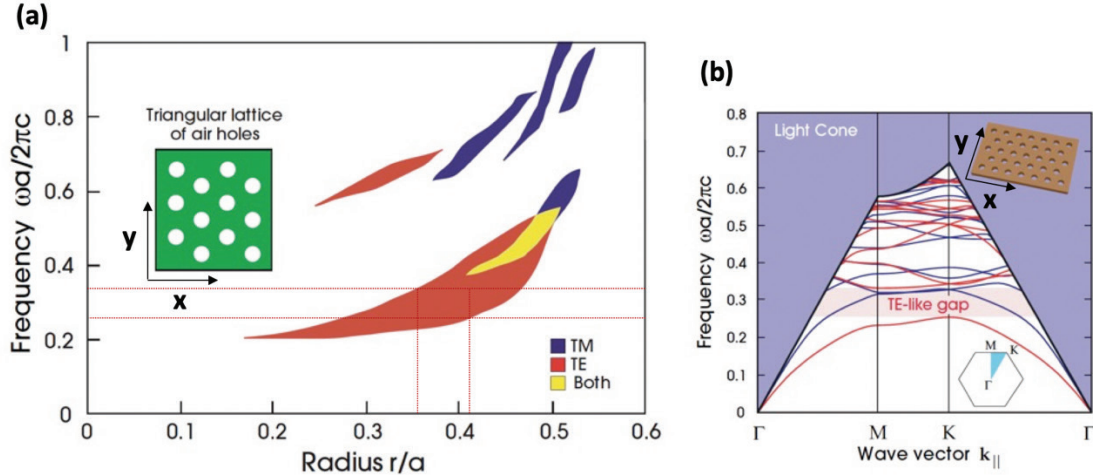


Fig. 1:10 – (a) Bandgaps map of TE(E_x, E_y, H_z) and TM(H_x, H_y, E_z) modes, for the case of 2D(x, y) PhC with a triangular lattice of air holes, versus of the normalized frequency. (b) Corresponding band structure of the 2D slab PhC over the irreducible Brillouin-Zone for a given r/a configuration. Modes confined by TIR are visible, outside the light cone shaded region. Reprinted and adapted with permission from [151].

Since periodicity of the PhC structures should be on the order of the wavelength in the medium, typically $\sim 0.1\text{-}1\mu\text{m}$, these structures can be fabricated using current nanotechnology techniques. Fabricating 3D PhCs is exceedingly challenging, and rather unpractical for making entire photonic circuits [153]. 2D PhCs as considered in Fig. 1:10, on the other hand, are not physically feasible, since they must extend infinitely in the third dimension. A trade-off was found in the form of quasi-2D or slab-PhCs, where the third dimension, is truncated to a finite height. Light propagating with a k_z vertical component is thus subjected to the formation of a Light Cone stemming from Snell-Descartes' law of refraction. The light cone dictates if incident light can transmit into the slab or gets reflected, and if light inside the slab can couple out or stays trapped bouncing inside the slab by Total Internal Reflection (TIR). The Light Cone is illustrated in **Fig. 1:10(b)**; it manifests as a curtain that “hides” portions of the perfect 2D PhC band structure across the irreducible Brillouin-Zone. Any component falling within the violet shadow region can radiate outside the 2D PhC slab. For QIP applications, these regions must be avoided by design in order to prevent the loss of single photons.

1.3.2 Photonic confinement in photonic crystal structures

The introduction of defects in a photonic crystal, for instance by filling air holes, creates new eigen-states in the photonic bandgap, where light can be trapped in discrete states or waveguided in a band. This is analogous to the electronic heterostructures described in subsection 1.2.1.

For instance, as depicted in **Fig. 1:11(a)**, removing a line of holes (line defect) in the triangular lattice of a 2D slab PhC generates a photonic waveguide, or a 1D photonic wire (by analogy to quantum wires for electrons). In such structures, light can delocalize, the eigen-modes supported are travelling waves that propagate in either a forward or backward direction with defined optical properties: a strong linear polarization along the y axis for modes of the lowest energy guided band (shown in red), and x polarization for the modes of the second band (shown in blue) [80]. Waveguide modes are best characterized by the group velocity $v_g = d\omega/dk = (1/\hbar) \cdot dE/dk = c/n_g$ extracted from the frequency (photon energy) dispersion, and equivalently by the group index n_g . When the frequency-dispersion is quasi linear, the group index is low, the group velocity is high, these regions are labelled as “fast-light” regions. On the contrary, as a result of the frequency-dispersion flattening when approaching

boundaries of the Brillouin-Zone, the group index diverges and the group velocity vanishes, light is thus slowed down, hence the name of “slow-light” regions [88]. Theoretically the group index can diverge to infinity, meaning that light can be completely stopped. However, in real devices the group index divergence is limited to typical values of $n_g \sim 40\text{--}100$ [154]. This is sufficient to realize on-chip compact delay lines providing frequency dependent delays of dozens of picoseconds [88]. The flat frequency-dispersion manifesting in slow light regions can distort optical pulses with a finite bandwidth, to realize zero-dispersion slow-light. The energy-dispersion can be rectified by local tailoring of structural parameters, such as hole radius [88], to suppress the group velocity dispersion (GVD). PhC structures can be further engineered. For example, the relative shift of half a lattice constant between the two sides of a waveguide turns regular PhC waveguides into chiral waveguides, in which the circular polarization of guided photons determines their direction of propagation [155], [156]. Current technological limitations cannot prevent fabrication disorder-induced effects. In particular, slow light regions are especially sensitive to it; near band-edges light can be trapped in local defects, an effect known as Anderson localization [89]. In such case, band-edges are smeared out and waveguide modes break down into discrete cavity modes that are randomly distributed spatially along the waveguide axis [92], [94], [157].

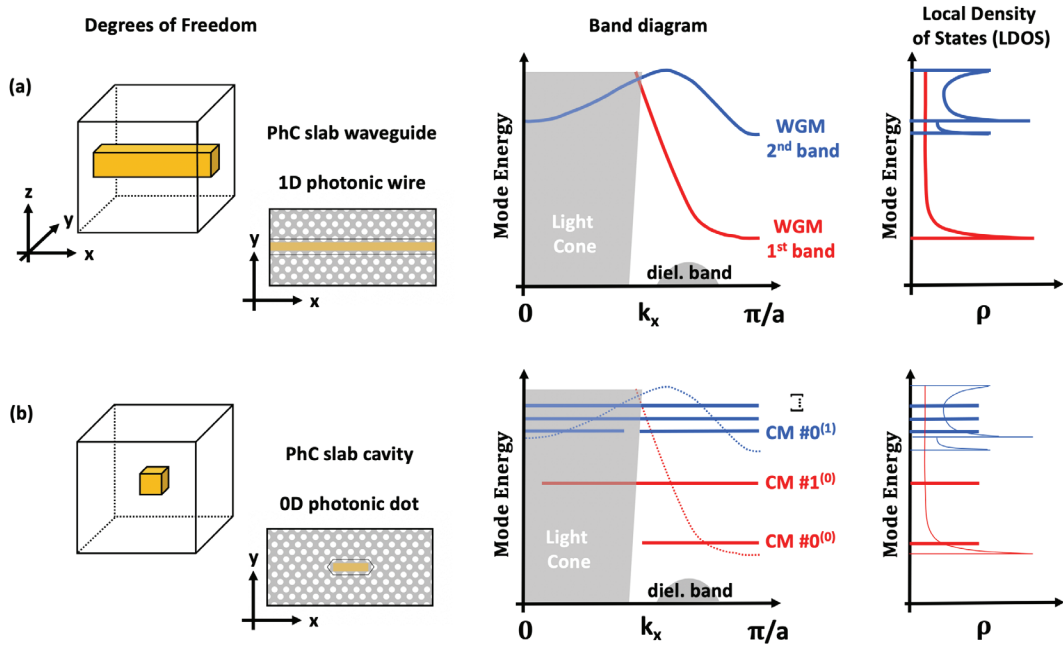


Fig. 1:11 – Two examples of defect structures in a slab 2D PhC: (a) waveguide, (b) cavity. Center: depiction of degrees of freedom (DOF), real space schematics, band structure along k_x , red: 1st band, blue: 2nd band. Light cone in gray. (Data traced from real numerical simulations). Right: corresponding local density of states (LDOS) spectra. An analogy between photonic confinement (PhC) and electronic semiconductor confinement (Fig. 1:3) is evidenced.

A cavity, or a 0D photonic dot, see **Fig. 1:11(b)**, can arise from further lateral confinement of a PhC waveguide by the addition of two terminations, which effectively breaks down the band structure. The eigen-modes supported by a cavity are standing waves, i.e. superpositions of forward and backward propagating waves, as a consequence, resonant photons can be trapped. As a result, tight cavity modes have a very flat dispersion, due to the larger content in spatial components of wavevectors, but the band structure of the parent waveguide starts to recover for sufficiently long $L_n \geq L_{n=35}$ cavities [158], with the formation of the various band edges.

PhC cavity modes are characterized by a figure of merit, the quality factor $Q = \omega \cdot \tau_{\text{cav}} / 2 = E / \delta E$ where ω ($E = \hbar\omega$) is the frequency of the cavity mode, τ_0 the characteristic lifetime of a photon inside the cavity and $\delta E = \hbar \cdot (2/\tau_{\text{cav}})$ the Fourier-transform limited FWHM of the cavity mode spectral line. The Q-factor basically characterizes the number of round trips a photon can realize inside the cavity before escaping. Recycling photons is

important to augment the interaction time with dipoles and is the core mechanism for producing laser oscillations. The optimization of Q-factors is understandably a very important research direction. In PhC cavities, improvements by several orders of magnitudes can be done by the displacement of a few PhC holes in order to remove k-components contained in the light cone [159]. The choice of hole shifts is not intuitive, and performant numerical optimization techniques, based for instance on genetic algorithms [160], [161], are required. Real Qs are, however, limited by fabrication disorder and scattering or absorption mechanisms. With III-V compound materials, typical values in the visible to near-infrared range are on the order of $Q \sim 10^3$ - 10^4 [162], [163] while higher Qs of $\sim 10^5$ - 10^6 are possible at telecom wavelengths [164], [165]. Due to the finite confinement lifetime in 2D slab PhC cavity, photons eventually escape both above and below the plane, which is why PhC cavities by themselves do not provide a solution for monolithic planar QIP schemes. A solution can be provided by cavities that are coupled in a chain to form a specific type of waveguides known as Coupled Resonators Optical Waveguides (CROWs) [166]. Some QIP applications may not rely on a monolithic planar integration since the emission, vertical or in-plane, can also be collected with optical fiber [167], [168]. Efficient recycling of the light emitted into the substrate can be achieved by modifying the substrate into a mirror by adding a Bragg reflector [169], [170].

Finally, PhC mode resonances can be tuned by digital etching [171] to remove dielectric materials layer by layer, or changing the optical confinement by local heating with a laser beam [172], [173] or resistive ohmic heater [174] to modify the semiconductor bandgap, or by the condensation of an inert gas, such as xenon [175], to modify the refractive index.

1.4 Quantum dots in photonic crystals

Photonic crystals can be realized within the semiconductor barrier materials that surround the QDs. This gives the ability to fabricate photonic crystal circuits for routing and processing of quantum light, in which modified light-matter interactions can also be used to enhance single photon emission and absorption. The physical principles and technological challenges involved are briefly reviewed.

1.4.1 Radiative transitions in photonic-crystal modified environments

The Jaynes-Cummings model is a quantum theoretical description of the interaction between a two-level system (2LS), usually an atom, here a QD, and a discrete mode of a lossless cavity. The system is assumed to be closed, isolated from external interactions, and the conservation of energy forbids the loss of excitations. Under such considerations the total Hamiltonian can be separated into three terms [176]:

$$\mathcal{H}_{JC} = \mathcal{H}_{2LS} + \mathcal{H}_{cav.} + \mathcal{H}_{int.} \quad (\text{Eq. 1:12})$$

$$\mathcal{H}_{2LS} = \frac{\hbar\omega_{QD}}{2} \cdot \sigma_z, \quad |g\rangle \text{ \& \; } |e\rangle \text{ 2LS states basis}$$

$$\mathcal{H}_{cav.} = \hbar\omega_c \cdot \left(a_c^\dagger a_c + \frac{1}{2} \cdot \mathbb{I} \right) = \hbar\omega_c \cdot a_c^\dagger a_c, \quad |n\rangle \text{ Fock states basis}$$

$$\mathcal{H}_{int.} = E_{ZPF} \cdot (a_c + a_c^\dagger) \cdot S = \frac{\hbar\Omega}{2} \cdot (a_c + a_c^\dagger) \cdot (\sigma_+ + \sigma_-)$$

The first term, \mathcal{H}_{2LS} , for the isolated two-level system, operates on the natural basis of a ground state $|g\rangle$ and excited state $|e\rangle$ by the use of the Pauli matrix operator σ_z . The second term, $\mathcal{H}_{cav.}$, for the pure cavity, is related to a harmonic oscillator and is expressed in the Fock states basis, where the modes can be populated by an integer number of photons $|n\rangle$. The last term, $\mathcal{H}_{int.}$, describes the interaction between the electric field of the cavity modes and the dipole of the two-level system. The expression involves a scalar term known as the vacuum Rabi splitting $\hbar\Omega$, or the coupling constant $\hbar g = \hbar\Omega/2$, which is proportional to the zero-point energy of the vacuum: the ground-state energy of the cavity empty of photons, related to the fluctuations of the electric-field in the cavity volume. Following the Rotating-Wave Approximation (RWA) and introducing of the detuning Δ , the total Jaynes-Cummings Hamiltonian can eventually be expressed as [176]:

$$\mathcal{H}_{JC} = \left(\hbar\omega_c \cdot \left(a_c^\dagger a_c + \frac{1}{2} \cdot \sigma_z \right) \right) + \left(\Delta \cdot \frac{1}{2} \cdot \sigma_z + \frac{\hbar\Omega}{2} \cdot (a_c^\dagger \sigma_- + a_c \sigma_+) \right) \quad (\text{Eq. 1:13})$$

$$\Delta = \hbar\omega_{QD} - \hbar\omega_c \text{ [meV], detuning}$$

$$|\pm, n\rangle = \frac{1}{\sqrt{2}}(|e, n-1\rangle \pm |g, n\rangle), \text{polariton basis}$$

$$\Delta E^{|n,\pm\rangle} = \hbar\Omega \cdot \sqrt{n} = \hbar(2g) \cdot \sqrt{n} \text{ [\mu eV]}$$

This Hamiltonian is expressed in the new basis of the polariton dressed-states $|n, \pm\rangle$, where both the number of excitations in the cavity mode fields and the states of the 2LS are intimately connected. The quantum-states $|n, +\rangle$ are known as the upper polariton (UP) branch while $|n, -\rangle$ are the lower polariton (LP) branch. When the new eigen-energies are plotted against the detuning between cavity and QD energies, the two polariton branches avoid crossing each other in the case of strong coupling. One branch starts from a dominant cavity mode at negative detuning and turns into a dominant 2LS state at positive detuning, and the reverse for the second branch. At “zero detuning”, $\Delta = 0$, there is a minimal energy separation $\Delta E^{|n,\pm\rangle}$ between the two branches, which is proportional to the vacuum Rabi splitting and the number of quanta populating the electric field of the polariton mode.

The description of a quantum dot interacting with a micro-cavity mode requires some adjustments, since the system can no longer be considered closed due to the presence of decay channels introducing losses of photons. A fraction of the photons emitted by the QD do not couple into the cavity mode, and photons in the cavity modes eventually escape due to a finite cavity lifetime. The modified modelling is usually done by expressing the physics through a Master equation that describes the time evolution of a density matrix operator representing the quantum state of the mixed system. This is done for instance in [177] for a QD embedded in a micro-pillar to incorporate the effects of both cavity and QD pumping, which are mandatory in order to describe phase-transitions between strong and weak coupling as a function of these parameters. The effect of phonons is omitted here but a treatment that includes them can be found in [118], [119], [178]–[181] to better describe the case of QD coupled to the cavity mode of a 2D slab PhC.

The complex Rabi splitting is introduced as [177]:

$$\frac{\hbar\Omega(\Delta)}{2} = \sqrt{(\hbar g)^2 - \left(\left(\frac{\hbar\Gamma_c - \hbar\Gamma_{QD}}{4} \right) + i \cdot \frac{\Delta}{2} \right)^2}, \quad (\text{Eq. 1:14})$$

$$\hbar\Gamma_c = \hbar\gamma_c - \hbar P_c = \hbar\kappa - \hbar P_c \text{ [\mu eV], (intrinsic cavity linewidth)}$$

$$\hbar\Gamma_{QD} = \hbar\gamma_{sp.} = \hbar\gamma_{QD} - \hbar P_{QD} = \hbar\gamma_{QD} - \hbar\gamma_{deph.} \text{ [\mu eV], (intrinsic QD linewidth)}$$

The strong coupling regime is defined by the condition $\hbar g > |\hbar\gamma_-| = \left| \frac{\hbar\kappa - \hbar\gamma_{QD}}{4} \right|$ neglecting pumping effects or expressed as $\hbar g > |\hbar\gamma_-| = \left| \frac{\hbar\Gamma_c - \hbar\Gamma_{QD}}{4} \right|$ accounting for incoherent pumping. In this case, the Rabi energy at zero detuning $\Delta = 0$ is a real quantity and photons can cycle between the two polaritons states, with complex energies expressed as [182]:

$$E_+ = \left\{ \hbar\omega_c + \sqrt{(\hbar g)^2 - \left(\frac{\hbar\Gamma_c - \hbar\Gamma_{QD}}{4}\right)^2} \right\} - i \cdot \frac{1}{2} \cdot \left(\frac{\hbar\Gamma_c + \hbar\Gamma_{QD}}{2}\right) \quad (\text{Eq. 1:15})$$

$$E_- = \left\{ \hbar\omega_c - \sqrt{(\hbar g)^2 - \left(\frac{\hbar\Gamma_c - \hbar\Gamma_{QD}}{4}\right)^2} \right\} - i \cdot \frac{1}{2} \cdot \left(\frac{\hbar\Gamma_c + \hbar\Gamma_{QD}}{2}\right)$$

The two spectral lines have center energies defined by the real parts specified within the brackets of **(Eq. 1:15)**. They are split by the energy $\hbar\Omega(\Delta = 0)$ that increases with the coupling strength g , and possess equal linewidths with a FWHM of $\left(\frac{\hbar\Gamma_c + \hbar\Gamma_{QD}}{2}\right)$, the average of the two original intrinsic linewidths, see **Fig. 1:12(a)** or [163], [183]. The third peak, appearing in between the two polariton branches, visible in the panels from -0.07nm to +0.02nm detuning and following the red plotted line, is not described by the model but corresponds to the bare cavity mode with a linewidth of $\hbar\Gamma_c$, clearly evidenced in [134], [163].

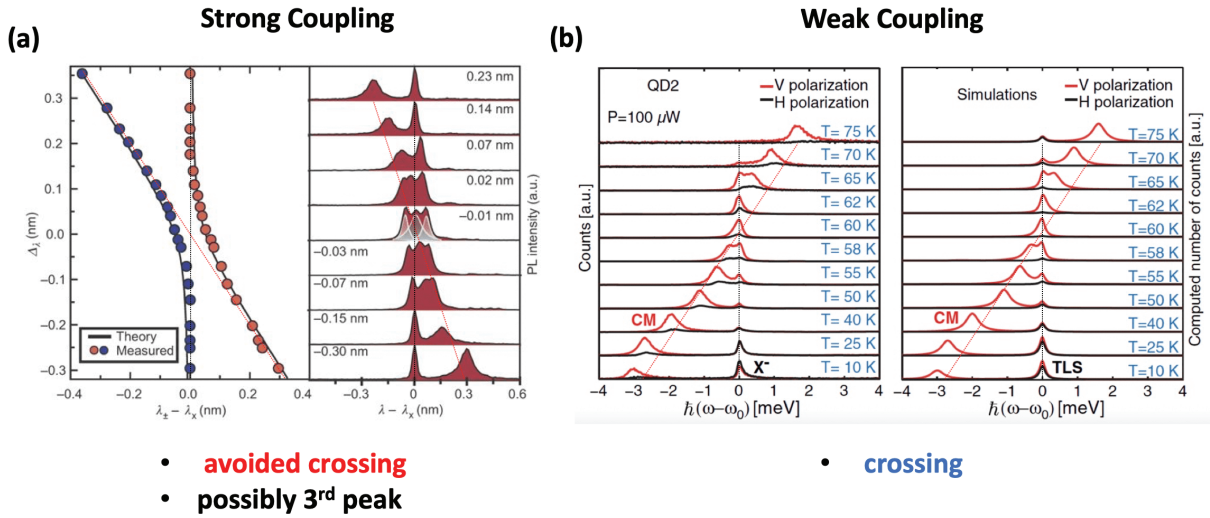


Fig. 1:12 – Experimental illustrations of (a) strong-coupling and (b) weak-coupling of a single QD interacting with the fundamental mode of a $L_{n=3}$ cavity during temperature tuning. Reprinted and adapted with permission from [182] for (a) and from [180] for (b).

In the other case, when $\hbar g < \left(\frac{\hbar\Gamma_c - \hbar\Gamma_{QD}}{4}\right) \approx \frac{\hbar\kappa}{4}$, the Rabi frequency is imaginary, the oscillations are strongly damped by the cavity loss. This case is known as the weak coupling regime, or the “bad cavity” regime if $\hbar\Gamma_c \gg \hbar\Gamma_{QD}$, in which case the two branches simply cross each other, see **Fig. 1:12(b)**. On resonance $\Delta = 0$, from **(Eq. 1:14)** and **(Eq. 1:15)** the complex energies are now expressed as:

$$E_{QD} = \hbar\omega_c - i \cdot \frac{1}{2} \cdot \left\{ \left(\frac{\hbar\Gamma_c + \hbar\Gamma_{QD}}{2}\right) + \sqrt{\left(\frac{\hbar\Gamma_c - \hbar\Gamma_{QD}}{2}\right)^2 - (\hbar \cdot 2g)^2} \right\} \quad (\text{Eq. 1:16})$$

$$E_c = \hbar\omega_c - i \cdot \frac{1}{2} \cdot \left\{ \left(\frac{\hbar\Gamma_c + \hbar\Gamma_{QD}}{2}\right) - \sqrt{\left(\frac{\hbar\Gamma_c - \hbar\Gamma_{QD}}{2}\right)^2 - (\hbar \cdot 2g)^2} \right\}$$

The two spectral lines have the same center energy defined by the real part of (Eq. 1:16), but possess two different linewidths distributed symmetrically around the mean of the original intrinsic linewidths, $\left\{ \left(\frac{\hbar\Gamma_c + \hbar\Gamma_{QD}}{2} \right) + \sqrt{\left(\frac{\hbar\Gamma_c - \hbar\Gamma_{QD}}{2} \right)^2 - (\hbar \cdot 2g)^2} \right\}$ for the QD line and $\left\{ \left(\frac{\hbar\Gamma_c + \hbar\Gamma_{QD}}{2} \right) - \sqrt{\left(\frac{\hbar\Gamma_c - \hbar\Gamma_{QD}}{2} \right)^2 - (\hbar \cdot 2g)^2} \right\}$ for the cavity line.

With the increase of the coupling strength g , the discrepancy between the FWHM decreases until clamping to the average with the onset of the strong coupling regime. The interaction is mostly one-sided, as the cavity enhances the spontaneous emission rate of the QD's dipole that is co-linear to the electric field. Part of the photons generated by the QD feed the cavity mode, and then are evacuated through the cavity decay channel before they have the chance to be absorbed back by the QD. The coupling strength $\hbar g$ is related to the interaction of the QD's dipole \mathbf{d}_{QD} with the local electric field $\mathbf{E}_c(\mathbf{r}_{QD})$ of the cavity at the position of the QD [80]:

$$\hbar g \propto |\mathbf{d}_{QD} \cdot \mathbf{E}_c(\mathbf{r}_{QD})| \approx |\mathbf{d}_{QD}| \cdot |\mathbf{E}_c(\mathbf{r}_{QD})| [\mu\text{eV}]. \quad (\text{Eq. 1:17})$$

$$|\mathbf{E}_c(\mathbf{r}_{QD})| = \sqrt{\frac{\hbar\omega_c}{2\varepsilon_0\varepsilon_r V_{eff}^{mode}}} [V \cdot m^{-1}]$$

$$|\mathbf{d}_{QD}| = q \sqrt{\frac{\hbar^2}{2m_e \hbar\omega_{QD}}} \cdot \sqrt{f} [C \cdot m]$$

(Eq. 1:18) shows that the coupling strength can be improved by either reducing the effective mode volume, using smaller cavities, such as modified H_1 [184], [185], H_0 [163] and nanobeam cavities [186], or by the increase of the oscillator strength of a QD. In $L_{n=3}$ cavities, the fundamental mode volume [187]:

$$V_{eff}^{mode} \approx \int \frac{\varepsilon_r(\mathbf{r})|E(\mathbf{r})|^2}{\max(\varepsilon_r(\mathbf{r})|E(\mathbf{r})|^2)} d^3r [\text{nm}^3] \quad (\text{Eq. 1:18})$$

is on the order of $\left(\frac{\lambda}{n}\right)^3$. In typical QDs, the oscillator strengths are in the range $f \sim 10$ -15. For a very thin, strongly confining QD with cylindrical symmetry, the oscillator strength can be estimated analytically and is proportional to the exciton area $f = 8 \frac{E_p}{\hbar\omega_0} \cdot \left(\frac{L}{a_0}\right)^2$ [80], i.e. related to the width of the QD. For a weakly confining QD, such as that formed by epitaxial growth interruptions, f is proportional to the exciton volume [80]. In both cases, larger QDs produce longer emission wavelengths (lower energies) due to a relaxed carrier confinement while producing larger oscillator strengths, both of which are beneficial for strong coupling. With the values mentioned, coupling strengths g on the order of 10-100 μeV can be expected and have indeed been observed (see Table 1:1). Strong coupling has been reported with QDs in different platforms [188]–[190].

When a QD's dipole interacts with the electric field of a cavity mode, the spontaneous emission rate of single photons can be enhanced, and the photons produced can be funneled efficiently into PhC cavity or waveguide modes. The spontaneous emission rate of a 2LS submerged in electromagnetic radiations is expressed as [80]:

$$\Gamma_{sp.}(\mathbf{r}_{QD}, \omega, \mathbf{d}_{QD}) = \frac{\pi \mathbf{d}_{QD}^2}{\varepsilon_0 \hbar} \omega \cdot \rho(\mathbf{r}_{QD}, \omega, \mathbf{e}_d) [\text{ns}^{-1}] \text{ (general)}, \quad (\text{Eq. 1:19})$$

$$\rho(\mathbf{r}_{QD}, \omega, \mathbf{e}_d) = \rho^{homog.}(\omega) = \frac{n\omega^2}{3\pi^2 c^3} [\text{m}^{-3} \cdot \text{s}] \text{ (homogeneous medium)}$$

$$\rho(\mathbf{r}_{QD}, \omega, \mathbf{e}_d) = \rho^c(\mathbf{r}_{QD}, \omega, \mathbf{e}_d) [\text{m}^{-3} \cdot \text{s}] \text{ (tailored medium)}$$

It is proportional to the squared norm of the dipole element and to the density of electromagnetic states at the location of the QD. In a homogeneous bulk medium, the local density of states is isotropic and only frequency dependent, and so does the spontaneous emission rate $\Gamma_{sp.}^{homog.}(\omega)$, however according to the dipole

approximation, the spatial emission from a single QD follows the radiative pattern of a Hertz dipole spatial distribution. In a tailored PhC structure, the local density of states, or the available radiative decay channels into which a single QD can emit are constrained by the mode structure and the gap effect, which leads to important anisotropic enhancement or inhibition of the spontaneous emission rate Γ_{sp}^c . For instance, in a photonic cavity, the density of states ρ^c corresponds to the comb of cavity modes with finite linewidths. In the weak coupling regime, the spontaneous emission rate is enhanced when the emitter's dipole is aligned spatially and spectrally on resonance with one such cavity mode, characterized by a specific spatial distribution of the amplitude and polarization of the electric field. This effect is known as the Purcell Effect [191]. The effective enhancement or inhibition factors then reads [80], [178], [192]–[194]:

$$Enh. = \frac{\Gamma_{sp}^c(\Delta=0)}{\Gamma_{sp}^{homog.}} = [F_P^{max} \cdot \zeta^2] \cdot \mathcal{L}(\hbar\omega_{res.}, \hbar\kappa, \hbar\omega_{res.}, \hbar\gamma_{QD}) \cdot \chi(\Delta = 0, T) \text{ [adim.]}, \quad (\text{Eq. 1:20})$$

$$Inh. = \frac{\Gamma_{sp}^{homog.}}{\Gamma_{sp}^c(\Delta=\pm\infty)} = \frac{\Gamma_{sp}^{homog.}}{\Gamma_{sp}^{nc} + \Gamma_{nr}} \text{ [adim.]},$$

$$F_P^{max} = \frac{3}{4\pi^2} \cdot \frac{\left(\frac{\lambda}{n}\right)^3}{V_{eff}^{mode}} \cdot Q \text{ [adim.]},$$

$$\zeta = \frac{e_d \cdot E_c(r_{QD})}{\max(E_c(r))} \text{ [adim.]},$$

$$\mathcal{L}(\hbar\omega_c, \hbar\kappa, \hbar\omega_{QD}, \hbar\gamma_{QD}) = \frac{1}{\left(1 + 2 \cdot \frac{\hbar\gamma_{QD} \cdot \hbar\omega_c}{\hbar\omega_{QD} \cdot \hbar\kappa}\right)} \cdot \left\{ \frac{\left(\frac{\hbar\kappa}{2}\right)^2 \cdot \left(1 + 2 \cdot \frac{\hbar\gamma_{QD} \cdot \hbar\omega_c}{\hbar\omega_{QD} \cdot \hbar\kappa}\right)^2}{\left(\frac{\hbar\omega_c}{\hbar\omega_{QD}}\right)^2 \cdot \Delta^2 + \left(\frac{\hbar\kappa}{2}\right)^2 \cdot \left(1 + 2 \cdot \frac{\hbar\gamma_{QD} \cdot \hbar\omega_c}{\hbar\omega_{QD} \cdot \hbar\kappa}\right)^2} \right\} \text{ [adim.]},$$

$$\chi(\Delta, T) \text{ [adim.]},$$

The enhancement $Enh. (\geq 1)$ is proportional to the maximum Purcell factor F_P^{max} , a structural parameter involving the mode volume V_{eff}^{mode} and the cavity Q-factor; the factor ζ^2 that quantifies a mismatch in the alignment of the QD's dipole with the local electric-field vector and the displacement with respect to the electric field maximum; the modified Lorentzian density of states for a single mode $\mathcal{L}(\hbar\omega_c, \hbar\kappa, \hbar\omega_{QD}, \hbar\gamma_{QD})$ with $\hbar\kappa$ describing the mode FWHM and $\hbar\gamma_{QD}$, the finite-linewidth of the QD transition [193]; and a temperature dependent factor $\chi(\Delta, T)$ [178] due to interaction with the phonon reservoir. The Purcell effect occurs if a non-zero spatial and spectral overlap of the 2LS dipole with the electric field of the cavity mode exists. The inhibition factor $Inh. (\geq 1)$ corresponds to the inverse of the enhancement factor very far from resonance with the cavity mode. For a perfect PhC it is theoretically infinite for emission within the bandgap, but for a real imperfect PhC emission stills occurs due to losses via other decay channels: leaky channels (Γ_{sp}^{nc}) or non-radiative recombination (Γ_{nr}) [192], [195], [196].

As a consequence of the Purcell effect, single photons produced by a QD are extracted more efficiently and can be transferred into targeted PhC cavity or waveguide modes with an efficiency given by the beta factor $\beta = \frac{\Gamma_{sp}^c}{\Gamma_{sp}^c + (\Gamma_{sp}^{nc} + \Gamma_{nr})} \approx 1 - \left(\frac{1}{Enh.} \cdot \frac{1}{Inh.}\right)$ [195], [196]. Many QIP applications require an on-demand, deterministic stream of indistinguishable single photons, ideally with a value of β near unity. In addition, thanks to the Purcell effect, the emission rate of the quantum emitters is not limited by the intrinsic lifetime; for example, QDs with spontaneous emission lifetime of 1ns can provide single photon fluxes at rates up to 10s of GHz with Purcell factors around 10. At the same time, charge carriers are forced to recombine faster, which is beneficial for reducing pure dephasing effects, and thus enhancing the coherence and spectral purity of the single photons.

However, phonon scattering is unavoidable in a solid-state environment and fundamentally prevents achieving both $\beta=1$ and perfect indistinguishability [197]. Indistinguishability may be improved by post-selection during propagation by the addition of extremely narrow-filtering resonant structures, e.g., in free-space [198].

reference	$\hbar\kappa$ [μeV]	$\hbar\gamma_{QD}$ [μeV]	$\hbar g$ [μeV]	$Enh.$	$Inh.$	β
SA [199]	($L_{n=3}, \#2$) $\sim 5'550$	~ 30	—	1.7	2.3	0.76
SA [199]	($L_{n=3}, \#0$) ~ 174	~ 30	~ 102	-	-	-
SC [194] [180]	($L_{n=3}, \#0$) ~ 440	~ 200	~ 50	2.5- 3	3	0.87-0.9
SA [195]	($L_{n=3}, \#0$) $\sim 4'400$	-	-	3.1	3.9	0.9
SA [196]	($L_{n=3}, \#0$) ~ 64	-	-	8	3	0.96
SA [192]	*($H_{n=1}, \#0$) ~ 395	-	-	11.4	4.5	0.98
SA [182]	($L_{n=3}, \#0$) ~ 100	~ 35	~ 76	16.7	8.7	0.99

Table 1:1 – Non-exhaustive summary of parameters found in the literature on the effective Purcell enhancement of the spontaneous emission rate, inhibition factor and beta factor for the emission from single QDs embedded in 2D slab PhC cavities. SA stands for self-assembled and SC for site-controlled QDs.

Table 1:1 gives a non-exhaustive overview of experimental parameters obtained for single photon emission from semiconductor QDs embedded in PhC cavities, reported in the literature. As for PhC waveguides, β values in between 0.96 and 0.99 have been reported with both self-assembled [200]–[202] and site-controlled QDs [203].

1.4.2 Technological challenges

The long-term goal of producing QD-based integrated quantum photonics for on-chip processing of quantum states of light at the single photon level is highly challenging technologically. Such integration practically requires a solid-state environment, which is a source of noise to the QD dipoles due to phonons, defects, spin interactions, and charge carrier diffusion, and is thus detrimental to coherence [204]. In addition, fabrication imperfections prevent producing identical QDs with perfectly reproducible optical features. This results in large inhomogeneous broadening of the QD transitions and makes it difficult to produce streams of indistinguishable single photons or collective quantum effects such as superradiance in a single photonic mode. To ensure large Purcell effect, pure single photon statistics, large coupling efficiency β , and control over directionality of single photon streams, QDs must be embedded at very specific locations in the tailored photonic environments, combining systems of cavities and waveguides. Achieving site control of the QD emitters is also essential in order to scale up the integration platform to include an arbitrary number N of quantum emitters.

Despite these challenges, significant progress has been achieved on several components of this developing platform. Among the sources of pure dephasing noise, free charge carriers can be dealt with by depletion of the QD barrier medium with a reversed-bias diode [205] and below barrier excitation [137]. Inhomogeneous broadening can be mitigated in principle by the implementation of external means to tune the QD emission energies. These include thermal resistive heaters [174], [206], electric fields generated by diodes [207], static strain fields produced by piezo-electric elements [208] or phase change materials [209], and magnetic field tuning of trions [210], [211]. However, such techniques cannot fully address the tuning ranges of at least several meVs as required

by typical inhomogeneous broadening levels, and they can generate cross-talks that make it difficult to address independently several emitters in close proximity. The photonic fabrication may be simplified by replacing PhC membranes waveguides with suspended nanobeams [137]. These nanobeams are simpler to fabricate and their optical confinement is ensured by TIR instead of the photonic gap effect. This approach yields modes with smoother intensity distribution (without a Bloch term), hence they are more tolerant to QD positioning errors. Moreover, they can be interfaced to electrical diodes in the same way [212], [213] or to nanoelectromechanical systems (NEMS) [214].

To control the location of the quantum emitters' dipoles, essentially two ways have been pursued. The first solution is to adapt the photonic structures to the constraints of the QD locations. In the case of randomly nucleating self-assembled QDs, sufficiently low surface dot density is a prerequisite. The technique consists in first performing micro-PL characterization of a sample region to identify and register the locations of QDs with promising optical features with the help of alignment marks, and subsequent fabrication of the photonic elements around them [215]. Since the positions of the selected QDs are not correlated, the probability for placing deterministically and monolithically $N > 1$ emitters within a given device decreases quickly with N . Single-photon generation using a wavelength-tunable single QD in both a PhC waveguide [213] or suspended nanobeam [212] were demonstrated with this approach. Processing of one-photon and two-photons states from an attenuated coherent laser beam by a single QD in a PhC waveguide [216], and few-photons switching from a single QD ($N=1$) strongly coupled to an $L_{n=3}$ cavity side-coupled to a PhC waveguide [217] were reported.

The second approach, employed in this thesis, is to adapt the QDs locations to the constraints of the envisioned photonic structures. It constitutes the logical choice to reproducibly fabricate functional elements with an arbitrary number N of quantum emitters. The integration scheme is based on the use of site-controlled QDs grown in specific patterns that match with the design of the tailored photonic environments to be fabricated. Relative alignment precision of better than 50nm can be achieved using proper alignment marks (see description in chapter 2). The successful integration of single pyramidal site-controlled QDs with PhC membrane cavities was first reported in [218]. More complex structures including entire systems of QDs integrated with PhC cavities [219]–[221], waveguides [144] and cavity-waveguide assemblies [144] were reported with this approach. Systems of 2 QDs resonantly coupled to the same optical mode of an $L_{n=3}$ cavity [222], 4 QDs interacting with a same mode of an $L_{n=7}$ cavity [223], and of 5 QDs multiplexing single-photons into a PhC waveguide [203] were demonstrated.

Last but not least of the challenges, for widespread applications beyond research, quantum effects should ideally persist at room temperature. More tightly bound QD excitons, such as those available in GaN [224], may provide a solution in this regard.

1.5 Scope and aim of this thesis

Based on the approach of integration of site-controlled QDs with PhC structures developed in previous thesis works [144], [219]–[221], [225], the current thesis addresses the development of functional devices for on-chip single photon manipulation.

Towards this endeavor, in **chapter 2** we describe a combination of numerical simulation and experimental techniques that are subsequently used for designing and producing PhC structured with tailored modes, interacting with systems of site-controlled QDs.

We make use of these tools in the three core chapters of the thesis, where we explore two novel photonic crystal cavities based on effective index tailoring and a model structure for testing several photonic functionalities.

Chapter 3 highlights a “defect-potential” PhC cavity in which the strength of the photonic confinement and the polarization properties of the confined modes can be controlled. Site-controlled QDs are inserted in these cavities and weak coupling of the emitted photons to selected cavity modes is demonstrated.

Chapter 4 builds on the knowledge acquired in chapter 3 to produce a novel, “tilted-potential” photonic cavity which supports unique Airy-Bloch modes. Combining both a slow-light “head” connected to a fast-light “tail”, these modes are good candidates for optimal extraction and unidirectional guiding of single photons emitted by QDs properly embedded in the cavity. Weak coupling of a single QD to such Airy-Bloch modes is demonstrated.

Chapter 5 presents a test platform consisting of two PhC waveguides coupled by a PhC cavity and equipped with grating couplers for connection to free-space beams. Several site-controlled QDs are integrated in different, predetermined locations of the integrated structure. Several functions possible with such generic structure, including coupling of external beams and QD emissions via the couplers as well as between the waveguides are evidenced and analyzed.

Finally, in **chapter 6**, we draw the conclusions from this study and give some perspectives on possible future directions.

Chapter 2 Numerical and experimental methods

The fabrication of a functional device, based on site-controlled quantum dots (QDs) embedded in a photonic crystal (PhC) structure, go through a cycle of implementation consisting of three phases.

First comes design, in order to come up with a blue-print accounting for realistic structure parameters. These parameters are derived from knowledge from: past or similar experiments, updated to state-of-the-art; of technical limitations; as well as a deep understanding of a support theory, with a dash of intuition. The design phase is supported by numerical modeling of photonic crystal structures using two finite-differences methods for solving Maxwell's equations either in 2D or in 3D. In the frequency domain, finite difference frequency domain (FDFD) is used, suited for the standing waves of PhC cavities modes resonances. In the time-domain, finite difference time domain (FDTD) is employed, for simulating propagation in PhC waveguides. This part is presented in **section 2.1**.

Second, illustrated in **section 2.2**, comes the fabrication of the devices according to the desired designs. The nano-fabrication of the embedded site-controlled QDs in the PhC structures goes through four sub-phases: patterning of the substrate, growth of QDs arrays, intermediate optical characterization of the characteristics and quality of the grown QDs, and finally fabrication of the properly aligned PhC structures on top of the QD arrays.

Third, optical characterization of the final devices or structures at intermediate steps is implemented. The optical tools include low-temperature micro-photoluminescence spectroscopy, also resolved in polarization and in time. The optical set-ups employed are presented in **section 2.3**.

2.1 Design of the photonic crystal structures

Careful design of the PhC structures needs to be implemented in order to ensure overlap of the mode resonances and spatial patterns with the emission wavelengths and positions of the embedded QD systems. The most important issues in this design phase are summarized in this section.

2.1.1 Constraints of QD embedding

The PhCs structures and their optical modes must be adapted to the configurations of the site-controlled QDs that are fabricated in a prior step. Several constraints are imposed on the PhC structures.

The first constraint is due to the specific emission energies (wavelengths) of the InGaAs/GaAs pyramidal QDs. In the structures considered here, the QD ensembles s-shells usually displayed center energies between $\sim 1.259\text{eV}$ ($\sim 985\text{nm}$) and $\sim 1.292\text{eV}$ ($\sim 960\text{nm}$) (cf section 2.2.3). This ensures transparency of the GaAs membranes employed.

To tune the QD emission into resonance with the photonic mode spectra, the membrane thickness t , the PhC pitch a and the holes radii r need to be adjusted. The GaAs membrane thickness ($\sim 264\text{nm}$) is selected to ensure near single slab-mode operation and to accommodate the etched pyramids in which the QDs are grown. The QDs treated here have typical pyramid side lengths of $s \approx 253 \pm 6\text{nm}$, resulting in pyramid depths of $h \approx 207 \pm 5\text{nm}$, and the QDs are grown at approximately the center of the GaAs slab [218]. The QD emission wavelengths are set to be as long as possible to ensure maximum transparency of the GaAs membrane material [226], without compromising

the QD optical quality. The pitch of the PhC triangular lattice must be close to the QD emission wavelength in the dielectric GaAs material $\lambda_n = \frac{\lambda_0}{n} \approx \frac{980}{3.5} \approx 280\text{nm}$. In order to provide sufficient tuning range of the PhC cavity resonances via systematic change in PhC hole radii [227]–[229], the pitch was set at $a=225\text{nm}$. Based on Fig. 1:10, a photon (resonance) energy range of $\sim 1.25\text{--}1.30\text{eV}$ translates into a normalized frequency range of $\frac{\omega a}{2\pi c} \sim 0.227\text{--}0.236$. There, the full TE PhC bandgap is open for values of the hole radii in the range $r \sim 0.25a\text{--}0.35a$ ($\sim 56\text{--}79\text{nm}$). A wider range of holes sizes can be selected to account for fabrication-related fluctuations.

2.1.2 Solving numerically Maxwell's equations

As evidenced in (Eq. 1:20), the interaction between a QD and the electric field relies on the proper spectral matching and spatial overlap of the QD dipole with an maximum of the field. It is thus essential to find out the modes' energies and spatial distributions in the designed structures to identify the best locations where QDs must be embedded. This is done by solving Maxwell's equations numerically. We use two complimentary techniques:

- In the frequency domain (FD), space is discretized, time is irrelevant. The equations are rewritten as an eigen-problem with discrete eigen-values (frequencies) and eigen-vectors (fields) (Eq. 1:10). The method is iterated until convergence under a specified threshold is attained. It is well suited to cavity modes (standing waves); the knowledge of \mathbf{H} (resp. \mathbf{E}) yields \mathbf{E} (resp. \mathbf{H}).
- In the time domain (TD), both space and time are discretized. The method relies on the use of a Yee grid [230], which intertwines \mathbf{E} & \mathbf{H} , to solve in sequence and consistently the four Maxwell's equations. Dipoles or current sources generate fields which propagate and can excite the many resonances.

In both cases, space is discretized with rectangular grids. The description of a triangular lattice requires the re-definition of an appropriate "unit" cell.

The Finite Difference Method (FDM) [231] belongs to the frequency domain class of techniques. It can be implemented in any dimension d and is quite popular for 1D and 2D where it is known to run quickly and efficiently. For 3D problems complexity increases, and it is eventually beaten by Finite Elements Method (FEM). After defining the dielectric constant distribution, the master equation (Eq. 1:10) is discretized, with the approximation of first-order spatial derivatives along direction x_k ($k = 0, \dots, d-1$) (d is the dimension):

$$\partial_{x_k} f = \frac{f(\dots, x_{k-1}, x_k + \Delta x_k, x_{k+1}, \dots) - f(\dots, x_{k-1}, x_k, x_{k+1}, \dots)}{\Delta x_k} \quad (\text{Eq. 2:1})$$

This is known as a forward difference; it can also be backward or centered. The operator $\nabla^{\wedge \frac{1}{\epsilon_r(r)}} \nabla^{\wedge}$ turns into a sparse matrix operator. Diagonalization of the final matrix returns the eigen-frequencies and the spatial patterns of the stationary modes. This is well suited to problems with boundary conditions, such as cavities or approximated waveguides without a free propagation character. This technique will be employed extensively in chapters 3, 4 & 5. The Matlab script that is used in this thesis was written Dr. F. Karlsson [158].

For application in our membrane structures, the modes are simulated in 2D using a regular effective index method to account for the reduction of the third z dimension (more details in section 2.1.4). These modes are TE(E_x, E_y, H_z) modes. The displayed mode patterns correspond to those at the center of the slab, in the plane ($x, y, z=0$). The 2D method does not give direct access to the components above the slab; as a consequence, far-field radiation cannot be obtained, and thus radiative optical losses cannot be estimated. However, it is possible to guess qualitatively the k -vector components that point vertically and would scatter out power into the light cone. Q factors thus cannot be estimated with this technique; instead, FDTD should be used (see further below).

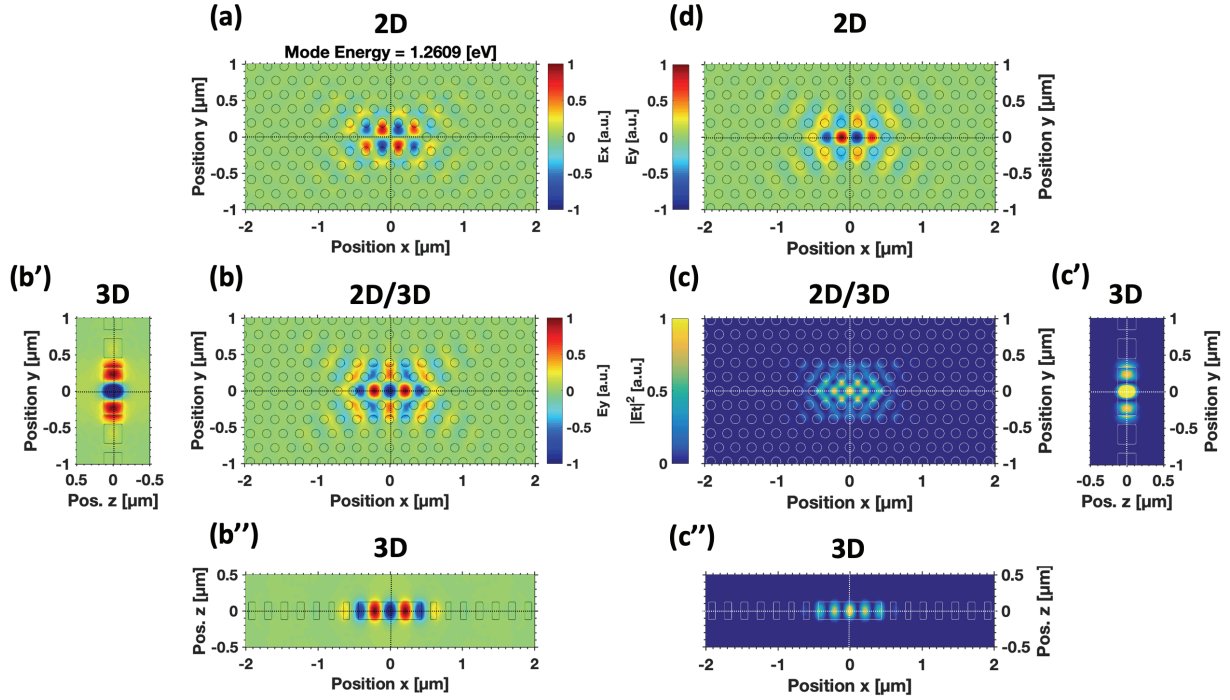


Fig. 2:1 – Numerical simulations of the fundamental TE mode of an optimized $L_n=3$ cavity with both 2D FDM and 3D FDTD. (a) E_x 2D ($x, y, z = 0$). (b-b'') E_y cross-sections: (b) 2D or 3D ($x, y, z = 0$) top view, (b') 3D ($x = 0, y, z$) side-view, (b'') 3D ($x, y = 0, z$) side-view. (c-c'') In-plane intensity $|E_t|^2$ cross-sections: (c) 2D or 3D ($x, y, z = 0$) top view, (c') 3D ($x = 0, y, z$) side-view, (c'') 3D ($x, y = 0, z$) side-view. (d) H_z 2D ($x, y, z = 0$). Numerical parameters: hole radius $r = 59.3\text{nm}$, pitch $a = 225\text{nm}$, slab thickness $t = 250\text{nm}$, spectral center wavelength $\lambda_0 = 983.3\text{nm}$: GaAs refractive index $n = 3.4453$ (3D), slab TE effective refractive index $n_{eff}^{slab} = 3.1425$ (2D) @ $T = 10\text{K}$.

Fig. 2:1(a, b, c, d) illustrates the application of the 2D FDM technique for calculating the patterns of the fundamental mode in an $L_n=3$ cavity, consisting of 3 removed holes in a GaAs membrane pierced with a triangular lattice of holes (see caption for details of the structure parameters). The component E_x of the field has an odd symmetry ($\Pi_x=-1$) by reflection over the $x=0$ axis and odd symmetry ($\Pi_y=-1$) by reflection over the $y=0$ axis. The lobes are pushed towards the center holes, at the edges, see **Fig.2:1(a)**. On the contrary, component E_y has double even symmetry, $\Pi_x=+1$ and $\Pi_y=+1$. This is the sign that this cavity mode belongs to the first photonic band. The extrema are located along the cavity axis, more specifically where the holes are missing. **Fig.2:1(c)** displays the in-plane intensity $|E_t|^2=|E_x^2+E_y^2|$ pattern. QDs should be embedded at the loci where the intensity is highest for optimal interaction. In particular, a symmetric QD located at the center (0,0,0) of the cavity would have its dipoles overlapping with an anti-node of field E_y and a node of field E_x . At resonance, photons emitted by the QD would co-polarize along y due to weak coupling. On the other hand, a QD embedded at a maximum of E_x would co-polarize along x ; however, the magnitude of the field is weaker than for E_y , therefore the effect would be weaker. **Fig.2:1(d)** shows the component H_z which has odd $\Pi_x=-1$ and even $\Pi_y=+1$ symmetries.

For the study of phenomena involving time: pulse propagation, time dependent variation of the refractive index and temporal decay of confined fields, the finite difference time domain (FDTD) method is relevant [232], [233]. The resonances of a structure are found by the use of point sources with given Gaussian spectral widths that are placed at various locations to stimulate the many optical modes with even or odd symmetries. Confined modes that are spectrally covered can trap part of the energy, which eventually decays in time. A probe properly positioned tracks the decays and, using a Fourier transform, can yield the various frequency components to trace back the modes. These modes can then be excited individually with resonant sources of reduced spectral bandwidths. Simulations can be implemented in 2D, and upgraded in a straightforward manner to 3D, the latter is very demanding in terms of computer resources, even with symmetry reduction. In this thesis, the grid mesh is based on a discretization of 20 pixels per unit of pitch $a=225\text{nm}$. Thick absorbing layers are also implemented all around the simulation volume to prevent reflections at the boundaries that can produce unwanted artefacts.

Fig. 2:1(b, b', b'') & (c, c', c'') illustrate the application of 3D FDTD, in comparison with the 2D method, to compute the spatial distribution of field E_y and intensity $|E_y|^2$ of the fundamental mode of the $L_{n=3}$ in a membrane PhC structure. The stationary pattern is simulated by the use of a continuous source and recorded after hundreds of time steps to avoid transient effects of high frequency components when the source is switched on. Only the cross-sections along the axis $x = 0$, $y = 0$ and $z = 0$ are displayed. As expected, the field is confined inside the slab and decays exponentially outside, with even symmetry $\Pi_z = +1$. The extrema naturally occur at the center of the slab. This is the reason why 2D FDM simulations are valid, as they effectively simulate the distributions in the plane $(x, y, z = 0)$ corresponding to the case of a perfect 2D PhC. The 3D FDTD simulations use the bulk GaAs refractive index estimated at a temperature of $T=10K$ at the mode energy. The 2D FDM simulation uses the effective refractive index for the slab thickness $t=250nm$ of the 3D case. Both methods agree; a side-by-side comparison of the component E_y is not shown because the spatial patterns are identical.

The $L_{n=3}$ cavity in **Fig. 2:1** design was optimized according to [161], providing a theoretical $Q \approx 200'000$ and a mode volume $V_{eff}^{mode} \approx \left(\frac{\lambda_0}{n}\right)^3$. The first three side holes on both the left and right are shifted outwards along x , respectively, by $s_{1x} = 0.2311a \approx 52nm$, $s_{2x} = 0.1507a \approx 34nm$, $s_{3x} = 0.048a \approx 11nm$. Q-factor values for such fabricated devices fall within $\sim 3'000-9'000$, orders of magnitude below the theoretical value; this is due to residual absorption losses at the Urbach tails of the GaAs material [162], as well as fabrication-induced disorder effects, not accounted for in the ideal model.

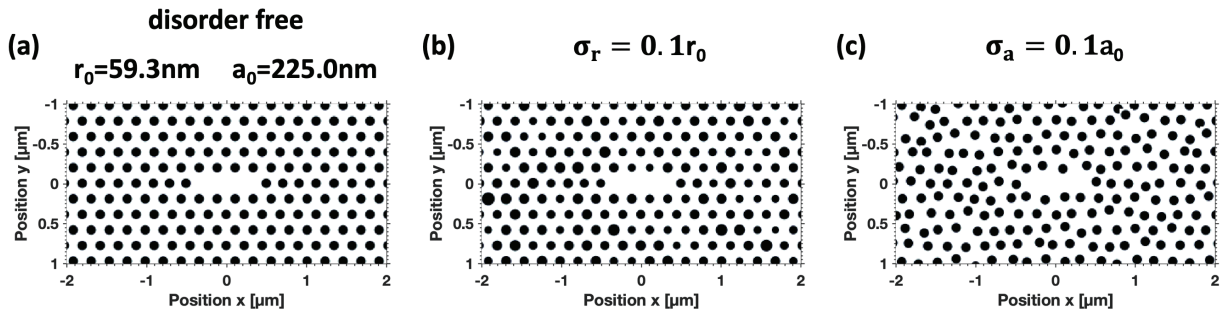


Fig. 2:2 – Illustration of fabrication-related disorder in 2D FDM simulations. (a) Disorder free case; (b) holes-size disorder $\sigma_r = 0.1r_0 \approx 6nm$; (c) holes-position disorder $\sigma_a = 0.1r_0 \approx 23nm$.

The hole sizes and positions of a structure can be modified by a systematic change in the nominal parameters during the lithography steps. This is employed, in fact, in our fabrication in order to cover a broad range of cavity resonances to match the QD emission wavelengths (see **section 2.2.3**). However, in actual devices there are always random fluctuations in hole sizes and positions, see **Fig. 2:2**; in this figure, parameters are exaggerated for the purpose of visualization and are not representative of state-of-the-art fabrication. This leads to PhC disorder effects with impact on the mode patterns and resonances, as discussed in more details in chapters 3 and 4.

Fig. 2:3 illustrates the use of 2D FDTD to simulate the propagation of a signal in a PhC waveguide. Regular PhC waveguides support both the forward and backward propagating components produced by conventional sources, see **Fig. 2:3(a, b, b')**. With modal sources, it is possible to excite either the forward or the backward component, see **Fig. 2:3(a')** compared to **(a)**.

This figure illustrates one issue with slow-light. The speed at which light propagates in a structure is related to the dispersion via the group velocity $v_g = c/n_g$, which is controlled by the group index $n_g = -c/(\partial\omega/\partial k)$. In a PhC waveguide, near a band-edge connected to a principal point of the Brillouin-Zone, the dispersion flattens, the group index diverges, and therefore light slows down. If a simulation with slow-light components does not run long enough, the components cannot propagate across the full structure and display a stationary spatial distribution, see **Fig. 2:3(b')** compared to **(b)**. It is thus important in a PhC circuit to have an estimation of the timescale involved to cover distances. For a realistic slow-light group index of ~ 50 , propagation over $\sim 1\mu m$ takes ~ 167 femtoseconds. On the other hand, with a typical fast-light group index of ~ 5 , propagation over $\sim 1\mu m$ takes ~ 17 femtoseconds.

This changes the strength of slow-light interaction: over a given distance, slow-light interacts longer with an object, therefore the effects of the interaction can be stronger.

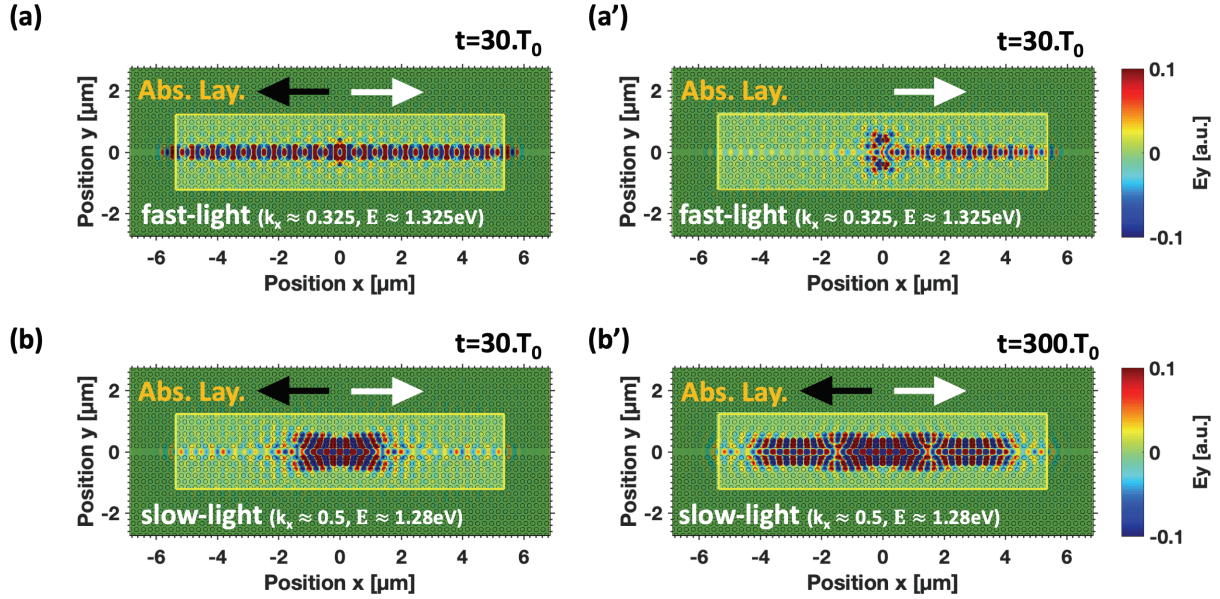


Fig. 2:3 – 2D FDTD numerical simulations of light propagation in a PhC waveguide. Top row: fast-light ($n_g \approx 5$) over 30 periods of time, (a) forward and backward propagation, (a') only forward direction with an eigen-mode source. Bottom row: slow-light near the band-edge ($n_g > 50$), (b) over the same 30 periods of time as in (a); (b') over 300 periods of time, both forward and backward propagation. Numerical parameters: hole radii $r = 66.6\text{nm}$, pitch $a = 225\text{nm}$, slab effective index $n_{eff}^{slab} = 3.1974$ (fast), 3.1573 (slow).

In this thesis, FDTD simulations were performed using Pymeeep, an open-source software package [234]. 2D FDM simulations were first run; with the knowledge of the optical modes structure, mode frequencies and slab effective index were then selected and used as input parameters for the 2D FDTD simulations that appear in chapter 5.

2.1.3 Effects of refractive index dispersion

To compare with experiments presented in subsequent chapters, properly simulating the optical modes structure at different wavelengths is paramount. This is complicated by the fact that the refractive index depends on photon energy. The dispersion effect for the bulk refractive index of GaAs is shown in **Fig. 2:4(a)** [226], [235], [236], and the corresponding dispersion effect on the slab effective refractive index of the lowest TE and TM modes of a 250nm thick GaAs slab in air is shown in **Fig. 2:4(b)**; the bulk value is shown as a dark grey line, and a yellow line depicts the index of air. The effect of changing the slab thickness is displayed in **Fig. 2:4(c)**. For the in-plane interaction of QDs with confined electric fields in the 2D slab PhC structures to be discussed, the relevant mode is TE_0 , where the electric field possesses a single anti-node across the thickness of the slab. In (b), the quasi-linear dependence of this mode on photon energy is highlighted.

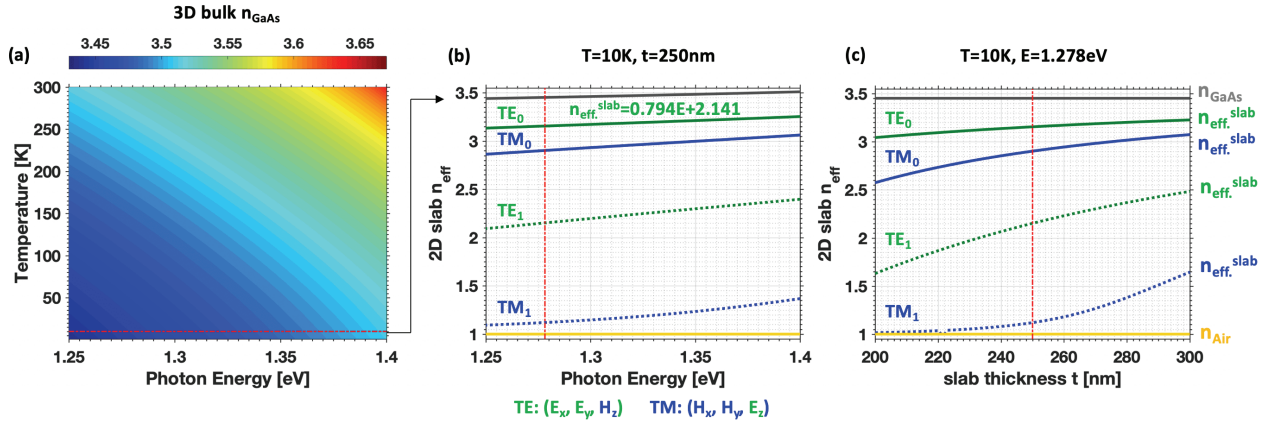


Fig. 2:4 – Computed: (a) 3D bulk refractive index of GaAs as a function of photon energy and temperature (parameters from [236]); (b) 2D effective slab index at a fixed temperature of $T=10\text{K}$ and for a slab thickness $t = 250\text{nm}$, as a function of photon energy; (c) 2D effective slab index at a fixed temperature of $T = 10\text{K}$ and constant photon energy $E = 1.278\text{eV}$, as a function of slab thickness. TE modes in green, TM modes in blue.

The effect of the dispersion on the calculated mode energies of a sample cavity (a tilted-potential structure discussed in chapter 4) is illustrated in **Fig. 2:5**. Here, ten modes of the structure were computed, using different assumptions on the effective slab index. The green diamonds represent the mode energies assuming a fixed index, corresponding to the slab effective index at the center of the mode spectrum. The black circles represent the corrected energies, obtained by iterating 2D FDM simulations, each time updating the spectral center energies with the newly found mode energies.

A significant deviation is noticeable when plotting the discrepancy between the green data points and the black circles (upper panel). The deviation increases linearly when moving away from the spectral center, as could be expected from the linear dependence of the slab effective index on energy pointed earlier. The slight vertical offset is due to a lack of precision when setting the spectral center. If an acceptable error of $\sim 1\text{meV}$ is arbitrarily set, using constant index is sufficient over $\sim 7\text{meV}$ s around the spectral center. This range can be increased up to $\sim 20\text{meV}$ s using a linear correction to account for an energy dependence of the slab's effective index, as shown with the blue square symbols. This approach is supported by the fact that the relative change in the mode energy is approximately:

$$\frac{\Delta E}{E} \approx - \frac{\Delta n_{\text{eff}}^{\text{slab}}}{n_{\text{eff}}^{\text{slab}}} \quad (\text{Eq. 2:2})$$

By reworking this formula, we obtain:

$$E^{(\text{correct.})}(\lambda) \approx E^{(0)}(\lambda_0) - \left(\frac{n_{\text{eff}}^{\text{slab}}(\lambda) - n_{\text{eff}}^{\text{slab}}(\lambda_0)}{n_{\text{eff}}^{\text{slab}}(\lambda_0)} \right) \cdot E^{(0)}(\lambda_0) \quad (\text{Eq. 2:3})$$

In other words, the energies can be corrected, simply by taking the green data points, evaluating the slab effective refractive indexes at these energies, and computing the relative variations of these effective refractive indices with respect to the effective refractive index of the spectral center. Thus, within this approximation and the $\sim 1\text{meV}$ criterion, the optical mode structure can be simulated with high fidelity, over patches of $\sim 20\text{meV}$. An extended optical modes structure can then be achieved by stitching these patches together, see application in chapter 3, 4 & 5. In the more specific case of PhC structures, the same approach holds for the waveguide modes' and cavity modes' effective index.

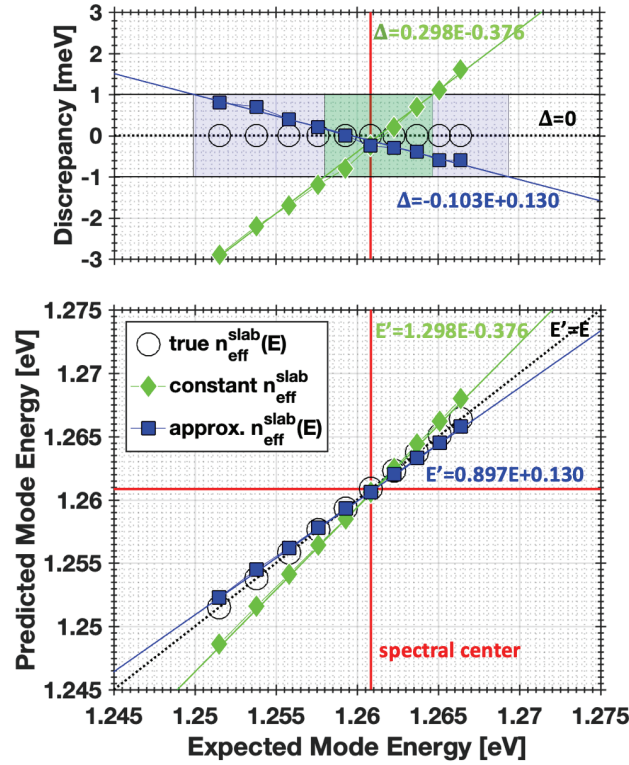


Fig. 2:5 – Calculated mode energies (lower panel) and discrepancies from exact energies (upper panel) illustrating the effect of the energy dependence of the slab effective refractive index when simulating a multi-mode cavity (a tilted-potential $L_{n=61}$ structure detailed in chapter 4). Black circles: each mode properly converged by adjusting $n_{\text{eff}}^{\text{slab}}$ with the mode energies. Green diamonds: modes predicted by a computation based on a single value of $n_{\text{eff}}^{\text{slab}}$ at the center energy. Blue squares: modes predicted by a computation based on a single value of $n_{\text{eff}}^{\text{slab}}$ at the spectral center energy but corrected with (Eq. 2:3).

2.1.4 Tailored-potential PhC cavities

Photonic crystal heterostructures can be made by the piece-wise stitching of uniform PhC subparts [164], [237]. This notion is further crystallized in the concept of a tailored-potential PhC cavity. In this case, the energy-dispersion is locally modified by change of structural parameters in real space, resulting in an alteration of the eigenmode energies (or effective refractive index) and the spatial distribution of the electro-magnetic field components. This is illustrated schematically in Fig. 2:6 for a single band, but it is reproduced for all bands. In the case of a regular L_n cavity (a), the corresponding infinitely long line defect has a lower band-edge (bottom green line) energy defining the bottom of the potential well for the confined photons. In the case of a 2D slab PhC, the height of the potential well is defined by the intersection of the band with the light cone, because modes at higher mode energy will leak, while for a 2D PhC it is defined either by the upper band-edge (top green line), since modes above it cannot exist due to the bandgap effect, or by the intersection with the air band, where modes delocalize. The left and right terminations are reflective boundaries that define the lateral extent of the potential well. Due to these boundary conditions, the waveguide band is effectively broken into discrete resonances, as this cavity confines fully localized modes with energies E_0, E_1, \dots (see blue lines). The otherwise regular profile of this potential well can be modified by local transverse shifts of the side-holes by amounts $s(x_i)$ at positions x_i , thus producing an effective potential well with an arbitrary profile [238]. This, in turn, modifies the energies as well as the envelope functions of the confined modes.

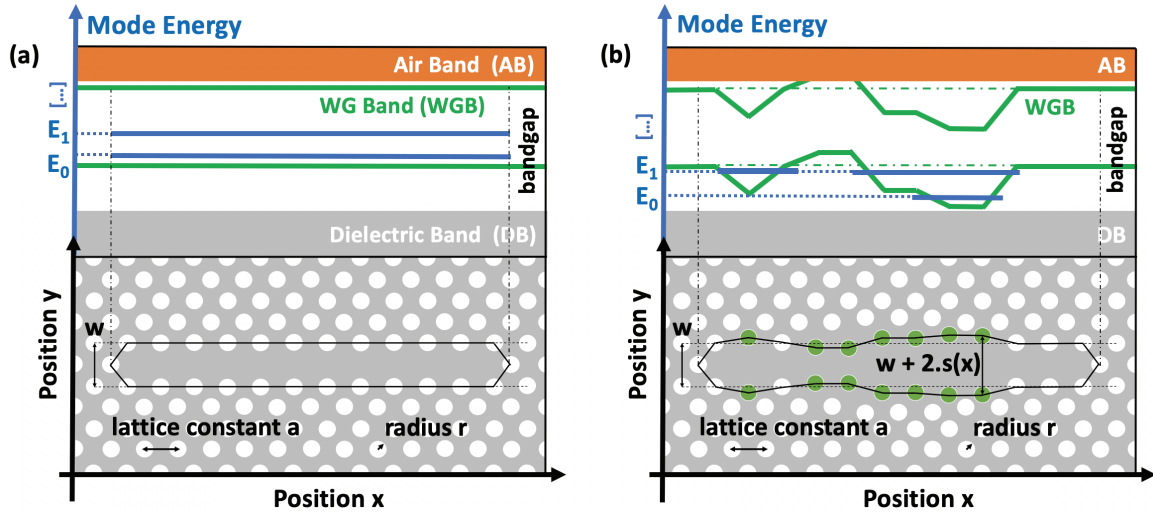


Fig. 2:6 – Illustration of 2D slab PhCs as potential landscapes in real space (x, y, n_{eff}^{mode}) . (a) L_n PhC cavity (also model for a PhC waveguide) acting as a reference. (b) Arbitrary tailored-potential L_n PhC cavity, based on local shifts $s \left(< \frac{\sqrt{3}}{2} a \right)$ of side-holes in transverse direction y .

The energy dispersion can be fully computed numerically, as is done in this thesis, or by means of a semi-analytical approach with an envelope function picture [239]. Conceptually, the photonic confinement potential landscape is redrawn following the spatial mismatch between the local energy dispersions [164] for the various sections of width $w + s(x_i) = w(1 + s(x_i)/w)$. The local energy dispersion of one such section can be obtained from the knowledge of the band structure and photonic modes of the equivalent virtual PhC waveguide, having a width $w + s(x_i)$ and complete translation symmetry. These can be obtained as a perturbation of the band structure and of the waveguide modes of the base PhC waveguide with width w . The latter can be computed numerically once, stored and retrieved each time it is needed for application to a different shift parameter $s(x_i)$. Using the notation in [239], in a perturbation approach the master equation for such a portion can be expressed as:

$$\Theta \mathbf{E}_{m\lambda}(\mathbf{r}) = \nabla^\wedge (\nabla^\wedge \mathbf{E}_{m\lambda}(\mathbf{r})) = \left(\frac{\omega_{m\lambda}}{c} \right)^2 \cdot \epsilon_r(\mathbf{r}) \cdot [1 + \Delta(s(x_i))] \cdot \mathbf{E}_{m\lambda}(\mathbf{r}), \quad i = 1, \dots, N \quad (\text{Eq. 2:4})$$

where $\mathbf{E}_{mn}(\mathbf{r})$ is the spatial distribution of the electric field of the unperturbed waveguide of width w , with energy dispersion $\hbar\omega_{mn}(\mathbf{k})$. Index m refers to the number of nodes along axis z of the TE slab mode envelope: TE_0, TE_1, \dots . Typically, we will be interested in $m=0$. Index n refers to the number of nodes along axis y of the waveguide modes' envelopes, $n=0, 1, \dots$ where $n=0$ corresponds to the 1st waveguide band, $n=1$ to the 2nd, etc. The index λ indicates perturbed quantities, $\mathbf{E}_{m\lambda}(\mathbf{r})$ is thus the new spatial distribution of the electric field inside the perturbed waveguide and $\hbar\omega_{m\lambda}(\mathbf{k})$ is the new energy dispersion. $\Delta(s(x_i))$ is the spatial perturbation in the slab dielectric constant that accounts for the displacement of the side-holes by $s(x_i)$. The perturbed modes can be expanded on the unperturbed basis of the w waveguide with weighted coefficients [239]:

$$\mathbf{E}_{m\lambda}(\mathbf{r}) = \sum_n \int W_{mn}(\mathbf{k}) \mathbf{E}_{mnk}(\mathbf{r}) d\mathbf{k} \quad (\text{Eq. 2:5})$$

The Fourier transform $F_{mn}(\mathbf{r})$ of the weights $W_{mn}(\mathbf{k})$ is defined as [239]:

$$F_{mn}(\mathbf{r}) = \int W_{mn}(\mathbf{k}) \cdot e^{i\mathbf{k} \cdot \mathbf{r}} d\mathbf{k} \quad (\text{Eq. 2:6})$$

from which one eventually obtains the envelope equation [239]:

$$\omega_{mn}^2 \cdot (-i\nabla) F_{mn}(\mathbf{r}) = \omega_{m\lambda}^2 \cdot [1 + \Delta(s(x_i))] \cdot F_{mn}(\mathbf{r}) \quad (\text{Eq. 2:7})$$

of the PhC tailored-potential heterostructure. This eigen-problem equation delivers all the important information provided that the modulation varies slowly over a unit cell (smooth slow envelope with features larger than pitch a), and that there is negligible coupling between the waveguide bands.

The spatial envelope functions and the dispersions of the subsections of waveguides of widths $w + s(x_1)$, $w + s(x_2)$, ..., $w + s(x_N)$ should then be stitched in real space by continuity and in reciprocal space by phase-matching. Eventually, the introduction of boundary conditions imposed by the left and right terminations of the PhC cavity will effectively break down the bands into the discrete cavity modes due to the lateral confinement in x . This will add a new index p , that indicates the number of nodes of the spatial envelopes along the x axis. After all this, one can get the final cavity modes spatial envelopes, which, when multiplied by the Bloch crystal term, yield the final cavity modes electric field $\mathbf{E}_{mnp\mathbf{k}}(\mathbf{r})$ and the final energy dispersion $\hbar\omega_{mnp}(\mathbf{k})$.

These photonic heterostructures can be implemented in a variety of alternative manners: by local change of holes sizes [88], [240], of the PhC pitch [164], or materials (dielectric constant) [241]. The energy-potential confinement picture is quite intuitive, as it directly outlines the spatial variation of the optical modes. This also provides some insight into Anderson localization by random holes shift disorder, as the effect can naturally be seen as causing fluctuations of the photonic confinement potential, forming potential traps to capture light at lower photon energies (near the band-edges).

2.2 Embedding pyramidal site-controlled QDs in PhC structures

Positioning QDs at the proper locations in suspended PhC structures is an exceptional challenge involving several critical steps. In the upcoming sections, details of the various steps are presented and discussed.

2.2.1 Substrate preparation for QD growth

The first fabrication phase consists in the patterning of the substrate with pyramidal recesses in which the site-controlled QDs will be grown. We start with 2" GaAs "membrane" wafers containing a $\sim 1\mu\text{m}$ thick $\text{Al}_x\text{Ga}_{1-x}\text{As}$ ($x \sim 0.7$) sacrificial layer on which the GaAs thin membrane layer is grown [242]. The membrane structures are grown by Molecular Beam Epitaxy (MBE) on semi-insulating GaAs substrates, misoriented from the (111)B surface by 3 degrees towards the $[-211]$ direction. The Al content is $x \approx 0.64$ and the GaAs membrane thickness is $\sim 264\text{nm}$. An Atomic Force Microscope (AFM, model XE-100 from PSIA, now Park Systems) was used to assess the surface roughness using the intermittent contact mode. As a consequence of the crystallographic misorientation, the surface is not atomically flat, and corrugations are formed by monolayer steps and step bunching. Over a patch of 700nm in width, a Gaussian distribution of the height fluctuations was estimated, yielding a root mean square roughness $R_q \approx 0.3\text{nm}$. These values point to a step-flow growth with monolayers ($\frac{1}{2}\text{aGaAs} \approx 0.3\text{nm}$) or possibly bi-layers of GaAs.

In order to be able to register the locations of written structures and to align patterns, Alignment marks (AMs) were fabricated in various parts of the wafer. These must be robust and outlive the many subsequent fabrication steps, and thus the AMs are etched into the substrate to a depth of $1.5\mu\text{m}$. To this end, the membrane and AlGaAs sacrificial layers are first removed in a large ($200 \times 200\mu\text{m}^2$) region, where the AMs are intended to be fabricated. In order to produce the AMs, a 300 nm thick SiO_2 layer is first deposited by Plasma Enhanced Chemical Vapor Deposition (PECVD) using a PlasmaLab100 machine from Oxford Instruments. An electron beam resist, Poly(methyl methacrylate) (PMMA), molecular weight 950k, is then spin-coated on top of it and soft-baked at 160° . The AMs are patterned as arrays of $10 \times 10\mu\text{m}^2$ square apertures using a Vistec EPBG5000+ electron beam lithography (EBL) machine. The resist is developed using a Methyl Isobutyl Ketone: Isopropyl Alcohol (MIBK:IPA) mixture to dissolve the exposed PMMA and generate the AM template. The pattern is then transferred into the SiO_2 mask by dry Reactive Ion Etching (RIE) with a PlasmaLab 80 machine made by Oxford Instruments, using CHF_3 gas. After etching, the PMMA layer is removed by an ultrasonic acetone bath, followed by IPA and water rinsing. The AMs are engraved into the GaAs substrate by a long Inductively Coupled Plasma (ICP) dry etching with a Sentech Plasma Etcher SI 500. The SiO_2 mask is then removed by wet etching in Buffered Hydrofluoric acid (BHF). More details of the process steps of the AMs fabrication are available in appendix. B.

The patterning design of sample B: A177-3-4B incorporates three different regions to be patterned with pyramidal recesses. The first consists of a “big” square of $2.4 \times 2.4 \text{ mm}^2$ surrounded by one AM at each corner. the big square region is composed of an outer “band”, $198 \mu\text{m}$ wide, and an inside square ($1944 \times 1944 \mu\text{m}^2$) divided into 4 bands $486 \mu\text{m}$ in height by $1944 \mu\text{m}$ in length. The basic writing unit, containing a single device (PhC cavity or waveguide), is a $18 \times 18 \mu\text{m}^2$ square², so each inside band is composed of 27×108 units = devices. The two top bands are designed to allow PhC structures with coupled elements that can be separated by 3 rows of holes; one of the two bands can incorporate a single pyramid within a potential $L_{n=3}$ cavity. The two bottom bands are similar except that there is only 1 row of holes separation. The $198 \mu\text{m}$ “band” around the center square contains homogeneous arrays of pyramids. The big square region is to be inscribed with triangular apertures of nominal sizes (pyramid side) $s_{\text{nom.}} = 180 \text{ nm}$ arranged on a triangular lattice of pitch $p = 450 \text{ nm}$. The second region is made by 5 medium squares of $720 \times 720 \mu\text{m}^2$, in which are written triangular apertures with $s_{\text{nom.}} = 140, 160, 180, 200$ and 220 nm . In each of these square, smaller apertures of size $s'_{\text{nom.}} = s_{\text{nom.}} - 20 \text{ nm}, s_{\text{nom.}} - 40 \text{ nm}, s_{\text{nom.}} - 60 \text{ nm}, s_{\text{nom.}} - 80 \text{ nm}$ are written every 10 lattice sites, i.e. every $4.5 \mu\text{m} \times 4.67 \mu\text{m}$, having QD emission wavelength control in mind [143]. And the third region is made by five “small” squares of $216 \times 216 \mu\text{m}^2$ patterned in the same fashion as the second region.

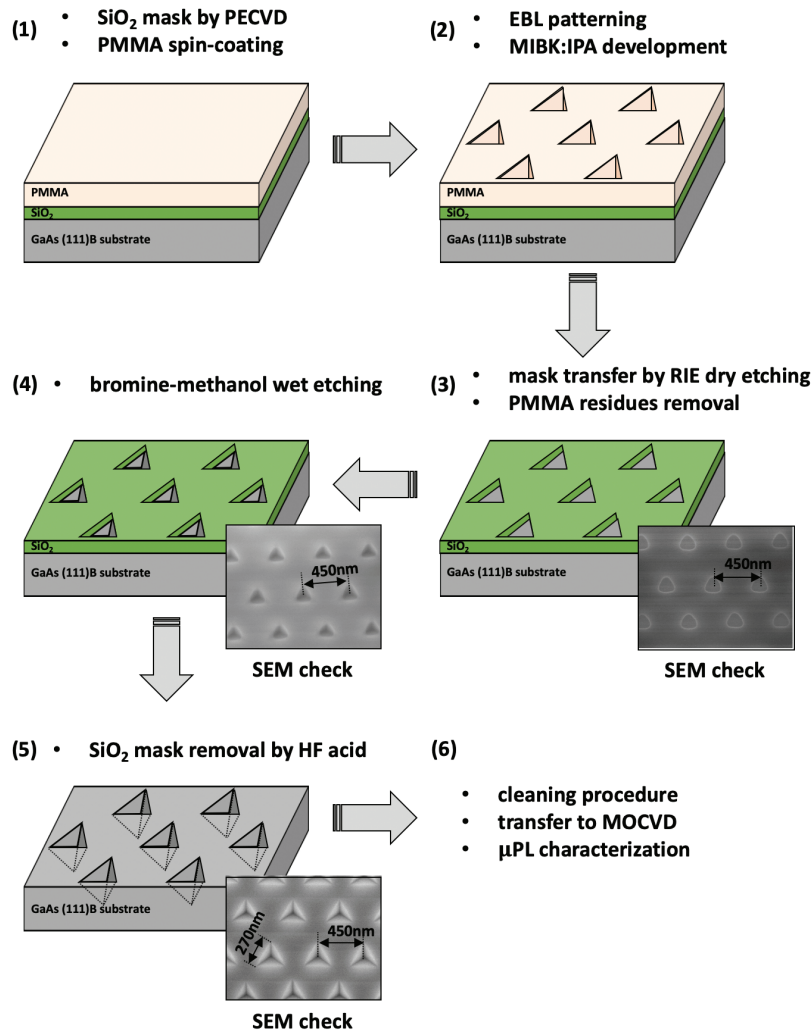


Fig. 2:7 – Fabrication steps involved in the patterning of the substrate with inverted pyramids for the growth of pyramidal site-controlled QDs. SEM images of representative structures are inserted.

The procedure for the patterning of inverted pyramidal recesses is illustrated in **Fig. 2:7**. **(1)** A SiO₂ layer is deposited by PECVD, PMMA is spin-coated on top of it and soft-baked. **(2)** The regions of interest are then patterned with triangular apertures arranged in a triangular lattice pattern of pitch $p=2a=450\text{nm}$ onto the PMMA layer by EBL, using the AMs for precise positioning (20nm). The resist is next developed using MIBK:IPA to open the apertures and generate a template. **(3)** The template is transferred into the SiO₂ layer down to the GaAs top surface by RIE. A first SEM quality check is performed with a JSM-6701F microscope by JEOL. Any left-over residues of PMMA are removed by acetone in ultrasonic bath, followed by Oxygen RIE. **(4)** The sample is dipped in a 0.06% Bromine:Methanol wet etching solution, which produces inverted pyramidal pits by exposing {111}A GaAs facets. The use of triangular openings in addition to the [111]B crystalline direction and the anisotropic chemical etching are the key ingredients to ensure high quality, uniform pyramidal structures. A second SEM quality check is made to verify the quality of the etching step. **(5)** The mask is then stripped by BHF and a third SEM quality check verifies the geometry and dimensions of the patterns. **(6)** In the particular samples used in this thesis, according to SEM observations, the measured pyramid sizes were $s_{\text{fab.}} \approx 253 \pm 5\text{nm}$ for the big square, $s_{\text{fab.}} \approx 205 \pm 5, 233 \pm 5, 253 \pm 5, 271 \pm 5, 297 \pm 5\text{nm}$ for the medium squares, and $s_{\text{fab.}} \approx 159 \pm 5, 157 \pm 5, 225 \pm 5, 272 \pm 5\text{nm}$ for the small squares. The process steps for the pyramidal recesses patterning are detailed further in appendix B.

2.2.2 Growth and characterization of pyramidal site-controlled QDs

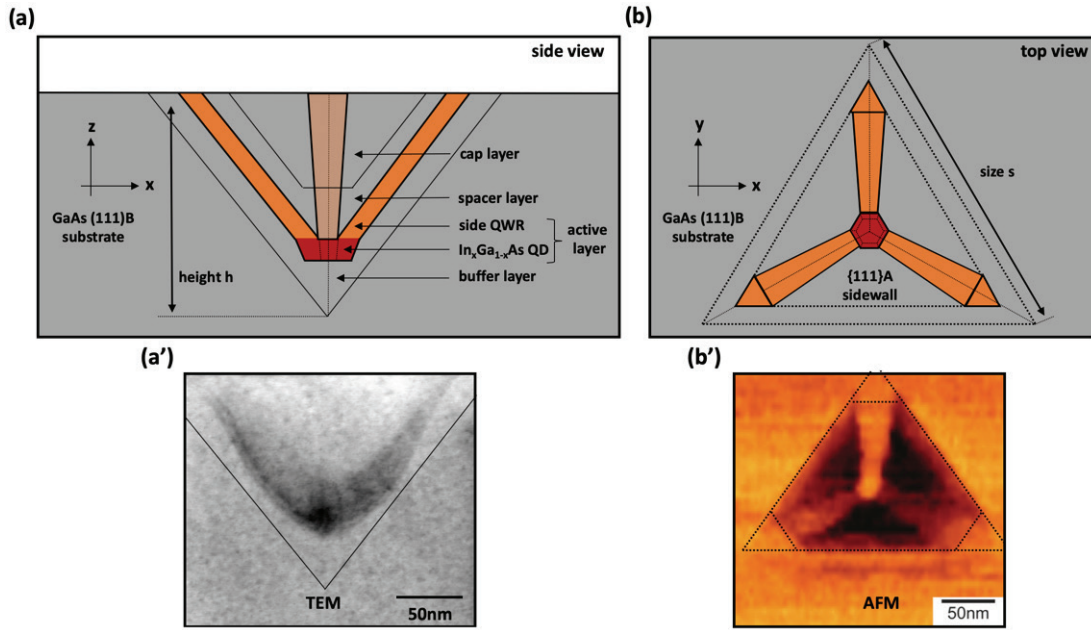


Fig. 2:8 – Illustration of the geometry and details of a pyramidal site-controlled QD grown by MOCVD. Schematic (a) side-view and (b) top view, (a') TEM image in cross-section [243], (b') AFM top image of a GaAs pyramidal template. Reprinted and adapted with permission from [244] for (b').

The patterned sample is next thoroughly cleaned, deoxidized, and introduced into the glove box of an MOCVD Aixtron 200 machine, then transferred into the reactor chamber, where it is placed on a rotating susceptor heated to the desired growth temperature ($T \approx 600\text{C}$). The growth of epitaxial layers of various III-V semiconductor materials with a control on composition and thickness down to monolayer precision is made using a mixture of metal-organic compounds and hydrides. The metalorganic group III precursors, e.g. Trimethylgallium (TMGa), are introduced from liquid sources and transported onto the sample by an inert N₂ carrier gas at a pressure of 20mBar. Arsine (AsH₃) is used for the group V component. The precursors are adsorbed onto the crystal surface of the substrate, decompose due to the high temperature, and the adatom products diffuse on the surface to the point of crystallization of the III-V material. Byproducts of carbon and hydrogen (hydrogen, ethane, ethene and methane) desorb and are evacuated from the reactor chamber. The geometry of the reactor and the rotating susceptor plate ensure the uniformity of the process.

The structure of the pyramidal site-controlled GaAs/InGaAs QDs, grown in such process, is illustrated in **Fig. 2:8**, in both side and top views. MOCVD growth takes place only within the pyramids since the metalorganic precursors decompose on the $\{111\}$ A pyramid facets rather than on the (111) B surface around them [245]. As a result, the actual growth rate inside the pyramids is much higher than on a non-patterned (111) A surface and is inferred from proper calibration growth runs. **Fig. 2:8(a)** displays cross sectional structure following the deposition of typical three QD-heterostructure layers. The first GaAs layer (grown using TMGa and Arsine) recovers the crystalline quality above the etched facets, which can be a source of trapped impurities and surface states that can have detrimental effects on the QD optical quality. This buffer layer also sets the vertical position of the grown QD, in particular adjusting it to the center of the membrane. The second layer, in which the QD is formed, is made by the combination of Triethylgallium (TEGa), Trimethylindium (TMIn) and Arsine reactants [122]. The crescent shaped QD is formed at the sharp, bottom of the pyramid due to a combination of growth rate anisotropy and capillarity [138]–[140], [245], [246]. Finally, the GaAs cap layer, grown with TMGa and Arsine, terminates the QD heterostructure and planarizes the pyramid recess, which is required for subsequent fabrication PhCs structures of high quality [247].

Fig. 2:8(a,b) depict schematically the morphology of a grown pyramidal GaAs/InGaAs QD grown on pyramids with sub- μm dimensions. The details of this structure are based on structural studies, including TEM and AFM images as those shown in parts (a') and (b'). The QD (dark red) at the apex of the inverted pyramidal pit is connected to three side quantum wires (QWRs) (orange) protruding along the edges and the three $\{111\}$ A sidewalls [248]. These QWRs may play a role in the feeding of the QDs via channeling of charge carriers produced in the barrier [248].

The TEM image reproduced in **Fig. 2:8(a')** was made using a thin slice of $\sim 100\text{nm}$ thickness specifically prepared by ion beam etching and observed in cross-section with a FEI Tecnai Osiris operated at 200kV. This leads to a distortion of the InGaAs QD, which is superimposed on the QWR and QW structures grown around it. This produces a QD image that is larger than the actual one. More accurate estimate of the QD size can be made based on the energies of the observed optical transitions [249].

The AFM top image [244] shown in **Fig. 2:8(b')** was realized on a pyramid array with pyramid size $s \approx 175\text{nm}$ and pitch $p \approx 400\text{nm}$ overgrown with thin GaAs layer. The associated detailed study confirms the aforementioned growth mechanisms, and also reveals that the original $\sim C_{3v}$ three-fold symmetry at the bottom of the pyramid evolves into a $\sim C_{6v}$ six-fold symmetry due to the capillarity at the pyramid wedges. This higher QD symmetry is helpful for achieving polarization-entangled photons from such QDs [148], [249], [250].

Detailed process steps of the QDs growth are available in appendix B.

2.2.3 Optical characterization of QDs arrays

A summary of the micro-photoluminescence (μPL) characterization of the QD emission spectra acquired right after MOCVD growth is displayed in **Fig. 2:9** (see section 2.3.1 for details on the optical setup). **Fig. 2:9(a)** provides a panoramic view of the spectral transitions ranging from the lowest energy states of the QDs to the GaAs bulk spectral signatures: carbon impurity and exciton related. These data were acquired near the center region of the QD arrays in the big square. The laser excitation source covers a region of about 10 QDs, so we cannot distinguish the origin of every QD emission line. At high excitation power $P_{\text{exc.}} \approx 2\text{mW}$ (blue), the lowest energy transitions inside the QDs are saturated and broadened. The QDs higher excited states or QWRs states are much brighter than the ground states, due to possibly shorter radiative lifetimes and especially larger volumes of the QWRs which result in more recombinations. These states are also brighter than the carbon impurity signature which can be a sign of the charge carriers being transferred from the barrier to the QWRs. The bulk exciton donor is weak because the substrate is semi-insulating. At lower pump power $P_{\text{exc.}} \approx 10\mu\text{W}$ (red), only the QD s-shell is saturated while the p-shell starts to populate. The presence of an important bulk Donor-Acceptor of Carbon line may indicate electron feeding channels, explaining why negative trions appear in the QD spectra (see chapters 3, 4 & 5).

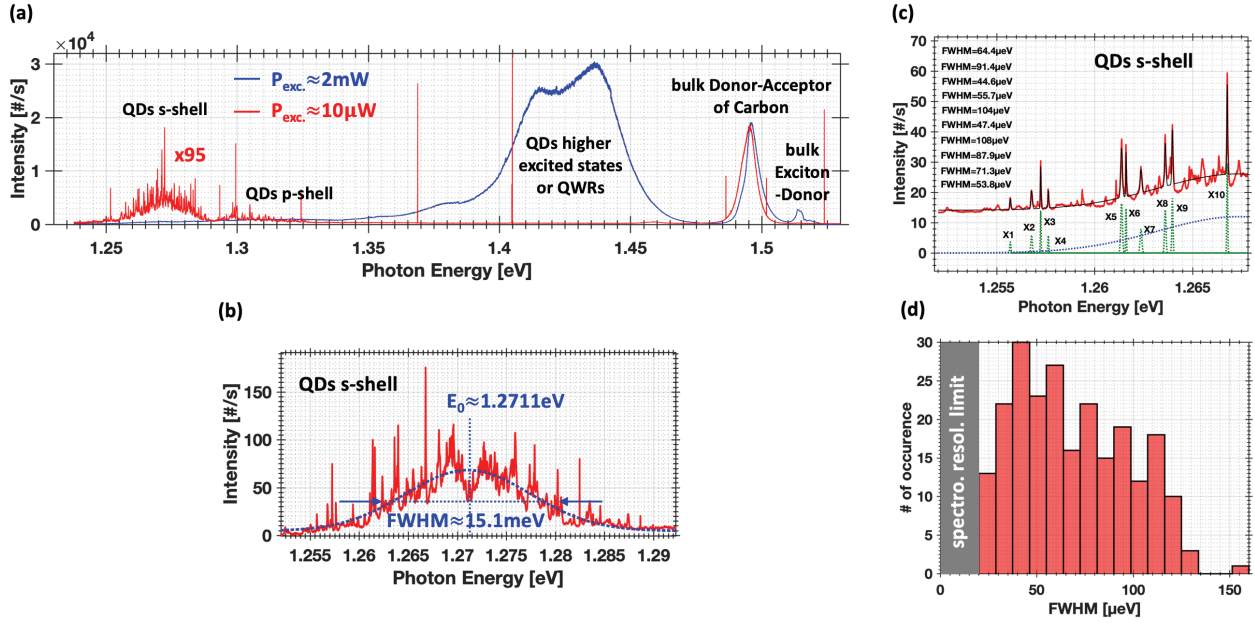


Fig. 2:9 – μPL characterization of QDs ensemble emission in sample A177-3-4A #5965 (presented in this thesis) right after MOCVD growth, and before PhC fabrication. (a) Panoramic spectra at high excitation power $P_{exc} \approx 2\text{mW}$ (blue) and low excitation power $P_{exc} \approx 10\mu\text{W}$ (red, signal magnified x95). Detection events artifacts are visible. Signal corrected to compensate variations in detector quantum efficiency versus energy. (b) Zoom on QDs s-shell emission with $\sim 15.1\text{meV}$ inhomogeneous broadening, spectral center energy $E_0 \approx 1.2711\text{eV}$ ($\lambda_0 \approx 975.4\text{nm}$). (c) Fits of (non-identified) excitons lines in the low-energy tail of the distribution. (d) Histogram of QD linewidths build with 231 lines from spectra taken at different locations with $10\mu\text{W}$ power. Temperature $T \approx 10\text{K}$, excitation energy: $\sim 1.7\text{eV}$ (above barrier).

Fig. 2:9(b) zooms in on the QD ensemble s-shell emission. The transitions are inhomogeneously broadened into a Gaussian of $\sim 15.1\text{meV}$ s full-width at half maximum, around a spectral center energy $E_0 \approx 1.2711\text{eV}$ ($\lambda_0 \approx 975.4\text{nm}$). **Fig. 2:9(c)** reports the fits of (non-identified) excitons lines in the low-energy tail of the s-shell spectrum with $10\mu\text{W}$ above barrier pumping. The photon energy dependence of the quantum efficiency reduces the detection efficiency at the lowest energies (longer wavelengths). This was corrected numerically by proper calibration. Finally, **Fig. 2:9(d)** shows a histogram of QD emission linewidths built from the fits of 231 lines as depicted in (c) from spectra taken at different locations. Since these spectra are acquired with above barrier excitation, the linewidths are impacted by pure dephasing. The distribution of linewidths has a mean of $\overline{\hbar\gamma_{QD}} \approx 69\mu\text{eV}$ s and a standard deviation of $\sigma_{\hbar\gamma_{QD}} \approx 29\mu\text{eV}$ s; for these statistics, we selected $[3.49\sigma_{\hbar\gamma_{QD}}/N^{(1/3)}] = 16$ bins of $(160 - 20)/16 \approx 9\mu\text{eV}$ s, based on Scott's rule [251]. The distribution is slightly skewed, has a minimum value of $\sim 20\mu\text{eV}$ s limited by the spectrometer resolution limit and peaks for the bin of $\sim 38\text{--}46\mu\text{eV}$ s.

2.2.4 Photonic crystal structure fabrication

Overlaying the PhC structures patterns on top of the already grown QDs arrays is a succession of challenging fabrication steps, pictured in **Fig. 2:10**. The AMs are used to precisely align the PhC features with respect to the QD positions, as demanded by the sample design. **(1)** A SiO_2 layer is deposited by PECVD, and PMMA is spin-coated and soft-baked. **(2)** The resist is exposed by EBL to pattern the hole arrays and developed with MIBK:IPA. **(3)** The pattern is transferred into the SiO_2 layer by RIE dry etching. Residues of PMMA are removed by acetone and ultrasound bath, followed by Oxygen RIE. **(4)** Before proceeding with the real sample, the ICP dry etching of the PhC holes down to the sacrificial layer is fine-tuned on a dummy (100) GaAs sample. The dummy sample is cleaved and observed by SEM to ensure that the holes are of the right size, straight, smooth and deep enough. **(5)** The membrane is then released by an HF acid etching that dissolves the sacrificial layer. The sample is then rinsed with water, transferred to a citric acid bath to remove residues, then rinsed thoroughly. The dummy (100) membrane sample is processed in parallel, then cleaved and observed by SEM to ensure that the release went as expected.

The process is then repeated with the (111)B membrane sample. To prevent the breaking of the membrane, the sample is left immersed in liquid and inserted in a nitrogen box for evaporation.

Detailed studies of the fabrication process show that the precision in relative alignment of the QDs to the PhC features is better than 50nm, and in most cases near 20nm [221]. This ensures proper spatial matching to the optical modes of the cavities, since typical lobes in the Bloch terms are ~ 100 nm wide.

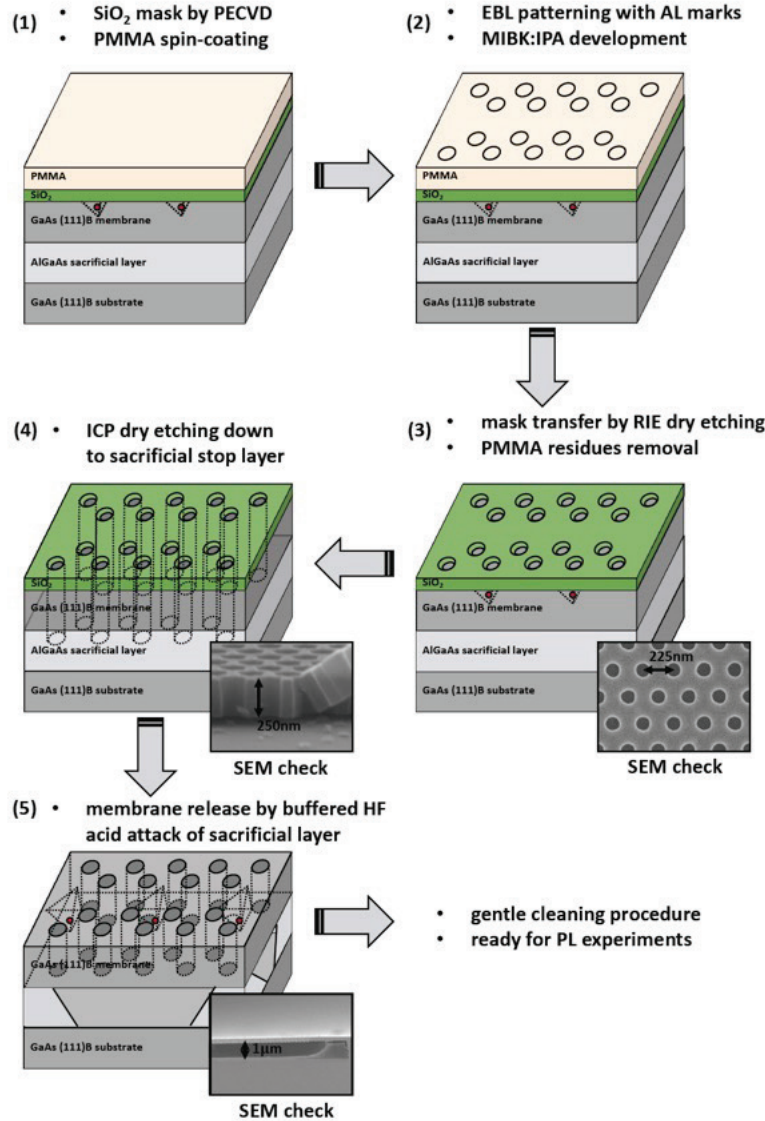


Fig. 2:10 – Fabrication steps, post QDs growth, involved in the making of suspended PhC structures. AMs, not detailed here, surround the patterned regions. SEM images of representative structures are inserted.

Since the QDs arrays have twice the pitch of the PhCs ($p = 2a$), and since the pitch a is fixed by design, ideally there should be one QD for every two holes in a PhC lattice line. Unwanted QDs are thus naturally removed by the etching of the holes during the ICP step. The important point is to remove the InGaAs QD core as the rest of the pyramid is filled with GaAs. In the sample used in this thesis, a full range of $r_{\text{nom.}} \in [30, 50]$ nm, corresponding to actual hole radii $r_{\text{fab.}} \in [47, 74]$ nm, was implemented to realize lithographic tuning of the optical mode energies to enter in resonance with the ground QDs s-shell states. **Table 2:1** compiles values of some hole sizes, the designed ones and the fabricated ones derived from SEM observations. The table also shows the corresponding values used in numerical simulations of the optical modes, together with a useful formula for estimating the r_{fab} from the $r_{\text{nom.}}$ values. The discrepancy between r and $r_{\text{fab.}}$ probably stems from a difference of few percent between the assumed and actual effective index of the membrane slab.

$r_{\text{nom.}} [\text{nm}]$	$r_{\text{fab.}} \approx 1.34r_{\text{nom.}} + 6.7 [\text{nm}]$	$r \approx 0.7r_{\text{fab.}} + 25 \approx 0.94r_{\text{nom.}} + 29.7 [\text{nm}]$
...
36	55.1 ± 2	63.6 ± 0.8
37	56.4 ± 2	64.5 ± 0.8
38	57.8 ± 2	65.4 ± 0.8
39	59.1 ± 2	66.4 ± 0.8
40	60.5 ± 2	67.3 ± 0.8
...

Table 2:1 – Correspondences between nominal radii $r_{\text{nom.}}$ set by design, fabrication radii $r_{\text{fab.}}$ based on SEM observations after ICP etching of a calibration dummy sample, and numerical simulation radii r imposed to match predictions with experimental μPL observations. For $r_{\text{fab.}}$ the uncertainty is related to one standard deviation in fabrication disorder or SEM inaccurate readings. For r the uncertainty is related to one standard deviation in statistical dispersion over few samples (not accounting for disorder), as a result of studies in chapters 3, 4 & 5.

Further details of the process steps of the PhCs making and release are available in appendix. B.

2.3 Micro-photoluminescence (μPL) spectroscopy

Characterization of the optical emission collected from both QDs and PhC structures requires a micro-photoluminescence (μPL) setup. Details of the versatile setup used are presented in the following section.

2.3.1 Micro-PL setup

The optical setup is depicted in **Fig. 2:11**. Starting from the upper-left corner, a part is dedicated to directing the laser pump beam on an excitation path and controlling its power. A frequency-doubled Neodymium-doped Yttrium Aluminum Garnet (Nd:YAG) diode-pumped solid-state laser (DPSSL, Millenia V from Spectra-Physics) generates 532nm wavelength green light to optically pump the principal Titanium-Sapphire (Ti:Sapph, Tsunami Spectra-Physics) laser with 5 Watts of power. The latter is tunable over a range of $\lambda_{\text{exc.}} \sim 710\text{-}940\text{nm}$ (up to 980nm according to specifications), from visible red to near infrared, and can work in both Continuous-Wave (CW) or mode-locked picosecond (ps) pulsed mode. The beam has a TEM_{00} spatial profile with a diameter $D^{\text{laser}} \leq 2\text{mm}$ and is characterized by a $>500:1$ vertical polarization ratio. The output power, read with a power-meter, can be adjusted from a few milliwatts down to tens of nanowatts, with the combination of two neutral-density filter wheels and two neutral density fixed plates. The excitation laser beam is redirected with mirrors and injected into a vertical microscope with beam-splitters to shine at normal incidence through the cryostat's window (ST-500 from Janis Research). The beam spot is focused to the diffraction limit onto the sample with an Olympus LMPlan 50X IR magnifying microscope objective possessing a numerical aperture $\text{NA} \approx 0.55$ with a focal distance $f^{\text{micro.}} \approx 180/50 \approx 3.6\text{mm}$, effective working distance $\text{WD}^{\text{micro.}} \approx 6\text{mm}$ and pupil width $D^{\text{micro.}} \approx 18\text{mm}$. In the next chapters, we mention the injected power, denoted $P_{\text{exc.}}$, measured by a trusted power-meter before the microscope. It is further reduced by the combined optical losses of the components along the path, and only about $\eta_{\text{tot.}} \approx 0.6\%$ of the original power level reaches through the cryostat window. The microscope objective creates a circular spot of an area $A^{\text{spot}} \approx 2 \times 2 \mu\text{m}^2$; in different studies, we use in addition a cylindrical lens to create instead an elliptical spot on the sample's surface with an area $A^{\text{strip}} \approx 2 \times 20 \mu\text{m}^2$. The power incident on the sample's surface translates into surface power densities $p_{\text{exc.}} = \eta_{\text{tot.}} P_{\text{exc.}} / A$, meaning $\sim (0.006 P_{\text{exc.}} / 4) \cdot 10^8$ and $\sim (0.006 P_{\text{exc.}} / 40) \cdot 10^8$ Watts/cm² for the two spot types, respectively.

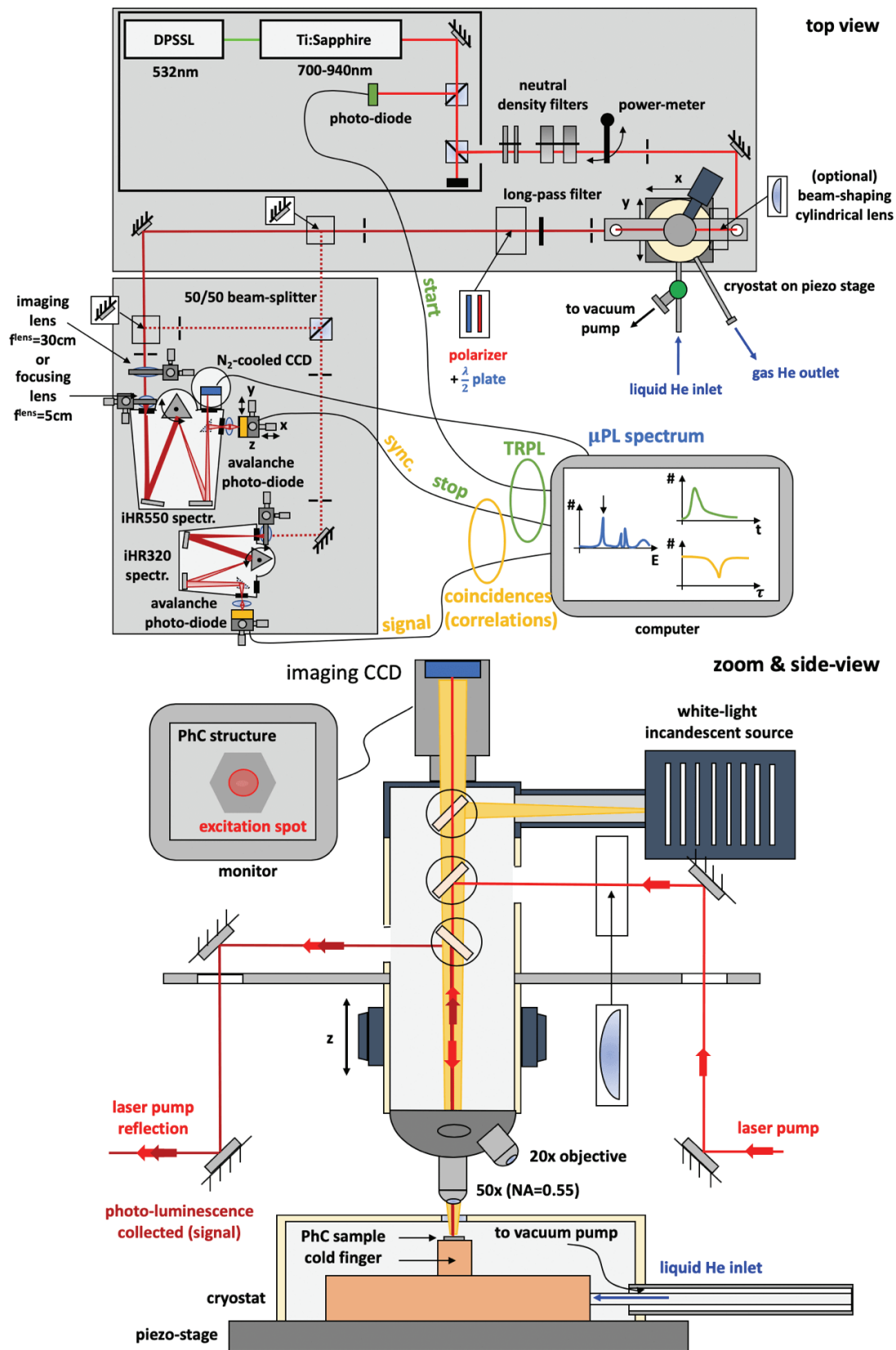


Fig. 2:11 – Schematics of the versatile μ PL setup used for QD and PhC structure optical characterization, including polarization-resolved and time-resolved spectra.

The sample is mounted on top of a copper cold finger, and thermal contact is ensured by a conducting silver paste applied with a brush. The inside of the cryostat is pumped for insulation to a vacuum level of 10^{-5} - 10^{-6} bars thanks to a secondary turbo-pump backed by a primary rotary vane pump. The sample can be cooled down to cryogenic temperature of 4-10 Kelvins using the cold finger, itself cooled by a flow of liquid Helium. The in-situ temperature is monitored, adjusted and stabilized by a Proportional-Integral-Derivative (PID) LakeShore temperature controller connected to a GaAs diode thermometer and resistive heater. The cryostat is itself fixed on top of two (XY) linear direct-drive ALS130H Aerotech nanopositioning motorized stage, providing a precise control over positions down to ± 50 nm accuracy with the aid of computer software. The sample's surface can be imaged onto a mounted Ultrak CCD B&W camera with the white light produced by a halogen lamp, illuminating the sample and reflected back. The beam-splitters in the imaging optical path are dichroic and prevent the damaging of the CCD by the intense reflected laser signal.

The collected photoluminescence is focused with an achromatic $f^{\text{lens}} \approx 50$ mm lens on the entrance slit of a iHR550 Horiba Jobin Yvon grating spectrometer with $f^{\text{spectr.}} = 55$ cm focal length. Light is diffracted by a $76 \times 76 \text{ mm}^2$ grating with $n = 1'200$ lines/mm and imaged on a liquid nitrogen -cooled silicon Horiba Jobin Yvon Spectrum One 3000 CCD camera. The array of 2048×512 pixels has a size of $27.6 \text{ mm} \times 6.9 \text{ mm}$ with $13.5 \mu\text{m} \times 13.5 \mu\text{m}$ pixels. The CCD has a typical dark count (baseline) of $\sim 1'000$ counts and noise of 1-3 electrons/pixel/hr plus read-out noise of 4-10 electrons/pixel. The baseline count can thus be subtracted to get the true μPL signal, which will have the residual 4-10 electrons/pixel noise, so a total count over the integration time of 50 counts will resulting signal-to-noise ratio of 5-10. The CCD is characterized by a dynamic range of maximum $65'535$ counts, with a decreasing quantum efficiency of $\sim 40\%$ to $\sim 10\%$ from 730nm to 1000nm. The number of illuminated grating lines is $N = n \cdot f^{\text{spectr.}} / f^{\text{lens}} \cdot D^{\text{laser}} = 66'000$ for $D^{\text{laser}} \approx 5$ mm measured in free space at the position of the lens. $\frac{\delta E}{E} = \frac{\delta \lambda}{\lambda} \approx \frac{1}{N}$, for $\lambda \approx 1 \mu\text{m}$, yields the theoretical resolution as $\delta \lambda \approx 15 \text{ pm}$, i.e., $\delta E \approx 19 \mu\text{eV}$. Unless specified otherwise, an entrance slit of $\sim 80 \mu\text{m}$ was typically used in all experiments, providing a decreased spectral resolution of $\sim 60 \mu\text{eV}$. For the data of Fig. 2:9, a higher spectral resolution spectrometer was used with an otherwise similar μPL setup: a Horiba Jobin Yvon FHR640 with $f^{\text{spectr.}} = 64$ cm focal length and $110 \times 110 \text{ mm}^2$ grating with $1'800$ lines/mm, interfaced to an Andor iDus 416 2000×256 pixels CCD, providing a $\sim 20 \mu\text{eV}$ spectral resolution for an $\sim 20 \mu\text{m}$ entrance slit. Spectral lines are fitted with Lorentzian functions to precisely estimate center energies and full-widths at half maximum, in particular for computing Q-factors of the photonic cavities investigated.

The addition of a linear polarizer and $\lambda/2$ -waveplate in the detection path resolves the state of polarization of the collected photons. The orientation of the waveplate is set by a Newport motion controller. The PL intensity is plotted in a polar plot as function of the waveplate angle with steps of 5-10 degrees, which reveals a full Malus' Law dependence for linearly polarized light. Linear polarization along the photonic cavity is labeled H whereas the orthogonal one is labeled V (see Chapters 3 and 4). Using these V and H polarization components, we often use the Degree of Linear Polarization (DOLP) as a function of position $\mathbf{r} = (\mathbf{x}, \mathbf{y})$ on the structure and the photon energy E:

$$DOLP(\mathbf{r}, E) = \frac{I_V(\mathbf{r}, E) - I_H(\mathbf{r}, E)}{I_V(\mathbf{r}, E) + I_H(\mathbf{r}, E)}, \quad (\text{Eq. 2:8})$$

In the same fashion, but using a $\lambda/4$ -waveplate instead, circularly polarized light can be analyzed.

2.3.2 Spatial imaging of PL spectra

The setup of Fig. 2:11 can be modified in order to provide 1D spatial information on the excited PhC structures, which is especially useful for studying their photonic mode structures [252]. This is accomplished by imaging the surface of the emitting structure (e.g., along a PhC cavity in which QDs are embedded as light sources) onto the entrance slit of the spectrometer. Each point x along the slit is transformed into a full spectrum in the y direction after dispersion by the grating spectrometer and focused on the CCD plane (see Fig. 2:12). As this process occurs in parallel for each x value, the x direction on the CCD displays the 1D spatial image of the emitting structure, while the y direction displays the wavelength.

As the monochromator has a 1:1 imaging ratio, the image on the CCD is identical (in the x direction) to the projection on the entrance slit. It should be noted that the second dimension of the imaged device is not imaged, as it is cut off by the entrance slit.

For acquisition of conventional PL spectra (i.e., without spatial information), the setup of Fig. 2:11 is used with a short-focal focusing lens in front of the spectrometer (see **Fig. 2:12(a)**). In this case, the spatial information along x is quenched (arrives at one or a few pixels on the CD, which are summed along x to give one information point), and a spectrum of the PL emitted from whatever point on the emitting surface is displayed along the y-axis of the CCD. When a long-focus imaging lens is used, an image of the emitting surface is obtained on the entrance slit, and a 1D spatially resolved spectrum is produced on the CCD camera (see **Fig. 2:12(b)**).

With the addition of a cylindrical lens before the entrance into the microscope (see Fig. 2:11), the laser beam, reshaped into a strip, can excite the full length of an L_n cavity and its embedded site-controlled QDs. Alternatively, the (diffraction limited) laser spot can be scanned along the length of the cavity to excite specific regions independently. In the first case, the combination of the focusing lens in front of the spectrometer (Fig. 2:12(a)) and the microscope objective forms a large microscope that provides a magnification of $M \approx f_{\text{lens}} / f_{\text{micro}} \approx 14$; i.e. one micrometer on the sample corresponds to $14\mu\text{m}$ imaged on the CCD, which is the size of a single pixel since the spectrometer provides a $\sim 1:1$ magnification. In Fig. 2:12(b), the imaging lens with $f_{\text{lens}} \approx 300\text{mm}$ and the total magnification is then $M \approx 83$. One micrometer on the sample then corresponds to $83\mu\text{m}$ on the spectrometer CCD, equivalent to ~ 6 pixels. This, together with the diffraction-limited imaging, sets a limit on the spatial resolution of the spectrally-resolved images. The Bloch term of the photonic wavefunctions (225 nm periodicity) thus cannot be resolved. The line-shaped laser spot can illuminate up to $\sim 20\mu\text{m}$ long regions on the sample that can be fully imaged, corresponding to $1660\mu\text{m}$, i.e. 120 pixels or one quarter of the CCD chip.

The grating still disperses simultaneously the spectrum along the other orthogonal axis (y) to display the emission spectrum, as depicted by the red, green and blue components in Fig. 2:12(b). However, in this mode, the spectral resolution is degraded to $\sim 110\mu\text{eV}$ with the usual $\sim 80\mu\text{m}$ entrance slit because a smaller portion of the grating is effectively illuminated. Indeed, the number of illuminated lines is now $N=11'000$ and $\frac{\delta E}{E} = \frac{\delta \lambda}{\lambda} \approx \frac{1}{N}$, for $\lambda \approx 1\mu\text{m}$, the theoretical best resolution is $\delta \lambda \approx 90\text{pm}$, i.e. $\delta E \approx 110\mu\text{eV}$.

Image distortion was also noticed with symmetric, quasi linear divergence of the images with increasing wavelength. The processed images shown in the following chapters correct this effect.

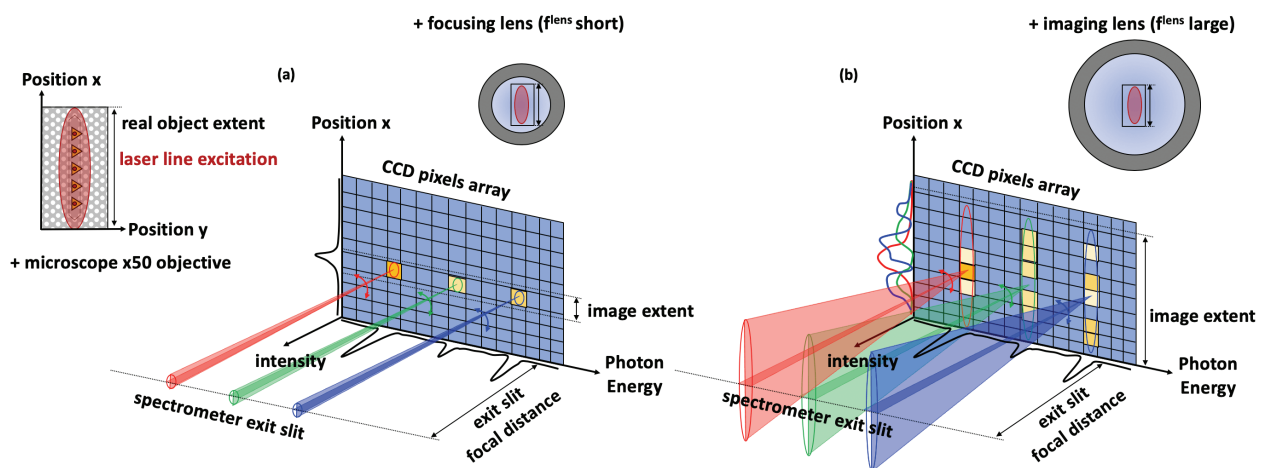


Fig. 2:12 – Schematics of the acquisition of μPL spectra on a 2D CCD array with: (a) with a focusing length ($f_{\text{lens}} \approx 50\text{mm}$) lens, (b) with an imaging lens ($f_{\text{lens}} \approx 300\text{mm}$). Here, in both cases the excitation is implemented with an elongated laser spot shaped by a cylindrical lens.

Fine calibration of the system's magnification (pixel size to sample size) was done by imaging of a long $L_{n=61}$ cavity with several embedded QDs. Higher order cavity modes span the full length of the cavity, with specially strong scattering of light at the edges. The length of the cavity, well-known from the fabrication process, can then be attributed to the pixels distance between two bright spots of scattered light from such a mode. A bright spot can be located within a precision of 1-2pixels, corresponding to 0.2-0.3 μm on the real sample. On the CCD, images may also be shifted due to manual positioning errors, inaccuracy of the motorized stage, and thermal drift. Images are thus sometimes re-centered using recognizable spectral features.

This technique is naturally suited to one-dimensional photonic structures, such as L_n cavities or waveguides (chapters 3 & 4). For 2D structures (chapter 5), the interpretation of spatially-resolved spectra becomes ambiguous and must be supported by numerical modeling.

2.3.3 Time-resolved PL spectroscopy

Time-resolved photoluminescence (TRPL) spectroscopy provides temporal information on radiative processes, typically on scales of picoseconds to nanoseconds. This is particularly useful for analyzing the characteristics of the QD emitters and the photonic cavities investigated in this thesis.

TRPL measurements require the synchronization of the photoluminescence signal measurement with the pulsed laser excitation. The Ti:Sapphire laser we employ can be switched to pulsed mode, by a mode-locking mechanism. In this mode, the laser provides train of pulses at a rate of 80 MHz (spacing of 12.5ns) with a pulse-width of $\sim 3\text{ps}$, corresponding to $\sim 0.02\%$ duty cycle. The pump pulse is split in two by a beam-splitter (see on **Fig. 2:11**) before injection into the excitation path. Part (about 20%) of the light is sent to a fast photodiode, and the resulting electrical pulse acts as a "start" event for the time measurement electronics, renewed at each cycle. The other part continues to the sample and pumps it. The resulting PL signal is sent to the spectrometer, acting as a monochromator to select and transmit a specified bandwidth of $\sim 100\text{-}150\mu\text{eV}$ through the exit slit. The signal is collimated with a lens and directed to a silicon single photon avalanche-photodiode τ -SPAD-fast by PicoQuant. The SPAD has an active area diameter of $500\mu\text{m}$. The device works near a critical point, and the absorption of a single photon triggers a large cascade of photons. The detection stops the time-of-flight measurement. Iteration and integration over many cycles form a histogram that shows the likelihood of finding photons of the given energy at a given point in time within the pulse cycle. The histograms are built thanks to the PicoQuant TimeHarp 260 PICO time-correlated single photon counting acquisition card to which the photodiode and SPAD are connected. The minimum time bin widths of 25 picoseconds combined to a maximum number of 32'768 time bins provide a maximum 819ns time range of detection.

According to the detector specifications, the detection efficiency decreases from 65% down to 10% efficiency over the 700-1000nm wavelength range. The temporal resolution of the instrument can be set between 150-400ps. The detector has a deadtime of $< 70\text{ns}$, and a dark count rate of < 500 counts per second (cps). In this type of measurements, due to count rates of $< 100\text{cps}$ in regular PL acquisition and the further reduction by detection efficiency, the width of both entrance and exit slits is increased to $\sim 100\mu\text{m}$.

The setup is first calibrated with the attenuated excitation laser signal. Since in this case the decay signal is faster than what the instrument can measure, the measured histogram provides a direct estimation of the impulse response function (IRF) of the SPAD, which was estimated as $\sim 200\text{ps}$ full-width at half maximum. The decay of excitons near-resonant with cavity modes was then measured at various steps in the course of temperature tuning experiments and deconvolved by accounting for the IRF modification of the signal. Lifetimes are extracted by fits based on a simple rate equations modeling of the emission with 3-levels (g, X, exc.) as explained in [194].

2.4 Conclusion of chapter and perspectives

This chapter introduced numerical techniques to model PhC structures and presented the notion of photonic potential tailoring by transverse shifts of selected side-holes of PhC cavities or waveguides to design novel functional elements for QIP applications. To simulate accurately broadband predictions of the optical mode structure that can be compared to experimental observations, it is necessary to apply an energy correction that accounts for the energy dependence of the refractive index in a PhC membrane.

The details regarding the fabrication of real PhC devices integrating pyramidal site-controlled QDs discussed in upcoming chapters were presented. The previously established technology allows for systematic and precise positioning (within $<50\text{nm}$) of quantum emitters, the dipoles of which can be coupled to the electromagnetic modes of such functional photonic elements. The technology ensures the reproducibility of fabricated structures across the chip, and the scaling up to an arbitrary number N of embedded quantum emitters. Common characterization techniques to map the optical mode structure, to analyze the QDs' properties and assess the strength of coupling interaction are described. In particular, an essential micro-photoluminescence method capable of diffraction-limited imaging of spectrally-resolved near-field patterns of the emitting structure is presented. The technique is upgraded to obtain polarization-resolved images, which is useful for identifying the contributions of the 1st and 2nd bands from the photonic dispersion. This way, photonic wavefunctions of the optical modes and the QDs' contributions to the feeding of modes can be revealed without ambiguity. The acquisition of time-resolved emission spectra is also briefly described.

With these tools at hand, the ground is laid for the study of novel devices based on the integration of pyramidal site-controlled QDs with tailored-potential PhC structures (chapter 3 & 4), and a coupled system of waveguides and cavity (chapter 5). These PhC structures incorporate either QD arrays, for the observation of the optical mode structure, or a few quantum emitters at specific locations, in views of the generation, extraction and funneling of single photons into resonantly coupled modes.

Chapter 3 Defect-potential photonic crystal cavity

Efficient simultaneous extraction of single photons from site-controlled quantum dots and their injection into extended photonic modes is crucial as a building block for quantum integrated circuits. Going beyond conventional PhC cavities and waveguides, the capability to tailor the photonic wavefunctions using “tailored-potential” photonic crystal structures can be useful for this purpose. Here we investigate such structure, consisting in a perturbed PhC waveguide (or long cavity) in which a site-controlled QD is embedded. In these “defect-potentials”, the center defect in the waveguide, about the extent of an $L_n=3$ conventional cavity, is formed by the outward shifts of selected side-holes. This yields a zone of lower photon energy (higher effective index) that can trap photons.

In **section 3.1**, the concept, design and computed mode structure of the defect potential cavities are presented, including their polarization features and the effect of optical disorder. **Section 3.2** is devoted to the fabrication of the defect potential cavities. Their optical modes structure and properties are then experimentally characterized in **section 3.3** by micro-photoluminescence techniques, using QD arrays as internal light sources. **Section 3.4** is dedicated to the observation of coupling of single QD emission into selected defect-potential modes, towards the goal of on-chip single photon generation and injection.

3.1 Defect-potential cavity : concept and computed mode structure

3.1.1 Concept

The defect-potential PhC cavity discussed here is based on a conventional PhC w1 waveguide made in a GaAs suspended membrane, terminated into a L_n cavity and modified by the addition of a deterministic “defect”. The “defect” is defined by shifting outwards several PhC holes, in one or more rows, next to the main waveguide defect line (see **Fig. 3:1**). These shifts locally alter the mode energy-dispersion, the energy of the photonic band-edge is decreased, generating a photonic potential trap, which yields confinement of discrete photonic modes to the vicinity of the defect, similar to the case of electrons in a potential (quantum well) trap. **Fig. 3:1** illustrates schematically the expected energies of the confined states and their position with respect to the barrier states confined in the waveguide parts.

Similar defect-potential PhC structures were considered and investigated in several published reports [164], [165], [238], [253]–[259]. The main interest in these structures was the prospect for inducing a relatively weak photonic confinement along the waveguide axis, which can result in extremely high Q-factors for the confined modes: a value of the Q factor as large as 55'000 was reported at $\sim 940\text{nm}$ ($\sim 1.32\text{eV}$) [258] and 700'000 at $\sim 1.55\mu\text{m}$ ($\sim 0.8\text{eV}$) in GaAs [165]. Here we concentrate on the unique polarization features of these modes, the effect of optical disorder and the potential for coupling the high-Q modes with site-controlled QDs for single photon injection applications.

In **Fig. 3:1** we illustrate two particular configurations of defect-potential cavities, used in the investigation presented in this chapter. The main part shows a configuration in which 2 holes in the first row and the associated 3 holes in the second row (next to the waveguide defect line) are shifted by s outwards. We designate this configuration as 1p2r s . A related configuration, designated 1p1r s is depicted in the inset. Intuitively, the latter configuration should result in a shallower defect potential, hence weaker confinement. For both configurations, the depth of the potential can be continuously adjusted by changing s . Obviously, fabrication-induced disorder due to

random position fluctuations of the PhC holes imposes a limit on the quality of the structures actually realized (see section 3.1.3).

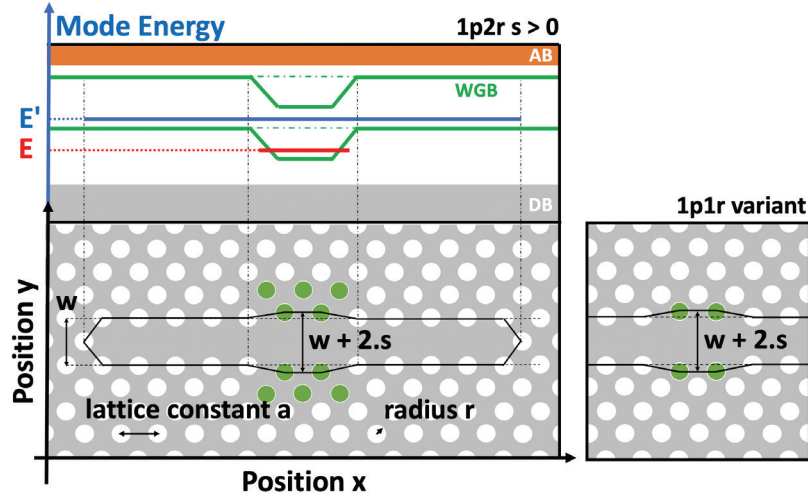


Fig. 3:1 – Schematic illustration of the defect-potential cavity and its effective implementation. (Bottom) Top view of a defect-potential PhC cavity; 1 pair & 2 rows (1p2r) variant, the sides holes highlighted in green are vertically shifted outwards along y , by an amount s . (Top) Diagrams of the waveguide band energy variation along position x resulting from the shifts in y ; the terminations of the cavity define boundaries of the photonic potential. In red, a cavity mode confined by the defect. In blue, a cavity mode extending across the cavity, above the band-edge of the virtual w_1 waveguide. Inset: 1 pair & 1 row (1p1r) variant.

3.1.2 Optical mode structure of a defect-potential cavity

The mode structure of a defect potential cavity is first studied here for the configuration 1p2r with $s=30\text{nm}$. **Fig. 3:2** displays energy-position images (7 stitched images for correcting dispersion effects, see section 2.1.3) and corresponding photonic band structures for the defect potential structure compared with the base uniform defect cavity. The $\sim 25\text{meV}$ s energy-position images are simulated using the 2D Finite-Difference method. For each image, the optical modes are computed with the slab effective refractive index evaluated at the corresponding spectral center, the energies are then corrected with (Eq. 2:3). This figure illustrates the optical mode structure and band structure of **(a, b)** a regular $L_n=61$ cavity against **(c, d)** a defect-potential $L_n=61$ cavity. It shows how the mismatch in the bands dispersion of such a photonic double heterostructure **(c)** produces a local confinement effect in real space **(d)**, as was evidenced in [164]. Our analysis here is more general, showing the effect on the second waveguide band and its associated confined modes. The effective potential of the first band is identified in red, and the second one in cyan blue. The depths of the defect-potentials correspond to the simulated energy of the shift in band-edge of a uniform waveguide of width $w + 2s = w\left(1 + 2 \cdot \frac{s}{w}\right) = w1.15$.

By analogy to electronic states in a quantum well, it is evident that certain modes are pulled down in energy from both bands and become localized at the defect region, see **Fig. 3:2(d)**. From the first red band, two modes are pulled below the original lower band-edge of the M side of the Brillouin-Zone. Following the notation of Chapter 2, these two modes should be identified as $E_{y,000\mathbf{k}}$ and $E_{y,001\mathbf{k}}$. We chose to label these two modes $\#0_M^{(0)}$ & $\#1_M^{(0)}$. The subscript index refers to the closest irreducible Brillouin-zone specific point, the superscript index in parenthesis refers to the band number, 0 (fundamental) for the first, 1 for the second; it also reflects the number of nodes along the y axis for the E_y component. In the same spirit, the number of the mode refers to the number of nodes along the x axis (still for the E_y component).

Mode $\#0_M^{(0)}$ is completely localized inside the defect-potential trap and is radiatively isolated in energy inside the bandgap region. Mode $\#1_M^{(0)}$ spans a larger extent because it has a higher energy and is barely pulled from the the band-edge into the defect. With a deeper defect potential, we should expect this mode to be further redshifted, and possibly the confinement of a third mode inside the trap.

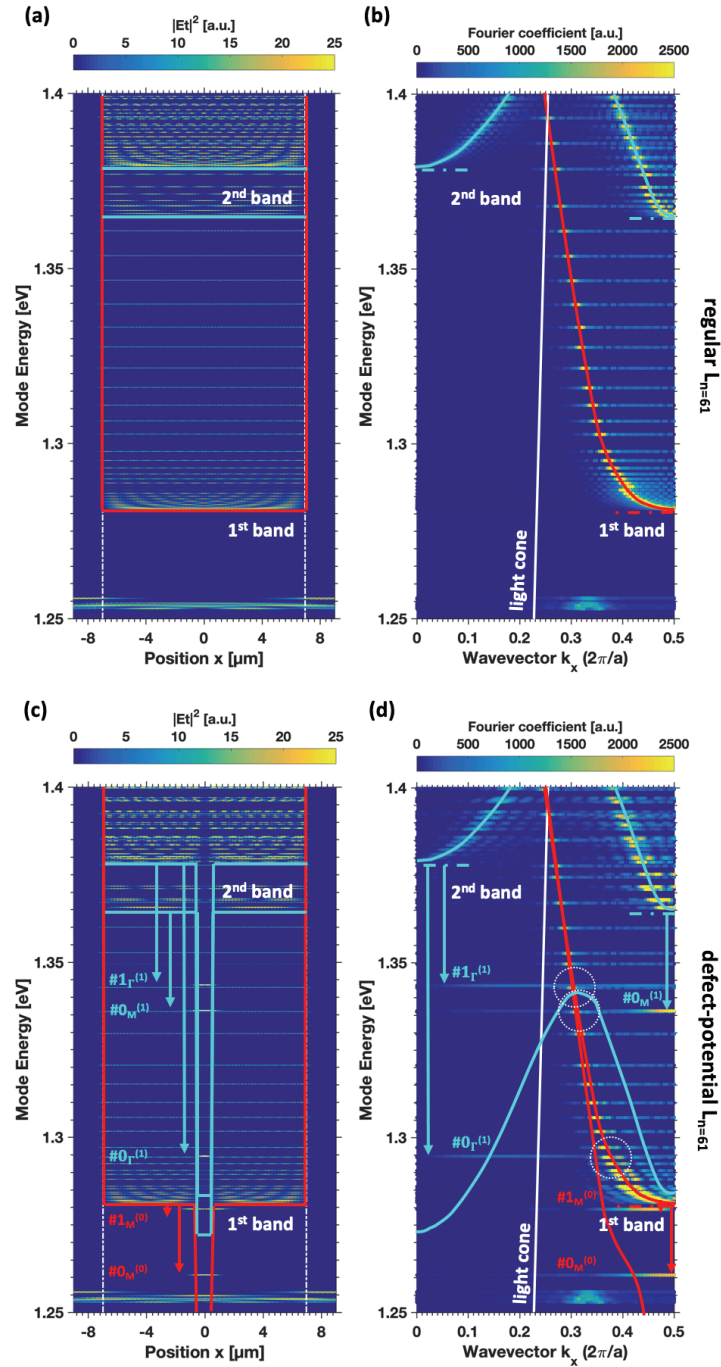


Fig. 3:2 – Numerical simulations of the photonic mode and band structures of a defect-potential cavity with configuration 1p2r, shift $s = 30\text{nm}$, compared to a regular cavity. (a,d) Confined mode structure: in-plane intensities $|E_t|^2$ of TE (E_x , E_y , H_z) confined modes, summed along y and plotted along x . White vertical dot-dashed lines specify the borders of the cavity. Horizontal lines refer to the band-edges of the original unperturbed $L_n=61$. Red and cyan colored lines highlight the effective photonic potentials of the two bands. (b,c) Band structure obtained from the Fourier transform of E_y component summed across k_y and plotted along k_x . The white line depicts the light cone. Horizontal continuous dot-dashed lines refer to the edges of the original unperturbed $L_n=61$. The arrows show the pulling of specified modes by the defect. White dot dash circles show the intersections of the 1st band of the long base cavity with the flat dispersions of the confined modes of the defect. Parameters: pitch $a = 225\text{nm}$, membrane thickness $t = 250\text{nm}$, holes radii $r = 67.4\text{nm}$. The resulting images are generated by the stitching of 7 energy patches with respective $n_{\text{eff}} = 3.142, 3.156, 3.171, 3.183, 3.202, 3.223, 3.243$.

The same occurs with the second band, with an additional but understandable twist. Here, three confined modes are noticeable. We could expect that a single deep trap occurs on either the M or Γ side, but it will soon become clearer why it is not the case. Since the band folds over itself and presents two band-edges in the range of energy displayed, two defects trap are generated: the Γ one pulling two modes $\#0_{\Gamma}^{(1)}$, $\#1_{\Gamma}^{(1)}$, and the M one pulling a single mode $\#0_M^{(1)}$.

Contrary to the confined modes of the first band that are pulled in the bandgap where no states of the PhC cavity exist, the confined modes of the second band co-exist among the quasi-continuum of the fast-light modes of the first band. So naturally, one might think that the confined and propagating modes could couple. If they do, the interband coupling should occur by spectral resonance and overlap of wavevector \mathbf{k} components, highlighted by the white dot circles in Fig. 3:2(c). Additionally, the potential traps on the M side, of both the first and second band, seem to be of similar depths (the one from the second band is possibly a bit deeper), while the potential trap on the Γ side of the second band is about twice deeper. This is reflected by the properties of these modes.

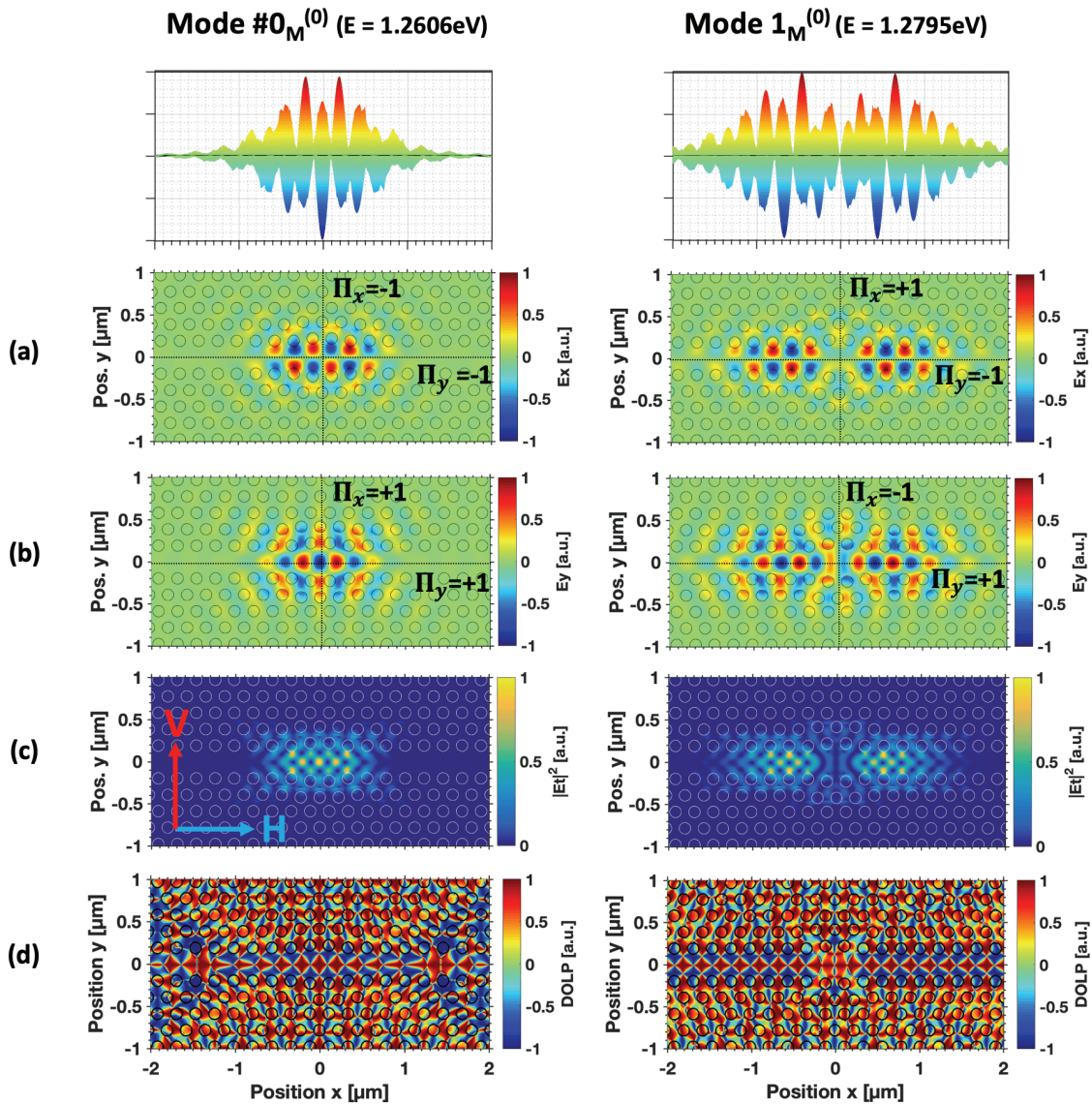


Fig. 3:3 – Properties of the confined modes pulled from the 1st band (extracted from Fig. 3:2). By columns, (a) Top-view of the normalized E_x distribution in the x-y plane; (b) top-view of the normalized E_y distribution in the x-y plane; on top: corresponding side-view of the normalized amplitude along x; (c) top-view of the normalized in-plane intensity $|E_t|^2$ distribution in the x-y plane; (d) top-view of the degree of linear polarization (DOLP) distribution in the x-y plane. Parameters: pitch $a = 225\text{nm}$, membrane thickness $t = 250\text{nm}$, $1p2r$, $s = 30\text{nm}$, holes radii $r = 67.4\text{nm}$, effective index of slab $n_{\text{eff}} = 3.142, 3.157$.

In **Fig. 3:3**, we depict the two confined modes $\#0_M^{(0)}$ & $\#1_M^{(0)}$ of the first band. Modes of the first TE band of a $w1$ or L_n cavity share the following common traits: **(a)** odd symmetry for E_x with reversal of y ($\Pi_y = -1$), **(b)** even symmetry for component E_y of the field under reversal of y (a parity projecting operator Π_y can be created, returning the eigen-value of the projector $\Pi_y = +1$). More specifically, mode $\#0_M^{(0)}$ possesses a single lobe envelope with even symmetry of the crystal Bloch term under x reversal ($\Pi_x = +1$) for E_y , and the following mode $\#1_M^{(0)}$, with two lobes, naturally has an odd symmetry ($\Pi_x = -1$). The opposite is true regarding parity for E_x . As can be seen from the intensities **(c)**, the E_y component is dominant, leading to **(d)** a characteristic signature of red vertically polarized diamonds along the main axis of the structure in the Degree of Linear Polarization (DOLP) scalar field (see (Eq. 2:9)). For simplicity, we will refer to these modes as V-polarized. These red diamonds are connected to blue diamonds at the edges, because the local polarization circles around in a complex fashion in space. This can be appreciated differently in [156] for a glide-plane waveguide. It is also worth noticing that the spatial pattern of mode $\#0_M^{(0)}$ is reminiscent of the fundamental mode of a $L_n=3$ or $L_n=5$ cavity while being integrated in a waveguide channel.

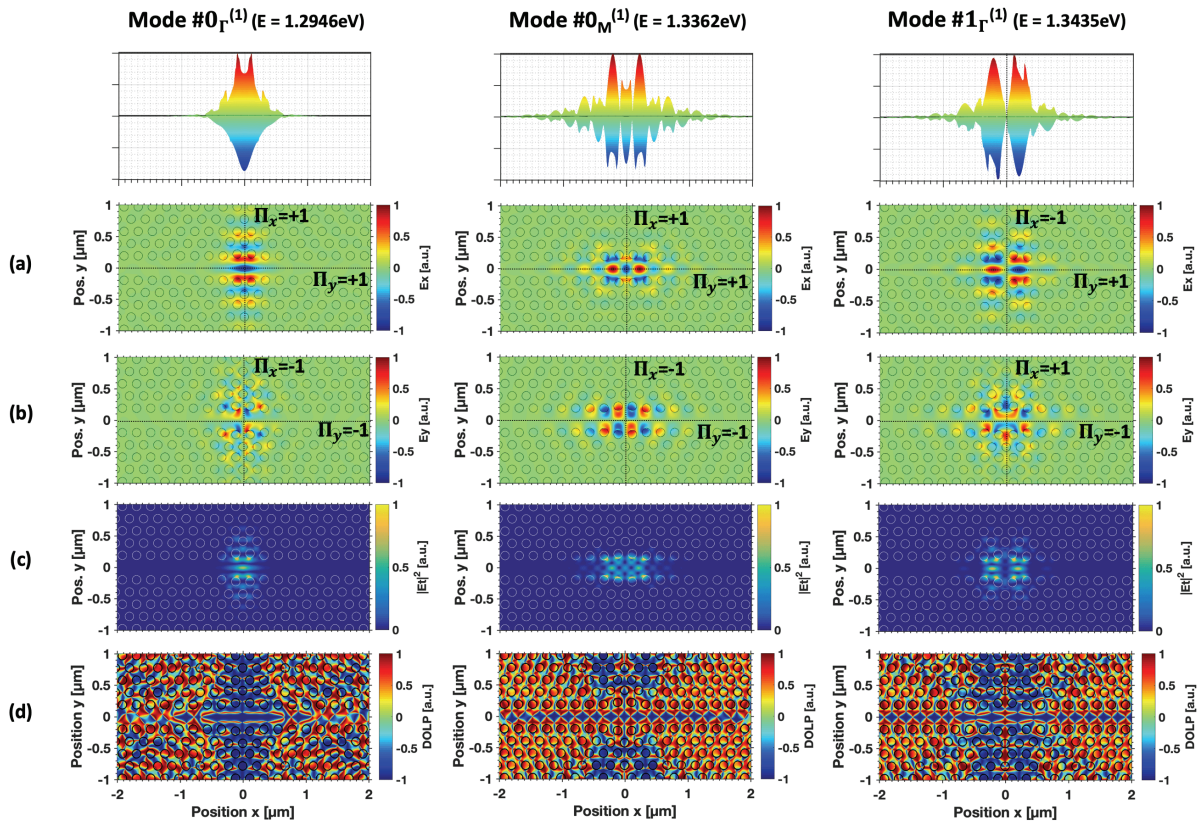


Fig. 3:4 – Properties of the confined modes pulled from the 2nd band (extracted from Fig. 3:2). By columns, **(a)** Top-view of the normalized E_x distribution in the x - y plane; **(b)** top-view of the normalized E_y distribution in the x - y plane; on top: corresponding side-view of the normalized amplitude along x ; **(c)** top-view of the normalized in-plane intensity $|E_t|^2$ distribution in the x - y plane; **(d)** top-view of the degree of linear polarization (DOLP) distribution in the x - y plane. Parameters: pitch $a = 225\text{nm}$, membrane thickness $t = 250\text{nm}$, $1p2r$, $s = 30\text{nm}$, holes radii $r = 67.4\text{nm}$, effective index of slab $n_{\text{eff}} = 3.169, 3.201, 3.207$.

In **Fig. 3:4**, we depict the three confined modes $\#0_R^{(1)}$, $\#0_M^{(1)}$ and $\#1_R^{(1)}$ pulled from the second band. These modes are characterized by: **(a)** even symmetry for E_x with reversal of y ($\Pi_y = +1$), **(b)** odd symmetry for component E_y of the field under reversal of y . More specifically, mode $\#0_R^{(1)}$ and $\#0_M^{(1)}$ possess a single lobe envelope with even symmetry of the crystal Bloch term under x reversal ($\Pi_x = +1$) for E_x , and the following mode $\#1_R^{(1)}$, with two lobes, naturally has an odd symmetry ($\Pi_x = -1$). The opposite is true regarding parity for E_y . As can be seen from the intensities **(c)**, the E_x component is dominant, leading to **(d)** a characteristic signature of blue

horizontally polarized diamonds along the main axis of the structure in the DOLP pattern. In the same spirit as before, these modes will be labelled as H polarized. Tails of the modes from the Γ side extend further in the PhC region than modes from the M side of the Brillouin-zone. The electric field bounces at a steeper angle against the edges of the waveguide. This difference is responsible for the discrepancy in depths of the potential traps that was mentioned earlier. Since the defect is oriented along y (as opposed to the waveguide oriented along x), modes of the second band, which are mostly H polarized, are naturally more sensitive than the V polarized ones. The modes of the second band, towards the Γ point, are even more sensitive to changes in the refractive index due to a larger overlap of the optical field patterns with the shifted holes. It is also worth noticing that mode $\#0_M^{(1)}$ appears as the first “excited” state of mode $\#0_M^{(0)}$, with exchange of the roles of E_x and E_y , and the field intensity being re-distributed towards the edges.

We focus next on the changes in energy of the three fundamental states, of the first band ($\#0_M^{(0)}$), and of the second band ($\#0_\Gamma^{(1)}$ & $\#0_M^{(1)}$), upon variations of structural parameters, since they are the most interesting for coupling to a single QD integrated at the center of the defect. The results are summarized in **Table 3:1**. The energies of the concerned modes were tracked with changes (one at a time of $\Delta r = \pm 5\text{nm}$, $\Delta t = \pm 10\text{nm}$ and $\Delta n = \pm 0.03$. These changes correspond to $\pm 1\%$ variations.

	1p2r, s=30nm	
#0_M⁽⁰⁾		
$r_0 = 67.4\text{nm}$	$\Delta r = \pm 0.7\text{nm} (\pm 1\%)$	$\Delta E = \pm 2.8\text{meV} (\pm 0.2\%)$
$t_0 = 250\text{nm}$	$\Delta t = \pm 2.5\text{nm} (\pm 1\%)$	$\Delta E = \mp 1.4\text{meV} (\mp 0.1\%)$
$n_0 = 3.445$	$\Delta n = \pm 0.03 (\pm 1\%)$	$\Delta E = \pm 10.5\text{meV} (\mp 0.8\%)$
#0_Γ⁽¹⁾		
$r_0 = 67.4\text{nm}$	$\Delta r = \pm 0.7\text{nm} (\pm 1\%)$	$\Delta E = \pm 3.4\text{meV} (\pm 0.3\%)$
$t_0 = 250\text{nm}$	$\Delta t = \pm 2.5\text{nm} (\pm 1\%)$	$\Delta E = \mp 1.2\text{meV} (\mp 0.1\%)$
$n_0 = 3.459$	$\Delta n = \pm 0.03 (\pm 1\%)$	$\Delta E = \pm 11.0\text{meV} (\mp 0.9\%)$
#0_M⁽¹⁾		
$r_0 = 67.4\text{nm}$	$\Delta r = \pm 0.7\text{nm} (\pm 1\%)$	$\Delta E = \pm 3.5\text{meV} (\pm 0.3\%)$
$t_0 = 250\text{nm}$	$\Delta t = \pm 2.5\text{nm} (\pm 1\%)$	$\Delta E = \mp 1.3\text{meV} (\mp 0.1\%)$
$n_0 = 3.478$	$\Delta n = \pm 0.03 (\pm 1\%)$	$\Delta E = \pm 10.8\text{meV} (\mp 0.8\%)$

Table 3:1 – Variations in the energy of three confined modes related to variations of holes radii and slab thickness, for the reference structure with holes radius $r_0 = 65.8\text{nm}$, slab thickness $t_0 = 250\text{nm}$ and refractive index $n_0 = 3.445, 3.459, 3.478$ ($n_{\text{eff},0} = 3.142, 3.169, 3.201$), 1p2r, s = 30nm.

The three modes react practically the same to the variations of the core parameters. No new confined modes were observed. The sign of a variation in energy is correlated with the sign of a variation in either holes sizes or refractive index, while it is anti-correlated in the case of the thickness of the slab. Intuitively, an increase in holes sizes decreases the volume of the cavity, and the electric fields are confined in a tighter space, resulting in blueshifts of the energies. An increase in the global refractive index increases the contrast with the surrounding air, and the light focuses more in regions of higher refractive index, producing blueshifts. An increase in the thickness of the slab does the opposite, as it relaxes the confinement. The least sensitive variation in energy comes from the thickness changes, about one third to one half of the variation stemming from a change in holes sizes. The strongest effect comes from the global refractive index; but 1% of the refractive index is actually a large value, with 0.1% being more usual, achieved for instance by $\Delta T \approx 50\text{K}$.

3.1.3 Binding energies of the defect modes

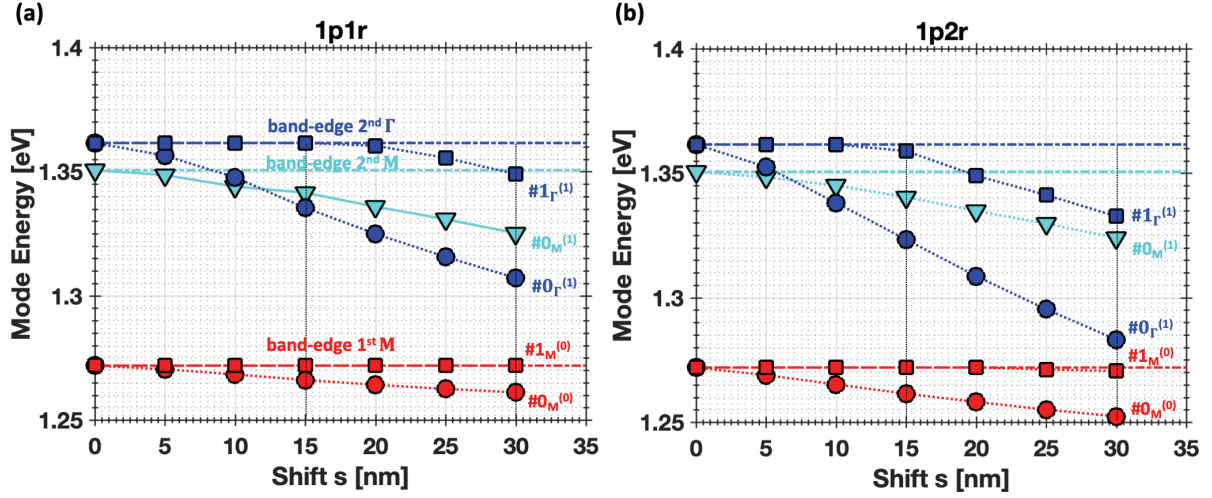


Fig. 3:5 – Calculated defect modes energy versus shift s (defect depth) for two defect configurations (denoted on top). The horizontal dot-dash lines display as a reference the various band-edges of the corresponding unperturbed $L_{n=61}$ cavity. Numerical parameters: pitch $a = 225$ nm, membrane thickness $t = 250$ nm, holes radii $r = 65.0$ nm, effective index of slab $n_{\text{eff.}} \in [3.134, 3.221]$.

So far, we dealt only with the 1p2r $s = 30$ nm configuration. In **Fig. 3:5** we draw a broader picture by showing the energies of the same defect modes as in Fig. 3:3 and 3:4 for 1p1r & 1p2r and several values of s . The radius is fixed for all configurations. For each value of the shift s , the modes confined by the defect were found by running a first simulation based on a single value of the slab effective refractive index. Then, each mode energy was converged within 100 μ eV fluctuations by updating the slab effective refractive index with the value computed from the new mode energy. We precise that the positions of the modes $\#0_\Gamma^{(1)}$ and $\#1_\Gamma^{(1)}$ in between the lines indicating the band-edges of the second band of the Γ and M side are in fact ill-defined and approximative. When these two modes originally extended at the band-edge are confined by the defect, their flat dispersion makes them co-exist and couple to modes from the M side, with which they hybridize. This intra-band coupling extends over a few meVs, several modes are modified, and it is quite difficult to track.

(a) and (b) show similar behavior of the modes in the two defect configurations: the fundamental $\#0_M^{(0)}$, $\#0_M^{(1)}$ and $\#0_\Gamma^{(1)}$ modes are the first to be pulled down for $s > 0$. It takes much deeper defects, deeper potential traps, to effectively attract the higher order modes $\#1_M^{(0)}$ & $\#1_\Gamma^{(1)}$. Over the 30nm shift range, in the case of 1p1r, mode $\#1_M^{(0)}$ does not leave the 1st band-edge and remains fully extended, and mode $\#1_\Gamma^{(1)}$ barely appears below the lowest band-edge of the second band, where it becomes unambiguously defined. On the other hand, in the case of 1p2r, mode $\#1_M^{(0)}$ redshifts in between $s=25$ and 30nm, and mode $\#1_\Gamma^{(1)}$ totally exits the 2nd band at about $s = 20$ nm. The redshifts rate of modes $\#0_M^{(0)}$, $\#0_M^{(1)}$ are fairly similar, whereas the modes from the Γ side display clearly a steeper variation. This is consistent with the fact that the modes, due to a large k_y , extend deeper along y in the PhC region surrounding the cavity, and overlap more with the shifted holes of the defect. In particular, due to this faster rate of evolution, the trajectories of modes $\#0_M^{(1)}$ and $\#0_\Gamma^{(1)}$; this occurs at $s \approx 12$ nm for 1p1r, and at $s \approx 6$ -7nm for 1p2r.

Table 3:2 shows that the addition of a second shifted row does not produce a linear variation in the energy shifts. The binding energy of modes $\#0_M^{(0)}$ for 1p1r $s = 15$ nm is about half that for 1p2r $s = 15$ nm, and the binding energy of mode $\#0_M^{(0)}$ for 1p1r $s = 30$ nm is about equal to that for 1p2r $s = 15$ nm. The change is approximately linear with s . The binding energies of mode $\#0_M^{(1)}$ are mostly the same for 1p1r $s = 15$ nm and 1p2r $s = 15$ nm, as well as for the two structures with $s = 30$ nm. The behavior is mostly insensitive to the existence of the second row. There is about a factor of 1.5 between the binding energies of $\#0_\Gamma^{(1)}$ 1p1r $s = 15$ nm and 1p2r $s = 15$ nm, as well as for the structures with $s = 30$ nm; the change here is sub-linear.

	1p1r, s = 15nm	1p1r, s = 30nm	1p2r, s = 15nm	1p2r, s = 30nm
$\text{BE}_\Gamma^{(1)}$	1361.5meV	1361.5meV	1361.5meV	1361.5meV
$\#1_\Gamma^{(1)}$		-12.5meV		-28.9meV
$\#0_\Gamma^{(1)}$	-26.1meV	-54.3meV	-38.2meV	-78.4meV
$\text{BE}_M^{(1)}$	1350.6meV	1350.6meV	1350.6meV	1350.6meV
$\#0_M^{(1)}$	-9.1meV	-25.4meV	-10.3meV	-26.6meV
$\text{BE}_M^{(0)}$	1271.9meV	1271.9meV	1271.9meV	1271.9meV
$\#1_M^{(0)}$				-1.4meV
$\#0_M^{(0)}$	-5.8meV	-10.8meV	-10.5meV	-19.6meV

Table 3:2 – Summary of calculated binding energies of the trapped modes with respect to the band-edges in several defect-potential structures. (Data extracted from Fig. 3:4).

3.1.4 Effects of disorder

The final goal in the context of the defect-potential cavities is to resonantly couple QD transitions to specific bound photonic states. It is thus essential to estimate the energy fluctuations and resilience of the target modes produced by realistic levels of fabrication disorder.

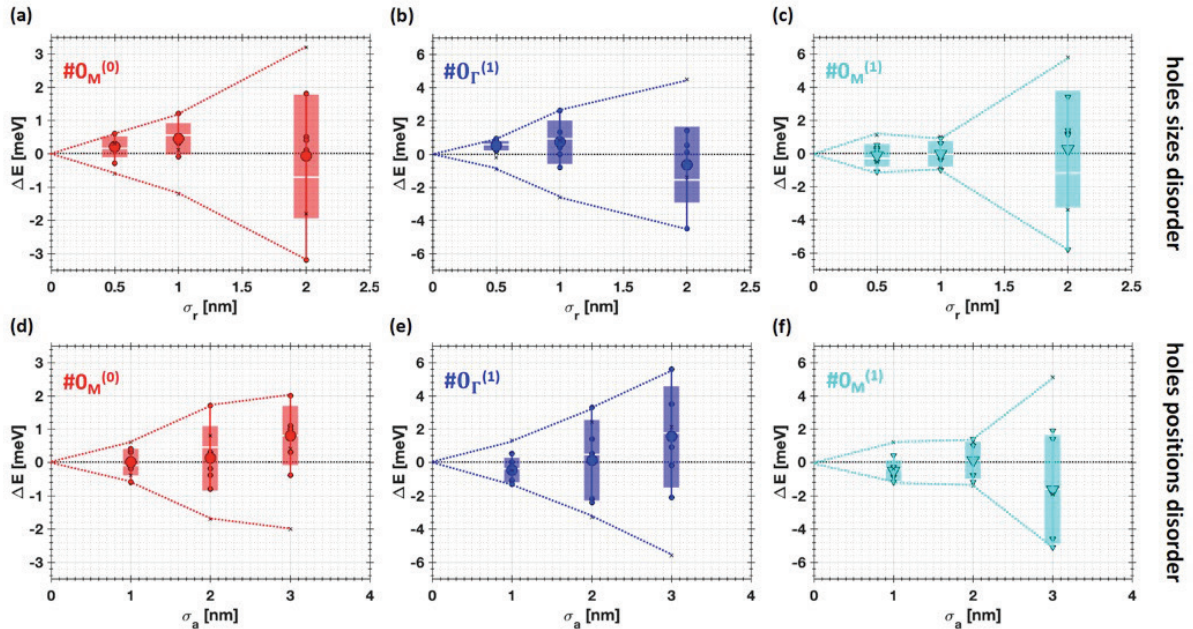


Fig. 3:6 – Calculated energy variations of three confined modes in a 1p2r s = 30nm defect-potential structure as a function of disorder level. (a-c) Holes sizes disorder with standard deviation σ_r of a Gaussian distribution. (d-f) Holes positions disorder with standard deviation σ_a of a Gaussian distribution. Results of 5 simulations per mode per disorder scenarios. The smaller symbols represent the actual results; the larger correspond to the averages. Shaded areas correspond to one standard deviation in energy. The vertical lines connect the minimum and maximum values, the white lines refer to the middle points. Data is symmetrized with the addition of mirrored min/max data points (small cross symbols). The dashed lines are visual cues. Numerical parameters: pitch $a_0 = 225\text{nm}$, membrane thickness $t = 250\text{nm}$, holes radii $r_0 = 67.4\text{nm}$, effective index of slab $n_{\text{eff}} = 3.142, 3.169, 3.201$.

The energy variations for the three fundamental confined modes $\#0_M^{(0)}$, $\#0_\Gamma^{(1)}$ and $\#0_M^{(1)}$ are displayed in **Fig. 3:6. (a-c)** in the case of disorder in PhC holes sizes, and **(d-f)** in the case of disorder in holes positions. Disorder is treated as explained in section 2.1.2. Disorder levels were explored in ranges of trusted values from two independent studies on our PhC crystals. The first estimated $\sigma_r \approx 2\text{-}3\text{nm}$ [252] from trying to match simulations with experimental observations. The second, based on statistical analysis of 100 holes in a single SEM picture using a computer vision script, found $\sigma_r \approx 0.4\text{nm}$ & $\sigma_a \approx 4.3\text{nm}$ [260]. As expected, in both cases the variations yield an increase in ΔE correlated to the increase in the standard deviation parameter. These energy variations are not sufficient for the confined modes to exit the deep confinement traps generated by the defect (see again Fig. 3:2).

This resilience also manifests for very shallow defects; in [257], a defect formed by only $s \approx 3\text{nm}$ shift showed a deterministic confinement in real fabricated structures.

In both disorder scenarios, modes **(b, e)** $\#0_{\Gamma}^{(1)}$ and **(c, f)** $\#0_M^{(1)}$ of the 2nd band are more sensitive to disorder than mode **(a, d)** $\#0_M^{(0)}$ of the first band, with $\sim 1.5\text{-}2$ larger variations in energy. This can be understood for $\#0_{\Gamma}^{(1)}$, referring back to Fig. 3:4, as the mode extends widely across the defect region and beyond in the y direction. This particular mode can thus “sense” the variations of more holes in the vicinity of the defect. For mode $\#0_M^{(1)}$ this is less obvious, due to the tighter confinement along y . The difference between mode $\#0_M^{(0)}$ and mode $\#0_M^{(1)}$ is likely explained by the difference in the envelopes’ spatial distributions. For the former, the intensity is concentrated on the axis of the L_n parent cavity, precisely on the lattice sites with missing holes. Disorder is thus essentially sensed by the weak tails of the mode. For the latter, extrema of intensity are located nearby the holes of the inner row of the defect. If these holes are perturbed, disorder is more effective.

Contrary to the disorder-free scenario, in which the orthogonality of the eigen-modes prevents mode hybridization, we find that disorder can induce such hybridization. This effect is illustrated in the following figures.

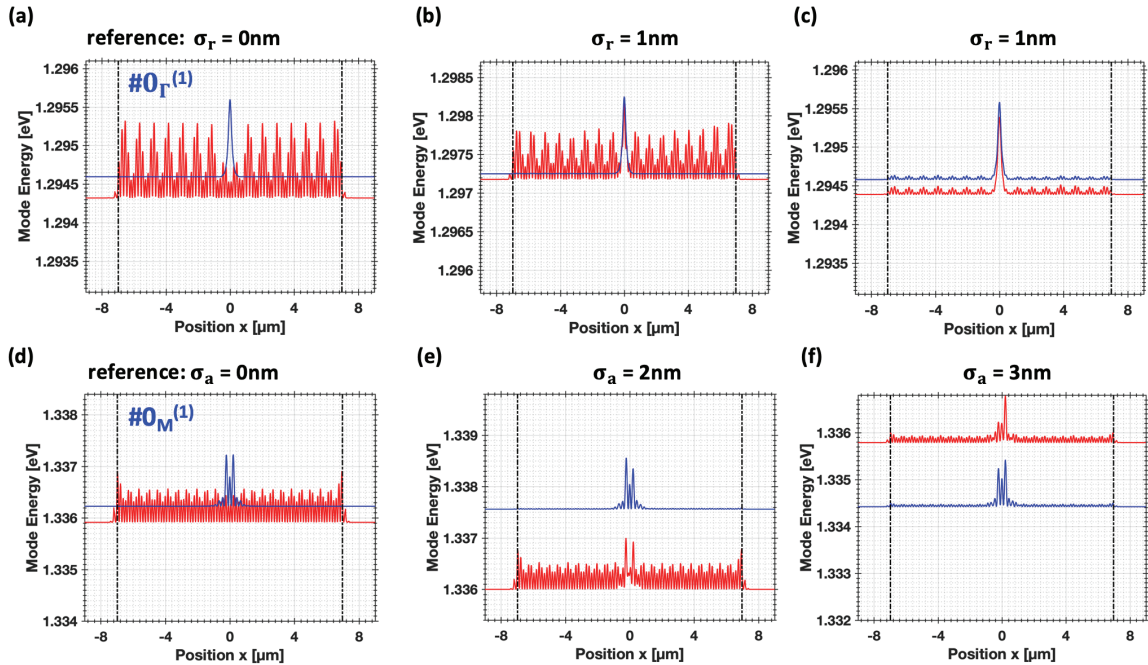


Fig. 3:7 – Interband hybridization of defect modes of the 2nd band with extended modes of the 1st band in a defect-potential structure, induced by disorder. (a,d) Reference modes configuration for the disorder free structure. In blue: confined modes of the 2nd band. Red: extended modes of the 1st band. (b,e) Weak hybridization in the presence of disorder. (c,f) Strong hybridization in the presence of disorder. Numerical parameters: pitch $a_0 = 225\text{nm}$, membrane thickness $t = 250\text{nm}$, holes radii $r_0 = 67.4\text{nm}$, effective index of slab $n_{\text{eff}} = 3.169, 3.201$. Corresponding disorder parameters are indicated.

In **Fig. 3:7**, the reference cases **(a, d)** show that the modes $\#0_{\Gamma}^{(1)}$ and $\#0_M^{(1)}$ do not naturally couple to a mode $\#n_k^{(0)}$ even if they have similar energies. The bound-states modes are well localized in the center defect region with exponential tails on both sides, while the fast-light modes extend over the complete length of the $L_{n=61}$ parent cavity. The disordered cases **(b, e)** show the realization of a weak coupling of modes $\#0_{\Gamma}^{(1)}$ and $\#0_M^{(1)}$ to modes $\#n_k^{(0)}$. In particular, the case of (e) shows that the effect occurs even at further reduced spectral overlap than in reference (d). In this scenario, the confined modes of the 2nd band remain confined, and their spatial distribution are practically not altered, but the recognizable features of these confined modes are imparted on the spatial distribution of the extended modes of the 1st band. The influence is unidirectional. The perturbed cases **(c, f)** show realizations of a stronger coupling where the modes of the two bands influence each other and become quite

undistinguishable. On one hand, the exponentially decaying tails resulting from the confinement of the defect-potential of the 2nd waveguide band are now replaced by extended oscillatory tails which now allow these modes to extend. On the other hand, the former extended modes of the 1st band gain the features of the former confined modes of the 2nd band, which become dominant while the amplitudes of the other oscillating parts are suppressed.

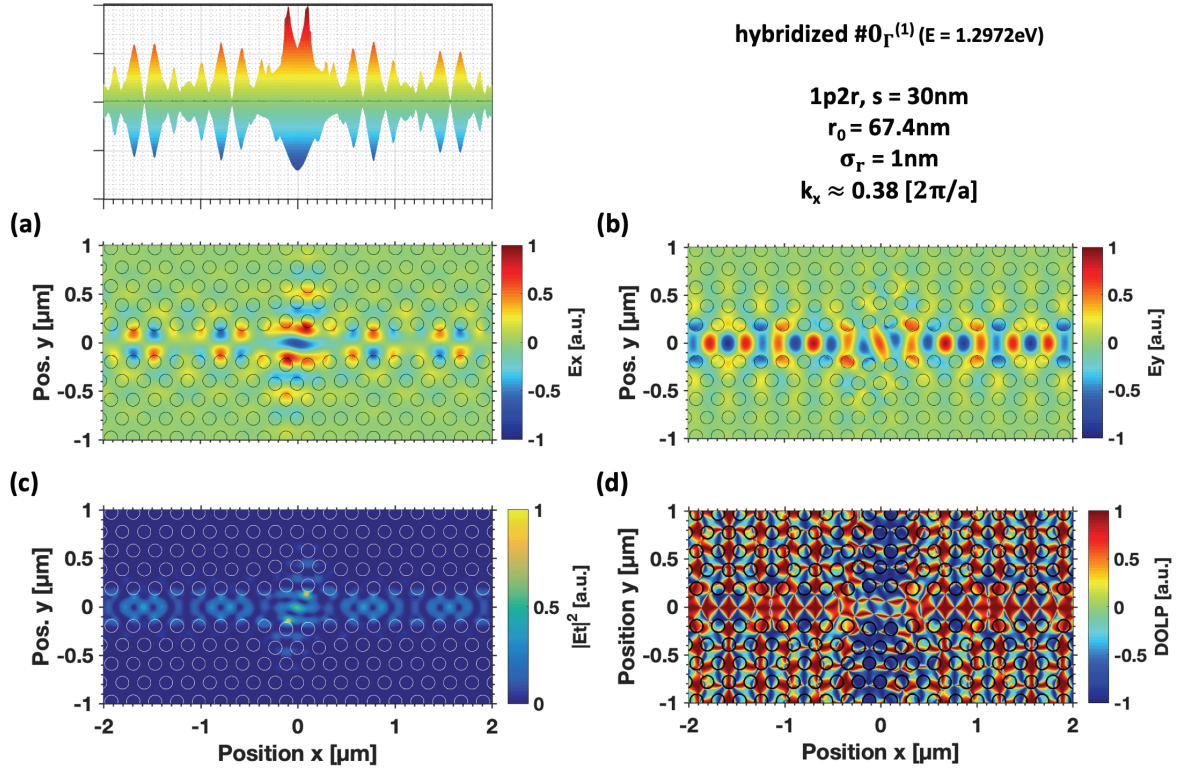


Fig. 3:8 – Properties of a strongly hybridized mode $\#0_{\Gamma}^{(1)}$ (x-y plane distributions). (a) Top-view of the normalized E_x distribution, on top: side-view of the amplitude distribution along x ; (b) top-view of the normalized E_y distribution; (c) top-view of the normalized in-plane intensity $|E_t|^2$ distribution; (d) top-view of the degree of linear polarization (DOLP) distribution. Parameters: pitch $a_0 = 225\text{nm}$, $\sigma_a = 0\text{nm}$, membrane thickness $t = 250\text{nm}$, 1p2r, $s = 30\text{nm}$, holes radii $r_0 = 67.4\text{nm}$, $\sigma_r = 1\text{nm}$, effective index of slab $n_{\text{eff}} = 3.169$.

Fig. 3:8 and **Fig. 3:9** depict the optical properties of hybridized modes with respectively mode $\#0_{\Gamma}^{(1)}$ and mode $\#0_M^{(1)}$. The spatial distributions of components E_x and E_y are presented in **(a, b)**. A comparison with the reference patterns of Fig. 3:4 shows that the signatures of the confined modes and extended modes are recognizable. The competition between the two components and the scattering from random disorder result in a complex re-distribution of the light intensity, see **(c)**. More interestingly, as shown in **(d)**, this results in a particular DOLP compound signature: the dominant character of confined modes of the 2nd band imparts their H-polarization in the center region, while the dominant aspect of extended modes of the 1st band switches the polarization to mostly V along the cavity axis. Since this effect appears to couple two orthogonal polarization states, it might be classified as a form of a bi-refrindexence effect [261].

The hybridization effect is tied to the geometry and the wavevectors \mathbf{k} . Cavity modes of the 2nd band oscillate mostly along the y direction, hence the dominant H-polarization, while extended modes of the 1st band oscillate mostly along the x direction, hence the dominant V-polarization. There are specific diagonal directions that allow for a resonant scattering phenomenon between the two modes, and they correspond to the loci where the flat dispersions of the confined defect modes can intersect with the quasi linear energy-dispersion of the $L_{n=61}$ cavity indicated by the dot white circles highlighted in Fig. 3:2.

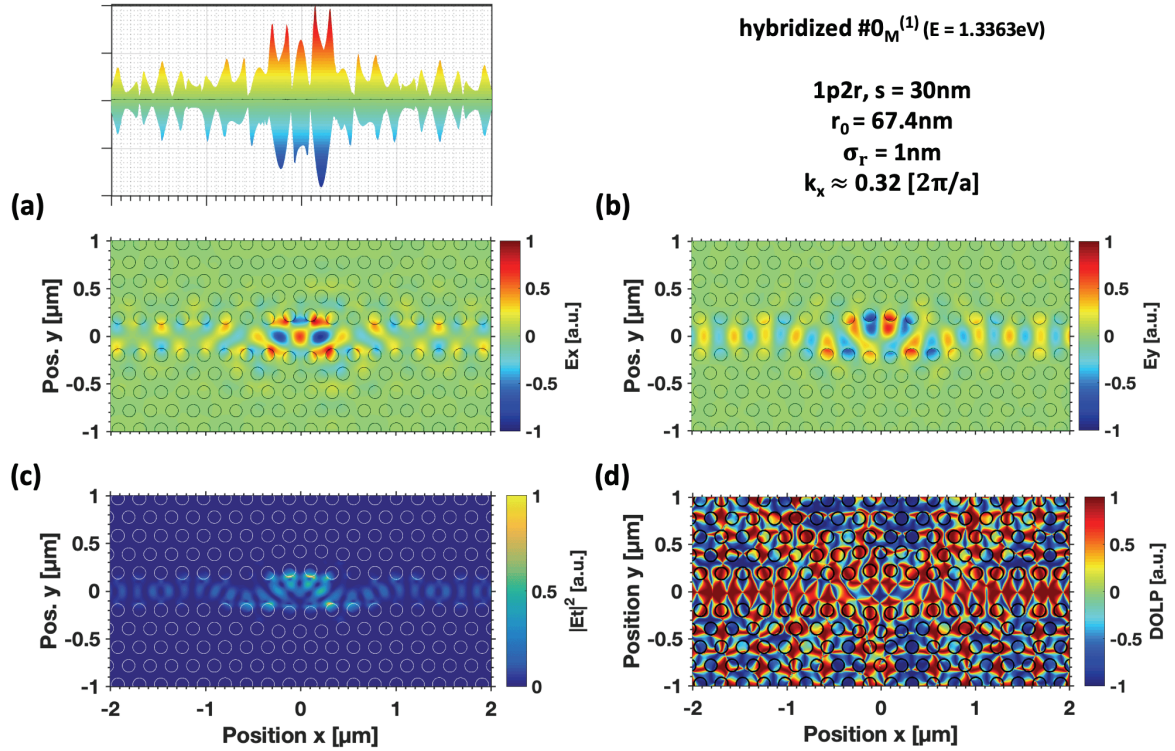


Fig. 3:9 – Properties of a strongly hybridized #0_M⁽¹⁾ (x-y plane distributions) (a) Top-view of the normalized E_x distribution, on top: side-view of the amplitude distribution along x ; (b) top-view of the normalized E_y distribution; (c) top-view of the normalized in-plane intensity $|E_t|^2$ distribution; (d) top-view of the degree of linear polarization (DOLP) distribution. Parameters: pitch $a_0 = 225\text{nm}$, $\sigma_a = 3\text{nm}$, membrane thickness $t = 250\text{nm}$, 1p2r, $s = 30\text{nm}$, holes radii $r_0 = 67.4\text{nm}$, $\sigma_r = 1\text{nm}$, effective index of slab $n_{\text{eff}} = 3.201$.

The phase-matching condition is specified by the congruence modulo 2π : $L_{n=61}^{\text{eff}} \cdot k_x^{(0)} \equiv L_{\text{defect}}^{\text{eff}} \cdot k_x^{(1)} + \Delta\phi^{\text{refl.}} + \Delta\phi^{\text{disorder}} [2\pi]$, with $L_{n=61}^{\text{eff}}$ & $L_{\text{defect}}^{\text{eff}}$ the effective lengths of the modes, $k_x^{(0)}$ is any of the wavevector describing the extended mode while $k_x^{(1)}$ is any value from the spectral content of the confined defect mode. $\Delta\phi^{\text{refl.}}$ is the relative dephasing introduced by reflections from the cavity terminations and the defect-potential and $\Delta\phi^{\text{disorder}}$ is the relative dephasing introduced by the random disorder. The effect works even at large detuning, which is likely a consequence of low Q factors for the modes of the 2nd band that allow for a non-zero spectral overlap between the modes. This is similar to the case of an $L_{n=3}$ cavity coupled to a PhC waveguide [262]. However, in that case the fundamental mode of a $L_{n=3}$ cavity comes from the lateral confinement of the waveguide mode of the 1st band, it is thus naturally compatible with a waveguide mode of the same band. An in-depth analysis would actually require a comparison of the Fourier spectra of the non-coupled modes with those of the new coupled modes in presence of disorder, in order to determine all the elements in the (k_x, k_y) plane that allow for a non-zero coupling constant.

3.2 Fabrication of defect-potential cavities

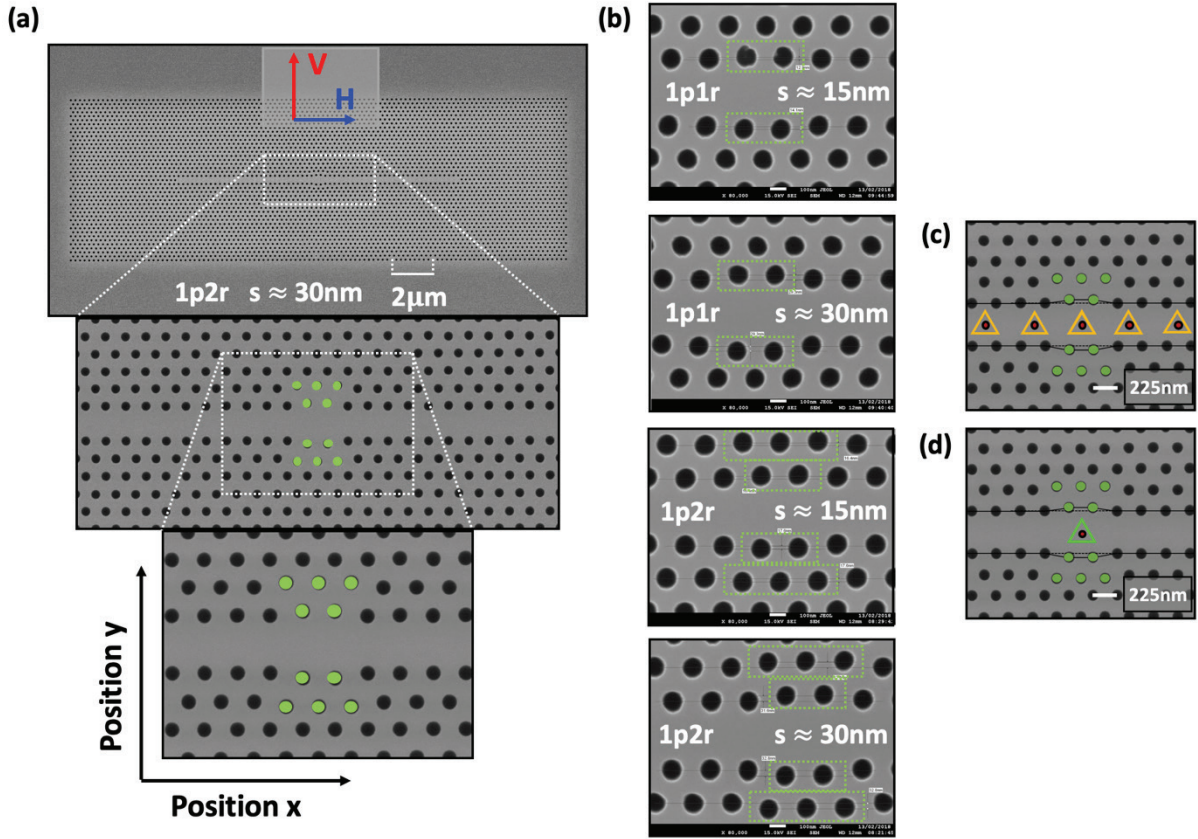


Fig. 3:10 – Scanning electron microscope top-view images of: (a) fabricated defect-potential PhC based on an $L_{n=61}$ cavity, with a zoom-in on the core of a 1p2r, $s \approx 30$ nm defect configuration; (b) Close-ups of several defect structures with designed shifts $s \approx 15, 30$ nm, for both 1p1r & 1p2r. Green circles highlight the shifted holes. (c), (d) Schematics of the pyramidal QDs system used for optical modes and QD coupling studies.

Fig. 3:10 displays electron micrographs from a dummy (100) GaAs membrane sample where the structures share identical design and parameters as those presented later in this Chapter. The structures are based on altered $L_{n=61}$ cavities with center defects defined by nominal shifts $s = 15$ or 30 nm, with both 1p1r and 1p2r configurations. The left and right terminations are also modified: the three first side-holes are shifted outwards along x respectively by $s_{1x} \approx 0.2311a$ (~ 52 nm), $s_{2x} \approx 0.1507a$ (~ 34 nm), $s_{3x} \approx 0.048a$ (~ 11 nm). These parameters were defined by the author of [161] with the original goal of optimizing the Q-factor of the fundamental mode of $L_{n=3}$ cavities, and the template was applied to all L_n cavities. (a) The cascaded insets show magnified views of an implemented 1p2r $s \approx 30$ nm defect, where the shifted holes are highlighted by the green markers. Positions x and y axis are defined in the sample plane, corresponding to the H and V polarization axis. (b) These insets exhibit one realization of each of the four fabricated configurations. The nominal shifts are estimated from hole center to hole center, and the upper and lower shifts have been reproduced with small discrepancies, respectively: $\sim (12.9, 14.1)$ nm for 1p1r $s = 15$, $\sim (29.3, 29.3)$ nm for 1p1r $s = 30$, $\sim (16.4, 17.6)$ nm for 1p2r $s = 15$, and $\sim (31.6, 32.8)$ nm for 1p2r $s = 30$. In addition, some irregularities in the roundness of holes are noticeable, they are likely caused by inhomogeneities in the etching plasma or in the substrate material itself. The fabricated PhC holes cover a wide range of $r_{\text{fab.}} \approx 47$ – 74 nm for coarse r/a tuning of the mode energies. Based on numerical simulations, the confined modes are predicted to appear in the ~ 1.240 – 1.378 eV photon energy range (900–1000 nm) at $T \approx 10$ K, enabling resonances with the s -shell transitions of the embedded pyramidal QDs (see again Fig. 2:9).

In the actual sample containing the QDs, made on the (111)B GaAs substrates, the defect-potential cavities have been implemented in two groups. The purpose of the first group (see **(c)**), inserted on one of the medium squares, is to observe the optical mode structure with site-controlled QDs acting mainly as broadband internal light emitters when pumped with high excitation power density. To this end, 30 site-controlled QDs are embedded every one PhC lattice site out of two; these QDs emit at photon energies $\sim 1.258\text{-}1.272\text{eV}$ ($\lambda_{\text{QD}} \sim 975\text{-}985\text{nm}$) at $T \approx 10\text{K}$. The first group of PhC structures includes a single repetition of r/a lithographic tuning for 1p1r and 1p2r, $s \approx 15$ and 30nm . Each repetition is comprised of 2×13 structures with radius r_{fab} ranging from ~ 47 to $\sim 63\text{nm}$ and from ~ 58 to $\sim 74\text{nm}$. The second group (see **(d)**), defined on the big square region, aims at studying the coupling between single site-controlled QDs and the confined modes of the deterministic defect. In this case, a single site-controlled QD is embedded at the center of the defect-potential cavities, emitting in the $\sim 1.264\text{-}1.279\text{eV}$ ($\lambda_{\text{QD}} \sim 970\text{-}980\text{nm}$) photon energy range at $T \approx 10\text{K}$. Each configuration 1p1r and 1p2r, with $s \approx 15$ or 30nm , is repeated 4 times; each series has 2×13 structures with radius r_{fab} ranging from ~ 47 to $\sim 63\text{nm}$ and from ~ 58 to $\sim 74\text{nm}$. For detailed layouts of the investigated structures, we invite the reader to consult appendix C.

3.3 Observation of defect modes

This part describes experimental observations of the optical mode structure of the fabricated defect-potential PhC cavities embedded with QDs arrays, using our micro-photoluminescence imaging technique. We compare the results both in qualitative and quantitative terms with the numerical modeling presented in section 3.2.

3.3.1 Defect mode spectra

In **Fig. 3:11**, the optical mode structures of a PhC defect-potential heterostructure with an embedded array of QDs is shown, acquired over a wide range of photon energies. The structure was illuminated by a high-power line-shaped laser beam, and a polarizer placed in the detection path was employed to separate the vertical (V) and horizontal (H) linear polarization components, which are characteristic signatures of respectively the 1st and 2nd “waveguide” bands [80]. The data can be directly confronted with the simulation of Fig. 3:2(d), the parameters of which were chosen to match with these spatially resolved spectral images. The delimitation of the various band-edges is extracted from the numerical modeling, as the band-edges are otherwise quite difficult to assert purely from experimental data. The band-edges are represented by the horizontal white dot-dashed straight lines. They correspond to the disorder-free case, not representing the real photonic potential corrugated by fabrication imperfections. The vertical white dot-dashed lines specify the photonic confinement potential, and the location of the two end reflectors of the PhC cavity.

Part **(a)** displays the V polarized component of the spectra and highlights a variety of effects. Anderson localization [263] occurs near the 1st band-edge approximately between $\sim 1.28\text{eV}$ and $\sim 1.29\text{eV}$; this $\sim 7\text{-}10\text{meV}$ range is representative [252] of the level of disorder involved. The spatial distribution of light intensities of the modes in this region appears to be quite random, and the modes do not extend all the way to the boundaries of the parent $L_{n=61}$ cavity. According to [94], the lower bound for the localization length is expected to be equal or larger than the length of a $L_{n=3}$ or $L_{n=5}$ cavity, i.e. $\sim 900\text{nm}\text{-}1.35\mu\text{m}$, about the size of the defect region. This is consistent with the observed sizes of the lobes of the localized modes. Around $\sim 1.26\text{eV}$, a single, well localized mode distinguishes itself from the extended modes at energies beyond the 1st band-edge at $\sim 1.28\text{eV}$. This is defect mode $\#0_{\text{M}}^{(0)}$, pulled down in energy and trapped by the defect region. The next visible mode at higher energy is mode $\#1_{\text{M}}^{(0)}$, recognizable by its two lobes separated by a center node. The mode is detached from the band-edge and starts to localize within the defect. The two lobes are asymmetric due to fabrication disorder. The modes appearing above $\sim 1.29\text{eV}$ constitute the fast light part. The spatial distribution of light intensities of these modes is more regular, as they are less impacted by the disorder since they are far from the photonic band-edge. In these modes, light travels freely from one end reflector to the other, as seen from the noticeable scattering at the left and right edges. This confirms the notion that these long L_n cavities are indeed terminated “waveguides” [158]. Light is also scattered out-of-plane near the center, for one mode out of two, coinciding with even symmetry $\Pi_x = +1$, due to the presence of the defect-region.

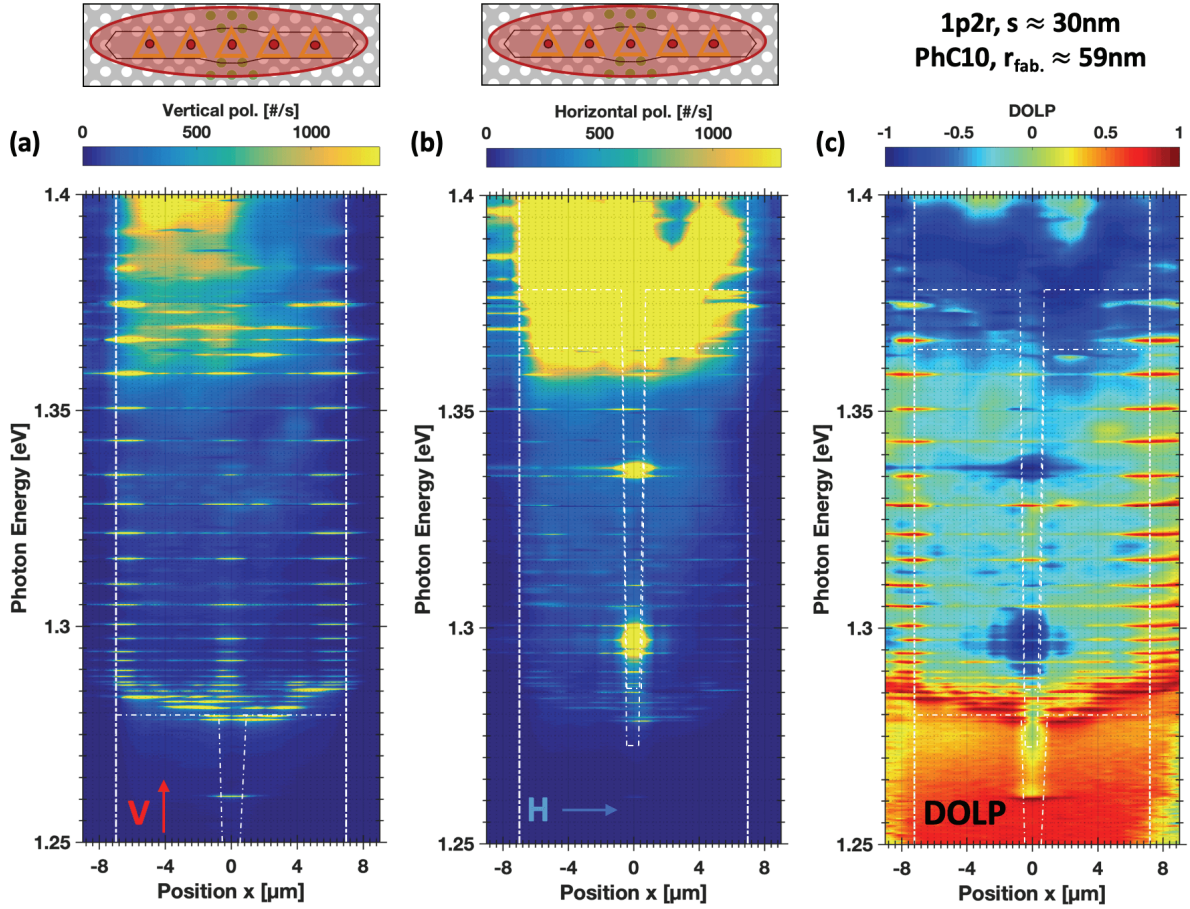


Fig. 3:11 – Measured optical mode structure of a defect-potential PhC cavity acquired over a spectral range of 150meVs. Upper panels show schematically the experimental pumping arrangements. (a) Vertically (V) polarized emission; (b) horizontally (H) polarized emission; (c) image of the degree of linear polarization (DOLP) derived from (a) and (b). White dot-dash lines are visual cues of the photonic defect potential, from simulation. Above barrier excitation, laser wavelength $\lambda_{\text{exc.}} \approx 730\text{nm}$, excitation power $P_{\text{exc}} \approx 2\text{mW}$. Temperature $T \approx 10\text{K}$. PhC hole radius $r_{\text{fab.}} \approx 59\text{nm}$, configuration 1p2r, $s \approx 30\text{nm}$. Photonic potential drawn with same numerical parameters as in Fig. 3:2.

Part (b) shows the H-polarized component. In particular, two bright modes, identified as the defect modes $\#0_{\Gamma}^{(1)}$ ($\sim 1.295\text{eV}$) and $\#0_{\text{M}}^{(1)}$ ($\sim 1.335\text{eV}$), are pulled down in energy and trapped by the defect-potential acting on the 2nd band. The 2nd band appears as a large bright region above $\sim 1.36\text{eV}$. The high intensity of this signal is due to a combination of several effects: feeding by the QDs' d-shells or QWRs states; over-saturation of the linear color scale that was used to visualize the dimmer parts of the image; the large DOS of the 2nd band and the low Qs of the modes as a result of important radiative losses via overlaps with the light cone (refer to Fig. 3:2(c)). The defect mode $\#0_{\text{M}}^{(1)}$ does not seem very well confined by the defect-potential, instead it appears to leak to the left of the cavity and seems to influence the brightness of the fast-light extended mode of the 1st band next to it. This is interpreted as the signature of the hybridization of these two modes, as was predicted in section 3.1.5, Fig. 3:7(d-f) and Fig. 3:8.

The latter interpretation is further supported by the DOLP pattern in (c). The DOLP synthesizes both (a) and (b) in a single picture, and the contributions of the 1st (red) and 2nd (blue) band can be immediately identified. The hybridized mode $\#0_{\text{M}}^{(1)}$ appears mostly blue (H-polarized), while the nearby interacting mode appears red (V-polarized) at the edges, and blue near the center. Looking more closely at the center region of the extended modes of the 1st band that overlap with the blue region of defect mode $\#0_{\Gamma}^{(1)}$, one mode out of two appears dark blue, while the others appear cyan corresponding to a more neutral linear polarization. The former are odd modes with $\Pi_x = -1$. They are thought to couple with bound-state mode $\#0_{\Gamma}^{(1)}$ and co-polarize horizontally, due to a higher compatibility of symmetries, as can be seen in Fig. 3:4. If hybridization does indeed occur with defect mode $\#0_{\text{M}}^{(1)}$,

it is not unreasonable to assume that it also happens with defect mode #0_r⁽¹⁾, as evidenced in section 3.1.5. On the contrary, the latter is an even mode with $\Pi_x = +1$ which likely does not couple with the odd symmetry mode. As a consequence, the positive DOLP of these V-polarized modes counteracts the negative DOLP of a H-polarized defect mode, resulting in a more neutral DOLP.

Defect mode #1_r⁽¹⁾ is not observed in the measured patterns of Fig. 3:11, despite a predicted confined mode with energy of $\sim 1.3435\text{eV}$ (see Fig. 3:2). Its absence is likely explained by the incompatibility between the mode pattern and the QDs array pattern used for its excitation. The QDs array possesses a pitch of twice the lattice constant $p = 2a$, starting with an inverted pyramid etched at the center of the structure. According to Fig. 3:4, none of the QDs would overlap with anti-nodes of the defect mode electric field, preventing the efficient feeding of the optical resonance. Assuming the defect mode is indeed there but not revealed, its existence is possibly hinted by the hybridization of the fast-light mode of the 1st band at $\sim 1.35\text{eV}$, which also presents a center region with a blue DOLP.

These near-field spectral images can be confronted to the ones presented in [257], in which the authors observed confined modes of the 1st and 2nd band for analogous but shallower deterministic defects, using SKQDs as internal emitters instead and scanned confocal imaging. Despite the random nucleation sites, the large surface density and large inhomogeneous broadening of SKQDs also make them suitable to observe optical mode structures. However, in that study, the choice of an open waveguide configuration and the absence of a polarization resolving measurements make it more difficult to definitely identify the origins of the defect modes.

Fig. 3:12 compares side by side the mode patterns of the four configurations 1p1r s $\approx 15, 30\text{nm}$ and 1p2r s $\approx 15, 30\text{nm}$ for identical PhC hole radius. Here the total emission intensity (**a-d**) is displayed instead of the individual V and H polarization contributions, and the DOLP maps (**a'-d'**) complement the information. In all four structures, the 1st and 2nd band's band-edges and the discrete modes align rather well, proving the reliability of the fabrication. The main qualitative mode structure as for Fig. 3:11 can be appreciated, with the different defect configurations essentially changing the binding energies of the different defect modes. The observation of confined modes of the 2nd band cannot be appreciated very clearly for the 1p1r s $\approx 15\text{nm}$ configuration in (a) but is supported by the DOLP pattern in (a').

Fig. 3:13 simplifies the comparison of the structures of Fig. 3:12 by removing the spatial dependence via integration of the intensities along position x for each photon energy. This representation corresponds to the recording of conventional spectra (without spatial resolution). It is more convenient for a quantitative comparison with the data of Fig. 3:5, but it also illustrates the importance of resolving spatial information with the imaging technique in order to analyse optical mode structures in general.

The experimental measurements show excellent agreement with the numerical modelling, provided the latter include the effect of fabrication-induced disorder ($\sigma_r = 2\text{nm}$ & $\sigma_a = 1\text{nm}$), basing on the energy variations reported in section 3.1.5. The predicted defect mode energies and variations overlap with the experimental spectral lines of the identified defect modes to within $\pm\sigma_E$ ($\sim 68\%$ confidence range). In **Fig. 3:13(a-d)**, another set of Anderson localized modes is seen in between the bottom band-edges of the 2nd band (cyan and dark blue). These modes cannot be seen that well in the near-field images due to the saturated linear color scales, but they are revealed here thanks to the logarithmic intensity scale.

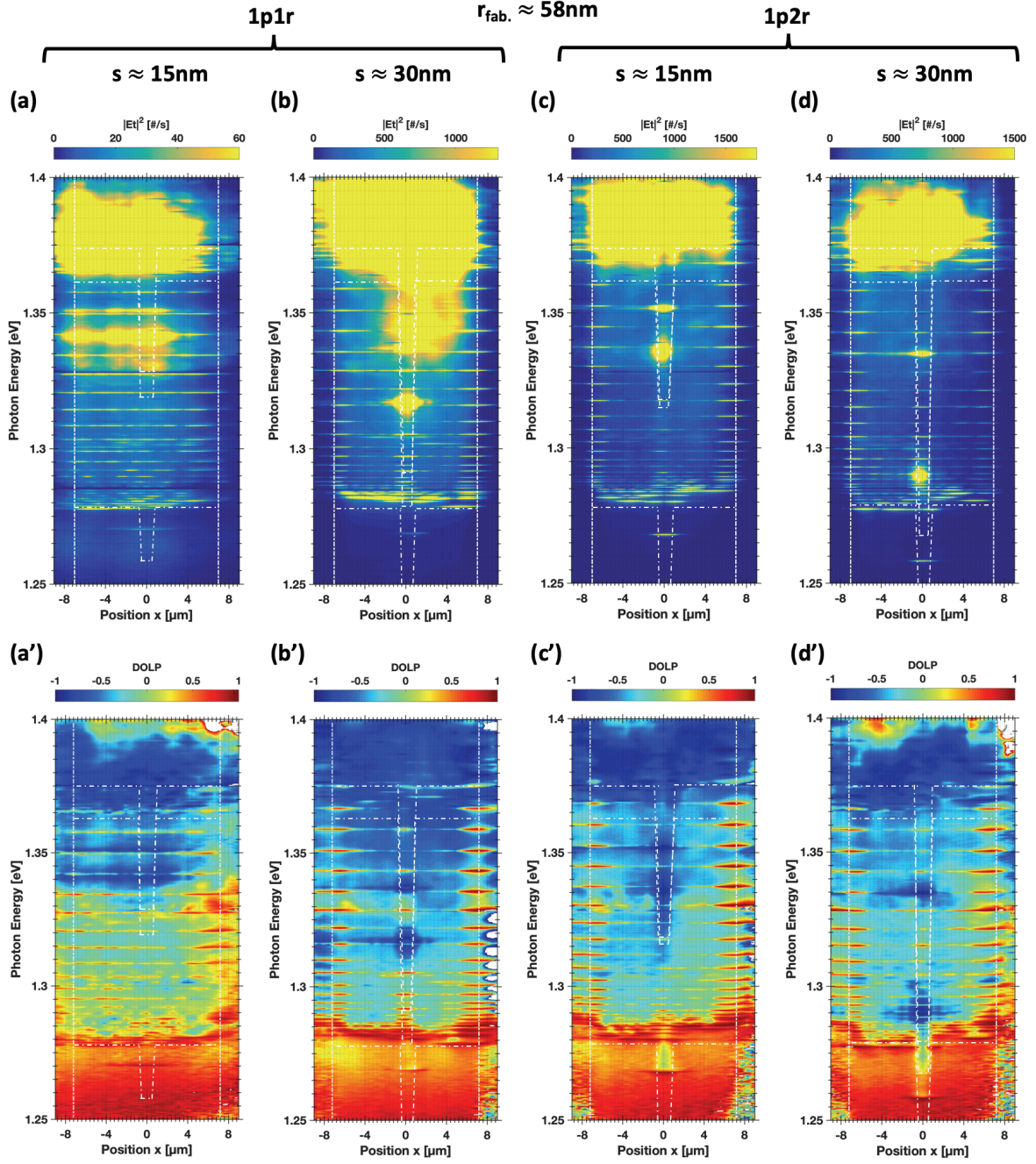


Fig. 3:12 – Comparison of the measured optical mode structure for four configurations of a defect-potential PhC cavity. (a-d) Total intensity maps, (a'-d') associated DOLP maps. (a,a') 1p1r, $s \approx 15\text{nm}$; (b,b') 1p1r, $s \approx 30\text{nm}$; (c,c') 1p2r, $s \approx 15\text{nm}$; (d,d') 1p2r, $s \approx 30\text{nm}$. White dot-dash lines are visual cues of the defect photonic potential and the couplers, from simulations. Above barrier excitation, laser wavelength $\lambda_{\text{exc.}} \approx 730\text{nm}$, excitation power $P_{\text{exc.}} \approx 2\text{mW}$. Temperature $T \approx 10\text{K}$. Radius $r_{\text{fab.}} \approx 58\text{nm}$. Numerical parameters: pitch $a = 225\text{nm}$, membrane thickness $t = 250\text{nm}$, holes radii $r = 66.6\text{nm}$, effective index of slab spectrally adapted.

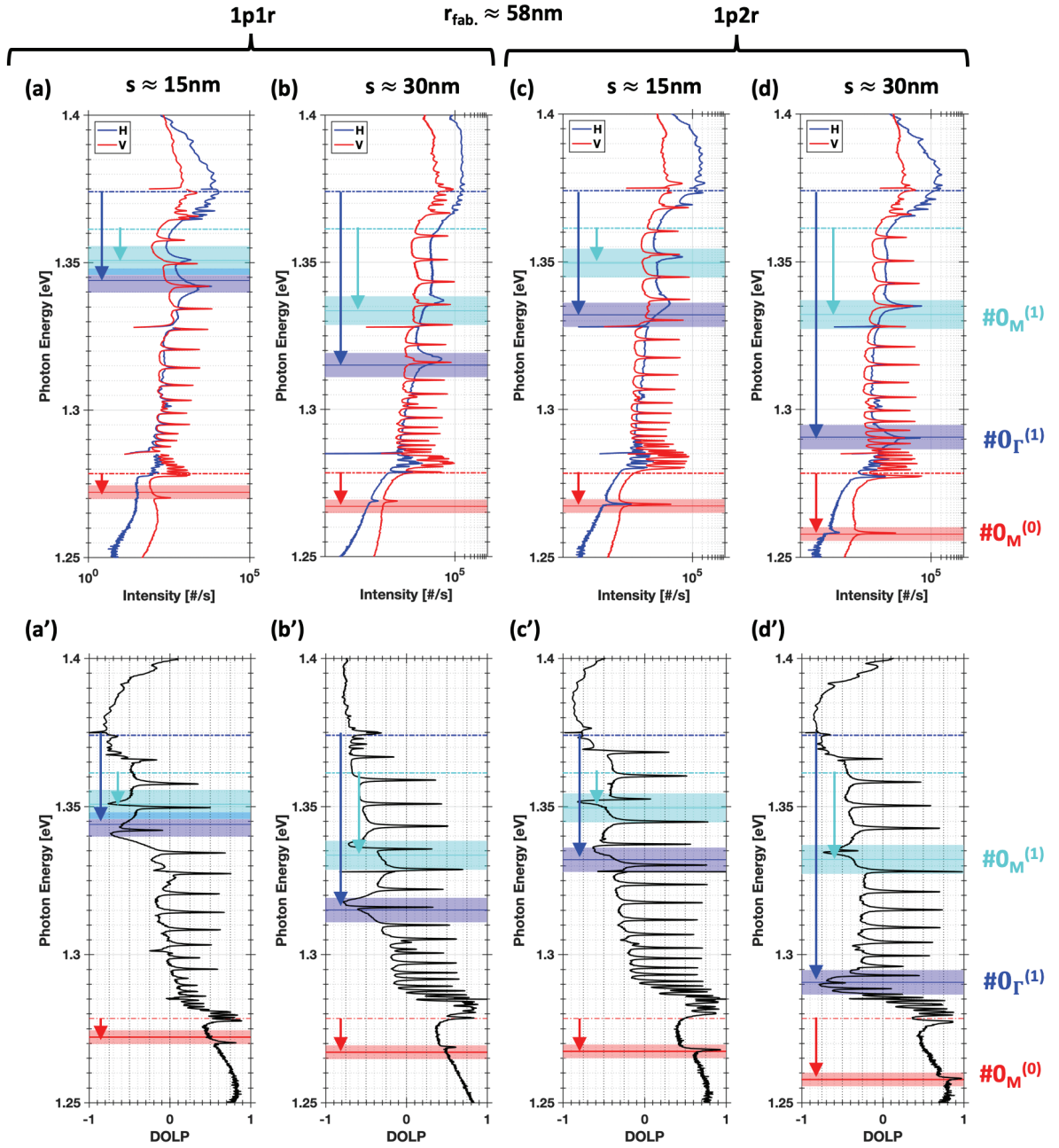


Fig. 3:13 – Comparison of measured polarized spectra (a)-(d) and extracted DOLP spectra (a')-(d') of two defect potential configurations and different shifts s . Extracted from Fig. 3:12 by integration across x . Overlays extracted from numerical simulations: dot-dash lines depict the band-edges, red: 1st band M side, cyan: 2nd band M side, dark blue: 2nd band Γ side. Solid lines display expected mode positions. Arrows show energy shifts due to hole shifts by s . Shaded areas show one standard deviation in energy accounting for $\sigma_r = 2\text{nm}$ & $\sigma_a = 1\text{nm}$. Numerical parameters: pitch $a_0 = 225\text{nm}$, membrane thickness $t = 250\text{nm}$, holes radii $r_0 = 66.6\text{nm}$, effective index of slab adapted to each converged mode.

3.3.2 Defect modes Q-factors

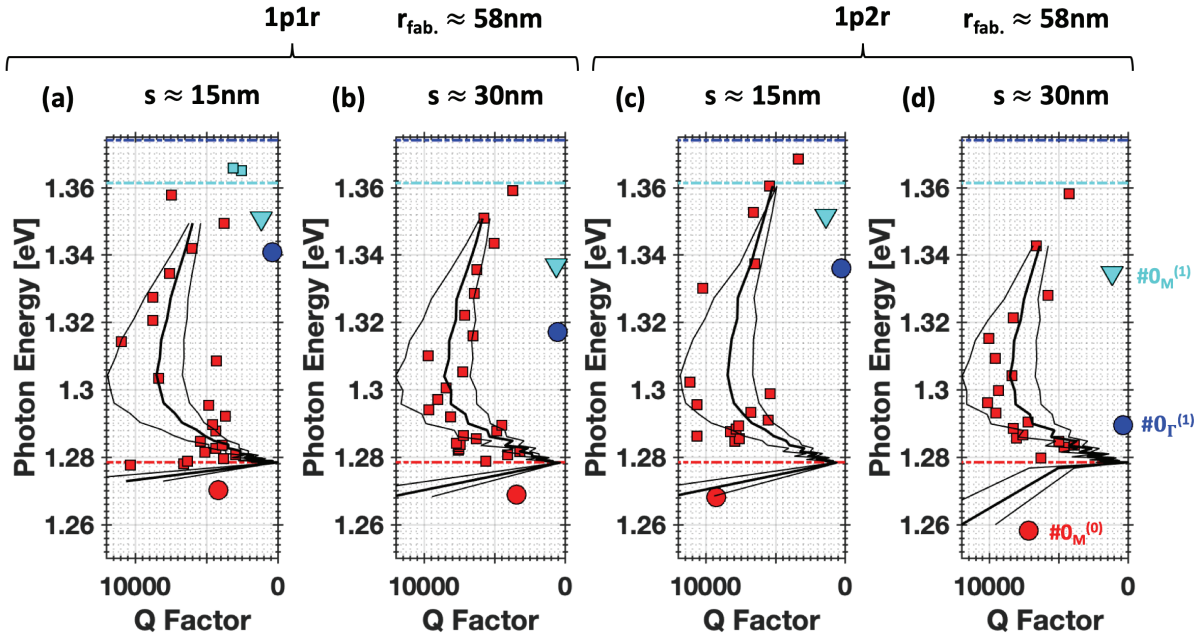


Fig. 3:14 – Experimental Q -actors for defect-potential PhC cavities; 1p1r: (a) $s \approx 15\text{nm}$, (b) $s \approx 30\text{nm}$ and 1p2r: (c) $s \approx 15\text{nm}$, (d) $s \approx 30\text{nm}$. Red symbols relate to 1st band modes and red dot-dash lines to 1st band M point band-edge from simulations. Cyan and dark blue symbols relate to 2nd band modes, cyan and dark blue dot-dash lines to respectively 2nd band, M point band-edge and Γ point band-edge from simulations. Black lines correspond to a physical Fabry-Pérot model [162], [264]. Extracted from data of Fig. 3:13.

Quality factors are among the most important figures of merit in cavity QED. The Q-factors of the four previous structures were extracted and are presented in **Fig. 3:14**. The discrete modes of the 1st band display Qs of $\sim 4'000$ - $10'000$, in agreement with values measured from previously grown samples [162] and comparable to what is found in the literature [256], [257]. The two bound-states $\#0_M^{(1)}$ and $\#0_\Gamma^{(1)}$ of the 2nd band have much lower Qs, ~ 100 s- $1'000$. These values are well below the maximum measurable value of $\sim 16'000$ at $\sim 1.25\text{eV}$ set by the $\sim 80\mu\text{eV}$ spectral resolution limit in imaging mode of our setup. 3D FDTD simulations of such L_n cavities usually predict Q values well above 10^3 - 4 . The experimental values suggest the importance other physical limiting mechanisms, such as Urbach band-tail absorption from the GaAs barrier materials and structural scattering losses which are usually not accounted for in numerical modeling.

The four graphs display a common trend for the modes of the 1st band that is well reproduced by the Fabry-Pérot model employed in [162], [264]. Using the same parameters determined there: $\alpha_1 = 0.22 \pm 0.12\text{mm}^{-1}$ (absorption), $E_a = 55 \pm 21\text{meV}$, and $\alpha_2 = 0.04 \pm 0.01\text{mm}^{-1}$ (scattering) yields excellent agreements with the experimental data. The mode energies were extracted from numerical simulations with $n_{\text{eff}} = 3.156$, translated to wavelengths, and used to extract the group indexes $n_g(E)$ and wavevectors $k_0(E)$. In Fig. 3:14, the solid center line corresponds to the ($E_a = 55\text{meV}$, $\alpha_1 = 0.22\text{mm}^{-1}$, $\alpha_2 = 0.04\text{mm}^{-1}$) combination, the thinner lines to ($E_a = 34\text{meV}$, $\alpha_1 = 0.10\text{mm}^{-1}$, $\alpha_2 = 0.03\text{mm}^{-1}$) and ($E_a = 76\text{meV}$, $\alpha_1 = 0.34\text{mm}^{-1}$, $\alpha_2 = 0.05\text{mm}^{-1}$). Using the same parameters here is justified by the following reasons: both samples are made on the same (111)B GaAs membranes, the defect-potential heterostructures are based on the same design of the parent $L_{n=61}$ cavities, fabrication relies on the same ICP dry etching process parameters, the level of PhC disorder similar, and the structures studied cover similar range of energies with a 1st band band-edge around $\sim 1.28\text{eV}$. According to this model, the total Q-factor is dominated by the lowest loss rate, either related to reflection losses or propagation losses. For long parent cavities, as is the case here, the reflection losses become negligible when compared to the propagation losses. We estimate propagation losses of $\alpha_p \approx 6 \pm 1\text{mm}^{-1}$ for $n_g \approx 5.8$ in the fast light-region (dispersive regime), while propagation losses increase rapidly with increase of the group index, $\alpha_p \approx 29 \pm 9\text{mm}^{-1}$ for slow-light characterized by $n_g \approx 24$, up to $\alpha_p \approx 93 \pm 26\text{mm}^{-1}$, $943 \pm 245\text{mm}^{-1}$ for Anderson localized modes with $n_g \approx 45, 151$ (diffusive regime).

The rise of the Q-factors when the photon energy decreases from ~ 1.36 to ~ 1.30 - 1.31 eV is linked to the reduction of the dominant absorption mechanism from the Urbach tail in the fast-light region. The decrease from ~ 1.30 - 1.31 eV to the band-edge is explained by the increase of the dominant scattering loss mechanism when moving from the dispersive guiding regime to the diffusive regime of Anderson localized modes. We assumed a constant effective length of $L_{\text{eff}}=62a$ even if the bound-states modes are confined to only a few lattice sites. Despite this short-coming, the model accounts for an increase of the Q-factor past the band-edge, because the defect mode $\#0_M^{(0)}$ is pulled down in energy by a significant amount, and the group index of the mode is thus much lower than for the Anderson-localized modes at the band-edge. As a consequence, the scattering losses are drastically reduced.

Based on Fig. 3:2(c), the various confined defect modes have a non-negligible amount of Fourier components within the light cone. The introduced deterministic defect is a non-negligible perturbation in the y direction that alters the spatial patterns of the many modes and their spectral contents. According to [159], this is likely to explain the lower Q values for mode $\#0_M^{(0)}$, and very low Qs for modes $\#0_M^{(1)}$ and $\#0_r^{(1)}$. Furthermore, since the $L_n=61$ cavity is extended along x, it is better suited for confining the modes of the 1st band. Further non-trivial optimization of the structure by shifting additional holes might help in this regard.

It should be underlined again that the overall Q factors can be increased from further reducing the impact of the Urbach tail absorption [265]–[267], which is set by the choice and purity of the barrier materials, by moving to longer wavelengths by adjusting the PhC r/a ratio accordingly. The record value of 700'000 in GaAs in a defect-potential-like structure was measured at $\sim 1.55\mu\text{m}$ [165], one order of magnitude larger than the value of 55'000 at $\sim 940\text{nm}$ [258]. Other ultra-high Qs were predicted or measured in PhC structures made in silicon (Si), which has a similar refractive index as GaAs but is highly transparent in this spectral range [164], [238], [253]–[255], [259]. At longer wavelengths, the structural parameters (e.g., the PhC holes) are also larger, resulting in smaller level of structural disorder. For InGaA/GaAs QDs, pushing to longer wavelengths requires larger Indium content, which ultimately compromises their optical quality.

3.3.3 Experimental binding energies

To compare the experimental binding energies of the bound-states defect modes to the numerical estimations reported in Table 3:2, the energies of the confined defect modes of interest were extracted for a collection of structures with different r/a ratio parameter. The raw data from the four configurations of 1p1r and 1p2r data is displayed in **Fig. 3:15**. The black dot boxes highlight the data that was shown previously in Fig. 3:13(a-d) and act as reference points. In this case of $r_{\text{fab.}} \approx 58\text{nm}$, the binding energies of $\#0_M^{(0)}$ to the band-edge $BE_M^{(0)}$ are respectively approximately **(a)** -8.1meVs, **(b)** -9.7meVs, **(c)** -10.6meVs and **(d)** -20.2meVs. The binding energy increases with increasing shift s, and it does it more significantly with the 1p2r configuration as compared to the 1p1r. Since the band-edges of the second band cannot be retrieved experimentally without ambiguity in order to estimate the binding energies without introducing large error bars, it is more appropriate to rely instead on the energy distance of the modes $\#0_r^{(1)}$ and $\#0_M^{(1)}$ with respect to mode $\#0_M^{(0)}$. These defect modes are specified in order by the dark blue filled circles, cyan filled triangles and red filled circles. The energy distances are estimated to be respectively (a) $\Delta E(\#0_r^{(1)} - \#0_M^{(0)}) \approx 70.6\text{meVs}$, $\Delta E(\#0_M^{(1)} - \#0_M^{(0)}) \approx 80.6\text{meVs}$; (b) $\sim 49.1\text{meVs}$, $\sim 68.4\text{meVs}$; (c) $\sim 68.1\text{meVs}$, $\sim 83.7\text{meVs}$ and (d) $\sim 31.6\text{meVs}$, $\sim 76.2\text{meVs}$. For both configurations, 1p1r and 1p2r, these energy distances decrease with increasing shift s, which confirms that the defect-potential depth grows faster for the 2nd band than it does for the 1st. Overall, graphs (a-d) show the reproduction of the confined defect modes at smaller and larger radii, with natural fluctuations of the mode energies stemming from fabrication disorder. The variations are however quite controlled and allow for linear regression fits to evaluate the trends, with most data points falling mostly in the shaded regions corresponding to $\pm\sigma_E \sim 68\%$ confidence ranges. Globally, defect modes' energies of a given band follow parallel redshift trajectories to their band-edge's energies with decrease of $r_{\text{fab.}}$, which means that the defect-potentials remain approximately the same in terms of confinement depth. However, the linear regressions fit also indicate a narrowing of the energy distance, especially pronounced in (d), between the 1st and 2nd bands' band-edges with reduction of the radius. This can be expected; from Fig. 1:10, the photonic bandgap is supposed to close with smaller values of the r/a ratio.

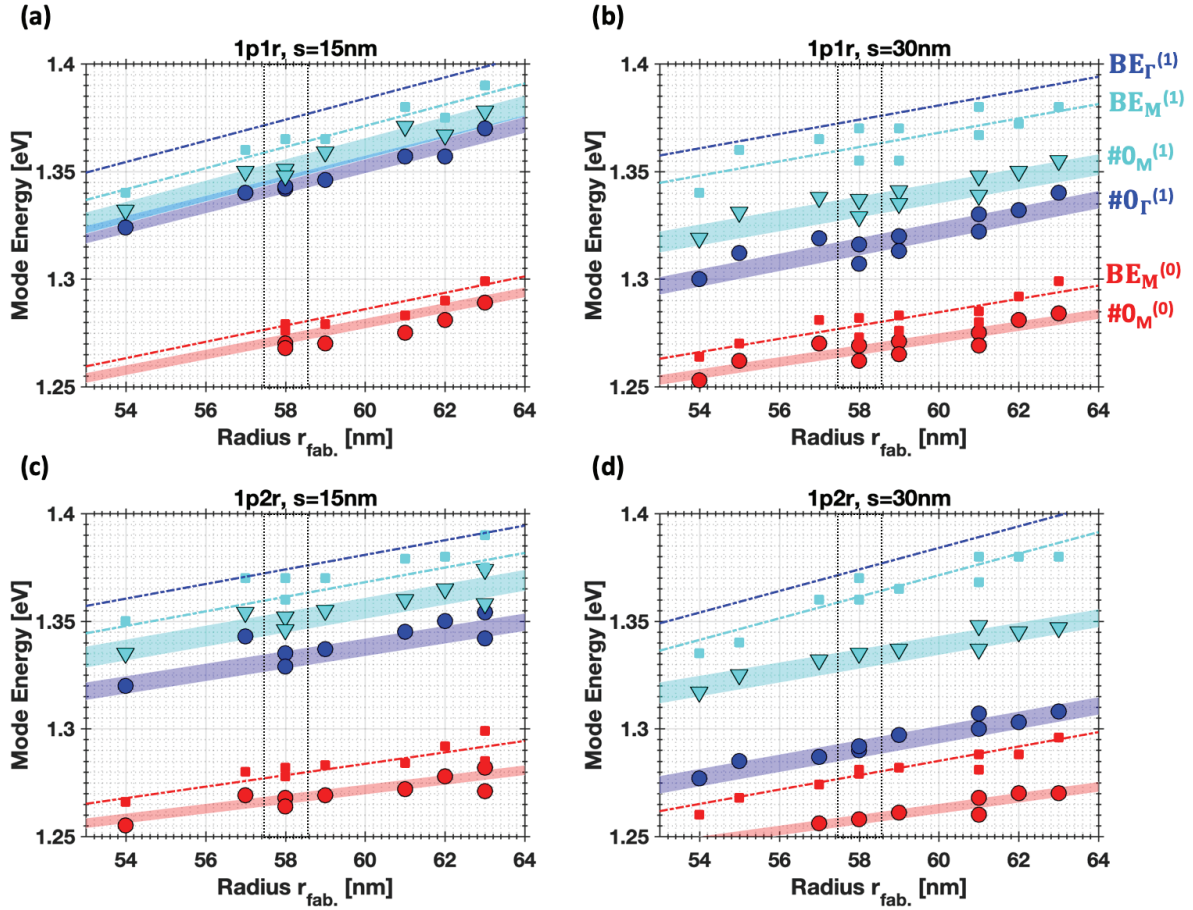


Fig. 3:15 – Band-edges and confined defect modes energies (symbols) for a collection of samples with different fabricated radius, extracted from data as shown in Figs. 3:12-13, for 1p1r (a) $s \approx 15\text{nm}$, (b) $s \approx 30\text{nm}$; 1p2r (c) $s \approx 15\text{nm}$, (d) $s \approx 30\text{nm}$. Filled square symbols indicate experimental data points for the band edges: $BE_M^{(0)}$ (red), undetermined $BE_r^{(1)}$ or $BE_M^{(1)}$ (cyan). Dot-dash lines indicate band-edges from linear regression fits of the square symbols, the cyan line is split in two vertically offset lines assuming a correspondence between $r_{fab.} \approx 58\text{nm}$ and $r_0 = 66.6\text{nm}$ (see Fig. 3:13 and black dot boxes) to indicate distinctly $BE_r^{(1)}$ (dark blue), $BE_M^{(1)}$ (cyan). Filled symbols for confined defect modes: $\#0_M^{(0)}$ (red circles), $\#0_r^{(1)}$ (dark blue circles), $\#0_M^{(1)}$ (cyan triangles). Broad shaded lines refer to the linear regressions fits of confined defect modes with one standard deviation in energy in the presence of $\sigma_r = 2\text{nm}$ & $\sigma_a = 1\text{nm}$. Above barrier excitation, laser wavelength $\lambda_{exc.} \approx 730\text{nm}$, $P_{exc.} \approx 2\text{mW}$. Temperature $T \approx 10\text{K}$. Numerical parameters: pitch $a_0 = 225\text{nm}$, membrane thickness $t = 250\text{nm}$.

The values of the energy distances for the four configurations are compiled in **Table 3:3** where experimental data are confronted with the numerical predictions of Fig. 3:5. The energy differences for the defect modes are extracted for each individual structure of a given hole size, and then the mean and dispersion of the distributions are estimated from these. The error bars of the simulated values are estimated from Fig. 3:6 assuming $\sigma_r = 2\text{nm}$ & $\sigma_a = 1\text{nm}$. Experiments and modelling predictions overlap reasonably well over few meVs, which means that the fabricated structures have a high degree of fidelity with respect to numerical predictions, supporting a reproducible and quasi-predictable confinement of the defect modes.

The results also agree qualitatively relatively well with the observations in [256], where the authors reported the energy distance between $\#0_r^{(1)} - \#0_M^{(0)}$. Their defect configuration would be equivalent to a more elaborate 1p3r ($s, 2s/3, s/3$) design, but qualitatively their choice of $s \approx 3, 6, 9, 12\text{nm}$ can be compared to our 1p1r and 1p2r configurations with $s \approx 5, 10, 15\text{nm}$. The decreasing energy differences with increasing potential depth (increased shift s) is observed in that case as well.

	1p1r, $s \approx 15\text{nm}$	1p1r, $s \approx 30\text{nm}$	1p2r, $s \approx 15\text{nm}$	1p2r, $s \approx 30\text{nm}$
$\Delta E(\#0_M^{(1)} - \#0_M^{(0)})$				
Experiment	$87.8 \pm 13.0\text{meV}$	$69.2 \pm 1.9\text{meV}$	$85.7 \pm 3.5\text{meV}$	$76 \pm 2.8\text{meV}$
Simulation (disorder)	$75.4 \pm 7.3\text{meV}$	$64.1 \pm 7.3\text{meV}$	$78.9 \pm 7.3\text{meV}$	$71.7 \pm 7.3\text{meV}$
$\Delta E(\#0_r^{(1)} - \#0_M^{(0)})$				
Experiment	$76.7 \pm 4.1\text{meV}$	$50.0 \pm 3.5\text{meV}$	$69.7 \pm 3.5\text{meV}$	$34.8 \pm 3.6\text{meV}$
Simulation (disorder)	$69.3 \pm 6.5\text{meV}$	$46.1 \pm 6.5\text{meV}$	$61.9 \pm 6.5\text{meV}$	$30.8 \pm 6.5\text{meV}$

Table 3:3 – Summary of experimental energy distance between the modes trapped by the defect-potential for all four variants of the implemented structures and comparison to numerical simulations. Experimental: statistical averages with one standard deviation in energy, extracted from Fig. 3:11. Simulation: values from Table 3:2 and error bars estimated with $\sigma_r = 2\text{nm}$ & $\sigma_a = 1\text{nm}$.

3.4 Integration with single site-controlled QDs

In this section, we report experimental evidences for the coupling of single site-controlled QDs to the two distinct, orthogonally polarized bound-states of the Defect-Potential PhC Cavities. These are interesting in the perspective of obtaining single photon extraction with polarization control.

3.4.1 Selective excitation of the V-polarized $\#0_M^{(0)}$ defect mode

Fig. 3:16 compares the intensity and DOLP maps of **(a, a')** a defect-potential optical mode structure of reference, acquired with an array of embedded QDs, to **(b, b')** the corresponding structure with a single QD integrated at the center of the defect region, as indicated by the vertical green dotted line. In both cases the structures are pumped at the same power level and using the cylindrical lens. In particular, the defect modes $\#0_M^{(0)}$ and $\#0_r^{(1)}$ are selectively excited by the spatial and spectral overlap of the feeding QD's s-shell and p-shell transitions, which are revealed by decreasing the pump excitation power **(c, c', d, d')**. Between **(a')** and **(b')**, it can be noticed that the extended modes of the 1st band provide a vertical (red) polarization background that neutralizes the horizontally polarized wide blue "sea" of the 2nd band brought down with the defect mode $\#0_r^{(1)}$. The latter is very dominant in **(b')**, spanning the full extent of the $L_{n=61}$ parent cavity. Furthermore, there is a non-negligible average net-zero DOLP in the bandgap, below the band-edge of the 1st band indicated by the lowermost black dot-dashed contour, with a DOLP of ~ 0.25 -0.5 (yellow-orange hue); a neutral polarization trail in the wake of the pulled-down defect mode $\#0_M^{(0)}$ is also visible. In **(c)**, the defect mode $\#0_r^{(1)}$ is seen to be overlapping with some extended fast-light modes of the 1st band. Light is not only localized in the vicinity of the trapped mode and scattered from the center, but it is also reaching to the left edge of the cavity. The pattern is asymmetric and does not leak to the right; this is likely to be the signature of the hybridization effect predicted and discussed in section 3.1.5. As seen from **(a', b', c')**, the excitation power plays a role in the stabilization of the DOLP. The surrounding net polarization reduces to fluctuations around DOLP-0 when the power is decreased, because with the dimming of the QDs transitions the confined optical modes cannot be fed steadily anymore. Finally, there is one more striking feature seen in **(c', d')**: a small H-polarized blue spot is visible at $\sim 1.273\text{eV}$, slightly blue-shifted from the defect mode $\#0_M^{(0)}$, and noticeable by an S-shape in the DOLP profile. This can be interpreted as a manifestation of the DOLP switching phenomenon observed and modelled in [221], induced by interference between a radiative emission channel of the quantum dot and a radiative emission channel of a spectrally nearby cavity mode.

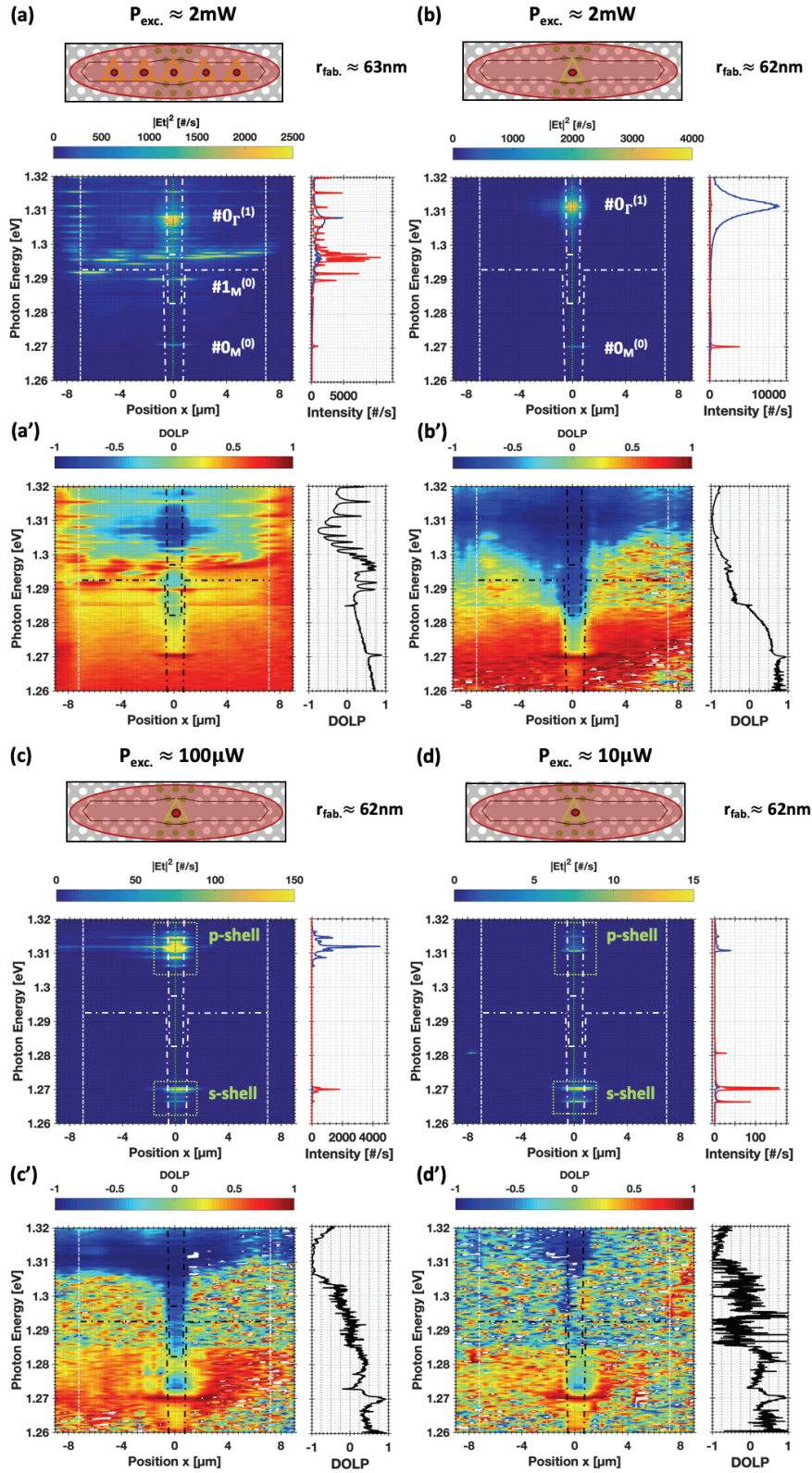


Fig. 3:16 – Selective excitation of defect-potential modes using a single site-controlled QD. Upper panels: schematics illustration of the excitation scheme. (a) Energy-position plot of optical modes patterns and (a') DOLP for $P_{exc} \approx 2mW$ on a reference structure: radius $r_{fab} \approx 63nm$, $1p2r, s \approx 30nm$. Energy-position plots of optical modes patterns and DOLP for (b,b') $P_{exc} \approx 2mW$, (c,c') $P_{exc} \approx 100\mu W$ and (d,d') $P_{exc} \approx 10\mu W$. Spectra and DOLP integrated across x shown on the sides. Vertical white dash-dot lines mark the extremities of the cavity. The vertical green dot line marks the positions of the single QD. Above barrier excitation, laser wavelength $\lambda_{exc} \approx 730nm$. Temperature $T \approx 10K$. Radius $r_{fab} \approx 62nm$, $1p2r, s \approx 30nm$.

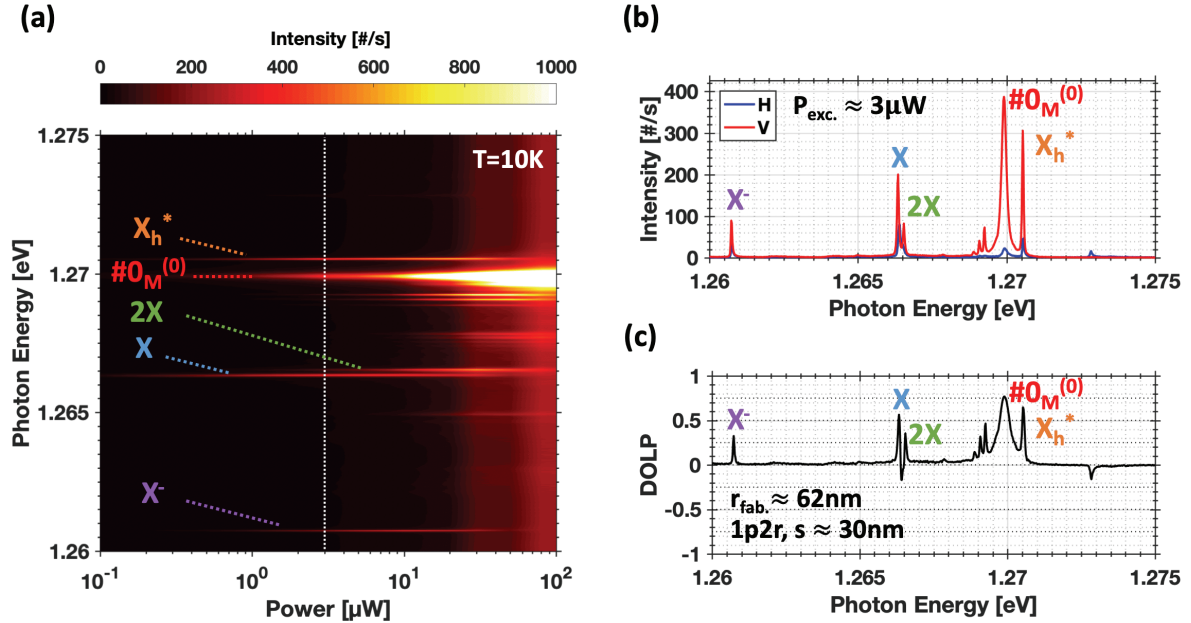
3.4.2 Weak coupling of a site-controlled QD with the V-polarized $\#0_M^{(0)}$ defect mode

Fig. 3:17 – Identification of spectral lines in a defect-potential PhC cavity integrated with a single embedded site-controlled QD. (a) Intensity spectra slices stitched together versus the incident excitation power. Identified cavity modes lines and QD lines are labelled. The data corresponding to the white dot line, at $P_{\text{exc.}} \approx 3 \mu\text{W}$, is shown in (b): intensity spectrum in both H & V polarizations; and (c): corresponding extracted DOLP. Temperature $T \approx 10\text{K}$. Above barrier excitation, laser wavelength $\lambda_{\text{exc.}} \approx 730\text{nm}$. Excitation scheme similar to Fig. 3:16(d). Radius $r_{\text{fab.}} \approx 62\text{nm}$, $1p2r, s \approx 30\text{nm}$.

Fig. 3:17 shows the characterization of the spectral lines pertaining to the s-shell of the QD appearing in the previous structure of Fig. 3:16 (b-d). The identification of spectral lines is performed by an excitation power dependence. The map in (a) was made by stitching intensity spectra taken at $P_{\text{exc.}} \approx 0.1, 0.2, 0.3, 0.5, 0.8, 1, 2, 3, 5, 8, 10, 20, 30, 50, 80$ and $100 \mu\text{W}$ with above-barrier spot excitation at the QD position. The cavity defect mode $\#0_M^{(0)}$ was identified thanks to its broader linewidth $\hbar\kappa \approx 185 \mu\text{eV}$ and non-saturating behavior. The remaining, thinner lines $\gamma < 100 \mu\text{eV}$ are QD lines. The lowest energy line, manifesting first at lowest pumping power, is assigned to the negative trion X^- , this is further certified by the presence of the $X - 2X$ couple $\sim 5.5\text{meV}$ s above [268], [269][220]. In this case, the biexciton $2X$ is anti-bound to the exciton by $E_{X,2X}^{\text{bind}} \approx +0.3\text{meV}$ [270]. Out of the two, the X is the first excitonic species to appear and rise alongside the X^- at the lowest levels of power. The $2X$ appears at higher excitation power because it requires the QD s-shell to fill at a rate faster than the recombination rate of the X . Usually, both the X^- and X reach a saturation plateau in intensity before eventually decaying, while the $2X$ intensity rises at the same power levels. Slightly blue-shifted to the defect mode cavity line, another QD line blue shifted with respect to the X line by $\sim 4.2\text{meV}$ s appears, triggered in conjunction with the X^- and X . Based on predictions from [110], it is attributed to the neutral excited hole state labelled X_h^* , where the hole occupies the light-hole-like band instead of the heavy-hole-like state. The triple feature to the left of the defect mode line may be related to the positively charged trion excited hole states, where two holes occupy both the heavy-hole and the light-hole-like states.

The identification of the lines is further clarified in (b) presenting the vertically V- & horizontally H-polarized intensity spectra and (c) the corresponding DOLP versus photon energy at $P_{\text{exc.}} \approx 3 \mu\text{W}$. These show the clear distinction in linewidths between cavity mode and QD lines, and the large DOLP of ~ 0.75 of the defect mode $\#0_M^{(0)}$. Owing to the high in-plane symmetry of the pyramidal structures, bare QDs transitions are not expected to favour more the V or H linear polarization [250], [271] in a homogeneous bulk medium. However, here the QD transitions are already co-polarized with the cavity modes, with values of the DOLP between ~ 0.25 and ~ 0.75 . At $\sim 1.273\text{eV}$, the feature with a negative DOLP corresponds to the blue spot in Fig. 3:16 (c', d') mentioned earlier.

The identification of the X-2X couple can be further established by a very specific DOLP pattern due to the H, V fine structure splitting [220]. In the particular case here, there are four spectral features: X^V , X^H and then $2X^H$, $2X^V$ with an FSS $\approx 50\mu\text{eV}$ s here. Typically, they generate a W-like signature in the DOLP, but if the X and 2X are close enough in energy, the double dip merges into a single dip, giving this characteristic V shape seen in (b).

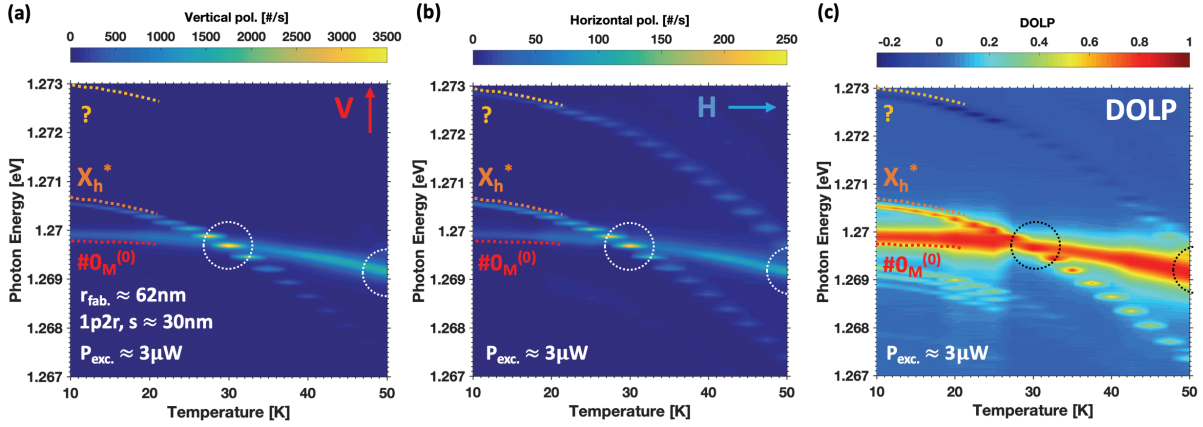


Fig. 3:18 – Temperature tuning of an excited hole state X_h^* and V polarized defect mode $\#0_M^{(0)}$ identified in Fig. 3:17. Intensity spectra slices stitched together versus temperature: (a) V polarization component, (b) H polarization component, and (c) associated DOLP. Dotted lines: Part quadratic red-shifting trajectories related to bandgap variation. Dotted circles highlight resonances of the X_h^* and another unidentified QD line with the same cavity mode. Above barrier excitation, laser wavelength $\lambda_{\text{exc.}} \approx 730\text{nm}$, excitation power $P_{\text{exc.}} \approx 3\mu\text{W}$. Excitation scheme similar to Fig. 3:16(d). Radius $r_{\text{fab.}} \approx 62\text{nm}$, $1p2r$, $s \approx 30\text{nm}$.

The X_h^* line is already strongly co-polarized with the defect mode $\#0_M^{(0)}$ at $T=10\text{K}$, an irrefutable signature of weak coupling [180]. The temperature tuning displayed in **Fig. 3:18**, with $3\mu\text{W}$ above barrier excitation, shows how the X_h^* and another non-labelled QD line are brought into resonance with this mode. **(a)** The V- and the **(b)** H-polarized intensity maps look similar; note, however, a factor of ~ 14 between the two intensity color scales. Part **(c)** combines the two previous graphs to plot the DOLP map, which is saturated at -0.2 for better visualization of the effect. The graphs were realized by stitching spectra taken at regular intervals of 2.5K and surface interpolation is applied to display smooth continuous maps. The QD lines trajectories appear discretized, which is a numerical artifact of the interpolation technique having difficulties in connecting the data points of the fast-varying quasi-quadratic variation. This issue can be dealt by increasing the number of sampling points with finer temperature steps. The trajectories of the X_h^* and defect mode are identifiable with their different quasi-quadratic redshift of the energy as a function temperature [181]. The variation of a QD spectral line is rather large over the temperature range $T \approx 10\text{K}$ to 50K , approximately $\sim 3.5\text{meV}$. This variation is due to the change of the semiconductor bandgaps of $\text{In}_x\text{Ga}_{1-x}\text{As}$ and GaAs materials [272]. The mode energy variation, on the other hand, is explained by the temperature dependence of the effective refractive index [236]; for GaAs , $dn/dT \sim 2.67 \cdot 10^{-4}\text{K}^{-1}$ at $\sim 850\text{nm}$ [273]. For the range $10\text{-}50\text{K}$, this amounts to a mode energy change of $\sim 0.5\text{meV}$. Thanks to this discrepancy in energy shift rates and the initial blueshift of the X_h^* by $\sim 0.6\text{meV}$ with respect to the cavity mode energy, the two trajectories coincide at a temperature of $T \approx 30\text{K}$. On resonance, a strong increase in intensity is observed as a manifestation of the Purcell effect. Departing from the resonance, the X_h^* spectral line loses its co-polarization to the cavity mode while the other spectral line, originally H-polarized and corresponding to the blue spot identified before in Fig. 3:16(c,d), strongly co-polarizes with the mode $\#0_M^{(0)}$ as it approaches resonance.

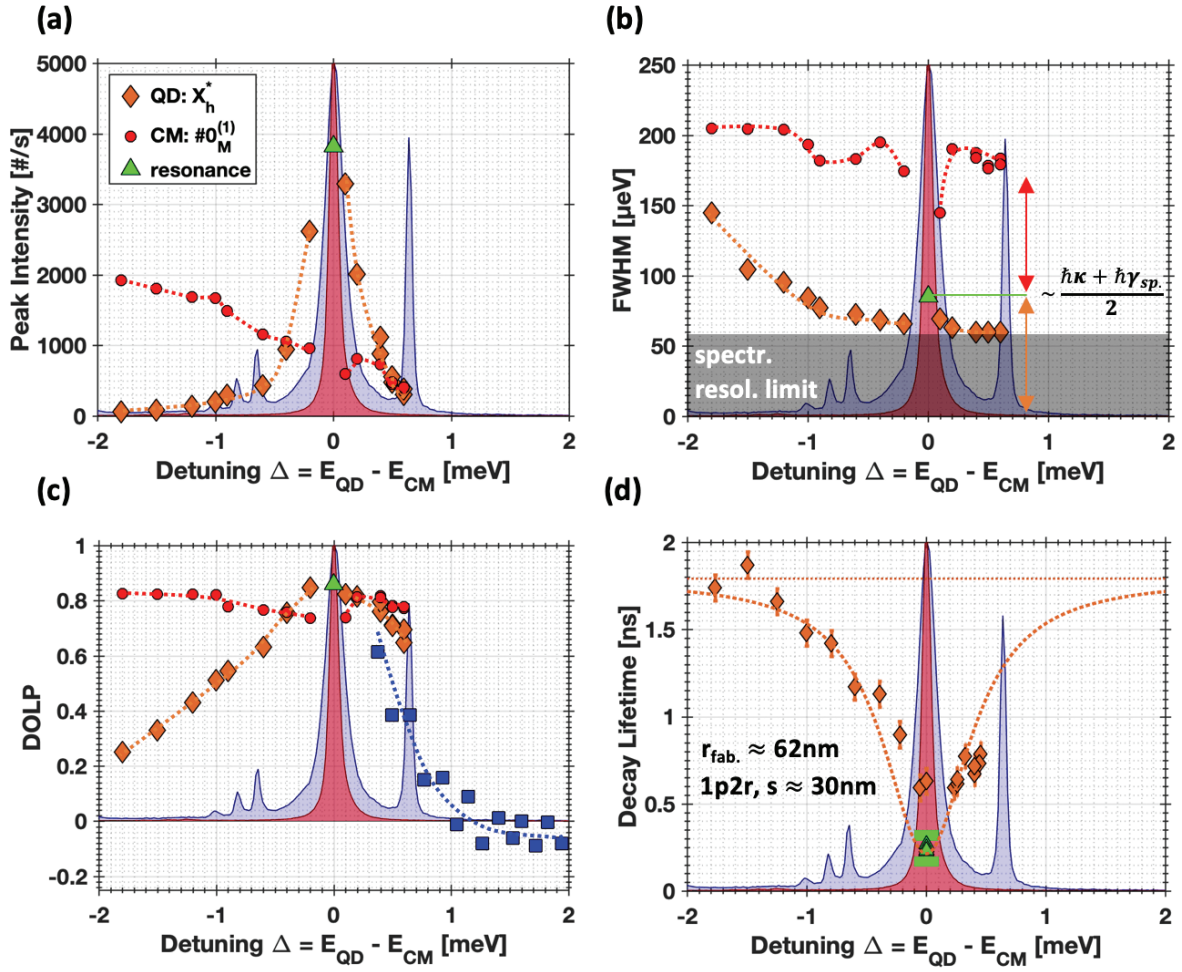


Fig. 3:19 – In-depth analysis of the coupling of a single QD to the V-polarized defect mode $\#0_M^{(0)}$. From the vertical polarized spectra using Lorentzian fits: (a) peak intensity, (b) full-width at half maximum; from both H & V polarized spectra: (c) degree of linear polarization, all versus detuning from cavity mode. Blue squares: unidentified QD transition. From time-resolved measurements: (d) decay lifetimes. Numerical parameters for the Purcell fit: $\hbar\kappa = 185\mu\text{eV}$, $\hbar\gamma_{QD} = 60\mu\text{eV}$. The blue shaded area is the initial normalized spectrum of the cavity mode (center) and the detuned QD line off resonance at $T \approx 10\text{K}$; the red shaded area shows the situation on resonance at $T \approx 30\text{K}$. Above barrier excitation, laser wavelength $\lambda_{\text{exc.}} = 730\text{nm}$, excitation power $P_{\text{exc.}} \approx 3\mu\text{W}$. Radius $r_{\text{fab.}} \approx 61\text{nm}$, $1p2r, s \approx 30\text{nm}$.

Fig. 3:19 plots several parameters as a function of the detuning with respect to the cavity mode energy to reveal in detail the characteristics of the weak coupling. Intensities (a) and FWHM of the X_h^* and cavity mode lines in (b) were obtained by the fit of the sum of two Lorentzians of the V-polarized spectra of Fig. 3:18. The DOLP in (c) was extracted from Fig. 3:18(c). The green triangle symbols correspond to the data points estimated from the spectral line shape, where both spectral lines are superimposed on resonance. Lifetime decays in (d) were obtained as per the methodology described in chapter 2. The dotted lines in (a-c) are visual guides for reading the trends. In (d), the orange dotted lines are associated with the physical interaction model of (Eq. A:1). The blue shaded area is the initial normalized spectrum at $T \approx 10\text{K}$ while the red shaded area corresponds to the normalized resonant spectrum at $T \approx 30\text{K}$.

The Purcell effect produces the important increase in intensity of the X_h^* occurring for near-zero detuning; the merged QD-CM displays a ~ 12 -fold increase as compared to the initially detuned exciton line. Along with it, comes a narrowing of the linewidth of the superposed spectral lines on resonance, as compared to the bare cavity mode, or accordingly, a broadening as compared to the bare QD transition. At zero detuning, the FWHM of the overlapping line is estimated to be $\sim 85\mu\text{eV}$, a noticeable discrepancy with the average of $\sim 123\mu\text{eV}$ computed from

the bare QD $\hbar\gamma_{QD} \approx 60\mu\text{eV}$ (spectrometer resolution limit), and the bare defect mode of $\hbar\kappa \approx 185\mu\text{eV}$ at large positive detuning. This suggests a narrower QD linewidth non-resolvable by the PL setup. At further negative detuning the X_h^* intensity vanishes due to thermally activated processes that can dissociate bound excitons [117]. On the contrary, at negative detuning, the cavity mode experiences a steady increase in intensity possibly due to the other non-identified QD line initially blue-shifted and progressively entering into resonance. The intensity and FWHM versus detuning (i.e. temperature) behaviors are comparable to the data shown in past reports with pyramidal site-controlled QDs weakly coupled to L_n PhC cavities [180], [181], [219]–[222].

The DOLP curve of the CM shown in (c) is almost flat with a value of 0.8, but slightly degrades to 0.75 on resonance. The X_h^* line shows a clear sign of V co-polarization with the CM when approaching resonance and depolarization with a steady decrease to eventually ~ 0.25 when moving away from resonance, at negative detuning. The second, non-labelled QD spectral line (blue squares) also shows a clear sign of V co-polarization with the CM when approaching resonance. This trend connects rather well with that of X_h^* to overall form the asymmetric S shape and DOLP switching phenomenon mentioned earlier and previously observed by statistical dispersion of detunings for pyramidal site-controlled QDs in PhC cavities [219]–[222]. The range of influence of this co-polarization effect is quite extended, over $\sim 2\text{--}3\text{meV}$ s, approximately $\sim 10\text{--}15$ times larger than the cavity linewidth.

In (d), the decay lifetimes were extracted with the fitting procedure referenced in chapter 2, section 2.3.3. The lifetimes of the X_h^* visibly decrease from an initial value of $\sim 0.78\text{ns}$ at $\Delta \approx +0.5\text{meV}$ down to $\sim 230\text{ps}$ on resonance $\Delta=0$. Past resonance, they increase to an estimated value of $\sim 1.74\text{--}1.87\text{ns}$ at large negative detuning. The fit displayed on the graph is based on equation (Eq. A:1), omitting the phonon modification factor $\chi(\Delta, T)$ and assuming $\tau_{leak} = \tau_{sp.}^{homog.}$, to keep three fitting parameters: $\tau_{sp.}^{homog.}$, F_p^{max} and ζ^2 . For this particular QD sample, the average lifetimes $\tau_{sp.}^{homog.}$ of the various transitions of isolated QDs before PhC fabrication were not measured as was done for other pyramidal QDs [220]. The fit returns $\tau_{sp.}^{homog.} \approx 1.79 \pm 0.08\text{ns}$, $F_p^{max} \approx 28$ and misalignment factor $\zeta^2 \approx 0.44$, eventually yielding an effective Purcell enhancement factor of $Enh. \approx 8.5 \pm 2.7$ (Eq. A:2), which is reasonably consistent with the ~ 12 -fold increase in intensity observed before. A more elaborate and accurate model will account for the phonon effects, which adds a temperature dependent profile [178], [274]. With only the enhancement factor $Enh.$ known (Eq. A:4), a minimum beta factor $\beta^{cav.} \approx 0.87 \pm 0.04$ coupling efficiency can be estimated, comparable with the data of Table. 1:1 in chapter 1. The lifetime $\tau_{sp.}^{homog.} \sim 1.8\text{ns}$ indicates a natural Fourier-transform limited linewidth of $\hbar\gamma_{sp.} \approx h/(2\tau_{sp.}^{homog.}) \approx 1\mu\text{eV}$, yielding an average of $\sim 93\mu\text{eV}$ with the cavity mode, in better agreement with the FWHM estimated on resonance.

Evaluated solely on the basis of coupling a single QD to the fundamental mode, the $L_{n=3}$ and Defect-Potential cavity are quite similar [194], [196]. Indeed, the fundamental mode of an optimized $L_{n=3}$ has an effective mode volume of $\sim 1.0(\lambda_0/n)^3$ [161] while the defect-mode of $\#0_{M(0)}$ effective mode volume is largely design-sensitive, effective mode volumes of $\sim 1.3(\lambda_0/n)^3$ [254], $\sim 1.7(\lambda_0/n)^3$ [259] up to $\sim 2.2(\lambda_0/n)^3$ [256] have been reported. At similar photon energies, our GaAs $L_{n=3}$ cavities present comparable Q factors between 3'000–9'000 ($\hbar\kappa$ between $\sim 140\text{--}430\mu\text{eV}$) [162]. Since F_p^{max} is proportional to $Q/V_{eff.}^{mode}$, and by extension the effective enhancement ratio $Enh.$, it is thus not surprising that the effective enhancement ratio extracted here is comparable to the values reported in [194], [221] and in Table 1:1. $L_{n=3}$ cavities fabricated in GaAs supporting larger Qs at longer wavelengths, of $\sim 24'000$ (at 1.258eV), $\sim 17'000$ (1.252eV), and $\sim 16'000$ (1.269eV) for the fundamental mode have been reported [134]. Single self-assembled QDs were strongly coupled with these cavity modes, with estimated coupling constants $\hbar g \approx 45\mu\text{eV}$, $69\mu\text{eV}$ and $109\mu\text{eV}$, respectively. The potential for achieving still higher values of Q-factors for optimized GaAs defect potential cavities has been reported in [258], where a defect mode with $Q \approx 55'000$ at 1.32eV was demonstrated, with strong coupling to a self-assembled QD with estimated $\hbar g \approx 51\mu\text{eV}$ coupling constant. Such optimized defect potential designs are also relevant for the study discussed here.

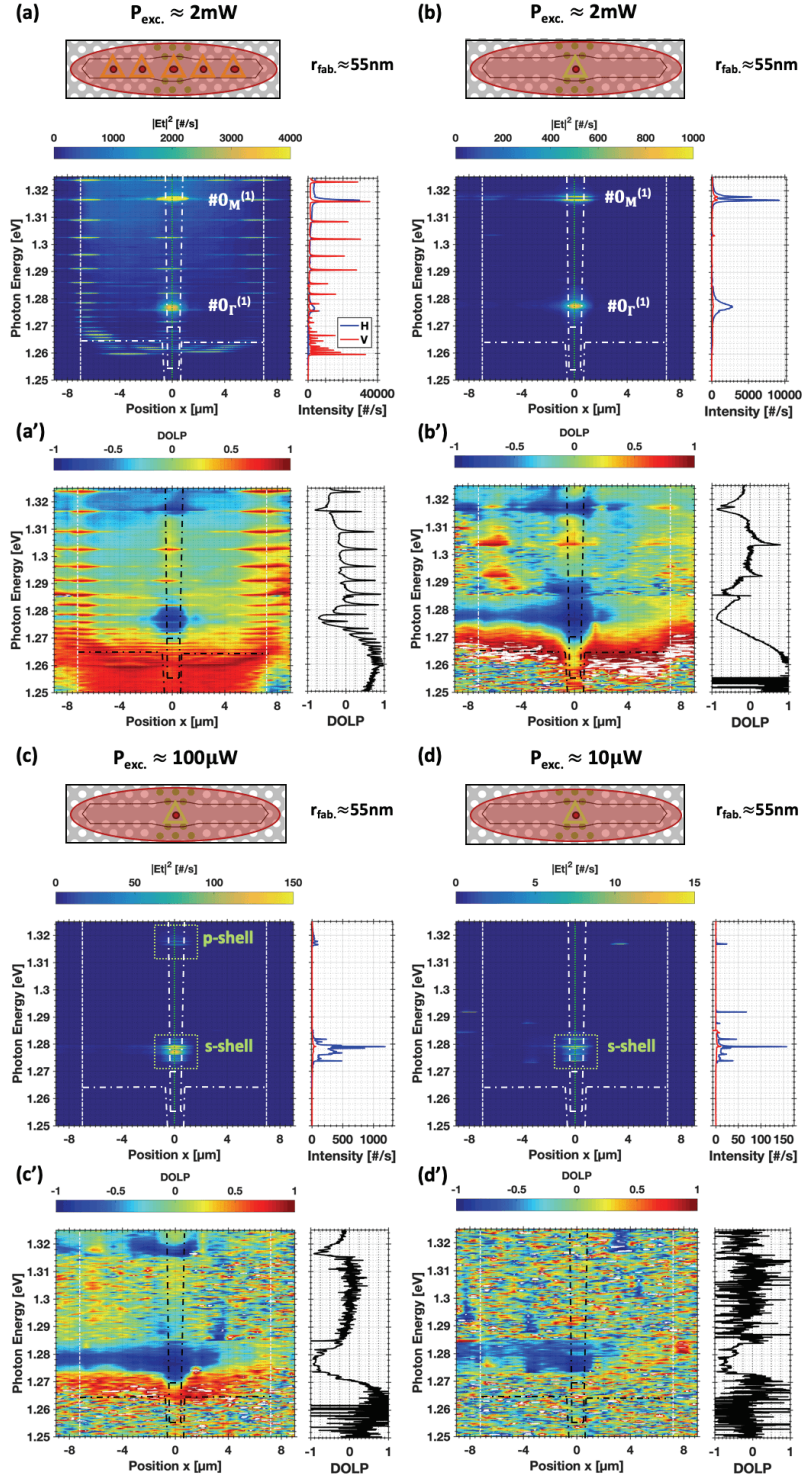
3.4.3 Selective excitation of the H-polarized $\#0_{\Gamma}^{(1)}$ defect mode

Fig. 3:20 – Selective excitation of defect-potential modes using a single site-controlled QD. Upper panels: schematics illustration of the cavity-QD system and excitation scheme. (a) energy-position plot of optical modes patterns and (a') DOLP for $P_{\text{exc.}} \approx 2\text{mW}$ on a reference structure: radius $r_{\text{fab.}} \approx 55\text{nm}$, $1p2r$, $s \approx 30\text{nm}$. Energy-position plots of optical modes patterns and DOLP for (b,b') $P_{\text{exc.}} \approx 2\text{mW}$, (c,c') $P_{\text{exc.}} \approx 100\mu\text{W}$ and (d,d') $P_{\text{exc.}} \approx 10\mu\text{W}$. Spectra and DOLP integrated across x shown on the sides. Vertical white dash-dot lines mark the extremities of the cavity. The vertical green dot line marks the positions of the single QD. Above barrier excitation, laser wavelength $\lambda_{\text{exc.}} \approx 730\text{nm}$. Temperature $T \approx 10\text{K}$. Radius $r_{\text{fab.}} \approx 55\text{nm}$, $1p2r$, $s \approx 30\text{nm}$.

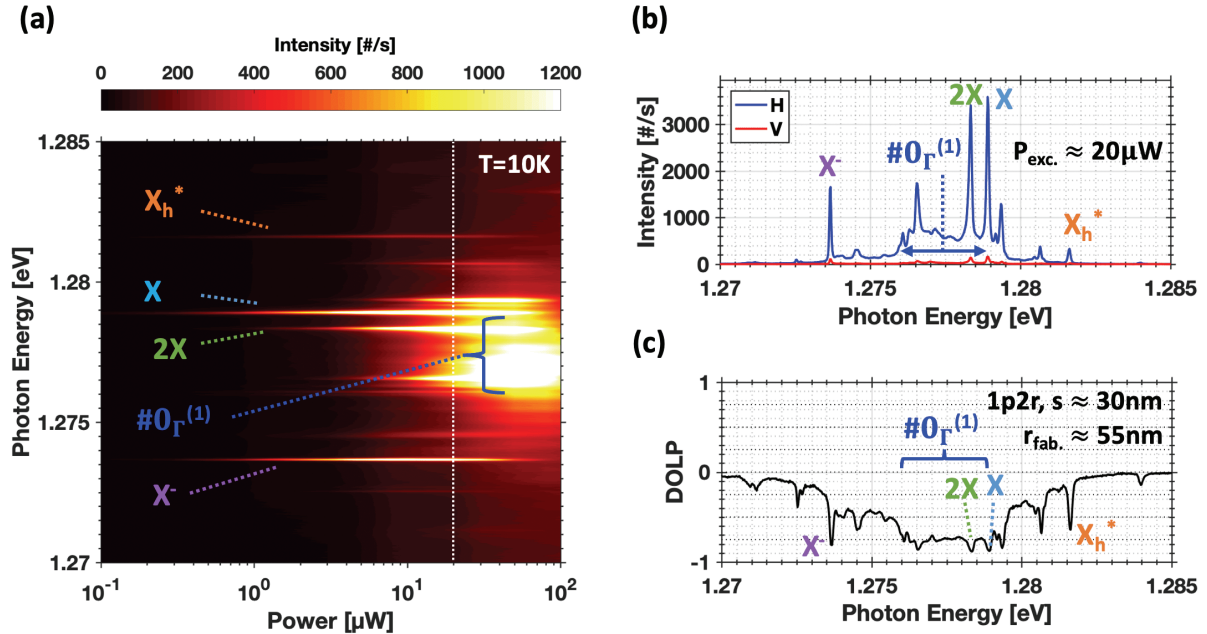
3.4.4 Weak coupling of a site-controlled QD with the H-polarized $\#0_{\Gamma}^{(1)}$ defect mode


Fig. 3:21 – Identification of spectral lines in a defect-potential PhC cavity with a single embedded site-controlled QD. (a) Intensity spectra slices stitched together versus the incident excitation power. Identified cavity mode line and QD lines are indicated and labelled. The data corresponding to the white dot line, at $P_{exc.} \approx 20 \mu W$, is shown in (b): intensity spectrum in both H & V polarizations, and (c): corresponding extracted DOLP. Temperature $T \approx 10K$. Above barrier excitation, laser wavelength $\lambda_{exc.} \approx 730nm$. Excitation scheme similar to Fig. 3:20(c) with spot shape. Radius $r_{fab.} \approx 55nm$, $1p2r, s \approx 30nm$.

The power-depended spectra of the structure of Fig. 3:20 are displayed in **Fig. 3:21(a)**, with the identification of several QD lines and defect mode $\#0_{\Gamma}^{(1)}$ ($\hbar\kappa \approx 2700 \mu eV$). Qualitatively, the configuration of the QD transitions is fairly similar to the one observed for the structure of Fig. 3:20. The lines appearing first at the lowest excitation powers are again recognized as the negative trion X^- , the neutral exciton X and the excited hole state X_h^* . The trion X^- is bound to the X by $\sim 5.2meV$ s while the X_h^* is blue shifted with respect to the X by $\sim 2.7meV$ s. The biexciton $2X$ appears at higher power and, in this case, it is bound to the X by $E_{2X,X}^{bind} \approx -0.5meV$.

Part **(b)** shows the V-polarized and H-polarized spectra measured at $P_{exc.} \approx 20 \mu W$; a higher power is required to excite unambiguously the cavity mode $\#0_{\Gamma}^{(1)}$. Nevertheless, its presence at the indicated energy range is represented by the strong negative DOLP background, as evidenced in part **(c)**. Clearly, the excitonic transitions exhibit negative-DOLP peaks superimposed on the DOLP feature of the cavity mode. This co-polarization is an evidence of the weak coupling.

The temperature tuning study, performed during above barrier spot excitation at $20 \mu W$ and reported by the maps in **Fig. 3:22**, shows the effect of the resonance between the QD lines with **(a)** a V-polarized and **(b)** two H-polarized modes, as well **(c)** the corresponding DOLP map for the system of Fig. 3:20. This time there is a factor of ~ 15 between the intensity scales of (a) and (b), but the color scale of (b) is saturated to facilitate the readability. The DOLP map is saturated by displaying only negative values for visualization purposes. Part (a) reveals the presence of two additional narrowband cavity fast-light modes from the 1st band, at $\sim 1.277eV$ and $\sim 1.283eV$, that could not be noticed before in Fig. 3:21(a). The first mode was hidden by the overwhelming brightness of the defect-mode $\#0_{\Gamma}^{(1)}$ with which it is superposed, but it can now be revealed thanks to the polarizer. This first mode is possibly hybridized, it is supposed to be a V-polarized mode but from the action of the defect mode, its DOLP is brought down to a net negative. The second mode was missed because it is not fed efficiently due to a lack of nearby spectrally overlapping QD transitions, but it does appear very faintly in Fig. 3:21(a) and it is clearly V-polarized as seen from (c). The crossing points of these modes with QD lines are specified by the white dot circles.

In the case of the upper mode, a clear increase of intensity is noticed when X_n^* enters in resonance with it, a signature of a Purcell enhancement. To interact with these two V-polarized fast-light modes via the E_y component of the electric field, these two modes must be of even symmetry in x , i.e. $\Pi_x = +1$. From part (b), only the effect of defect mode $\#0_{\Gamma(1)}$ can be noticed. This mode is crossed by the 2X-X couple of spectral lines, but the enhancement of the intensity is difficult to assess quantitatively here. This is understandable since $Enh.$ is related to $F_P^{max} \propto Q/V_{eff}^{mode}$, despite a spatial confinement comparable or smaller to that of $\#0_M^{(0)}$ that could ensure a large $g \propto 1/\sqrt{V_{eff}^{mode}}$, the quality factor is very low $Q \approx 500$ (cavity linewidth $\hbar\kappa \approx 2700\mu\text{eV}$) since the components of the defect mode intercept a large part of the light cone. This value is in fact $\sim(1/14)^{\text{th}}$ of the Q of mode $\#0_M^{(0)}$ in section 3.4.1 which provided a ~ 12 -fold enhancement of the intensity, so overall $Enh. \approx 1$ is likely. From (c), the ~ 7 -10 meVs extent of the H co-polarization effect of the many QD lines by defect mode $\#0_{\Gamma(1)}$ is clear.

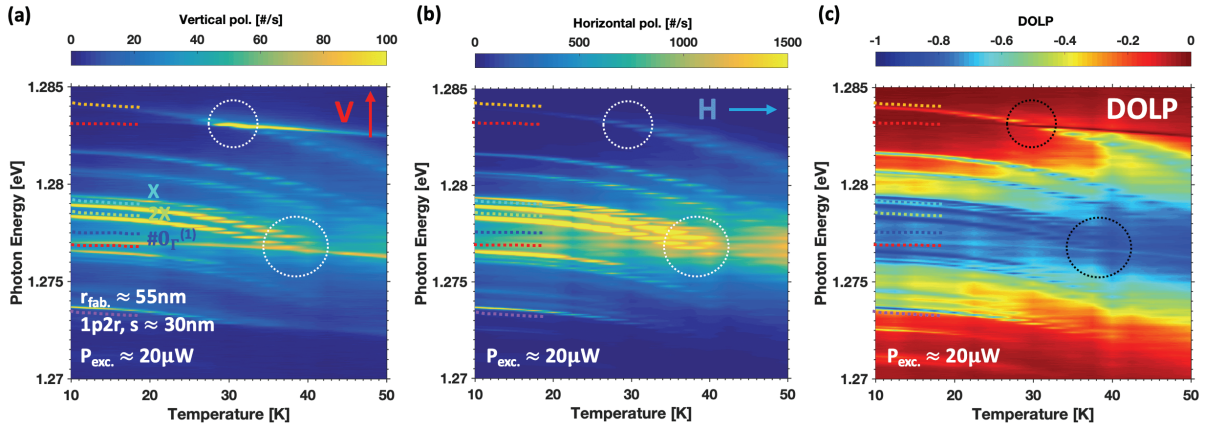


Fig. 3:22 – Temperature tuning of several spectral lines of excitons and H-polarized mode $\#0_{\Gamma(1)}$ identified in Fig. 3:21. Intensity spectra slices stitched together as a function of the temperature: (a) V-polarization component, (b) H-polarization component, and (c) associated DOLP. Part of the quadratic trajectories related to spectral line shifts are displayed in dotted lines. Two more extended cavity mode lines of the 1st band are revealed. Dotted circles highlight resonances of QD lines with cavity modes. Above barrier excitation, laser wavelength $\lambda_{exc.} \approx 730\text{nm}$, excitation power $P_{exc.} \approx 20\mu\text{W}$. Excitation scheme similar to Fig. 3:20(c) with spot shape. Radius $r_{fab.} \approx 55\text{nm}$, $1p2r$, $s \approx 30\text{nm}$.

The very low Q and large range of influence of the $\#0_{\Gamma(1)}$ defect mode prevents the proper study of a single QD transition coupling to the single defect mode, as done for the structure of Fig. 3:16. Mode $\#0_M^{(1)}$ is also an interesting object of study, but the available fabricated holes radii cannot enable a resonance with a QD s-shell transitions.

3.5 Conclusion of chapter and perspectives

This chapter presented a study of a photonic heterostructure: the defect-potential PhC cavity, consisting of a deterministic defect made by shifting a few selected holes in an $L_{n=61}$ cavity. The study combined numerical modelling of the optical modes and the analysis of the optical properties of fabricated structures. Experimental observation of the optical modes was accomplished using site-controlled pyramidal QDs embedded in the PhC structures and spatially-resolved optical spectroscopy of the photoluminescence.

The optical modes in these structures can be separated into two classes: V-polarized modes and H-polarized modes originating, respectively, from the first and second discretized waveguide bands. In each situation, the optical modes are further subdivided in two groups: modes locally confined by the defect-potential below each original band-edge, and modes fully extended across the cavity above these band-edges. By analogy to a quantum well, the number of trapped photonic modes is related to the width and depth of the defect-potential controlled by structural parameters, here implemented by transverse hole shifts. The confined defect modes bound to the 2nd band co-exist in energy among the quasi-continuum fast-light modes of the 1st band to which they are orthogonal in perfect, disorder-free structures. However, we showed that disorder effects can induce hybridization of these defect modes with nearby extended modes by inter-band coupling, resulting in the delocalization of the defect modes with a peculiar and traceable polarization signature.

Indeed, the essential features of the mode structure were observed with selective excitation from spectrally overlapping QD transitions. The fundamental defect mode displays design-sensitive, promising high Q values up to 9'300 at $\sim 1.26\text{-}1.27\text{eV}$, that may be further increased by optimizing the defect configuration, and a spatial extent (i.e. mode volume) practically on par with $L_{n=3,5}$ PhC cavities, ideal for coupling to a single QD. In fact, the deterministic weak coupling of the excited hole state X_h^* transition of a single pyramidal site-controlled QD with the fundamental defect mode of the 1st band with a high $Q \approx 6'900$ ($\hbar\kappa \approx 185\mu\text{eV}$) was demonstrated, with the help of temperature tuning. Characterization of the weak coupling involved a variety of clear resonant detuning-dependent signatures: intensity increase, linewidth decrease, co-polarization, and decay time reduction of the QD emission. An effective Purcell enhancement ratio of the spontaneous emission rate of $Enh. \approx 8.5 \pm 2.7$ as well as coupling efficiency of at least $\beta^{cav.} \approx 0.87 \pm 0.04$ were extracted.

These types of photonic heterostructures can lead to novel functional elements, beyond conventional coupled PhC cavities and PhC waveguides, supporting simultaneously cavity-like parts for local interaction with precisely positioned QDs and waveguide-like components for efficient connectivity between them. A deeper understanding may turn the disorder-enabled hybridization effect into a deterministic effect. In this way, highly symmetric QDs supplying single photons with both orthogonal in-plane polarization states could be polarization-coupled to such hybrid delocalized states for propagation, useful for QIP applications.

Chapter 4 Tilted-potential photonic crystal cavity

Based on the knowledge acquired with the study of the defect-potential cavity, a more elaborate tailored-potential photonic crystal structure is presented, as a suitable candidate cavity for the need of a robust single-photon injector for future realization of quantum integrated circuits. The tilted-potential device supports photonic wave-functions with a main lobe, where the electric field is strongest, attached to an extended tail that ensures connectivity of the extracted photons. With a correlation between main peak position of the electric field and mode energy, these modes are optimal for simultaneous local extraction and in-plane transmission to remote locations of single photons from wavelength-multiplexed, site-controlled quantum dots.

In **section 4.1**, the concept is introduced and explained qualitatively and intuitively. **Section 4.2** goes through the numerically assisted design and preliminary study of these cavities. Effects of the limitations of state-of-the-art technology due to fabrication errors are also considered. **Section 4.3** is devoted to the demonstration of fabricated structures. Their optical modes structure and properties are then experimentally characterized in **section 4.4** by micro-photoluminescence techniques using QDs arrays as internal light sources. **Section 4.5** is dedicated to the coupling of single QDs to selected modes of a tilted-potential cavity, towards the goal of on-chip single photon injection. The chapter ends with discussion of perspectives of the application of such cavities.

4.1 Tilted-potential photonic crystal cavity: concept

In this section we introduce the concept of the Tilted-Potential PhC Cavity, basically a triangular potential well for photons, and show how it emerges from the combination of the Defect-Potential structures studied in chapter 3.

4.1.1 From defect-potential to tilted-potential PhC cavities

Fig. 4:1 shows qualitatively what to expect when combining several defect-potential sections of increasing depths to generate a staircase-potential. We start conceptually with an L_n cavity, along an x axis. In **(a)**, a defect-potential cavity is produced at the left end by shifting several holes by an amount s_B and supports at least one confined photonic mode, depicted in blue. In **(b)** and **(c)**, the same is done to generate cavities at the center and right side of a L_n cavity, with $s_R > s_G > s_B$. The in-line combination of the three defects **(a-c)** is expected to lead to the scenario depicted in **(d)**: the three sub-cavities are coupled continuously and cover the full length of the parent L_n cavity. The three defect-potentials thus add up to a staircase-potential profile. The three “defect” eigen wavefunctions evolve to generate the new extended wavefunctions of the hybrid structure with modified eigen-energies. Based on the eigen-energies and potential profile, it is expected that the new wavefunctions will exhibit a main lobe originating from the corresponding defect cavity, and tails extending throughout the L_n base cavity. This form suits efficient coupling of the emission of a properly positioned QD, as further discussed below.

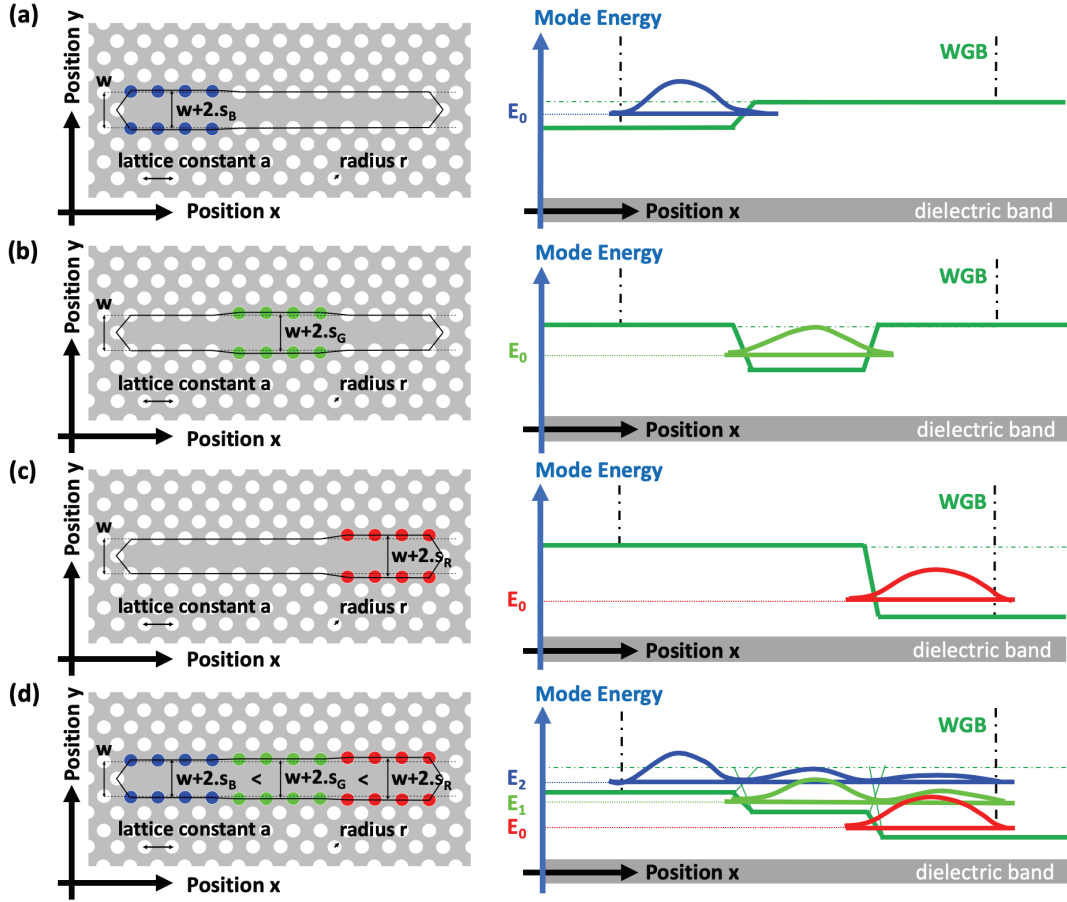


Fig. 4:1 – Schematics depicting the formation of a staircase-potential cavity by the combination of an arbitrary number (here 3) of defect-potential cavities (see details in chapter 3). Left: top views showing side-shifted holes in a long $L \times w$ cavity; right: corresponding energy-potential wells and confined wavefunctions. (a), (b) and (c) show single defects of increasing depth; (d) shows the staircase potential formed by combining the three.

4.1.2 Analytic solutions

The stitching of a large number of defect potentials as in Fig. 4:1 can be approximated as a photonic cavity of triangular effective index profile (referred to here as a tilted-potential cavity). Insight into its eigenstates can be gained by recalling the analogous problem of electrons in a triangular potential well [275], [276]. Such wells can be obtained, for example, by applying an electric field on a free electron. The 1D stationary Schrödinger equation applied to such a case is:

$$\frac{\partial^2}{\partial x^2} \psi(x) - \left[\frac{2m}{\hbar^2} (-e\mathcal{E}x - E) \right] \psi(x) = 0, \quad (\text{Eq. 4:1})$$

where m is the mass of the electron, $-e$ its charge, \mathcal{E} the external electric field, ψ the wavefunction and E its energy. The solutions to this problem can be expressed using Airy functions of the first kind,

$$Ai(\bar{x}) = \frac{1}{\pi} \int_0^{+\infty} \cos \left(\frac{t^3}{3} + \bar{x} \cdot t \right) dt, \quad (\text{Eq. 4:2})$$

yielding [277] the wavefunctions ψ as

$$\psi(x) = A \cdot Ai \left[\left(\frac{2m}{\hbar^2 e^2 \mathcal{E}^2} \right)^{\frac{1}{3}} \cdot (-e\mathcal{E}x - E_n) \right], \quad (\text{Eq. 4:3})$$

with eigen energies E_n :

$$E_n \approx \left(\frac{\hbar^2}{2m}\right)^{\frac{1}{3}} \left(\frac{3\pi(-e)\varepsilon}{2} \left(n - \frac{1}{4}\right)\right)^{\frac{2}{3}}. \quad (\text{Eq. 4:4})$$

To illustrate the analogous problem for photons, let us now consider a graded dielectric medium, for instance a doped glass plate of thickness L_x along x and infinite dimensions in both y and z . For simplicity, we assume it is enclosed by two metallic coatings in $x = 0$ and $x = L$. The doped glass is characterized by a linearly increasing dielectric “constant” $\varepsilon_r(x, y, z) \approx \varepsilon_r(x)$. We consider a plane wave with electric field $\mathbf{E} = (0, E_y, 0)$ polarized along y and propagating along z , launched into the slab with a wavevector $\mathbf{k} = (k_x, k_y, k_z)$. The field will bounce back and forth between the metallic plates, gaining a phase flip of π each time it is reflected. The Master equation (Eq. 1:10) gives:

$$\nabla \cdot (\nabla \times \mathbf{E}(\mathbf{r})) = \left(\frac{\omega}{c}\right)^2 \cdot \varepsilon_r(\mathbf{r}) \cdot \mathbf{E}(\mathbf{r}), \mathbf{r} = (x, y, z) \quad (\text{Eq. 4:5})$$

The refractive index ($n^2 = \varepsilon_r$) gradient is defined by

$$n(x) = n_0 + (n_{L_x} - n_0) \cdot \frac{x}{L_x}, \text{ for } 0 \leq x \leq L_x \quad (\text{Eq. 4:6})$$

Focusing on component E_y , the problem eventually translates into the wave equation

$$\frac{\partial^2}{\partial x^2} E_y(x) - \left[\beta^2 - \left(\frac{\omega}{c}\right)^2 \left(1 + 2 \cdot \frac{(n_{L_x} - n_0)}{n_0} \cdot \frac{x}{L_x}\right) \right] E_y(x) = 0, \quad (\text{Eq. 4:7})$$

which is similar to (Eq. 4:1). By analogy, E_y follows an Airy function spatial distribution:

$$E_y(x) = E_0 \cdot \text{Ai} \left[\beta^2 - \left(\frac{\left(\frac{\omega}{c}\right)^2}{\left(2 \cdot \frac{(n_{L_x} - n_0)}{n_0} \cdot \frac{1}{L_x}\right)^2} \right)^{\frac{1}{3}} \cdot \left(1 + 2 \cdot \frac{(n_{L_x} - n_0)}{n_0} \cdot \frac{x}{L_x}\right) \right] + K, \text{ for } 0 \leq x \leq L \quad (\text{Eq. 4:8})$$

In the case of the PhC cavities as of Fig. 4:1 (d), , the photonic wavefunctions consist of products of Bloch terms and envelope functions. The graded average effective index of such cavities would then support Airy functions, as further detailed below.

4.1.3 Structure parameters

An implementation of the tilted-potential cavity in a PhC membrane structure is depicted in **Fig. 4:2**. A regular PhC w1 waveguide is terminated into a L_n cavity by the addition of two reflective boundaries, it is then altered by linearly shifting side-holes from one extremity to another towards the exterior, symmetrically along y , which breaks the symmetry along x . The width of the cavity as a function of position x is defined as $w(x) = w + 2 \cdot s(x) = w \left(1 + 2 \cdot \frac{s(x)}{w}\right)$ with $s = 0$ for the first hole to the maximum value $s = s_{\max}$ for the last one.

Due to the adiabatic widening, a whole PhC waveguide band will appear to shift down linearly in mode energy. As a consequence, the confined modes of the cavity will redshift and their spatial distributions will be reshaped to conform to the triangular photonic confinement potential. Modes at high enough energy (E' in blue), above the band-edge of the virtual w1 waveguide are little perturbed and extend fully across the cavity. On the other hand, modes in the vicinity of the tilted band-edge (energy E in red) feel the perturbation more strongly and will exhibit a correlated mode energy-position dispersion. These modes will be referred to as Airy-Bloch modes and are the main subject of interest for this chapter. As was the case for the defect-potential, we expect this scheme to repeat for each band of optical modes of the PhC structure, and for both TE (E_x, E_y, H_z) & TM (H_x, H_y, E_z) modes.

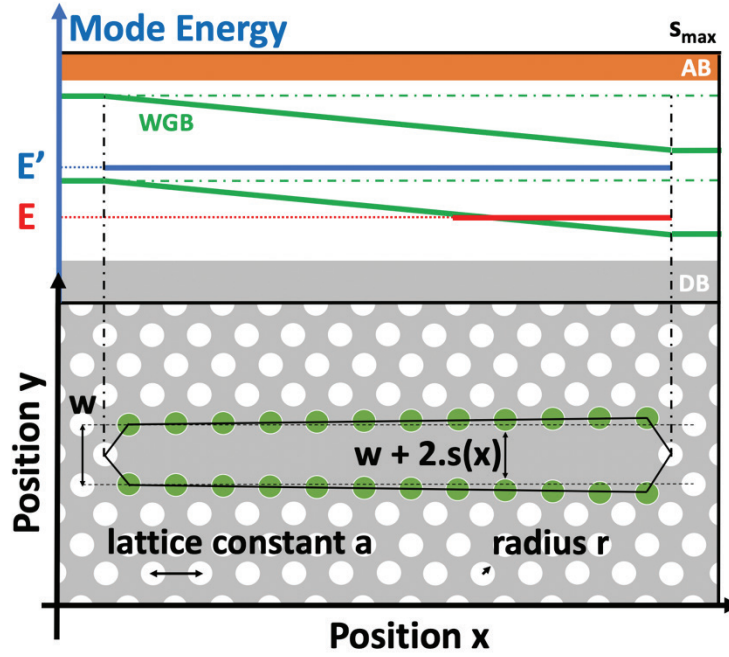


Fig. 4:2 – Schematic illustration of the tilted-potential cavity and its effective implementation. (Bottom) Top view of a tilted-potential PhC cavity; the sides holes highlighted in green are linearly shifted outwards along y , starting from the left end, increasingly from $s = 0$ to $s = s_{\max}$. (Top) Diagrams of the waveguide band energy variation along position x resulting from the shifts in the transverse direction y ; the terminations of the cavity define boundaries of the photonic potential. In red, one of the cavity modes confined by the tilted-potential, which are the focus in this chapter. In blue, a cavity mode above the band-edge of the virtual w_1 waveguide.

4.2 Tilted-potential photonic crystal cavity: computed mode structure

In this section, we implement and study numerically the properties of the Tilted-Potential cavity implemented in a slab PhC cavity using 2D FDM modeling. We go through the optical modes structure, examine its sensitivity to variations of core parameters, and report the impact of actual fabrication disorder on hole sizes and positions in view of making a realistic device.

4.2.1 Optical mode structure

The optical mode structure was simulated with the same methodology as in Chapter 3. The base structure is a $L_{n=61}$ cavity, and the gradient of the potential was implemented in two ways. For the first geometry, the hole centers are shifted linearly from 0 at the first hole to s_{\max} at the last one; the shifts can thus be fractions of nanometer. The second geometry takes into account a real fabrication limitation: the minimum position accuracy of 1nm imposed by the EBL machine we used. This geometry corresponds to the design of the real fabricated structures presented further below. It was used to simulate structures with $s_{\max} = 10, 15, 20, 25$ & 30nm, with uniform shifts at several segments of the cavity. For $s_{\max} = 10$ nm, the staggered steps consist in two non-shifted holes and ten groups of six holes shifted respectively by 1, 2, 3, ... up to 10nm. For $s_{\max} = 15$ nm, we set four non-shifted holes, fourteen groups of four holes shifted respectively by 1, 2, 3, ... up to 14nm and the last two holes shifted by 15nm. For $s_{\max} = 20$ nm, there are three non-shifted holes and nineteen groups of 3 holes shifted respectively by 1, 2, 3, ... up to 19nm, and the last two shifted by 20nm. For $s_{\max} = 25$ nm, the staggered steps consist in alternating groups of three and two holes shifted by 1, 2, 3, ... up to 24nm, and the remaining two holes shifted by 25nm. And finally, for $s_{\max} = 30$ nm, 2 non-shifted holes and 30 groups of 2 holes shifted respectively by 1, 2, 3, ... up to 30nm.

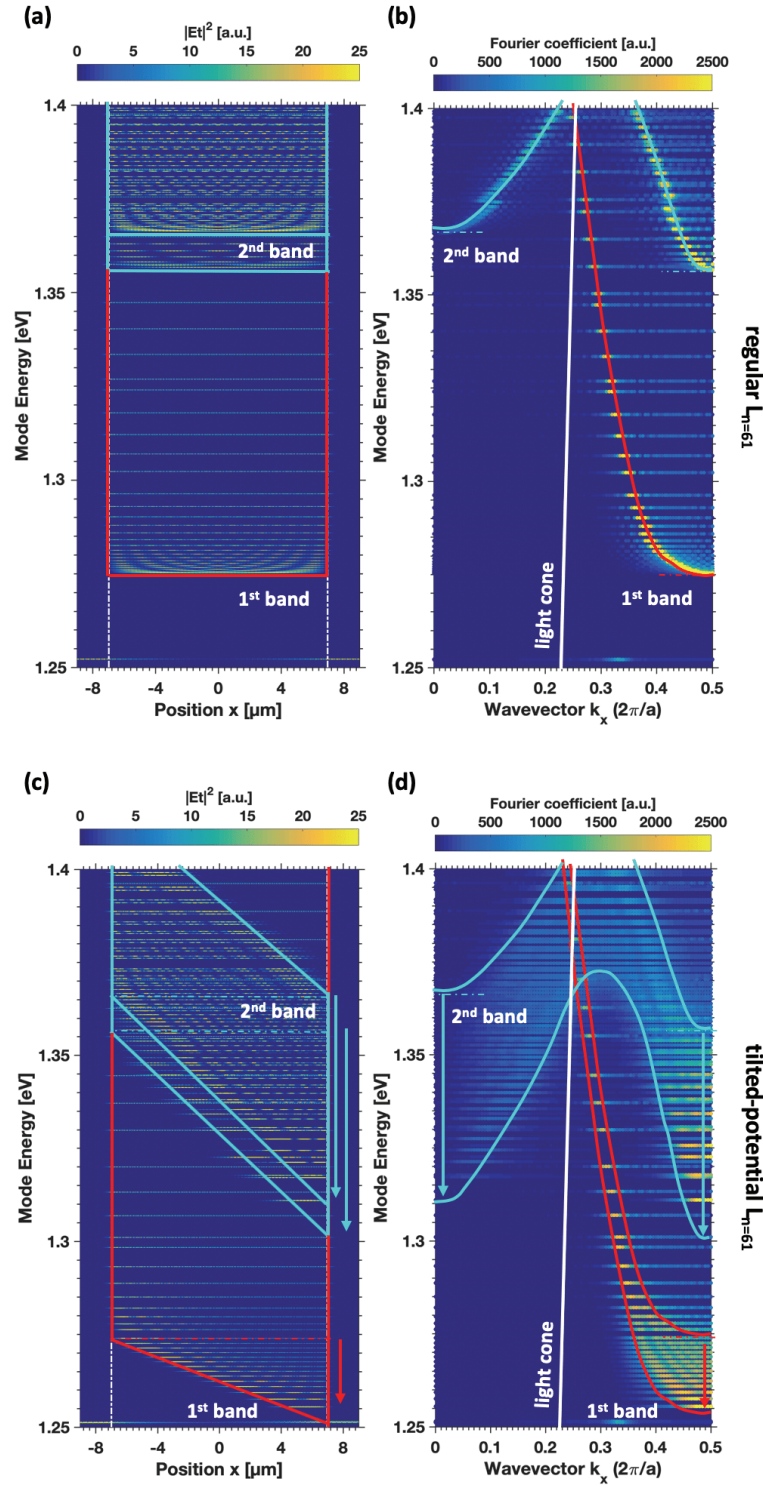


Fig. 4:3 – Numerical simulations of the photonic mode and band structures of a tilted-potential cavity, compared to a uniform cavity. (a, c) Mode structure: in-plane intensities $|E_t|^2$ of TE (E_x , E_y , H_z) confined modes, summed along y and plotted along x . White vertical dot-dashed lines specify the borders of the cavity. Horizontal lines refer to the band-edges of the original unperturbed $L_{n=61}$. Colored lines highlight the photonic potentials of the two bands. (b, d) Bands-structure: from the Fourier transform of E_y component summed along k_y and plotted along k_x . The white line depicts the leaky light cone. Horizontal continuous dot-dashed lines refer to the band-edges of the original unperturbed $L_{n=61}$. The arrows show the tilts of the band-edges. Parameters: pitch $a = 225\text{nm}$, membrane thickness $t = 250\text{nm}$, holes radii $r = 65.8\text{nm}$, end shift $s_{\text{max}} = 20\text{nm}$. The resulting images are generated by the stitching of 6 patches of 25 meVs widths with respectively $n_{\text{eff}} = 3.146, 3.163, 3.182, 3.202, 3.223, 3.243$.

Fig. 4:3 displays the calculated mode structure and band structure for **(c, d)** a tilted-potential $L_{n=61}$ cavity ($s_{\max}=20\text{nm}$, staggered constant shifts s) as compared to **(a, b)** the reference base uniform $L_{n=61}$ cavity. The colored contours are visual cues of the photonic confinement potentials of the 1st band (red) and the 2nd band (cyan). The horizontal dot-dashed lines of the same colors refer to the band-edges of the unperturbed $L_{n=61}$, sharing the same numerical parameters but with $s_{\max} = 0$, and serve as references. It is apparent that the band-edges of the tilted-potential cavity are quasi-linearly tilted. As was done in Chapter 3, the photonic confinement potentials can be drawn by following the contour resulting from the superposition of the shifted band structures of the various waveguide sections of widths w , ..., $w + 2.s(x)$, ..., $w + 2.s_{\max}$. These shifted contributions are visible as “fringes” in (d), when looking at the broadened part of the first band near the M ($k_x = \pi/a$) point of the irreducible Brillouin Zone.

The modified envelope functions of the tilted-potential modes, assuming the form of the Airy functions, is reflected also in the band structure patterns. They are described by the mode head, where the maximum of the electric field resides, and the oscillating tail (see Fig. 4:4). The head part is cavity-like; it is associated with a local slow-light character due to the proximity to the tilted band-edge and relates to a rather flat and broad distribution of k_x values (superposition of harmonics). On the other hand, the tail part is waveguide-like and is linked to a fast-light character, which is described by fewer k_x components.

The 2nd band is tilted with a potential slope that is approximately twice steeper than the first band. This is consistent with the evidences presented in Chapter 3 with respect to the defect-potential. Modes of the second band are more sensitive to the change introduced by the shifted holes because their fields extend more in the y direction. Since the 2nd band displays triangular photonic potential well, other Airy-Bloch modes must be supported. From this point on and for the rest of the chapter, the focus will be on the 1st band for which the mode shapes are most suitable for the end goal of integration with site-controlled QDs.

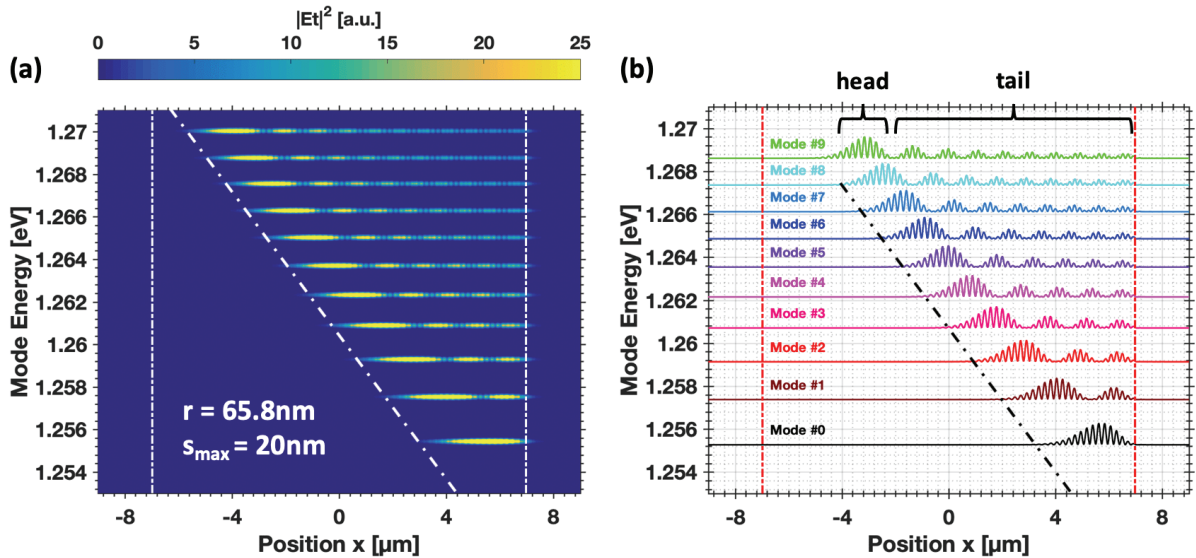


Fig. 4:4 – Numerical simulation of the in-plane $|E_i|^2$ intensity distributions of the lower-energy modes (1st band) in a tilted-potential cavity: zoom-in on the region of interest in Fig. 4:3. (a) Energy-position plane presentation, with mode intensity integrated along the y -direction. (b) Normalized spatial intensity along x of the first ten confined Airy-Bloch modes. Vertical white/red dash-dot lines mark the left and right boundaries of the cavity. The tilted white/black dash-dot line specifies the band-edge. Parameters: pitch $a = 225\text{nm}$, membrane thickness $t = 250\text{nm}$, end shift $s_{\max} = 20\text{nm}$, holes radii $r = 65.8\text{nm}$, effective index of slab $n_{\text{eff}} = 3.146$. Reprinted and adapted with permission from [278]. © The Optical Society.

Fig. 4:4(a), zooms in on the energy-position patterns of the modes of the 1st band of Fig. 4:3. Cross sections of the modes are shown in Fig. 4:4 (b). The Airy-Bloch wavefunctions are labelled as a function of the number of nodes in the envelope functions. Following the same logic as in chapter 3, they correspond to $\#0_M^{(0)}$, $\#1_M^{(0)}$, ..., $\#N_M^{(0)}$. The slow modulation of the Airy envelope functions is superposed on the fast oscillation of the Bloch crystal term, correlated with the lattice pitch a . The white and black dot-dash lines act as visual cues for the triangular photonic potential. The modes display exponentially decaying tails towards the tilted band-edge, and at the right boundary of the cavity. The heads and tails of the Airy mode profiles can be appreciated. The head of the wavefunction is pinned to the tilted band-edge and the tail extends along the remaining part of the cavity. The Airy-Bloch modes are almost evenly spaced in energy. Indeed, the triangle potential is approximately one half of a parabolic potential that would produce evenly-spaced harmonic oscillator states.

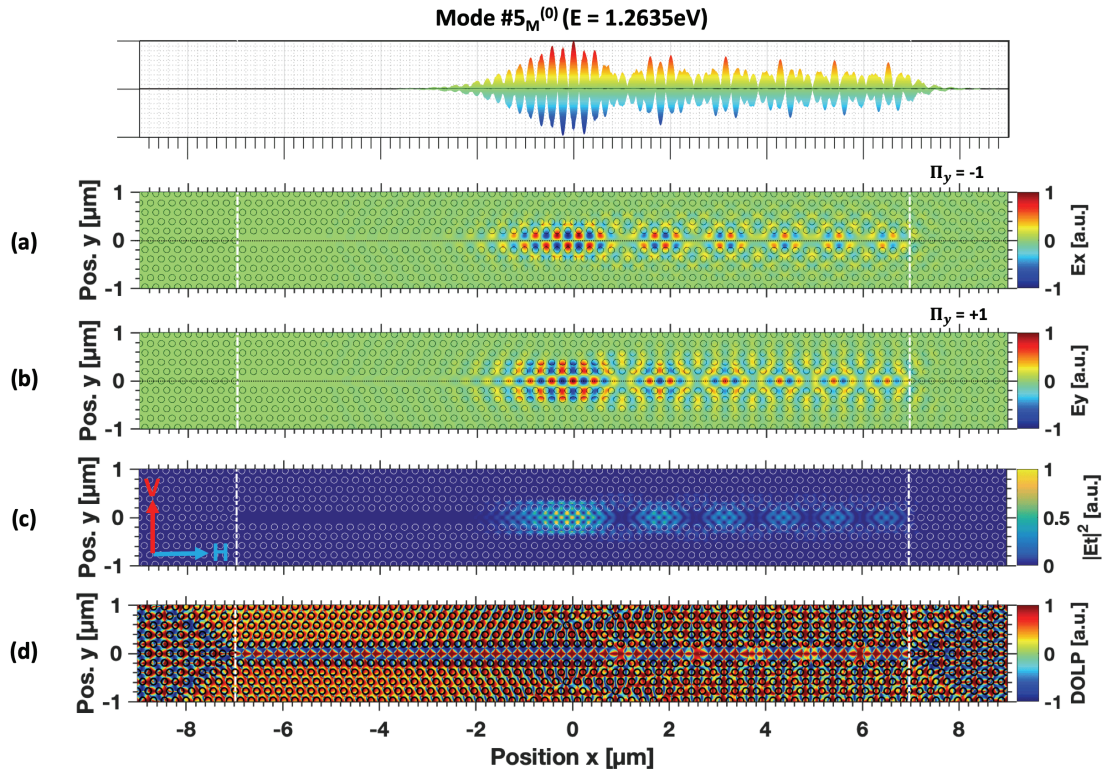


Fig. 4:5 – Properties of an Airy-Bloch mode (mode #5 from the 1st-band, extracted from Fig. 4:4). (a) Top-view of the normalized E_x distribution in the x-y plane; (b) top-view of the normalized E_y distribution in the x-y plane; on top: corresponding side-view of the normalized amplitude along x; (c) top-view of the normalized in-plane intensity $|E_t|^2$ distribution in the x-y plane; (d) top-view of the degree of linear polarization (DOLP) distribution in the x-y plane. Parameters: pitch $a = 225\text{nm}$, membrane thickness $t = 250\text{nm}$, end shift $s_{\text{max}} = 20\text{nm}$, holes radii $r = 65.8\text{nm}$, center effective index of slab $n_{\text{eff}} = 3.146$.

Fig. 4:5 shows in more detail the spatial patterns of Airy-Bloch mode #5 of Fig. 4:4. As expected from a mode of the 1st band, (a) the component E_x of the electric field has an odd symmetry $\Pi_y = -1$ under y reversal, with maxima touching the side-holes, while (b) the component E_y has an even symmetry $\Pi_y = +1$ with maxima aligned with the missing holes. Both components naturally share the same Airy spatial envelope (see side-view on top). (c) displays the distribution of the total in-plane intensity. Due to the prevalence of the E_y component, the primary maxima of intensities coincide with the missing holes' locations and are all located inside the head of the photonic wavefunction. The head's FWHM spans ~ 2 micrometers. (d) shows the spatial distribution of the DOLP, with this it is evident that the intensity maxima coincide with a dominant, vertical V (positive, red) polarization. Near the upper and lower edges of the line defect, polarization is rotated to mostly horizontal H (negative, blue) one.

	$s_{\max}=20\text{nm}$	
$r_0 = 65.8\text{nm}$	$\Delta r = \pm 0.7\text{nm} (\pm 1\%)$	$\Delta E = \pm 2.7\text{meV} (\pm 0.2\%)$
$t_0 = 250\text{nm}$	$\Delta t = \pm 2.5\text{nm} (\pm 1\%)$	$\Delta E = \mp 1.4\text{meV} (\mp 0.1\%)$
$n_0 = 3.4470$	$\Delta n = \pm 0.03 (\pm 1\%)$	$\Delta E = \mp 10.8\text{meV} (\mp 0.9\%)$

Table 4:1- Variations in the energy of Airy-Bloch mode #6 related to variations of core parameters: holes radii, slab thickness, in the case of the reference structure with holes radius $r_0=65.8\text{nm}$, slab thickness $t_0 = 250\text{nm}$ and refractive index $n_0 = 3.4470$ ($n_{\text{eff},0} = 3.146$), $s_{\max} = 20\text{nm}$.

In the same spirit of chapter 3, it is useful to evaluate the dependence of the optical mode structure on the choice of adjustable numerical parameters to match with experimental data. The data reported in **Table 4:1** was extracted from the variations in energy of an arbitrarily selected Airy-Bloch mode (#6) located in the middle of the band of interest in response to large variations of the core parameters. Simulations were performed without energy correction and were run several times by updating the slab effective refractive index with the new estimated energy of the mode, until convergence of the mode energy within $100\mu\text{eV}$ variations. Usually 4-5 iterations were necessary. Only one parameter was modified at a time, the others being set to their reference value. Global uniform holes sizes were simulated with values of $r = 60.8, 65.8, 70.8\text{nm}$, thickness $t = 245, 250, 255\text{nm}$, and refractive index $n = 3.4125, 3.4470, 3.4815$. The variations in parameters were then normalized to correspond to 1%, for a fairer comparison. Varying the radii or the thickness of the slab results in anti-correlated variations of the energy. An increase of the holes size generates a blue-shift due to a stronger optical confinement. On the contrary, an increase in the slab thickness generates a redshift, by relaxation of the optical confinement. One percent variation in global holes sizes result in a variation of energy that is about twice that with one percent variation in thickness. The variation of the refractive index, thus slab effective refractive index, produces a larger change in energy, by a factor of 4, with respect to the radius' variation, and the sign is correlated with the sign of the index variation.

4.2.2 Extraction of a figure of merit: dE/dx , sensitivity to parameters

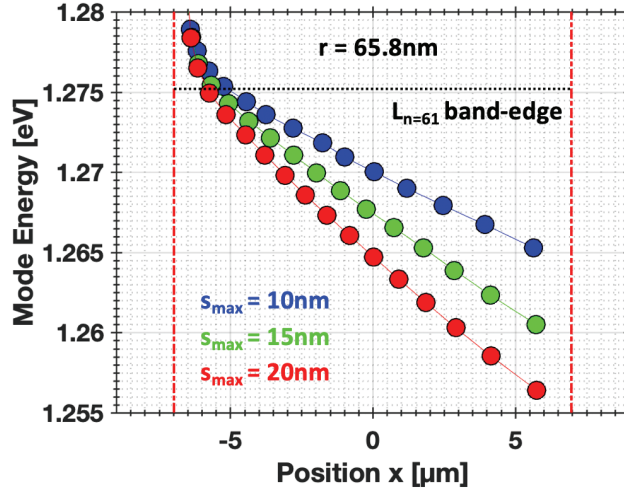


Fig. 4:6 – Calculated mode energy versus position of the main lobe of the Airy-Bloch modes (see examples of mode patterns in Fig. 4:4) for several values of s_{\max} . The horizontal black dot line displays as a reference the band-edge of the corresponding unperturbed $L_{n=61}$ cavity. Parameters: pitch $a = 225\text{nm}$, membrane thickness $t = 250\text{nm}$, holes radii $r = 65.8\text{nm}$, center-wavelength effective index of slab $n_{\text{eff}} = 3.146$.

The tilted-potential cavity modes are characterized by an almost linear variation of mode energy E with the position x of the mode head (maximum intensity). This is illustrated in **Fig. 4:6**, which reports the energy-position pattern of the mode heads for the structure previously considered, for several values of s_{\max} . Maximal shifts $s_{\max} = 10, 15, 20\text{nm}$ redshift, respectively, by $\sim 10, 15, 20\text{meV}$ s the lowest energy mode, with respect to the reference band-edge. Since the energy-position dispersion is practically linear, it is natural to select the gradient dE/dx corresponding to the symbols in Fig. 4:6 as a parameter that characterizes the ensemble of Airy-Bloch mode. Specifically, the gradient is extracted by selecting the loci of the maxima of the Airy-Bloch modes in the linear variation part and applying a linear regression of the form $E = (dE/dx) \cdot x + B$.

$s_{\max} = 20\text{nm}$		dE/dx [meV/ μm] (approx.)
		1.52
$r_0 = 65.8\text{nm}$	$\Delta r = \pm 5\text{nm}$ ($\pm 7.7\%$)	$\Delta(dE/dx) = \pm 0.05\text{meV}/\mu\text{m}$ ($\pm 3.3\%$)
$t_0 = 250\text{nm}$	$\Delta t = \pm 5\text{nm}$ ($\pm 2\%$)	$\Delta(dE/dx) = \pm 0.01\text{meV}/\mu\text{m}$ ($\pm 2.0\%$)
$n_0 = 3.447$	$\Delta n = \pm 0.03$ ($\pm 1\%$)	$\Delta(dE/dx) = \pm 0.00\text{meV}/\mu\text{m}$ ($\pm 0.0\%$)

Table 4:2 – Sensitivity of the slope dE/dx on variations of structural parameters: holes radii, slab thickness and slab effective refractive index for $r_0 = 65.8\text{nm}$, slab thickness $t_0 = 250\text{nm}$ and refractive index $n_0 = 3.4470$ ($n_{\text{eff},0} = 3.146$), $s_{\max} = 20\text{nm}$. dE/dx extracted from a linear fit of the loci of the maxima of the first ten Airy-Bloch modes.

It is interesting to analyze how this figure of merit depends on the adjustable numerical parameters, especially the hole radius, which is a lithographing tuning parameter. In **Table 4:2**, the calculated slope dE/dx of the reference structure presented earlier is reported, as well as its sensitivity to variations of core parameters. The gradient is barely impacted by these changes. This figure of merit is thus a valid choice to compare tilted-potential cavities of the same shift s_{\max} but having different structural parameters.

s_{\max} [nm]	dE/dx [meV/ μm] (proper)	dE/dx [meV/ μm] (approx.)
10	0.97	0.88 (-8.2%)
15	1.38	1.26 (-8.7%)
20	1.67	1.52 (-9%)
25	1.90	1.71 (-10%)
30	2.14	1.95 (-8.9%)

Table 4:3 – Expected gradient dE/dx for $s_{\max} = 10, 15, 20, 25$ & 30nm . Comparison between values from a proper method where all modes are converged individually by simulating them at their right refractive index, and the approximation method employed in this thesis (see Chapter 2). dE/dx extracted from a linear fit of the loci of the maxima of the first ten Airy-Bloch modes.

Table 4:3 compiles the calculated gradients for $s_{\max} = 10, 15, 20, 25, 30\text{nm}$ for disorder-free numerical structures. These values will later serve as comparative reference points for discussing the experimental data. The slopes were estimated in two different manners. One rigorous, where the 10 Airy-Bloch modes are converged individually to their proper eigen-energies, representing the perfect proper value. And the other, where the energies of the 10 Airy-Bloch modes are corrected with the formula of (Eq. 2:3). In this case, simulations are based on the single value of the effective refractive index of an Airy-Bloch mode chosen at the center of the triangle potential. Values from the second method are underestimated by 8-10%. This is explained by the lack of accuracy from the energy correction (see again Fig. 2:5). With the increase of s_{\max} , the span of energy of the Airy-Bloch modes increases too. Since predictions are made around a middle point, the farthest mode energies are over-corrected, resulting in a mode compression along the photon energy axis, which leads to a tilt smaller than real.

4.2.3 Effects of disorder

Fig. 4:7 gives a global picture of the impact of holes sizes disorder on the optical mode structure. For clarity, the visualization of the Airy-Bloch modes is simplified again, similarly to Fig. 4:6 earlier. A mode is associated here with the position of its maximum of intensity and its energy. Based on 10 simulations, the average energies and positions of 10 Airy-Bloch modes were estimated (colored filled circles), as well as the corresponding standard deviations (shaded areas). These values are plotted against the data points of a disorder-free structure (black circles). A deterministic structure is a structure that is resilient to disorder; such a behavior is characterized by overlap of the two circle symbols and standard deviations curbed within reasonable margins. Otherwise the photonic wavefunctions are not anymore well-defined Airy-Bloch modes. There is a correlation between the maximum allowed magnitude of disorder, still preserving extended wave functions, and the tilt of the potential.

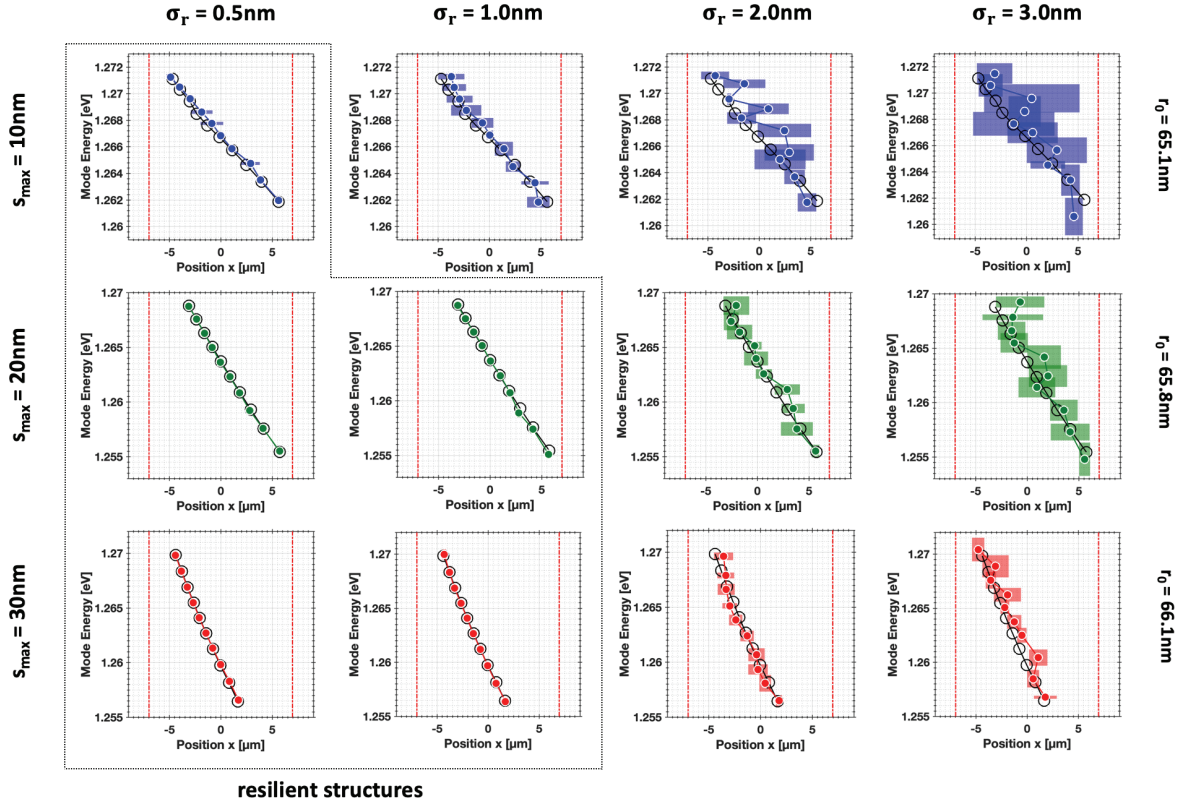


Fig. 4:7 – Numerical simulations showing the impact of holes sizes disorder on the slope dE/dx , for several values of s_{\max} and standard deviations $\sigma_r = 0.5, 1.0, 2.0, 3.0\text{nm}$ around $r_0 = 65.1, 65.8, 66.1\text{nm}$. Black empty circles display the loci of 10 modes of a disorder-free structure. Colored filled circles specify the average locations of the maxima of the same Airy-Bloch modes extracted from 5 simulations. The shaded rectangles illustrate the associated one standard deviation in position σ_x by one standard deviation in energy σ_E . The dot line represents the threshold of disorder level beyond which, for a given s_{\max} , a structure deviates significantly from the quasi disorder-free scenario characterized by overlap of the circle symbols. Parameters: pitch $a = 225\text{nm}$, membrane thickness $t = 250\text{nm}$, spectral center effective index of slab $n_{\text{eff}} = 3.174, 3.146, 3.145$.

Table 4:4 summarizes these observations. To evaluate quantitatively the overlap of the symbols, we compute the discrepancies in mode energy $\Delta E = E - E_{\text{ref}}$ and position $\Delta x = x - x_{\text{ref}}$ of the energy-position maxima for the 10 Airy-Bloch modes, between the disorder-impacted case and disorder-free case. The vectors $(\Delta E, \Delta x)$ thus estimate the precision of the overlap. The accuracy would be characterized by (σ_E, σ_x) which are represented by the color rectangle shaded regions displayed in the Fig. 4:7. The global mean and standard deviations are extracted and reported in Table 4:4, as a function of the magnitude of disorder and for each value of s_{\max} . The gradient dE/dx is also evaluated for the nine segments of any two successive energy-position maxima, and again the global mean and standard deviations are derived. This value can then be compared to the expected slopes in Table. 4:3. A resilient structure is characterized by a commensurate value of the mean(dE/dx); beyond a certain disorder level threshold $\sigma_r^{\text{thres.}}$, this mean(dE/dx) deviates significantly. In the case of $s_{\max} = 10\text{nm}$, $\sigma_r^{\text{thres.}}$ is in between $\sigma_r = 0.5\text{nm}$ and $\sigma_r = 1.0\text{nm}$. In the cases of $s_{\max} = 20\text{nm}$ and 30nm , $\sigma_r^{\text{thres.}}$ is in between $\sigma_r = 1.0\text{nm}$ and $\sigma_r = 1.5\text{nm}$. The exact values were not resolved by lack of data points.

$s_{\max} = 10\text{nm}$	mean(ΔE) [meV]	mean(Δx) [μm]	mean(dE/dx) [meV/ μm]
$\sigma_r = 0.5\text{nm}$	0.14 ± 0.05	0.12 ± 0.25	0.90 ± 0.19
$= 1.0\text{nm}$	0.10 ± 0.14	0.23 ± 0.51	1.7 ± 1.35
$= 2.0\text{nm}$	0.25 ± 0.26	0.83 ± 1.55	0.59 ± 1.35
$= 3.0\text{nm}$	-0.01 ± 0.48	0.93 ± 1.35	0.48 ± 3.15

$s_{\max} = 20\text{nm}$	mean(ΔE) [meV]	mean(Δx) [μm]	mean(dE/dx) [meV/ μm]
$\sigma_r = 0.5\text{nm}$	-0.01 ± 0.09	-0.03 ± 0.04	1.53 ± 0.19
$= 1.0\text{nm}$	-0.12 ± 0.14	0.01 ± 0.06	1.58 ± 0.28
$= 2.0\text{nm}$	0.06 ± 0.21	0.21 ± 0.54	2.08 ± 2.87
$= 3.0\text{nm}$	0.18 ± 0.36	0.53 ± 1.02	0.28 ± 4.58

$s_{\max} = 30\text{nm}$	mean(ΔE) [meV]	mean(Δx) [μm]	mean(dE/dx) [meV/ μm]
$\sigma_r = 0.5\text{nm}$	0.06 ± 0.08	-0.01 ± 0.04	2.19 ± 0.29
$= 1.0\text{nm}$	-0.01 ± 0.09	0.0 ± 0.04	2.34 ± 0.49
$= 2.0\text{nm}$	-0.27 ± 0.19	0.06 ± 0.39	6.80 ± 9.42
$= 3.0\text{nm}$	0.74 ± 0.28	0.20 ± 0.50	-0.38 ± 2.52

Table 4:4 – Compilation of the statistical mean and standard deviations for discrepancies in energy ΔE and position Δx from the mode energy-position maxima of ten Airy-Bloch modes in the case of $s_{\max} = 10, 20$ and 30nm for various levels of holes sizes disorder $\sigma_r = 0.5, 1.0, 2.0$ & 3.0nm . Gradients are computed for the nine segments of successive energy-position maxima and then averaged. Gray shading for scenario where the gradient is not commensurate with values of Table. 4:3. Data extracted from the graphs in Fig. 4:7.

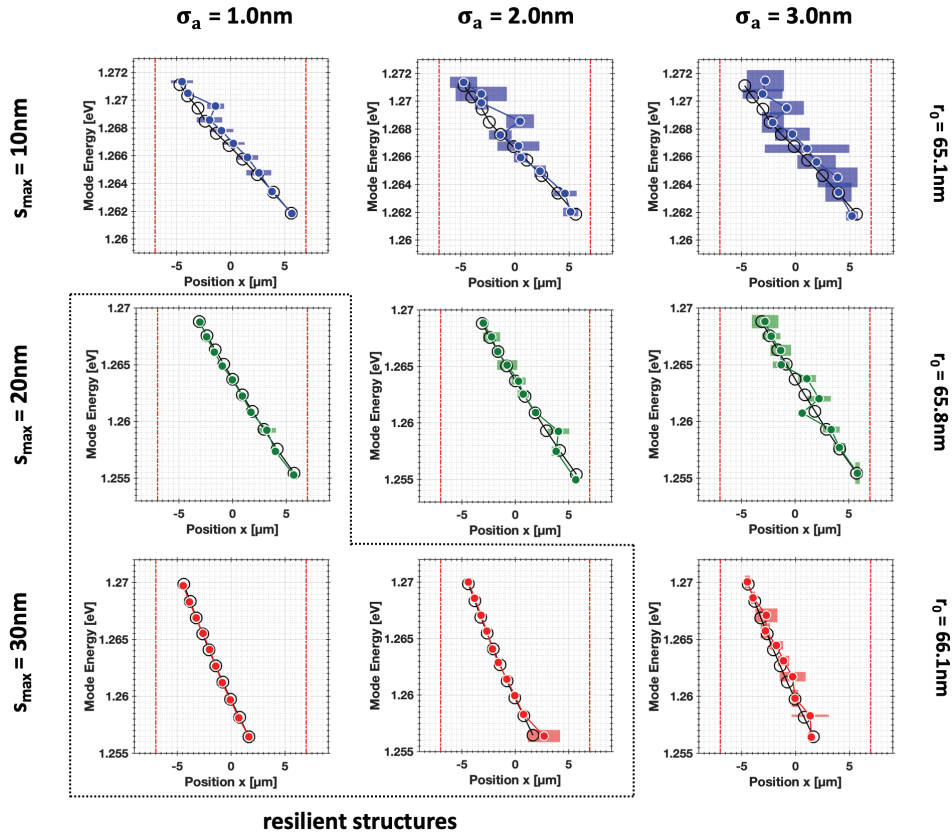


Fig. 4:8 – Numerical simulations showing the impact of holes positions disorder on the slope dE/dx , for several values of s_{\max} and standard deviations $\sigma_r = 0.5, 1.0, 2.0, 3.0\text{nm}$ around $r_0 = 65.1, 65.8, 66.1\text{nm}$. Black empty circles display the loci of 10 modes of a disorder-free structure. Colored filled circles specify the average locations of the maximum of the same Airy-Bloch modes extracted from 5 simulations. The shaded rectangles illustrate the associated one standard deviation in position σ_x by one standard deviation in energy σ_E . The dot line represents the threshold of disorder level beyond which, for a given s_{\max} , a structure deviates significantly from the disorder-free scenario characterized by overlap of the circle symbols. Parameters: pitch $a = 225\text{nm}$, membrane thickness $t = 250\text{nm}$, spectral center effective index of slab $n_{\text{eff}} = 3.174, 3.146, 3.145$.

Fig. 4:8 and **Table 4:5** are a repeat of the study above, but for the case of holes position disorder. Observations are similar, only the quantitative values of the parameters differ. Here, the disorder thresholds are somewhat clearer: in the case of $s_{\max} = 10\text{nm}$, $\sigma_r^{\text{thres.}}$ is below $\sigma_a = 1.0\text{nm}$; in the cases of $s_{\max} = 20\text{nm}$, $\sigma_r^{\text{thres.}}$ is in between $\sigma_a = 1.0\text{nm}$ and $\sigma_a = 2.0\text{nm}$; and for $s_{\max} = 30\text{nm}$, $\sigma_r^{\text{thres.}}$ is in between $\sigma_a = 2.0\text{nm}$ and $\sigma_a = 3.0\text{nm}$.

$s_{\max}=10\text{nm}$	mean(ΔE) [meV]	mean(Δx) [μm]	mean(dE/dx) [meV/ μm]
$\sigma_a=1.0\text{nm}$	0.14 ± 0.11	0.36 ± 0.49	0.60 ± 0.93
$=2.0\text{nm}$	0.15 ± 0.17	0.35 ± 0.99	8.29 ± 21.66
$=3.0\text{nm}$	-0.04 ± 0.29	0.94 ± 0.82	1.50 ± 4.79

$s_{\max}=20\text{nm}$	mean(ΔE) [meV]	mean(Δx) [μm]	mean(dE/dx) [meV/ μm]
$\sigma_a=1.0\text{nm}$	-0.1 ± 0.07	0.03 ± 0.13	1.65 ± 0.44
$=2.0\text{nm}$	0.0 ± 0.16	0.12 ± 0.40	0.48 ± 3.39
$=3.0\text{nm}$	-0.02 ± 0.14	0.21 ± 0.72	5.27 ± 12.52

$s_{\max}=30\text{nm}$	mean(ΔE) [meV]	mean(Δx) [μm]	mean(dE/dx) [meV/ μm]
$\sigma_a=1.0\text{nm}$	-0.02 ± 0.04	-0.02 ± 0.05	2.21 ± 0.24
$=2.0\text{nm}$	0.17 ± 0.11	0.07 ± 0.34	2.18 ± 0.57
$=3.0\text{nm}$	0.25 ± 0.15	0.16 ± 0.31	2.42 ± 7.69

Table 4:5 – Compilation of the mean discrepancies in energy ΔE and position Δx from the mode energy-position maxima of ten Airy-Bloch modes in the case of $s_{\max} = 10, 20$ and 30nm for various levels of holes position disorder $\sigma_a = 1.0, 2.0$ & 3.0nm . Gradients are computed for the nine segments of two successive energy-position maxima and then averaged. Gray shading for scenario where the gradient is not commensurate with values of Table. 4:3. Data extracted from the graphs in Fig. 4:7.

The threshold values $\sigma_r^{\text{thres.}}$ or $\sigma_a^{\text{thres.}}$ increase monotonously with increasing s_{\max} . This is intuitive, since a given configuration of disorder can be seen as a fixed corrugated potential that is superimposed on the tilted photonic potential. Due to the wave character of light, locally trapped optical modes can also escape potential barriers by evanescent coupling and tunneling, and the tilt facilitates the process. In a regular PhC waveguide, fast-light modes are less impacted by disorder because their energies are well above the Anderson localization energy range, while slow-light modes near the band-edge are localized. For the same reason, the tilted-potential structure offers a form of resilience to such localization. With the tailored dispersion, photonic wavefunctions can “fly” more easily above the corrugations of the energy potential created by disorder.

We note that the three structures of different s_{\max} were simulated with different holes sizes, due to the selection of different reference points for the center Airy-Bloch modes, obtained from experimental data. We mentioned before in section 4.2.2 and 4.2.3 that this has very limited effects on the results and thus should not compromise the conclusions of this study.

4.3 Fabrication of tilted-potential photonic crystal cavities

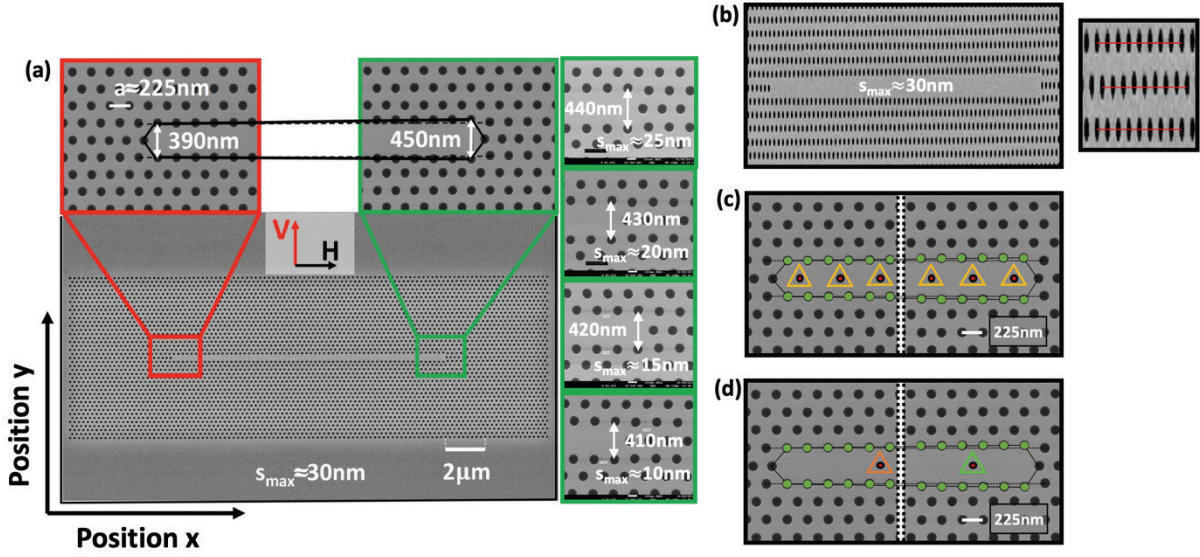


Fig. 4:9 – Scanning electron microscope top-view images of: (a) a fabricated tilted-potential PhC $L_{n=61}$ cavity, with magnified view of the two cavity edges in the case of $s_{\max} = 30\text{nm}$, and right edges of other structures with designed $s_{\max} = 25, 20, 15, 10\text{nm}$; (b) the same structure as in (a) but compressed along x to appreciate the smoothness of the gradient. A zoom highlights the disorder related to holes positions. Schematics of the pyramidal QD patterns used for (c) optical modes characterization and (d) for the study on single QDs coupling to Airy-Bloch modes. Reprinted and adapted with permission from [278]. © The Optical Society.

Fig. 4:9 displays electron micrographs from a dummy (100) GaAs membrane sample where the structures share identical design and parameters as those presented in this chapter. (a) The implemented tilted-potential cavities are all based on regular $L_{n=61}$ cavities, in which the holes are shifted up to maximum shifts of $s_{\max} = 10, 15, 20, 25$ and 30nm . The left extremity of the cavity (red rectangle) has a base width of $w = \sqrt{3}a \approx 390\text{nm}$ measured from holes center to center. The right extremity (green rectangle) supports widths $w + 2.s_{\max} = \sqrt{3}a + 2.s_{\max} \approx 410, 420, 430, 440$ and 450nm . As was mentioned in chapter 3, the left and right terminations of all L_n cavities are also modified, the three first side-holes are shifted outwards along x , respectively by $s_{1x} = 0.2311a (\sim 52\text{nm})$, $s_{2x} = 0.1507a (\sim 34\text{nm})$, $s_{3x} = 0.048a (\sim 11\text{nm})$. For $s_{\max} \approx 30\text{nm}$, the x -compressed image in part (b) allows the appreciation of both the tapering and the level of disorder in the PhC hole patterns. The slope appears very smooth to the eye but it is in fact staggered, the 62 holes are shifted in pairs by increments of 1nm , the details for the other values of s_{\max} were specified earlier in section 4.2.1. The tilted-potential PhC structures are all located on the same sample as the defect-potential PhC cavities, so naturally the fabricated PhC holes also cover a wide range of $r_{\text{fab.}} \approx 47\text{--}74\text{nm}$, allowing a coarse r/a tuning of the mode energies. According to the previous numerical simulations the Airy-Bloch modes are predicted to appear in the $\sim 1.240\text{--}1.378\text{eV}$ photon energy range ($900\text{--}1000\text{nm}$) at $T \approx 10\text{K}$.

In the actual sample containing the QDs, the tilted-potential cavities have been implemented in two families, respectively on the medium square and on the big square regions. (c) The first family, with 30 site-controlled QDs embedded every one lattice site out of two, comprises a single series of tuning of the r/a ratio for $s_{\max} = 15, 20, 25$ and 30nm . Each of these repetitions is made of 21 structures where the radius $r_{\text{fab.}}$ is systematically incremented from ~ 47 to $\sim 74\text{nm}$ in steps of 1nm . The repetition for $s_{\max} = 10\text{nm}$ is made by 2×13 structures, in which the radius $r_{\text{fab.}}$ ranges from ~ 47 to $\sim 63\text{nm}$ and from ~ 58 to $\sim 74\text{nm}$. The difference in implementation comes from management of the available space on the sample. The purpose of this first group is to observe the optical mode structure with site-controlled QDs acting mainly as broadband internal light emitters when pumped with large excitation power density. The ground shell of these QDs produce photons at $\sim 1.258\text{--}1.272\text{eV}$ ($\lambda_{\text{QD}} \sim 975\text{--}985\text{nm}$) at $T \approx 10\text{K}$.

(d) The second family, aims at studying the coupling between single site-controlled QDs and few Airy-Bloch modes. To this purpose, only 2 site-controlled QDs are embedded at specific locations: $-3.375\mu\text{m}$ (-15a) and $+6.075\mu\text{m}$ (+27a) from the center of the cavity. This spacing of $9.45\mu\text{m}$ is larger than the estimated charge carrier diffusion range ($\sim 4\text{--}4.5\mu\text{m}$) so that the two QDs can be excited independently. Configurations with each value of $s_{\text{max}} = 10, 15, 20, 25$ or 30nm are repeated 4 times, with again 2×13 structures with radius r ranging from ~ 47 to $\sim 63\text{nm}$ and from ~ 58 to $\sim 74\text{nm}$. Here the QDs emit at $\sim 1.264\text{--}1.279\text{eV}$ ($\lambda_{\text{QD}} \sim 970\text{--}980\text{nm}$) at $T = 10\text{K}$.

For detailed layouts of the investigated structures, see appendix C.

4.4 Observed optical mode properties

This part is devoted to experimental observations of the optical mode structures and properties of the fabricated Tilted-Potential PhC Cavities with QDs arrays using the micro-photoluminescence imaging technique described in Chapter 2. We compare the fidelity of the results both in qualitative and quantitative terms with numerical simulations.

4.4.1 Optical mode spectra

Fig. 4:10 illustrates the polarization resolved energy-position map of the tilted-potential structure covering a large range of photon energies, in the particular case of $s_{\text{max}} \approx 20\text{nm}$. It can be directly confronted with the predictions of section 4.2.1. **(a)** focuses on the vertically (V) polarized component of the optical mode, which is the dominant feature of modes of the 1st band of confined states. The region of the discretized Airy-Bloch modes appears between 1.25 and 1.275eV , where one can identify the “heads” of the modes, that shift regularly from the right to the left side of the cavity with increasing mode energy. The “heads” are connected to their trailing tails and discrete numbers of secondary lobes can be observed. This means that the band-edge is indeed tilted quasi linearly, as indicated by the white dot-dashed line. Well above 1.275eV , the higher-order Airy-Bloch modes are fully extended over the length of the $L_{n=61}$ tilted-potential cavity, with a brighter diffraction-limited lobe always located on the left-edge of the cavity. Scattering at the right-edge can still be seen, but it appears much fainter than, for instance, the symmetric defect-potential of chapter 3.

Part **(b)** focuses on the horizontally (H) polarized component and shows a very bright tilted feature pertaining to the 2nd band. This feature is a signature of the overlay of the Airy-Bloch modes from both the Γ and M points of the Brillouin Zone. The tilt associated with this 2nd band is much steeper than the analogous part for the 1st band, as foretold by simulations. This overwhelming brightness is again a combination of two effects: first, as a result of the band folding over itself there is a large density of modes; second, these modes intersect with the light cone (see Fig. 4:3) and are thus more lossy, the Q factors are low, and the modes are difficult to distinguish individually. These two effects prevent the precise identification of “heads” and “tails” components for these other Airy-Bloch modes.

Part **(c)** synthesizes the previous observations by combining both polarization via the DOLP map of the full optical modes structure. Clearly, the 1st band is strongly V-polarized, while the 2nd band is mostly H-polarized. In addition, similarly to the defect-potential, it is interesting to notice that the energy part below the tilted band-edge of a band carries a non-negligible polarization in correlation with the band, despite the absence of confined optical modes. This shows again how much of an impact a PhC environment could have on QDs, contrary to a quasi-isotropic bulk medium.

Part **(d)** displays the same data in a more conventional format, removing the spatial information by integration of the signal along the cavity axis. It is equivalent to using smaller imaging magnification. The regular μPL spectra focus on the first Airy-Bloch modes and allow for easier quantitative estimations. The first six Airy-Bloch modes are dominantly V-polarized along y , with a DOLP of ~ 0.75 , the seventh shows a DOLP of 0.5 , and the remaining drop to 0.25 . At higher energies, the background DOLP starts to dip towards negative values due to the influence of the 2nd band.

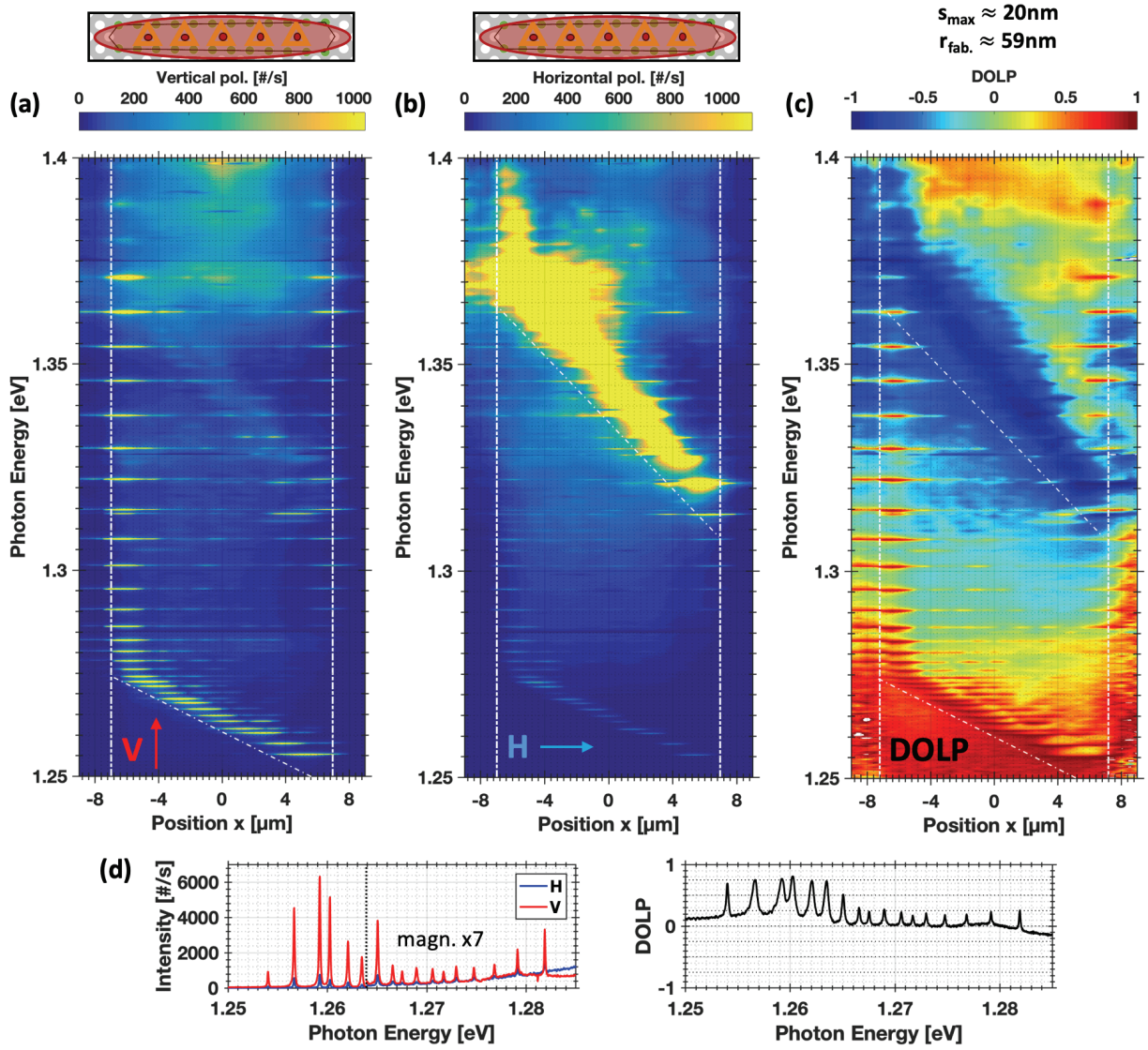


Fig. 4:10 – Measured optical mode structure of a tilted-potential PhC cavity acquired over a spectral range of 150meVs. Upper panels show schematically the experimental pumping arrangement. (a) vertically (V) polarized image; (b) horizontally (H) polarized image; (c) image of the degree of linear polarization (DOLP) processed from (a) and (b); (d) regular μ PL spectra, H & V polarized, of the first Airy-Bloch modes (the part above dotted line is magnified 7 times) and corresponding DOLP. Above barrier excitation, laser wavelength $\lambda_{\text{exc.}} \approx 730\text{nm}$, excitation power $P_{\text{exc}} \approx 2\text{mW}$. Temperature $T \approx 10\text{K}$. PhC hole radius $r_{\text{fab.}} \approx 59\text{nm}$, $s_{\max} \approx 20\text{nm}$.

Fig. 4:11, zooms on the Airy-Bloch modes region; it confronts the results of 2D FDM numerical modeling of the modes with the experimental mode patterns for three values of $s_{\max} \approx$ (a) 10, (b) 20, (c) 30nm. Focusing first on the center column of experimental data, the Airy Bloch modes are identifiable, with principal lobes, and tails comprising the secondary lobes which number can practically be counted. The photonic confinement for $s_{\max} \approx 10\text{nm}$ is not fully deterministic and representative of a tilted-potential, indicating a level of disorder beyond the threshold for this structure. On the other hand, for $s_{\max} \approx 20$ and 30nm the tilted-potential mode structures are quite regular and well defined, indicating that the level of disorder is below thresholds.

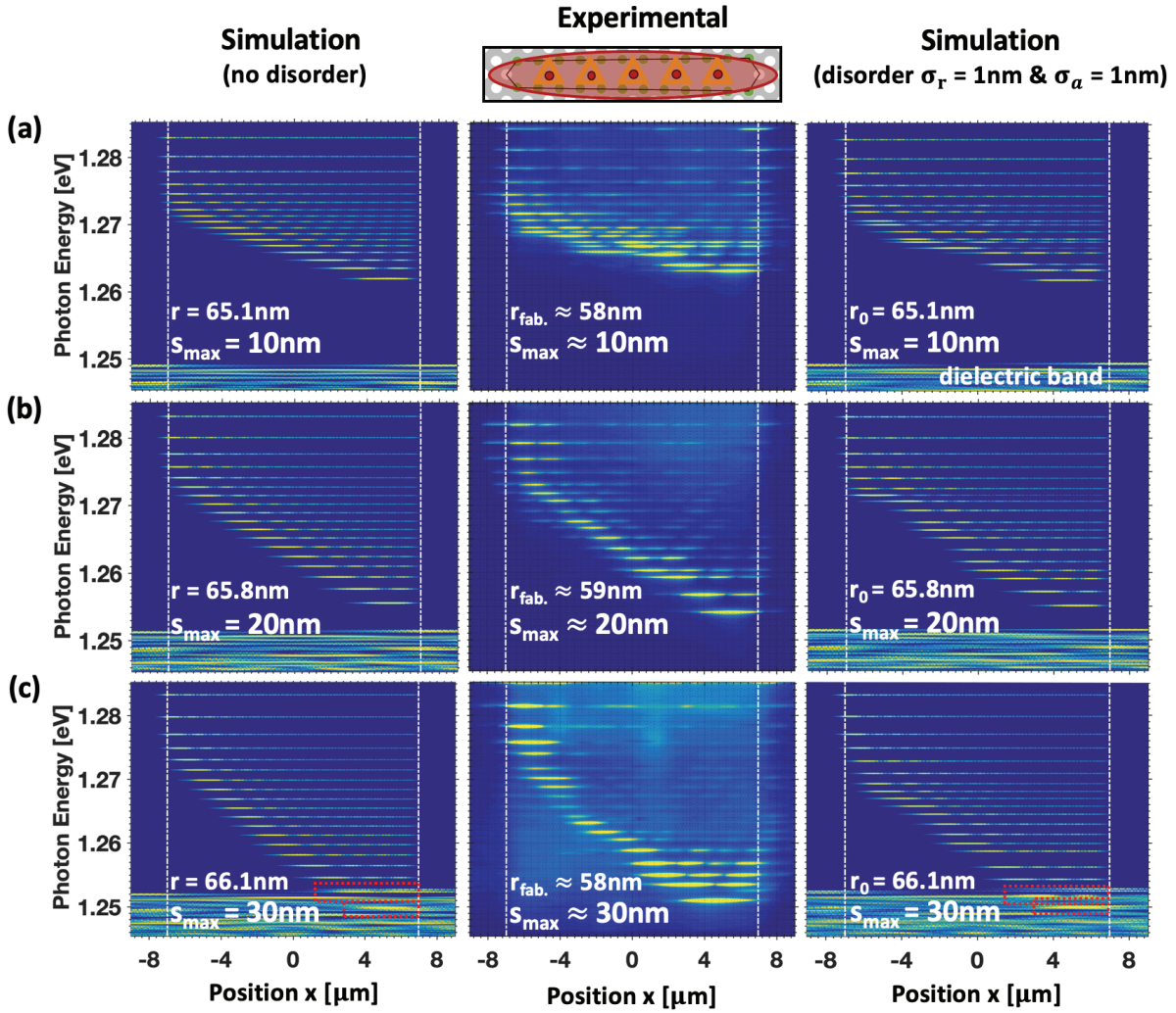


Fig. 4:11 – Comparison of simulated and measured spectrally-resolved near-field patterns of tilted-potential PhC cavities with (a) $s_{\max} \approx 10$, (b) 20 and (c) 30nm: simulated without disorder (left column); measured (center column); simulated with disorder (right column). Brightness scale for measured patterns corresponds to intensity (linear scales). Upper panel shows schematically the experimental pumping arrangement. White dash-dot lines mark the left and right boundaries of the cavity. The red dot boxes point to modes buried underneath the dielectric band. Above barrier excitation, laser wavelength $\lambda_{\text{exc.}} \approx 730\text{nm}$, excitation power $P_{\text{exc}} \approx 2\text{mW}$. Temperature $T \approx 10\text{K}$. Radius $r_{\text{fab.}} \approx 58\text{nm}$, $s_{\max} \approx 10\text{nm}$; radius $r_{\text{fab.}} \approx 59\text{nm}$, $s_{\max} \approx 20\text{nm}$; radius $r_{\text{fab.}} \approx 58\text{nm}$, $s_{\max} \approx 30\text{nm}$. Simulations parameters: pitch $a = 225\text{nm}$, membrane thickness $t = 250\text{nm}$, center effective index of slab $n_{\text{eff.}} = 3.147, 3.146, 3.145$. Reprinted and adapted with permission from [278]. © The Optical Society.

We next focus on the left and center columns, where simulations do not include fabrication disorder. Based on the experimental graphs, the wavelength of an Airy-Bloch mode selected in the middle of the triangular-part of the photonic potential is used to define the reference spectral center, from which the slab effective refractive index is computed. The pitch and thickness of the membrane were set respectively to $a = 225\text{nm}$ and $t = 250\text{nm}$, as usual. The tilt parameter s_{\max} is set in accordance with the structure. The simulation hole radius r was then tuned in order to match the mode energy of the simulated reference mode with that of the experimental mode. The energy correction of the other modes was conducted as per the usual procedure with (Eq. 2:3). The predictions already show reasonable qualitative, and almost quantitative agreements although, as expected, they do not reproduce some distortions that are observed, since these effects arise from fabrication disorder. On the right column, using these numerical parameters, disorder is introduced in the simulations on both the holes sizes and positions with

plausible levels (confer study in chapter 3). The newly simulated optical mode structures succeed in reproducing qualitatively the nature and magnitude of the effects, i.e., the perturbations of the modes' energies and of the spatial distributions of intensity. These two effects effectively break the quasi linear energy-position dispersion of the mode heads.

Interestingly, in the experimental near-field images, we cannot notice the existence of the dielectric band states. A reason might be that these slab modes are delocalized, thus the intensities are weaker and travel through the bulk. For the same reason, PhC waveguide modes cannot be imaged efficiently unless there are important residual reflections/scattering or Anderson localization [252].

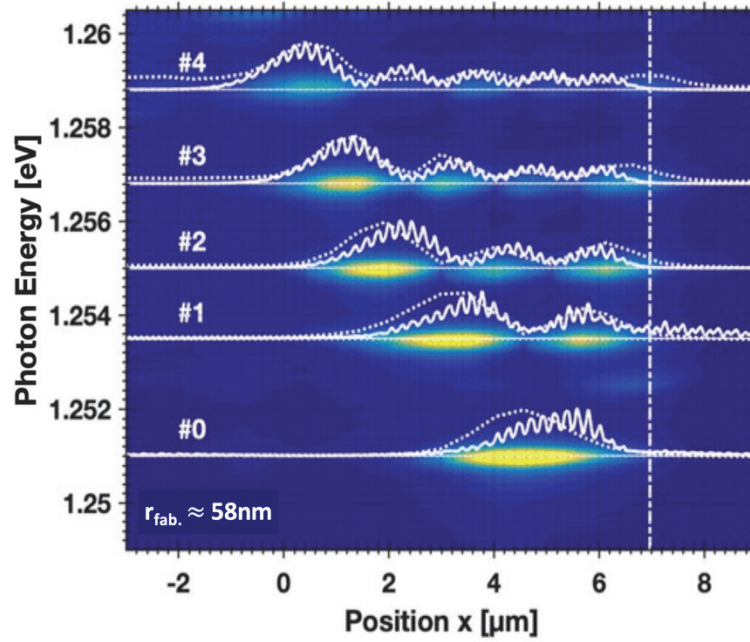


Fig. 4:12 – Comparisons of measured and simulated near field patterns of the lowest energy Airy-Bloch modes in the case of $s_{\max} \approx 30\text{nm}$ from Fig. 4:12. Image: measured spectrally-resolved intensity patterns. Dotted lines: measured (normalized) x-profiles obtained directly from the energy-position plots, solid line: normalized simulated near-field patterns, intensity integrated along the y-direction for $r = 66.5\text{nm}$, without disorder. Calculated modes are vertically shifted to fit mode energies. Radius $r_{\text{fab.}} \approx 58\text{nm}$, $s_{\max} \approx 30\text{nm}$. Reprinted and adapted with permission from [278]. © The Optical Society.

Fig. 4:12 further zooms in and compares the experimental, diffraction-limited Airy envelopes intensity patterns with disorder-free numerical simulations, for the structure with $s_{\max} \approx 30\text{nm}$. The plotted lines, from numerical simulations, display the Airy-Bloch mode intensities integrated along y. On mode #1, the simulated oscillations propagate beyond the right boundary of the cavity, which is related to a hybridization effect with the dielectric band but is not apparent in the experimental data. The simulated mode energies were artificially adjusted to the experimental mode energies, to facilitate comparison. The experimental data was scaled as usual and rigidly offset in position by a fraction of μm , which is reasonable considering the difficulty to center the cavity and the drift of the piezoelectric stage over time during measurements. With these considerations in mind, the match between experiment and simulation is quite good with respect to the locations of the mode heads and nodes, number of lobes and their relative amplitudes. Thus, we conclude that the experimental photonic wavefunctions are Airy-Bloch wavefunctions generated by a triangular potential. Despite the proximity to the band-edge, the modes are quite regular and well defined, suggesting the relative resilience to Anderson localization that was discussed earlier.

4.4.2 Airy-Bloch modes Q -factors

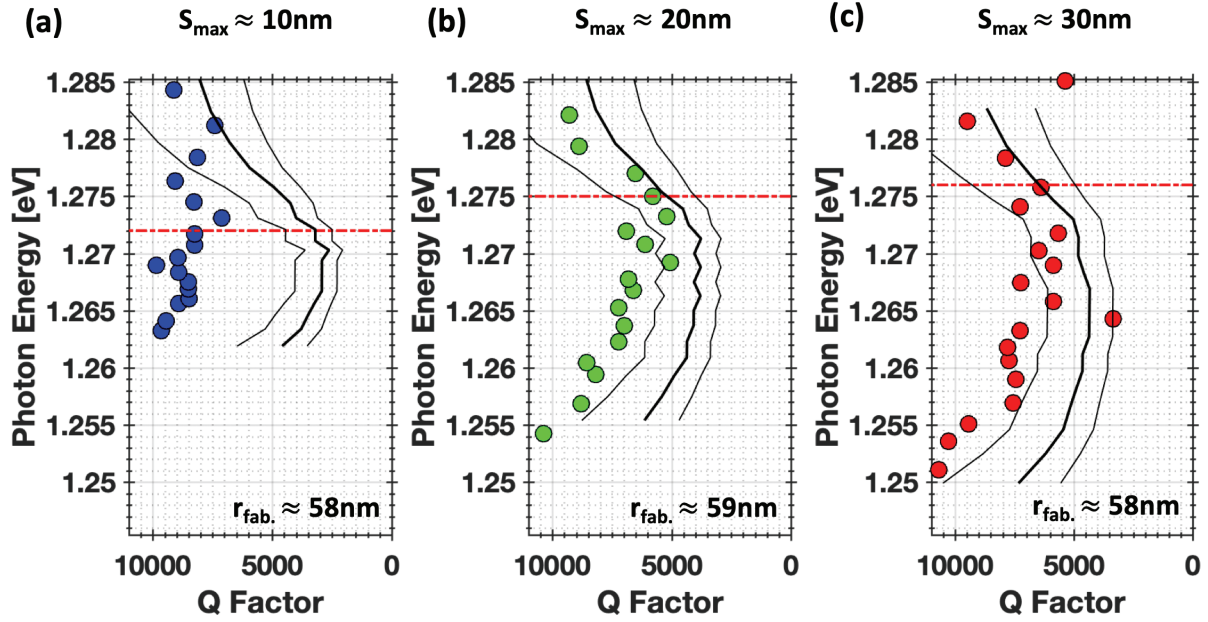


Fig. 4:13 – Experimental quality Q factors for the first Airy-Bloch modes of tilted-potential PhC cavities with (a) $s_{\max} \approx 10\text{nm}$, (b) $s_{\max} \approx 20\text{nm}$ and (c) $s_{\max} \approx 30\text{nm}$. Red dot-dash lines relate to 1st band M point band-edges from simulations. Data extracted from measurements shown in Fig. 4:11. Black lines are derived from a physical Fabry-Pérot model. Radius $r_{\text{fab.}} \approx 58\text{nm}$, $s_{\max} \approx 10\text{nm}$; radius $r_{\text{fab.}} \approx 59\text{nm}$, $s_{\max} \approx 20\text{nm}$; radius $r_{\text{fab.}} \approx 58\text{nm}$, $s_{\max} \approx 30\text{nm}$. Temperature $T \approx 10\text{K}$.

Fig. 4:13 reports the Q -factors of tilted-potential cavities extracted from experimental data for $s_{\max} \approx$ (a) 10, (b) 20 and (c) 30nm, displayed as a function of the mode energies. Overall, independently of s_{\max} , the Q -factors of the first Airy-Bloch modes located near the band-edge are relatively high, with values mostly in the range $\sim 5'000$ - $10'000$. These values are similar to those reported in chapter 3 and of various L_n cavity modes fabricated in a previous sample [162]. They are also similar to the Q -factors of Anderson localized modes, located near the lowest band-edge of long cavities, reported in the literature [92]. These values are also well below the maximum measurable value of $\sim 16'000$ at $\sim 1.25\text{eV}$, set by the $\sim 80\mu\text{eV}$ spectrometer resolution limit. Therefore, despite state-of-the-art fabrication, the Q s are limited by physical absorption and scattering mechanisms in these samples.

In fact, the three graphs in Fig. 4:13 display a common trend, exhibiting a dip near the band-edge of the base $L_{n=61}$ cavity, and a rise towards the bottom of the tilted-potential energy. This is consistent with the observations and discussions of chapter 3, section 3.3.2, using the same parameters for a Fabry-Pérot model illustrated by the collection of black lines in the graphs. This model is detailed in [162], [264], [144]. The total Q is controlled by the combination of the reflection losses and propagation losses by the relation $1/Q_{\text{tot.}} = 1/Q_{\text{refl.}} + 1/Q_{\text{prop.}}$. Depending on the energies, one mechanism may dominate over the other. For long L_n cavities, near the band-edge, the reflection losses become rapidly negligible by comparison to the propagation losses. The drop of the Q s from ~ 1.285 to ~ 1.272 - 1.276eV is associated to the dominant scattering mechanism that was observed for the defect-potential. It occurs with the fast-light to slow-light transition, with the flattening of the dispersion, divergence of the group index and especially Anderson localization. According to [97] the widening of a $w1$ PhC waveguide to a $w1.5$ reduces the propagation losses by moving away from extreme slow-light operation. Contrary to a regular $L_{n=61}$ with a flat band-edge, the tilted-potential supports a tilted band-edge, which renders the dispersion to be more linear, more fast-light-like; this means that the group index diverges less. Indeed, the tilted-potential cavity is generated by the adiabatic widening of the line defect in the transverse direction, from a $w1$ to a $w\left(1 + \frac{2s_{\max}}{\sqrt{3}a}\right) = w1.05$, $w1.10$, $w1.15$ with $s_{\max} = 10, 20, 30\text{nm}$, respectively. The effective length of the lower energy Airy-Bloch modes decreases with decreasing energy due to the tilted band-edge, which likely reduces the propagation losses. In

addition, the Urbach absorption tail [265]–[267] is a property the material choice (here GaAs) and its quality. Its contribution can be diminished by moving further away from the photonic band-edge of the barrier by decreasing the radius r . For a constant radius r , compared to a regular $L_{n=61}$, the Airy-Bloch modes are redshifted thanks to the tilted-potential, thus the contribution is naturally less important. All these considerations likely explain why past a certain point the Q factors rise again.

Finally, from Fig. 4:3(c) we can see that there are less components within the light cone as compared to the confined modes of the defect-potential (see Fig. 3:2(c)). This suggests a much better and smooth tailoring of the modes, which can be responsible for larger Q s, as was also evidenced using a Gaussian confinement profile thanks to a PhC heterostructure [164].

4.4.3 Experimental energy-position slopes dE/dx

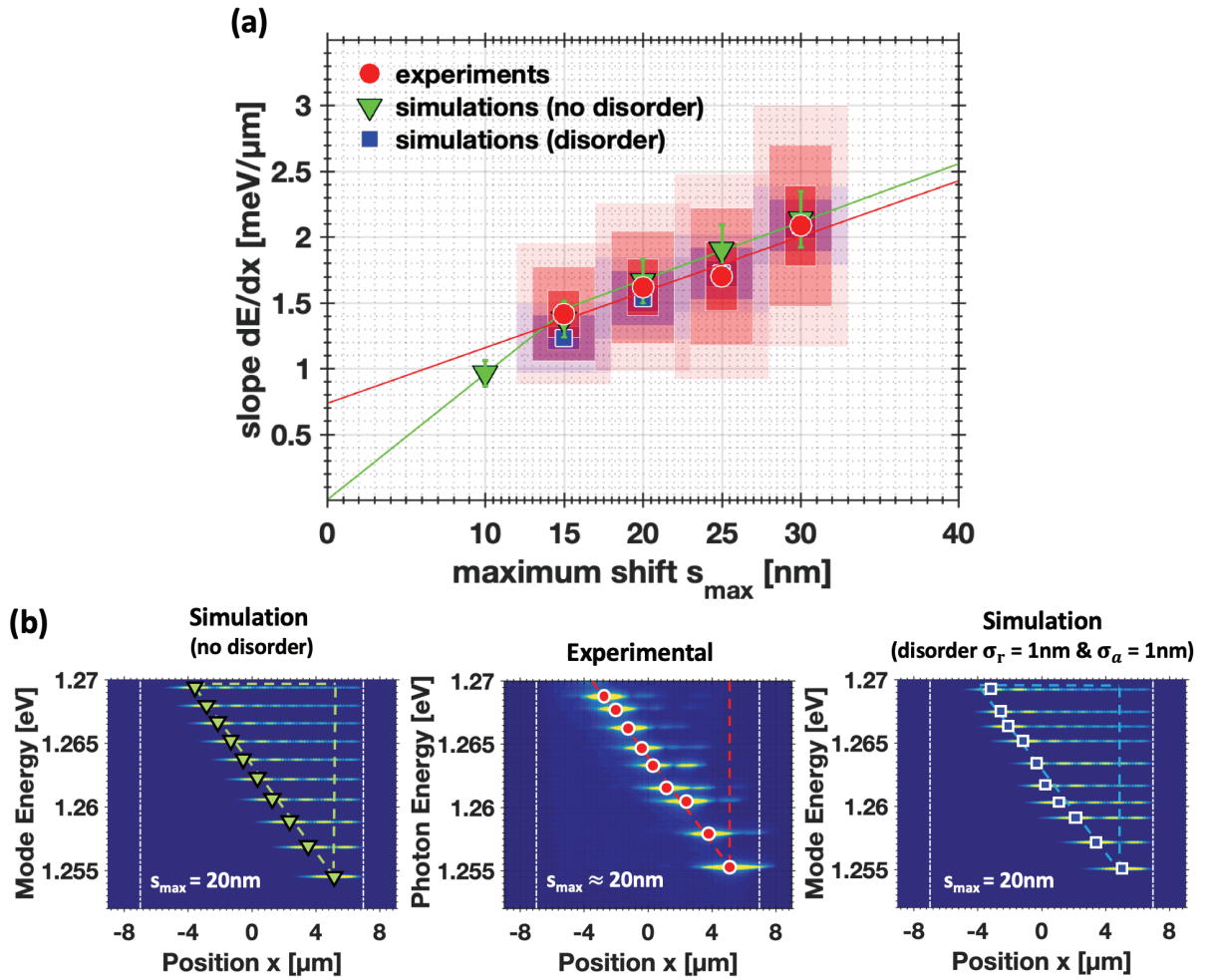


Fig. 4:14 – (a) Comparison of measured and simulated slopes $\frac{dE}{dx}$ of the Airy-Bloch mode main lobe positions versus maximum hole shift s_{max} . Red circles: experiment; shaded areas correspond to the statistical 1, 2, 3 σ variations of slopes measured from several structures and $\pm 1, 2, 3\text{nm}$ uncertainty in actual s_{max} values. Blue squares: simulations including disorder; shaded areas correspond to the statistical 1, 2, 3 σ variations of slopes extracted from simulations including both $\sigma_r = 1\text{nm}$ and $\sigma_a = 1\text{nm}$ for Gaussian distributions of hole radii and positions. Solid lines are linear fits to the corresponding symbols. Green triangles: slope values extracted from simulations without disorder; error bars correspond to 10% percent uncertainty in parameters. Solid green lines: linear for $s_{\text{max}} = 10\text{--}15\text{nm}$ and $s_{\text{max}} = 15\text{--}30\text{nm}$. (b) illustration of the procedure: energy-position mode patterns of selected corresponding measurements and simulations indicating the main lobe positions; $s_{\text{max}} = 20\text{nm}$. Reprinted and adapted with permission from [278]. © The Optical Society.

In **Fig. 4:14**, the experimental values of the gradient dE/dx extracted for several tilted-potential structures of different s_{\max} are compiled statistically with the averages (red filled circles) and standard deviations (red shaded areas). They are confronted with the values obtained from numerical simulations with (blue squares) and without (green triangles) disorder. The statistics are based on varying populations: 6 samples for $s_{\max} \approx 15\text{nm}$, 9 samples for $s_{\max} \approx 20\text{nm}$, 15 samples for $s_{\max} \approx 25\text{nm}$ and 10 samples for $s_{\max} \approx 30\text{nm}$. The 6 data points for $s_{\max} \approx 10\text{nm}$ were removed because, apart from a single or two structures very close to disorder free predictions, the other energy-position maps did not allow for a proper retrieval of meaningful dE/dx gradients. The blue data points accounting for fabrication related disorder were obtained as follows. For each value of s_{\max} , 10 simulations were run including both $\sigma_r = 1\text{nm}$ & $\sigma_a = 1\text{nm}$. The slopes dE/dx were extracted as usual, from linear regressions based on the loci of the mode maxima. From the statistics, averages and standard deviations of dE/dx were estimated to display the 2σ ($\sim 68\%$), 4σ ($\sim 95\%$) and 6σ ($\sim 99.7\%$) confidence intervals of the Gaussian normal distributions, represented by the blue shaded rectangles. Only 10 simulations per s_{\max} were ran due to time and resources constraints and the need to manually verify individual samples. The green symbols correspond to the values that were estimated rigorously in section 4.2.3. The blue data points were computed using the approximative energy correction that intrinsically comes with an 8-10% error in the estimation of the gradient (see section 4.2.2). The green bars actually account for 10% error, and the blue square averages fall within these, as expected.

The overlap of both the red and blue shaded areas provide information on the disorder level effectively present in the fabricated structures. The averaged slopes of all three symbols match to a very reasonable extent. The red regions are possibly overestimated, partly due to the low spatial resolution of the energy-position pictures (4 pixels per imaged spatial micrometer) which prevents accurate location of the true maxima. Nevertheless, the blue shaded confidence intervals are smaller than the red ones. It seems the red 2σ areas overlap better in energy with the blue 4σ , likely suggesting stronger disorder levels of $\sigma_r = 2\text{-}3\text{nm}$ & $\sigma_a = 1\text{nm}$ (or another equivalent combination), as discussed in chapter 3, section 3.1.4.

The green curve of the disorder-free slope dE/dx , was obtained by the stitching of two linear regression fits. The first linear part shows a steep increase for values below $s_{\max} \leq 15\text{nm}$, and values better behaved for $s_{\max} \geq 15\text{nm}$. The gradient dE/dx for $s_{\max} = 0\text{nm}$, corresponding to a regular cavity with a flat band-edge, is not well defined since the modes nearby the band-edge are symmetric and do not have Airy envelopes. However, this scenario constitutes a limiting case, by continuity, the gradient dE/dx should vanish to zero. A linear regression fit of the experimental average red data points yields a slope parallel to the second green line, with a vertical offset of only $0.2\text{meV}/\mu\text{m}$. This indicates a precise tailoring of the tilted-potential, where the slope is indeed well controlled by the s_{\max} shift parameter. The deviations occur approximately at the $dE/dx \approx 1.3\text{meV}/\mu\text{m}$ hinge point; considering the energy is $\sim 1.3\text{eV}$, this gives a ratio $dE/E \sim 10^{-3}$. Based on (Eq. 2:2) this also corresponds to a local quasi deterministic variation of the mode effective refractive index $dn_{\text{eff},\text{mode}}/n_{\text{eff},\text{mode}} \sim 10^{-3}$ due to the holes shifts.

4.5 Integration with single site-controlled QDs

In this section, we present experimental evidences for the coupling of single site-controlled QDs to selected Airy-Bloch modes of Tilted-Potential PhC Cavities.

4.5.1 Selective excitation of Airy-Bloch modes

Fig. 4:15 illustrates the selective excitation of Airy-Bloch modes by spatial and spectral matching of the feeding QD transitions. In **(a)** is shown the case of a reference structure with an array of QDs, excited with the usual 2 milli-Watts and line-shaped laser beam to evaluate the optical mode structure ($s_{\max} \approx 20\text{nm}$). In **(b)**, the selected structure has almost the same structural parameters. However, only two site-controlled QDs are embedded at the left and right parts of the tilted-potential cavity. The structure is optically pumped with the same conditions: same power level and laser spot shaped by the same cylindrical lens. The locations of the two quantum emitters are indicated by the orange and green dot-dash lines; they apparently intersect in particular with the specific lobes of Airy-Bloch modes, that are excited in the process. The selectively excited Airy-Bloch modes need to be matching the QDs both spatially and spectrally in order to feed the modes. Due to the many QD transitions excited at such high pump level, the QDs emit in a broadband range of photon energies, and thus many confined modes can be fed.

However, due to the specific positions of the QD emitters, only modes with significant spatial overlap with the point-like sources are excited.

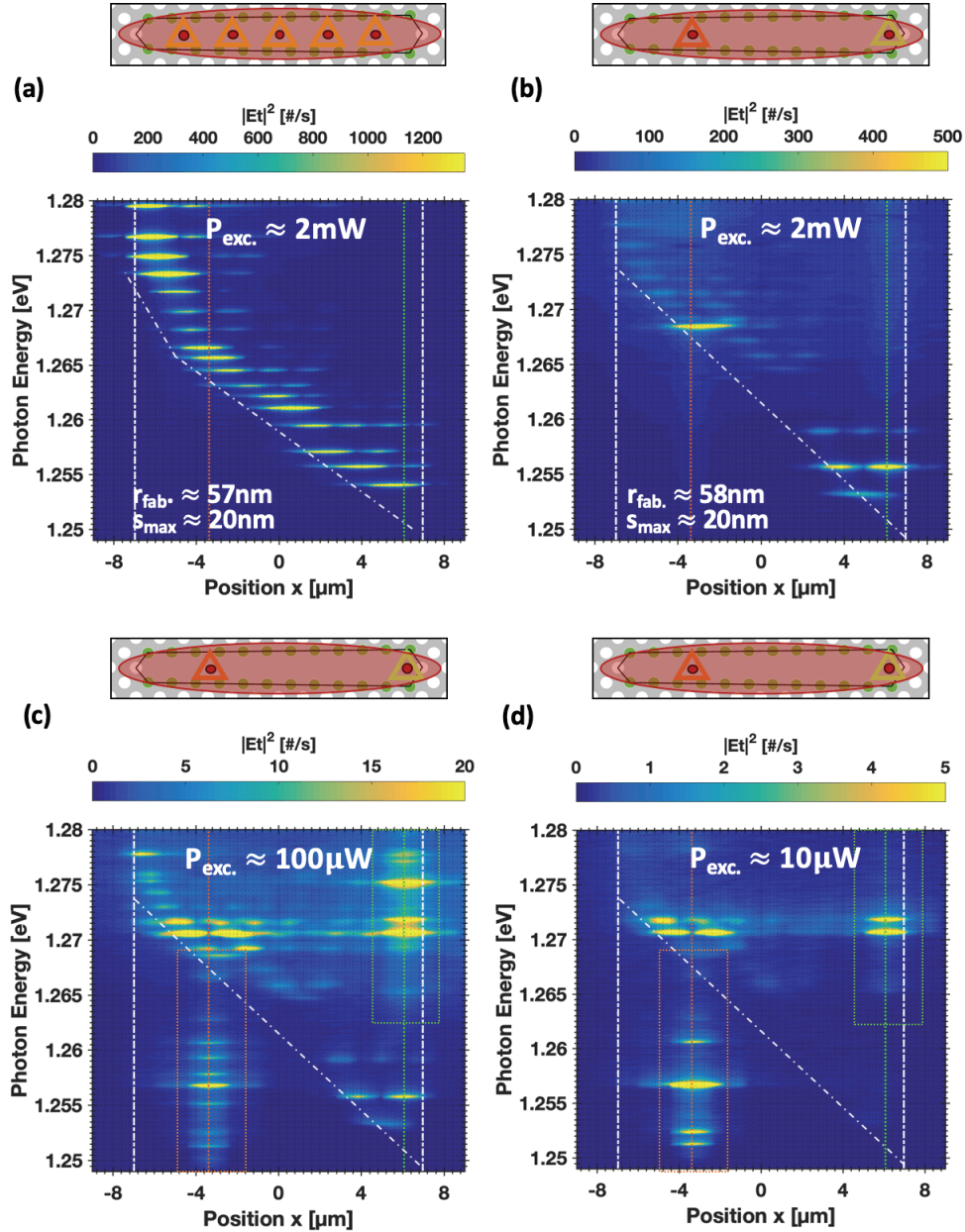


Fig. 4:15 – Selective excitation of Airy-Bloch modes using single site-controlled QDs, placed at specific positions along a tilted-potential cavity ($s_{\max} = 20\text{nm}$). Upper panels: schematics illustration of the cavity-QD system and excitation scheme. (a) Energy-position plot of optical mode patterns for $P_{\text{exc.}} \approx 2\text{mW}$ on a reference structure with multiple QDs: radius $r_{\text{fab.}} \approx 57\text{nm}$, $s_{\max} \approx 20\text{nm}$. Energy-position plots of optical mode patterns in structures with two QDs, for (b) $P_{\text{exc.}} \approx 2\text{mW}$, (c) $P_{\text{exc.}} \approx 100\mu\text{W}$ and (d) $P_{\text{exc.}} \approx 10\mu\text{W}$. Vertical white dash-dot lines mark the extremities of the cavity. Tilted white dash-dot line the band-edge. Vertical orange and green dot lines mark the positions of the two QDs. Above barrier excitation, laser wavelength $\lambda_{\text{exc.}} \approx 730\text{nm}$. Temperature $T \approx 10\text{K}$. Radius $r_{\text{fab.}} \approx 58\text{nm}$.

In (c), the various transitions of the QDs are revealed when decreasing the excitation power. They correspond to the s-shell and p-shell transitions, with the left-QD energies spanning over $\sim 1.25\text{-}1.27\text{eV}$ (orange rectangle), and the right-QD emitting at $\sim 1.265\text{-}1.28\text{eV}$ (green rectangle). The s-shell transition of the left-QD sits below the tilted band-edge of the cavity modes and is far-detuned from the Airy-Bloch modes at higher energies, with the main lobes overlapping this QD. However, excitation of these modes is possible via the p-shell QD transitions, near

1.27eV. In addition, the same Airy-Bloch modes can be fed by the right-QD, through their extended tails; but this excitation is less effective due to the small mode intensity there. Clearly, the Airy-Bloch modes at ~ 1.255 eV cannot be excited by the s-shell or higher energy transitions of either QD. Nevertheless, these Airy-Bloch modes are weakly excited, which could be explained by scattering of the left-QD light off the photonic potential boundaries of the cavity.

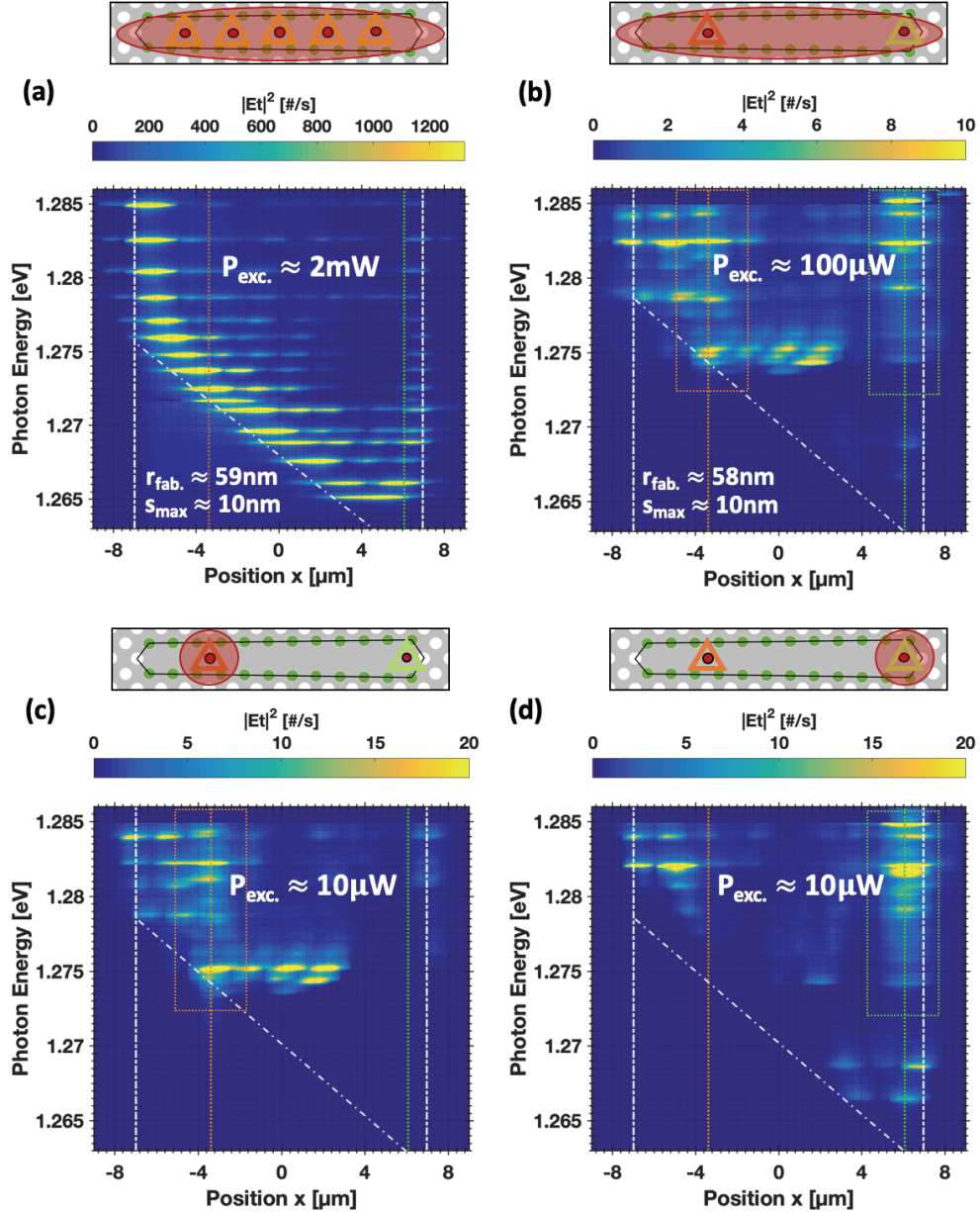


Fig. 4:16 – Selective excitation of Airy-Bloch modes using single site-controlled QDs, placed at specific positions along a tilted-potential cavity ($s_{\max} = 10\text{nm}$). Upper panels: schematics illustration of the cavity-QD system and excitation scheme. (a) Energy-position plot of optical modes patterns for $P_{\text{exc.}} \approx 2\text{mW}$ on a reference structure with multiple-QD excitation: radius $r_{\text{fab.}} \approx 59\text{nm}$, $s_{\max} \approx 10\text{nm}$. Energy-position plots of optical modes patterns for (b) 2-QD excitation at $P_{\text{exc.}} \approx 100\mu\text{W}$, and single-QD excitation with (c) $P_{\text{exc.}} \approx 10\mu\text{W}$ (d) $P_{\text{exc.}} \approx 10\mu\text{W}$. Vertical white dash-dot lines mark the extremities of the cavity. Tilted white dash-dot line the band-edge. Vertical orange and green dot lines mark the positions of the two QDs. Above barrier excitation, laser wavelength $\lambda_{\text{exc.}} \approx 730\text{nm}$. Temperature $T \approx 10\text{K}$. Radius $r_{\text{fab.}} \approx 58\text{nm}$.

This trend in mode excitation characteristics extends to even lower pump levels, as seen in (d). Here, only the left-QD excites the higher order Airy-Bloch modes, of which the main lobes overlap the QD spatially and the resonant energies are spectrally aligned with its p-shell transitions. None of the Airy-Bloch modes can be excited by the right-QD, as it does not overlap neither spectrally nor spatially with the main mode lobes. It should be noted

that the pyramidal site-controlled QDs can exhibit off-resonant weak coupling via phonons exchange, which at low temperatures occurs with detuning range of $\leq 2\text{-}3\text{meV}$ s [181]. This is contrary to SKQDs, in which the wetting layer makes possible coupling with much larger detuning [279]–[281]. These observations are consistent with the Airy-Bloch mode selective excitation demonstrated here.

Fig. 4:16 further illustrates selective Airy-Bloch mode excitation, this time with single QD pumping and a tilted-potential structure with $s_{\text{max}} \approx 10\text{nm}$. Part **(a)** shows the case for a reference structure with an array of QDs, as before. The structure pumped with two QDs (see **(b)**) shows QD emission lines that match spectrally each other better than in the structure of Fig. 4:15 (both QD emissions span the range $\sim 1.275\text{-}1.285\text{eV}$). Spot excitation at each of the QDs (see **(c)** and **(d)**) more clearly highlights the individual spectra of the two QDs. Whereas the ground state transitions of the left-QD well match some higher-order Airy-Bloch modes, the right-QD excites via its ground state transitions only some propagating modes of the parent long cavity. The right-QD very weakly excites lower-energy Airy-Bloch modes, probably through low energy tails of the QD emission that can arise from defects or charged excitons.

4.5.2 Weak coupling of a single site-controlled QD with an Airy-Bloch mode

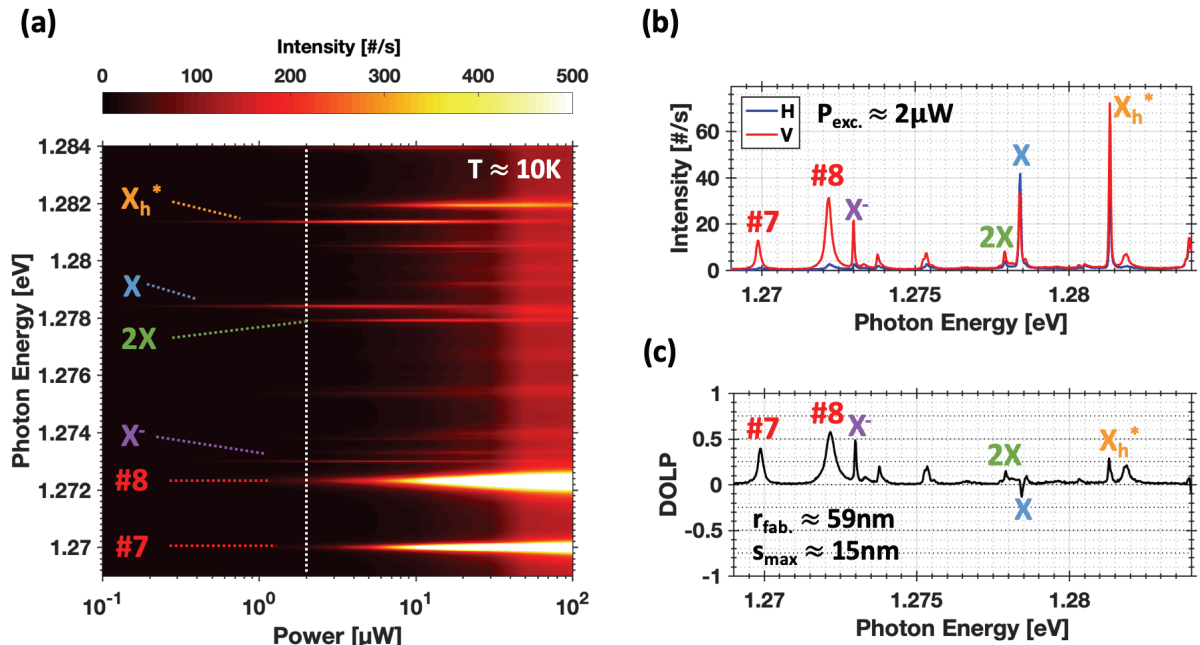


Fig. 4:17 – Identification of spectral lines in a tilted-potential PhC cavity with two embedded site-controlled QDs (focus on the left-QD as in Fig. 4:16(c)). **(a)** Spectra versus excitation power map; identified cavity modes and QD spectral lines are indicated. **(b)** Polarization resolved spectrum at $P_{\text{exc.}} \approx 2\mu\text{W}$ (dashed white line in **(a)**). **(c)** DOLP spectrum of **(b)**. Temperature $T \approx 10\text{K}$. Above barrier excitation, laser wavelength $\lambda_{\text{exc.}} \approx 730\text{nm}$. Radius $r_{\text{fab.}} \approx 59\text{nm}$, $s_{\text{max}} \approx 15\text{nm}$.

Fig. 4:17 shows the characterization of the spectral lines of a QD embedded at the left part of the tilted-potential structure as in Fig. 4:16(c), with $r_{\text{fab.}} \approx 59\text{ nm}$ and $s_{\text{max}} \approx 15\text{nm}$. The identification of spectral lines is performed by an excitation power dependence. The map in **(a)** was made by stitching intensity spectra taken at $P_{\text{exc.}} \approx 0.1, 0.2, 0.3, 0.5, 0.8, 1, 2, 3, 5, 8, 10, 20, 30, 50, 80$ and $100\mu\text{W}$, all with above barrier spot excitation. Two cavity modes are identified thanks to their broad linewidths $\hbar\kappa \approx 160\mu\text{eV}$ and $\hbar\kappa \approx 217\mu\text{eV}$ and their non-saturating behavior. The modes are labelled #7 and #8 by comparison to a numerical simulation of the mode pattern using proper structural parameters. The faint traces of poorly fed, other higher-order Airy-Bloch modes can be seen, almost evenly spaced every $\sim 2\text{meV}$ s; in particular one is seen at $\sim 1.282\text{eV}$. The thinner lines with $\hbar\gamma < 100\mu\text{eV}$ are QD lines. The lowest energy line that appears first is assigned to the negative trion X; this is further confirmed by the presence of the bound 2X-X couple approximately $\sim 5\text{meV}$ s higher in energy.

In this case $E_{X,2X}^{bind} \approx -0.5\text{meV}$. Similar to chapter 3, the prominent line, which is blue shifted by $\sim 3\text{meV}$ s with respect to the X, and is triggered in conjunction to the X- and the X lines, was attributed to the neutral excited hole-state X_h^* [110]. Part (b) shows the V-polarized and H-polarized spectra measured at $P_{exc} \approx 2\mu\text{W}$, and (c) presents the corresponding DOLP versus photon energy. These show more clearly the distinction in linewidths of cavity modes versus QD spectral lines and the close to vertical polarization signatures of these Airy-Bloch cavity modes of the 1st band. The DOLP values of $\sim 0.4\text{-}0.55$ are comparable to the values for the high order Airy-Bloch modes of Fig. 4:11(d). The QD transitions are already influenced by the polarization of the modified PhC medium, and the values are also consistent with Fig. 4:11(d). The 2X-X fine structure H, V splitting can be seen, although it is less pronounced than for the sample of chapter 3.

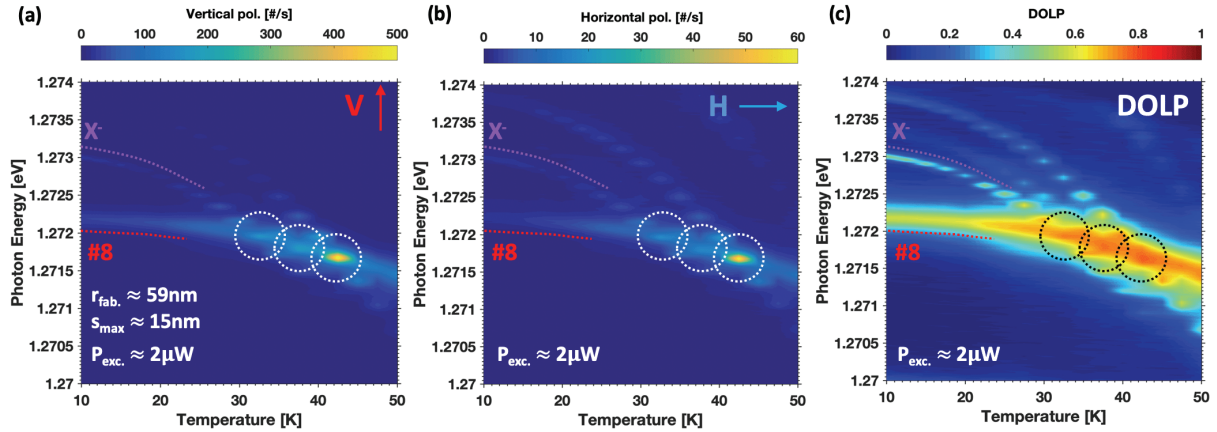


Fig. 4:18 – Temperature tuning of the negatively charged exciton (trion) X^- and Airy-Bloch mode #8 identified in Fig. 4:17. Spectral maps show (a) V-polarization component, (b) H-polarization component and (c) associated DOLP. Quadratic red-shifting trajectories are displayed in dotted lines. Dotted circles highlight crossings of the X^- and two others unidentified QD lines with the cavity mode #8. Above barrier excitation, laser wavelength $\lambda_{exc.} \approx 730\text{nm}$, excitation power $P_{exc.} \approx 2\mu\text{W}$. Excitation scheme similar to that of Fig. 4:17(c). Radius $r_{fab.} \approx 59\text{nm}$, $s_{max} \approx 15\text{nm}$.

The X^- line is already strongly co-polarized at 10K with the Airy-Bloch mode #8, a clear evidence of weak coupling [180], [181]. The temperature tuning of the emission spectra displayed in **Fig. 4:18**, with $2\mu\text{W}$ above barrier spot excitation, shows how the QD emission lines are brought into resonance with this mode. (a) The V- and the (b) H-polarized intensity maps look similar, but there is a factor of ~ 8 between the two intensity color scales. Part (c) combines the two previous images to generate the DOLP map, which is saturated at zero value for visualization purposes. The graphs were realized by stitching spectra taken at regular intervals of 2.5K and interpolation is applied to display smooth continuous maps. For the same reason as discussed in chapter 3, the QD lines trajectories appear modulated due to this interpolation technique. The trajectories of the X^- and the cavity mode are clearly visible with their different quasi-quadratic variations as a function of temperature. Owing to this discrepancy, and since the X^- was initially blue-shifted from the CM at $\sim 1.272\text{eV}$ by approximately $\sim 1\text{meV}$, the two paths cross into a resonance at a temperature of $T \approx 32.5\text{K}$. Two more resonances by other QD lines with the same CM are also visible at $T \approx 37.5\text{K}$ and $T \approx 42.5\text{K}$, as marked by the white and black dot circles. They come from excited states, non-labelled QD spectral lines, originating at $T=10\text{K}$ respectively at $\sim 1.2733\text{eV}$ and $\sim 1.2738\text{eV}$. The latter resonance shows very clearly an important (more than $\sim 5\text{-fold}$) increase in intensity at the resonance point, due to the associated Purcell effect. The trajectories are better seen in (c). All three lines display a clear V-co-polarization effect with respect to the V-polarization of the Airy-Bloch mode #8.

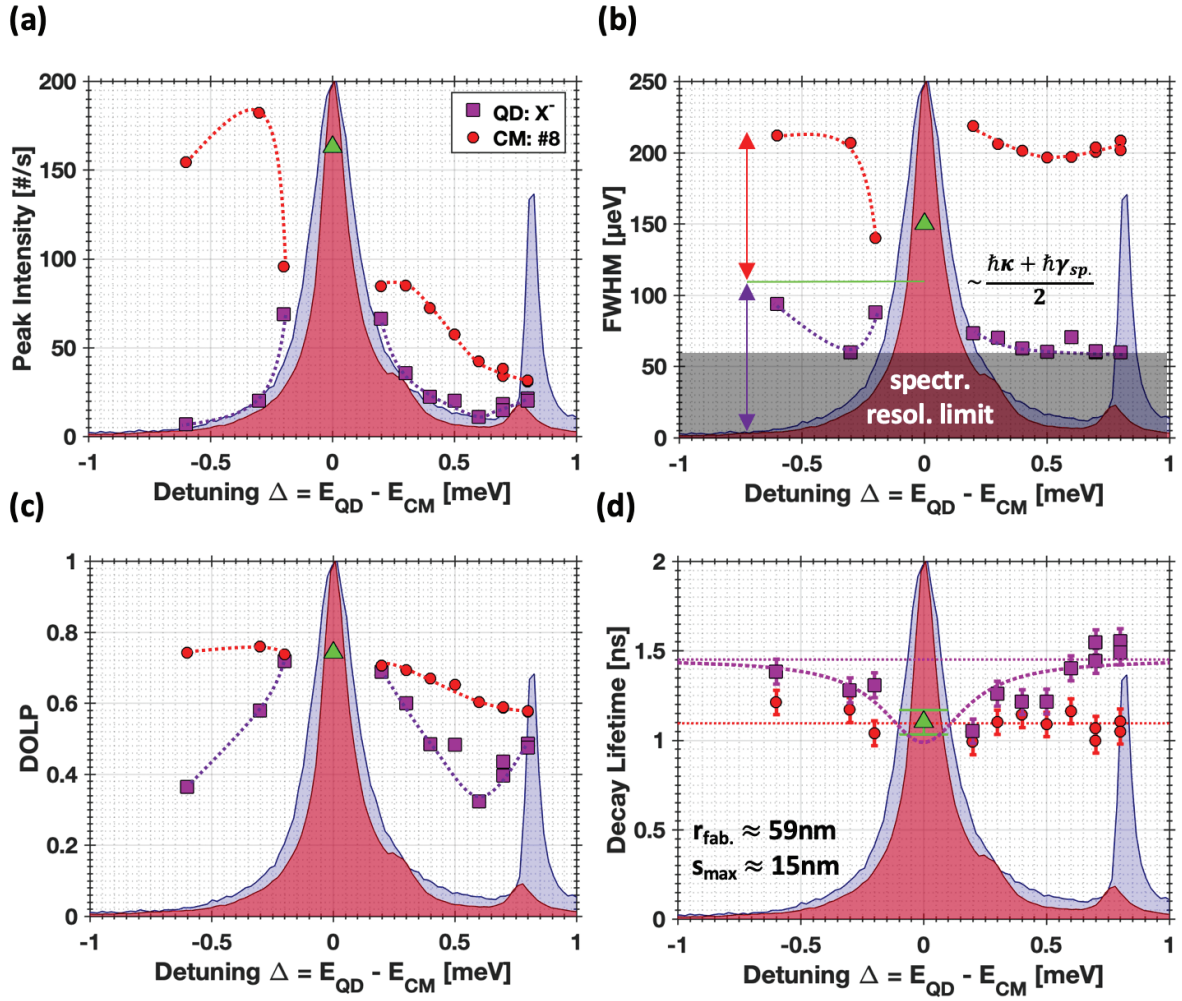


Fig. 4:19 – In-depth analysis of the weak coupling of a single QD to an Airy-Bloch mode. Data in (a-c) extracted from Fig. 4:18 and displayed as a function of the detuning with respect to the Airy-Bloch cavity mode #8 energy. From the vertical polarization signal using Lorentzian fits: (a) peak intensity, (b) full-width at half maximum. From both H & V polarizations: (c) degree of linear polarization. From time-resolved measurements: (d) decay lifetimes. Numerical parameters for the Purcell fit: $\hbar\kappa = 217\mu\text{eV}$, $\hbar\gamma_{QD} = 60\mu\text{eV}$. Blue shaded area: starting normalized spectrum of the cavity mode (center) and the detuned QD line at $T \approx 10\text{K}$; red shaded area: situation on resonance at $T \approx 32.5\text{K}$. The two bumps visible in the latter, at $\Delta = +0.25\text{meV}$ and $+0.8\text{meV}$ correspond to the two blue-shifted non-labelled QD lines visible in Fig. 4.18. Above barrier excitation, laser wavelength $\lambda_{\text{exc.}} \approx 730\text{nm}$, excitation power $P_{\text{exc.}} \approx 2\mu\text{W}$. Radius $r_{\text{fab.}} \approx 59\text{nm}$, $s_{\text{max}} \approx 15\text{nm}$.

The more detailed characteristics of the weak coupling are presented in **Fig. 4:19**, which plots the various relevant quantities as a function of the detuning with respect to the cavity mode energy. The study here focuses only on the first complete resonance at $\sim 1.2719\text{eV}$, to display the phenomenon at both positive and negative detuning values. Intensities in (a) and FWHM of the X- and cavity mode lines in (b) were obtained from the fit of the sum of two Lorentzians based on the V-polarized spectra. The DOLP in (c) was read from Fig. 4:18. Lifetime decays in (d) were obtained by time-resolved PL measurements (see chapter 2). The green triangle symbols correspond to the data points estimated on resonance, where the QD and mode lines superpose. The dotted lines in (a-c) are visual guides to the eye. In (d), the magenta dotted line is based on the physical interaction model of (Eq. A:1). The blue and red shaded areas are respectively the initial normalized spectrum at $T \approx 10\text{K}$ and the normalized resonant spectrum at $T \approx 32.5\text{K}$.

The Purcell effect is manifested first by the enhancement in intensity of the X- line near zero detuning; the overlapped QD-CM line shows an enhancement by a factor of ~ 8 as compared to the exciton line at large detuning. This enhancement is accompanied by the narrowing of the overlapping QD-CM line on resonance, compared to the bare Airy-Bloch cavity mode. On resonance, the FWHM of the overlapping line takes a value of $\sim 150\mu\text{eV}$, close to the average $\sim 139\mu\text{eV}$ of the bare QD $\hbar\gamma_{\text{QD}} \approx 60\mu\text{eV}$ (spectrometer resolution limit) far away from resonance, and of the bare CM with a width of $\hbar\kappa \approx 217\mu\text{eV}$. At further negative detuning the X- intensity eventually vanishes and its linewidth broadens, likely due to exciton dissociation with increasing temperature [117]. The mode intensity variation is not symmetric with respect to the resonance, possibly also due to the second and third resonances occurring in turns. Both the intensity and FWHM versus detuning (via temperature variations) behaviors can be compared to the study of chapter 3 and previous works on pyramidal site-controlled QDs weakly coupled to L_n PhC cavities [194], [219]–[221].

The DOLP profile of the CM shown in (c) is not flat, but surprisingly decreases from ~ 0.77 to ~ 0.6 for increasing detuning. The QD on the other hand, shows complete co-polarization with the cavity mode at zero detuning, and its DOLP drops to ~ 0.3 – 0.4 for both negative and positive detuning of $\sim 0.6\text{meV}$. The range of influence of this co-polarization effect, $\sim 1.2\text{meV}$, is roughly the full spectral width of cavity mode #8. As indicated by the red spectrum, two bumps are seen, one at the base of the merged resonance line at $\Delta = +0.25\text{meV}$ and the other at $+0.8\text{meV}$. These correspond to the two blue-shifted, non-labelled QD lines visible in Fig. 4:18, approaching resonance. Between $+0.6$ and $+0.8\text{meV}$ detuning the QD DOLP increases to $+0.5$, this is supposedly an effect of Airy-Bloch #9 expected at $\sim 1.274\text{meV}$ (see the faint trace in Fig. 4:17), which still influences the polarization despite not being well fed and visible in Fig. 4:18. This resonant co-polarization effect is in good agreement with observations reported with pyramidal site-controlled QDs in other types of PhC cavities in [180], [181], [221].

The decay times of the different spectral lines, shown in (d), were extracted using the time-resolved PL setup described in chapter 2, section 2.3.3. The lifetime of the Airy-Bloch mode is fairly constant with an average value of 1.1ns over the range of detuning. While not as pronounced as in the samples discussed in chapter 3, the decay times of the X- still visibly decreases from a maximum value of $\sim 1.6\text{ns}$ down to the lifetime of the CM $\sim 1.1\text{ns}$. At zero detuning, the decay time measured should be a combination of those of the merged spectral lines. It is thus not clear if the CM is limiting the measurement of faster decays. The weak Purcell effect on the exciton lifetime can be partially ascribed to the poor overlap of the QD with the maximum intensity peak of the mode. We estimate a factor $\zeta^2 \approx 0.1$ from the ratio of the intensity at the position of the QD to that at the maximum intensity at the mode “head”. Omitting effects of phonons and assuming $\tau_{\text{leak}} = \tau_{\text{sp.}}^{\text{homog.}}$, because the data does not evidence clearly the behavior evidenced in [194], three free parameters $\tau_{\text{sp.}}^{\text{homog.}}$, F_p^{max} and ζ^2 are kept in expression (Eq. A:1), with which a fitting yields $\tau_{\text{sp.}}^{\text{homog.}} = 1.45 \pm 0.08\text{ns}$, $F_p^{\text{max}} = 20$ and $\zeta^2 \approx 0.04$ misalignment factor in agreement with the observation. From these two parameters, an effective Purcell enhancement factor of $Enh \approx 1.3 \pm 0.1$ was estimated with (Eq. A:2). Another factor leading to a decreased Purcell effect is the relatively large volume of the Airy-Bloch modes. The mode volume of the fundamental modes of L_n cavities grows practically linearly with the axial length. Mode #0_M⁽⁰⁾ of the defect-potential was approximately $\sim 2\mu\text{m}$ long, while the Airy-Bloch mode #8 is roughly $\sim 14\mu\text{m}$ long, giving a ratio of ~ 7 , on the other hand the Qs of the two modes are comparable, $Q_{\text{defect}} \approx 6'900$ and $Q_{\text{tilted}} \approx 5'900$. Between the two enhancement ratios, there is a factor of $Enh_{\text{defect}}/Enh_{\text{tilted}} \approx 5.8$ that is commensurate with the product of the ratio of the Qs divided by the ratio of the mode volumes, i.e. of the longitudinal extent of the two modes, since $Enh. \propto F_p^{\text{max}} \propto Q/V_{\text{eff. mode}}$. Based on only the known enhancement factor $Enh.$, a minimum beta factor $\beta^{\text{cav.}} \approx 0.24 \pm 0.06$ coupling efficiency can be estimated with (Eq. A:4), comparable to the data of Table. 1:1 in chapter 1.

By solving equation (Eq. 1:16) with the value of linewidth $\sim 150\mu\text{eV}$ on resonance, a coupling constant $\hbar g \approx 50\mu\text{eV} < \frac{(\hbar\kappa - \hbar\gamma_{\text{sp.}})}{4} \approx 54\mu\text{eV}$ can be extracted, comparable to that of the defect structure in chapter 3. This linewidth of $\sim 150\mu\text{eV}$ on resonance is attributed to the dominant QD transition. The linewidth of the cavity might be estimated at $\sim 67\mu\text{eV}$ with the second expression from (Eq. 1:16), distributed symmetrically around the average of $\sim 109\mu\text{eV}$, as indicated in Fig. 4:19(b).

The tilted-potential structure may be compared to the composite structure comprising a $L_{n=3}$ PhC cavity side-coupled to a PhC semi-waveguide [83], [144], [282], [283] since both support photonic wavefunctions with a localized component and an extended part. In the case of the composite structure, an enhancement of the intensity of the spontaneous emission as high as ~ 7 was reported [144]. This can be explained by a more favourable alignment and overlap factor $\zeta^2 \approx 0.6-1.0$ and possibly a stronger local confinement in the $L_{n=3}$ in that case.

4.6 Conclusion of chapter and perspectives

This chapter presented the case study of a more elaborate photonic heterostructure: the tilted-potential PhC cavity. It is implemented here by the staggered shifts of all side holes, from one end of the cavity to the other, up to maximum shift value of s_{\max} smaller than the pitch. The study combined again both numerical modelling of the optical modes and the analysis of experiments conducted on fabricated structures. Intuitively the tilted-potential can be thought as the sum of defect-potentials displaced along the cavity axis and of regularly increasing depths. This adiabatic tapering effectively breaks the symmetry along the cavity axis and forms a triangular potential below the band-edges of the base waveguide. Such a new type of photonic potential supports Airy-Bloch cavity modes, where Airy function envelopes modulate the Bloch crystal term. It locally defines a more intense cavity-like main lobe on the narrower side of the cavity, connected to an oscillating waveguide-like tail comprising secondary lobes, extending towards the wider side. Due to the tilt of the photonic band-edges, the location of the main-lobes follows the quasi linear slope of the potential. This characteristic is encompassed by the gradient dE/dx related to the mode energy and position of the main lobe that is defined and analyzed. The slope is fully controlled by the single structural parameter s_{\max} . A study on disorder effects demonstrates that the tilted-potential structures display some resilience to Anderson localization up to certain threshold levels of fabrication disorder, which increases with increasing s_{\max} . Intuitively, the tilt allows the parts of the photonic wavefunctions, that would be trapped by potential corrugations in a flat potential, to tunnel out and delocalize over the full length of the PhC cavity. The experimental data showed a quasi-deterministic behavior of the mode structure with gradients dE/dx commensurate with the numerical predictions provided $s_{\max} \geq 15\text{nm}$, imposed by the disorder level involved in this sample. This behavior and the relatively large Q-factors in the range $\sim 5'000-10'000$, provided the basis for achieving with such structures a deterministic weak coupling of a single pyramidal site-controlled QD to a single Airy-Bloch mode. The experimental characterization of the Purcell Effect involved a variety of clear resonance detuning-dependent signatures: QD intensity increase, mode linewidth decrease, co-polarization and decay time reduction of the QD emission. A modest enhancement of the spontaneous emission rate of $Enh. \approx 1.3 \pm 0.1$ was estimated, possibly limited by the large mode volume and imperfect spatial overlap. The effect is associated with an estimated coupling constant of $\hbar g \approx 50\mu\text{eV}$ below and a coupling efficiency factor $\beta^{cav.} \approx 0.24 \pm 0.06$.

The Airy-Bloch photonic wavefunctions are reminiscent of the ones manifesting in the $L_{n=3}$ cavity side-coupled to a semi-waveguide system, which is known to be efficient for single photon extraction and in-plane transmission towards a remote destination when coupled to a properly positioned QD. By analogy, the tilted-potential cavity coupled to a waveguide channel might produce an efficient single photon injector. Finally, the specific intrinsic feature of “mode energy versus position of the main lobe” correlation may provide an elegant mean for the compact wavelength-multiplexing of several properly positioned, wavelength-shifted QDs emitters resonantly interacting with the main lobes of various targeted Airy-Bloch modes.

Chapter 5 Towards a functional integrated QD-PhC device

Departing from tailored-potential structures, the focus is now shifted back to the original, broader picture of a GaAs-based monolithic, functional integrated quantum photonic devices incorporating site-controlled quantum dots embedded in a photonic crystal circuit.

Following this endeavor, a more complex model circuit was fabricated and explored, involving a variety of elements as a showcase to demonstrate the potential of this platform. With the possibility of on-chip generation of single photons, processing of these photons by a resonant QD coupled to a cavity has in fact been considered but not fully accomplished [217], [284]. As a generic device, we consider here a system of two PhC waveguides coupled via a PhC cavity, equipped with grating couplers serving as input and output ports to free space beams. Site-controlled QDs are inserted in order to explore interaction with particular confined modes. The study also explores the prospects of on-chip generation of single photons by in-plane quasi-resonant excitation through optical injection via the couplers. The results also provide insights on requirements for future on-chip laser sources that could be interfaced with photonic cavities and waveguides structures in views of on-chip QD optical pumping.

This test platform is introduced in **section 5.1**, which also discusses how various parts of the model structure can represent important functionalities of a more general integrated chip. **Section 5.2** covers details on the components of the fabricated structures. In **section 5.3**, the experimentally observed optical mode structure is interpreted. In-plane injection of laser light for quasi-resonant pumping of the embedded QDs is illustrated in **section 5.4**.

5.1 Typical functional devices and their experimental model

A QIP circuit based on the integration of site-controlled QDs inside PhCs involves a non-trivial combination of engineered cavity and waveguide elements to realize specific functions. This section reviews several such functionalities that can be achieved with combinations of PhC cavities and waveguides. A fabricated device that encompasses several such functionalities is then presented and its separate components are analyzed in view of the desired functionalities.

5.1.1 Example of functional integrated QD-PhC devices

Several examples (non-exhaustive list) of functional QIP elements for processing single photons is presented in **Fig. 5:1**. Different functionalities have already been proposed with basic single cavities or single waveguides incorporating systems of QDs (upper panel). An H_1 cavity with a degenerate (H & V) fundamental cavity mode tuned in resonance with a virtual state at the middle energy between X and 2X states can produce polarization-entangled pairs of photons [285] which can be collected with an optical fiber. A network of such cavities could be used for scaling up this effect, since the polarization-resolved HOM effect has been reported for photons emitted by remote QDs [286]. The experimental generation of such two-photon states based on the leapfrog virtual process was demonstrated [258] using a single QD in resonance with a structure analogous to the defect-potential. The correlated transport of such two-photon states in a waveguide can be altered by the addition of site-controlled QD in resonance [216], [287].

Several combinations of such elements can be constructed for functions more complex than photon extraction or routing. The middle panel of **Fig. 5:1** depicts the simpler combinations of two PhC elements. The 2C structure represents a photonic molecule consisting of the coupled modes of two single-mode PhC cavities, with a site-controlled QD inserted in one cavity, and with the 2X two-photon virtual transition [114] in resonance with its mode. The resonant excitation of the QD generates a path-entangled two-photon N0-0N state [288]. A quantum interference process removes the possibility of having the two photons separated, each in a different cavity. With another site-controlled QD in the second cavity, a four-photon N0-0N state could be realized [288].

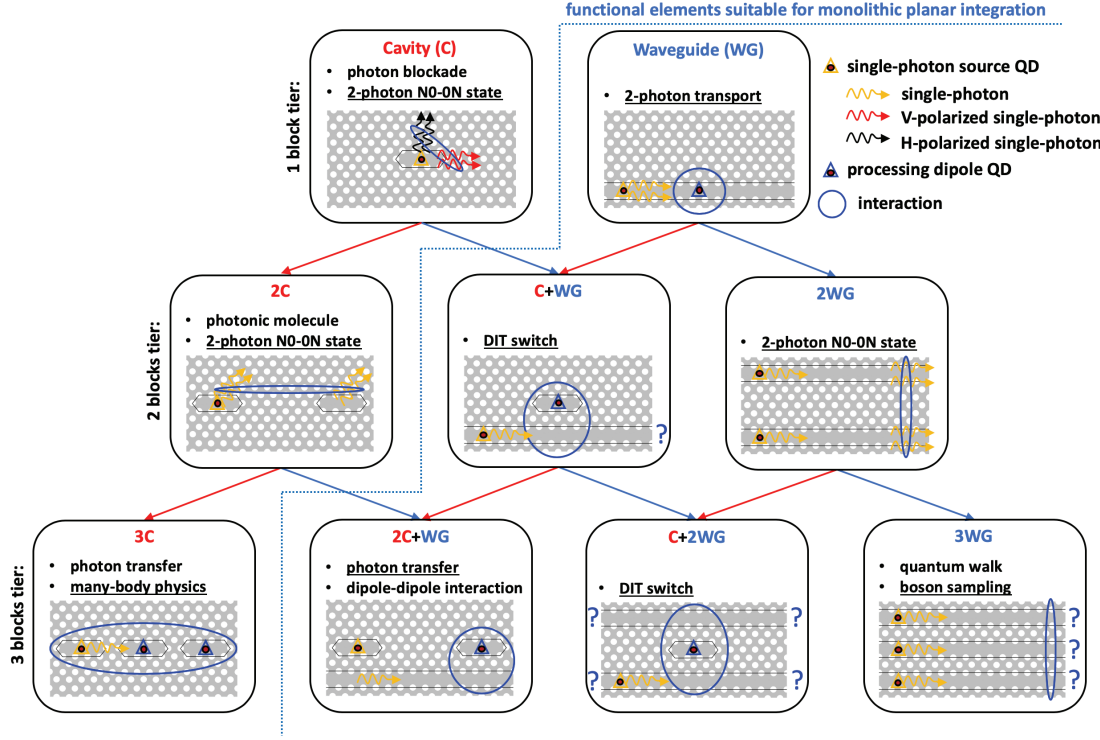


Fig. 5:1 – PhC functional elements for QIP devices. Top panel: the basic photonic elements: a PhC cavity for strong confinement and a PhC waveguide for routing. Middle and bottom panels: functional integrated circuits with increasing complexity; functionality indicated in the insets. Site controlled QDs are integrated at specific positions according to desired functionality (see text).

The C+WG structure in the middle panel provides a non-linear routing switch based on a dipole induced transparency (DIT) effect [284], [289], [290]. The scheme requires a site-controlled QD which coupling to a cavity mode, itself coupled to a waveguide mode, can be modified. If the QD is out of resonance, the channel is opaque for incoming single photons. If resonant, the dipole interferes with the optical field and renders the channel fully transparent [290]. Encouraging experimental results have been demonstrated [37], [217], [291]. The 2WG configuration, with a 50/50 coupling ratio functions as a classical beam-splitter. It thus exhibits the Hong-Ou-Mandel (HOM) effect [98], [292] when two incident single photons interfere in it. The reflection and transmission can mutually interfere and produce a path-entangled two-photon N0-0N state. To this end, two resonant site-controlled QDs must be integrated, one in each waveguide, and excited simultaneously. The effect has been demonstrated with two remote QDs placed in separate cryostats [70].

The bottom panel of **Fig. 5:1** shows more complex combinations of three PhC elements. The 3C (extendible to more cavities) structure provides a platform for studying quantum many-body physics arising from polariton-polariton interaction [293]. One site-controlled QD per cavity is required. They must be all strongly coupled to a delocalized super-mode to transmit the excitation from a QD to another by radiative coupling [294]. In the 2C+WG configuration, the waveguide acts as a fast-light bus to radiatively connect the two distant optical fields of the cavities. The three PhC elements must be strongly coupled together so that the field can beat periodically between the two cavities [295], [296]. Single photons generated by a single resonant QD embedded in one of the cavities

can then be transferred all the way to the other cavity [262], [297], in which another strongly coupled and resonant site-controlled QD could absorb them.

The C+2WG structure in the bottom panel is classically known as an add-drop filter [298]. It is an extension of the C+WG structure and hence also presents the capability for DIT with a tunable site-controlled QD embedded in the cavity. With a regular cavity, two states are allowed: complete transparency or full scattering [289], [290], [299]. With a ring resonator, supporting travelling waves, the switching operation is complete [284], [299] and routes the signal from one waveguide to the other. Contrary to the C+WG case, the single photon is not lost. The interference between the outputs of two such devices can herald successful entanglement of two remote dipoles [284]. Finally, the 3WG (or more waveguides) structure creates linear arrays in which the relative phases and coupling distances can be adjusted. Site-controlled QDs would be required to feed the waveguides with configurable Fock states. This can be done either with the routing and delaying of the single-photon stream generated by a single site-controlled QD [214], [300], or alternatively, by the simultaneous excitation of spatially multiplex site-controlled QDs. These arrays are useful to probe the phenomena of quantum walk [301], [302] of single photons self-interfering during propagation, or boson sampling of multiple indistinguishable, path entangled single photons [303] relying again on the HOM effect.

5.1.2 Experimental model

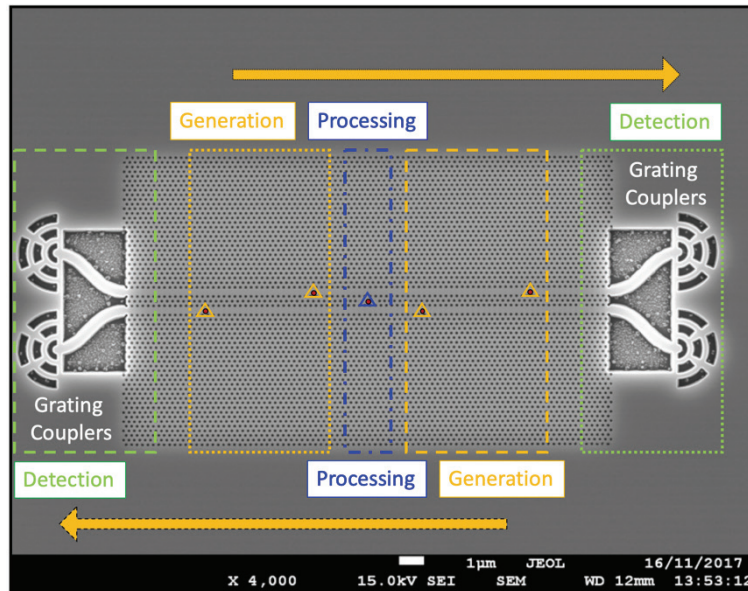


Fig. 5:2 – SEM image of a fabricated model structure for a functional QD-PhC devices incorporating a single cavity coupled to two waveguides (C+2WG) and several embedded site-controlled QDs. The four output ports are connected to grating couplers by suspended nanobeams. Generation, Processing and Detection regions are specified respectively in yellow, blue and green (as in Fig. 1:1). Dotted (dashed) line regions are associated together. Note that the device is asymmetric.

We selected one of the functional elements of Fig. 5:1, the C+2WG structure, as an experimental model for investigating the ingredients of several functionalities (see Fig. 5:2). The fabrication process and structural details are presented in section 5.3. This device already forms a simple QIP circuit in itself, including the three regions of Generation of quantum light with embedded site-controlled QDs, Processing, and eventual Detection of single photons. It consists of two PhC waveguides coupled via an $L_{n=3}$ cavity, interfaces between PhC region and suspended nanobeams, and grating output/input couplers. As indicated in Fig. 5:2, several sub-components serve for different generic functionalities. These are treated separately in what follows, before considering the operation of the entire structure as a whole.

5.1.2.1 Generation: single photon extraction and transport

The part of generation (yellow) encapsulates two PhC waveguides, with embedded single QD sources. Fully understanding this section requires the knowledge of the mode structure of a single PhC waveguide and how a QD couples to the waveguide modes. The generation, extraction and guiding of single photons in single PhC waveguides integrated with pyramidal site-controlled QDs, has already been reported with $\beta \geq 0.98$ coupling efficiency [203]. The Purcell effect in waveguides is weaker than in cavities, owing to the extended photonic wavefunctions. The Purcell effect is proportional to the group index n_g [80], rather than being proportional to $Q/V_{\text{eff,mode}}$ in a cavity structure. In other words, the closer one is to the photonic band-edge, the slower is the light, and the larger is the interaction between the mode electric field and a QD's dipole. But in real structures, photons can easily be trapped near band-edges by Anderson localization arising from fabrication imperfections. Anderson localized modes are basically random cavity modes produced in a disordered waveguide. They exhibit significant interaction with coupled QDs [92], but they prevent free light propagation and are associated with enhanced out-of-plane scattering losses [97]. This is why PhC waveguides are currently better used in the fast-light regime to allow efficient photon transfer.

The identification of the mobility-edge, of the propagating and Anderson-localized mode regimes in PhC waveguides coupled with pyramidal QDs using spatially-resolved spectra has been reported [252]. Here we examine the same effects in PhC waveguides similar to the ones used in our model system. In **Fig. 5:3**, spatially-resolved spectra (details in chapter 2) of a PhC waveguide ($\sim L_n=87$) connected to two grating couplers incorporating five pyramidal site-controlled QDs, with different configurations of photo-excitations, are displayed. The QDs are evenly spaced with $x=-9.0, -4.5, 0, +4.5, +9.0\mu\text{m}$. An above barrier, high-power excitation with a strip-shaped laser beam reveals the approximate location of the photonic band-edge, visible by the Anderson localized modes appearing as bright spots at random locations. At photon energies above the Anderson band, light is guided from one grating to the other by the PhC waveguide. Below the Anderson band, light does not propagate along the waveguide due to the PhC bandgap. Light is still visible in the vicinity of the grating couplers because of residual scattering of the QD light and emission from parasitic QDs remaining at the coupler regions. In **(b)**, the low-power spot excitation of the center QD reveals its s- & p- shell excitonic lines, which are below the band-edge in this case. In **(c)**, with a medium-power spot excitation, more QD states are filled, in particular the d-shell emits light above the photonic band-edge. The distinction between no guiding and waveguiding regimes can be seen. The Anderson-localized modes spatially overlapping with the single QD source reappear. Despite the decaying of the radiation in the photonic bandgap, some QD emission still reaches both the left and right couplers. This is even more visible in **(d)**, with still higher-power spot excitation. In this case, the low-energy shells of the QDs are saturated. The light that is not coupled to a guiding mode mostly scatters vertically at the location of the QD, while above the band-edge guided modes are visible. A sharp and intense Anderson mode can also be noticed right above the band-edge. Parts **(e-f)** show similar observations, this time with the first left and right site-controlled QDs excited. The distance between the QDs is large enough to prevent the diffusion of carriers from feeding multiple QDs.

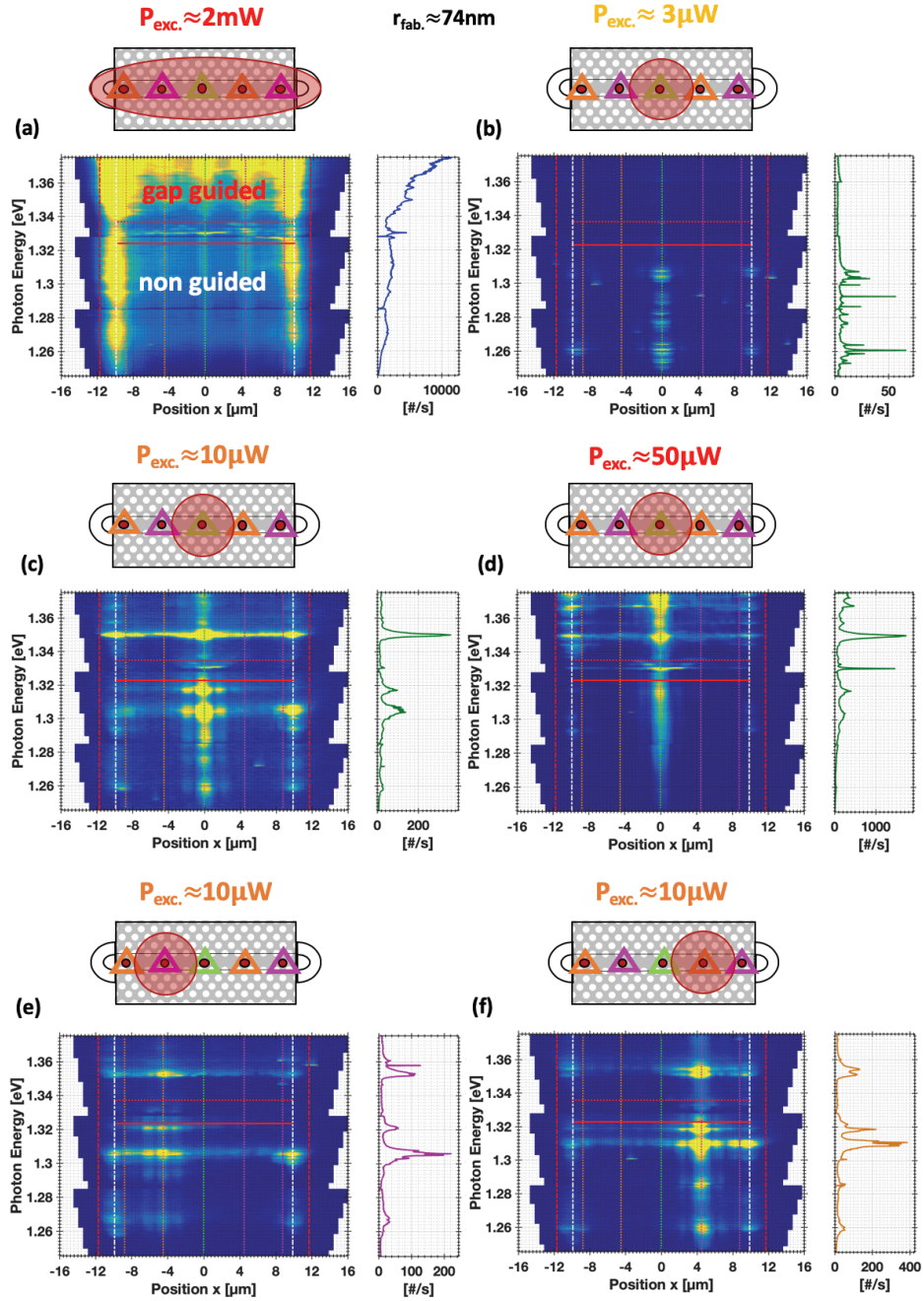


Fig. 5:3 – Measured optical mode structure of an open waveguide with five embedded QDs and terminated by two grating couplers. Upper panels show schematically the experimental pumping arrangement. Spectra shown on the sides are integrated across x . (a) High-power line-excitation to locate the band-edge (red-line) with the Anderson localized modes (between the red and dotted dark red-line). Below the band-edge: radiation spreads through the PhC structure but is dampened by the photonic bandgap; above the band-edge: waveguiding by the line defect within the photonic bandgap. QD (b)-(d) Spot excitation of the center QD at different indicated power. Spot excitation of (e) the first left QD, (f) the first right QD at indicated power. Radius $r_{\text{fab}} \approx 74\text{nm}$. Above barrier excitation, laser wavelength $\lambda_{\text{exc}} \approx 730\text{nm}$. Temperature $T \approx 10\text{K}$.

5.1.2.2 Processing: single photon directional coupling

The processing section (blue) is made of a QD embedded in a $L_{n=3}$ cavity itself coupled to two waveguides. The coupling of a QD to a single cavity mode has already been discussed in chapters 3 & 4, and the DIT aspect for a QD embedded in a cavity side-coupled to one or two waveguide(s) has been mentioned in section 5.1.1. We thus focus here on illustrating the remaining aspects: the coupling of several PhC waveguides and the resonances of the $L_{n=3}$ cavity.

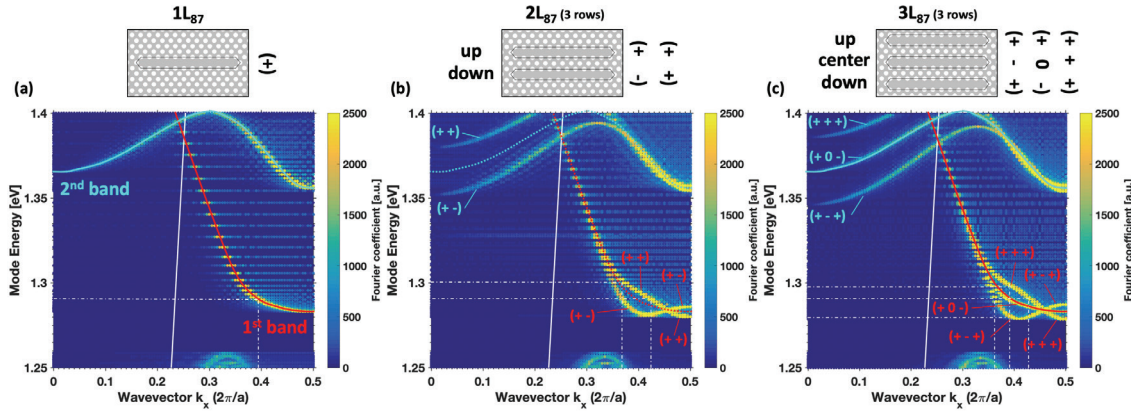


Fig. 5:4 – 2D FDM simulations of the photonic dispersion within the optical bandgap for (a) single $L_{n=87}$ cavity, (b) two coupled $L_{n=87}$ cavities with 3 rows separation, (c) three coupled $L_{n=87}$ cavities with 3 rows separation. The dispersions are obtained by Fourier transform of component E_y and integration across k_y . Supermodes symmetries are shown. White dot-dashed lines indicate both the splits in mode energy for a single value of k_x or the splits in k_x for a single value of the mode energy. Numerical parameters: radius $r = 66.6\text{nm}$, pitch $a = 225\text{nm}$, thickness $t = 250\text{nm}$, $n_{\text{eff}}^{\text{slab}} = 3.192$, spectral center $E = 1.325\text{eV}$.

cf. Fig. 5:4(b)	$ + - \rangle$	$ + + \rangle$
$ \text{up}\rangle$	$\frac{1}{\sqrt{2}}$	$\frac{1}{\sqrt{2}}$
$ \text{down}\rangle$	$\frac{1}{\sqrt{2}}$	$-\frac{1}{\sqrt{2}}$

cf. Fig. 5:4(c)	$ + - + \rangle$	$ + 0 - \rangle$	$ + + + \rangle$
$ \text{up}\rangle$	$\frac{1}{2}$	$\frac{1}{\sqrt{2}}$	$\frac{1}{2}$
$ \text{center}\rangle$	$-\frac{1}{\sqrt{2}}$	0	$\frac{1}{\sqrt{2}}$
$ \text{down}\rangle$	$\frac{1}{2}$	$-\frac{1}{\sqrt{2}}$	$\frac{1}{2}$

Table 5:1 – Matrices of amplitude coefficients c_p connecting (top row) supermodes and (left column) individual spatial modes basis for 2 (see Fig. 5:4(b)) and 3 (see Fig. 5:4(c)) coupled waveguides. The amplitude coefficients are calculated by coupled-mode theory.

Fig. 5:4 captures the essential features of PhC waveguide-waveguide coupling. It shows the band structure with increasing number $n = 1, 2 \& 3$ of PhC waveguides (approximated by $L_{n=87}$ cavities) separated by 3 rows of holes. (a) is the textbook reference case of a single PhC waveguide, $n=1$. When two PhC waveguides are coupled as in (b), new eigen-states are created due to the non-zero spatial overlap of the waveguided modes considered separately. These new eigen-states (also known in the literature as super-modes) are associated with new eigen-energies. The energy-dispersion of the reference case splits symmetrically into two bands around the former 1st

and 2nd band, forming a symmetric band $|+ + \rangle$ where the electric field components in both PhC waveguides have the same phase, and an anti-symmetric band $|+ - \rangle$ where they have opposite signs. The energy split is a non-trivial function of the wavevector \mathbf{k} . It is almost vanishing for fast-light modes since the original independent waveguide modes are strongly confined within their respective waveguide, and as a consequence they do not overlap spatially significantly. On the contrary, the split is important for slow light modes, where the slowing-down of light increases the effective coupling. The split is also very large for modes towards $k_x=0$, as seen from the 2nd coupled bands, because these modes are associated with large k_y , the components of which hit the waveguides walls at almost normal incidence and are thus more likely to leak and overlap with one another. By reduction of the coupling between the two waveguides, for instance by increasing the distance between the waveguides, the split between these two new bands eventually vanishes, and the reference case can be almost completely restored. Similarly, in (c), with $n=3$ PhC waveguides, three new bands related to three super-modes form: even $|+ - + \rangle$ where the electric field components in the two outer waveguides have a π -shifted phase relative to the center waveguide, odd $|+ 0 - \rangle$ where the electric field component of the center waveguide is suppressed, and even $|+ + + \rangle$ where all electric field components are in phase. As evidenced by the red-dotted line, the odd mode follows the energy-dispersion of the reference case $n=1$, and the two even modes surround it, with energy splits more pronounced than with $n=2$.

The amplitude coefficients describing the weights of each individual waveguide in the coupled structures are displayed in **Table 5:1**. The coefficients of the individual waveguides, shown here for the case of two and three coupled waveguides, are derived from coupled mode analysis [304], [305]. These amplitudes of the supermodes can be engineered by varying the coupling strengths between the waveguides [305].

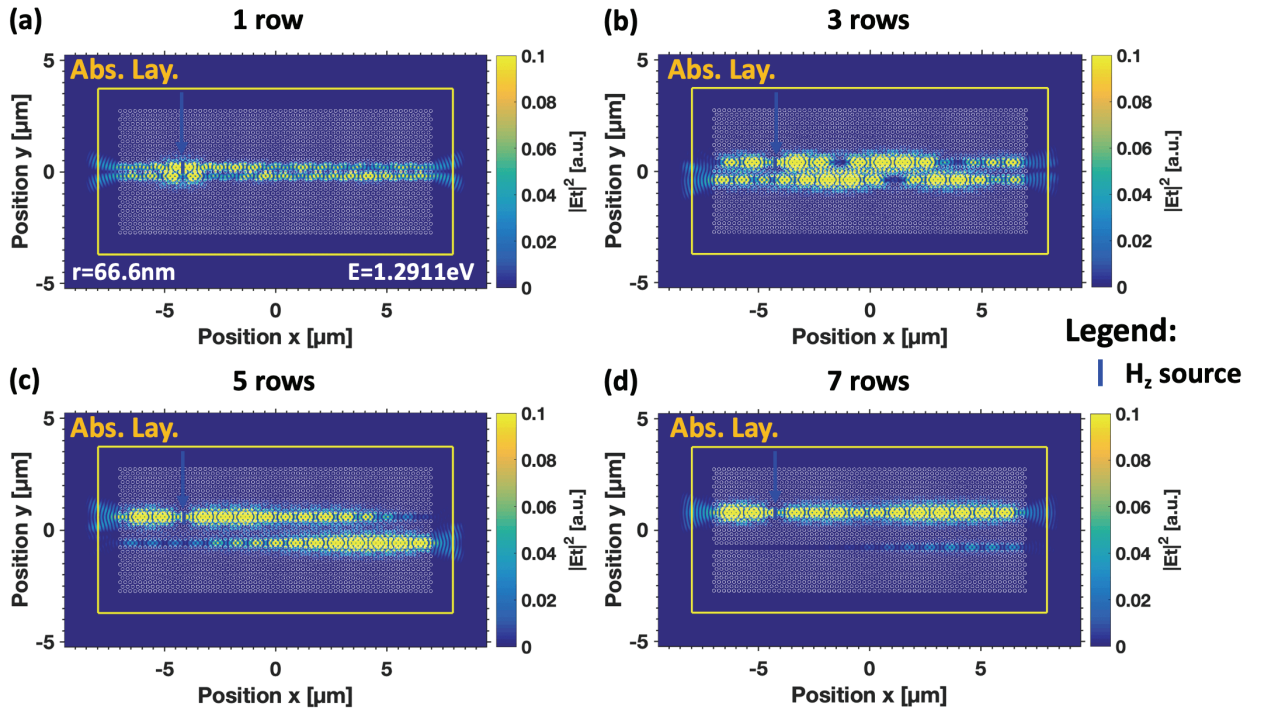


Fig. 5:5 – 2D FDTD simulations of two coupled PhC waveguides terminated by open boundaries. Exchange of power at a given photon energy $E = 1.2911\text{eV}$ for a fixed length but different separation: (a) 1 row of holes, (b) 3 rows (almost 50/50 split), (c) 5 rows and (d) 7 rows. Continuous sources are in the upper waveguides, represented by the blue arrows, with $\sim 400\text{-}500\mu\text{eV}$ bandwidth. The surrounding absorbing layer prevents parasitic reflections. Numerical parameters: radius $r = 66.6\text{nm}$, pitch $a = 225\text{nm}$, thickness $t = 250\text{nm}$, $n_{\text{eff}}^{(\text{slab})} = 3.166$.

The formation of these supermodes is a necessary condition for achieving coupling among the different components of the system (here, the two waveguides and the cavity). The actual coupling process taking place at the resonance conditions should be evaluated by considering the local excitation of a launched field (e.g., at a waveguide port) followed by its propagation along the structure via supermode beating.

Fig. 5:5 illustrates such evaluation of coupling with two PhC waveguides. Due to the complex photonic dispersion, it is more convenient to use FDTD simulations to follow the coupling. **Fig. 5:5(a-d)** present the results of such simulations in a two-waveguide PhC system of finite length ($L = 62a = 13.95\mu\text{m}$) for a photon mode energy $E = 1.2911\text{eV}$, using the same launching point indicated by blue arrow, but with increasing number of spacing rows of holes. For a single row **(a)**, the overlap between the optical modes of the waveguides is very large, and the transfer between the two PhC waveguides is hard to track, but the interferences in the output ports evidence efficient coupling. For three rows separation **(b)**, the coupling length to completely couple to the second PhC waveguide is $L_{100\%}^{(3r)} \approx 2.5\mu\text{m}$. Since the structure is longer, there is a regular back and forth light exchange between the two channels. For five rows separation **(c)**, the coupling strength is further reduced, and the coupling length is much larger at $L_{100\%}^{(5r)} \approx 10.9\mu\text{m}$. For 7 rows separation **(d)**, the coupling length $L_{100\%}^{(7r)}$ is larger than the length of the simulated device, and the two waveguides can be considered almost independent. For the deterministic coupling of a waveguide to another waveguide via an intermediate cavity instead of directional coupling, it is essential that the two waveguides can be considered independent, i.e., separated by a sufficiently large number of rows.

The $L_{n=3}$ cavity (visible in Fig. 5:2) can serve three purposes. The first is to couple a single site-controlled QD's dipole with a locally tightly confined electric field of a relatively high-Q cavity, in order to enable Purcell enhancement for the efficient extraction of single photons into the PhC waveguided modes. Second, because of its fewer, discrete optical resonances, it can resonantly bridge the photonic bands of the PhC waveguides, which enables resonant directional coupling. Third, the directional coupling over the specific range of photon energies can be modified by the DIT optical non-linearity of a QD resonantly coupled to the cavity. It is thus essential to also acquire knowledge of the optical mode structure of the isolated $L_{n=3}$ in order to estimate around which mode energies these connections can occur [83], [306].

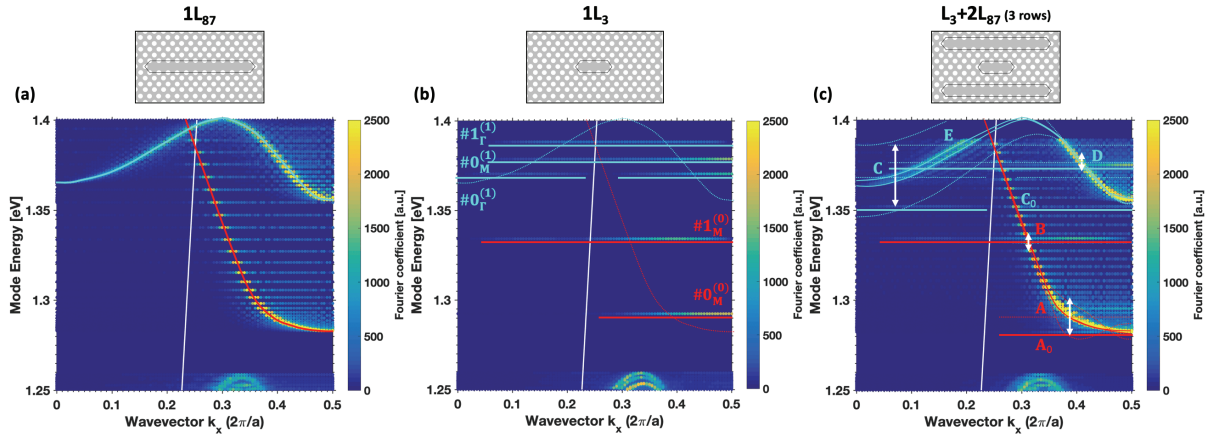


Fig. 5:6 – 2D FDM simulations of the photonic dispersion within the optical bandgap for (a) $L_{n=87}$ cavity (repeat from Fig. 5:4(a) for comparison), (b) L_3 cavity, (c) L_3 cavity coupled to two $L_{n=87}$ cavities with 3 rows separation. The dispersions are obtained by Fourier transform of component E_y and integration across k_y . Solid lines are specific to a structure, dotted lines are visual cues. L_3 cavity modes are labelled following the notation of chapter 3. Intersections of bare $L_{n=3}$ modes with waveguide dispersions are labelled A, B, C, D and E; A_0 and C_0 are specific ones. Arrows indicate range of resonant coupling around these points. Numerical parameters: radius $r = 66.6\text{nm}$, pitch $a = 225\text{nm}$, thickness $t = 250\text{nm}$, $n_{\text{eff,slab}} = 3.192$, spectral center $E = 1.325\text{eV}$.

Fig. 5:6 captures the complex photonic dispersion manifesting in the system consisting of a $L_{n=3}$ cavity coupled in between two PhC waveguides (approximated by $L_{n=87}$ cavities), with elements separated by 3 rows of holes. Part **(a)** reproduces the band structure of a single $L_{n=87}$ from Fig. 5:4(a), for comparison. Part **(b)** reports the photonic dispersion of the first five cavity modes of a modified single $L_{n=3}$ cavity obtained by Fourier transform of the component E_y and summation across k_y (i.e. projection over k_x). The three side holes on both side of this modified cavity are shifted outwards along x , by $s_{1x} \approx 0.2311a$ ($\sim 52\text{nm}$), $s_{2x} \approx 0.1507a$ ($\sim 34\text{nm}$), $s_{3x} \approx 0.048a$ ($\sim 11\text{nm}$) respectively, in order to maximize the Q-factor of the fundamental mode [161]. The labelling follows the notation introduced in chapter 3 with the defect-potential structure. It differs from that of [306], where modes are labelled by their symmetries $[\Pi_x \Pi_y]$. Here, for the two modes originating from the lateral confinement of the 1st band: the component E_x of mode $\#0_M^{(0)}$ possesses $[-1 -1]$ symmetries, while component E_y is characterized by $[+1 +1]$. For $\#1_M^{(0)}$ E_x : $[+1 -1]$, E_y : $[-1 +1]$. As for the modes of the 2nd band: $\#0_\Gamma^{(1)}$ E_x : $[+1 +1]$, E_y : $[-1 -1]$, $\#0_M^{(1)}$ E_x : $[+1 +1]$, E_y : $[-1 -1]$ and $\#1_\Gamma^{(1)}$ E_x : $[-1 +1]$, E_y : $[+1 -1]$. Modes of the 1st band are again mostly V-polarized (indicated in red) while modes of the 2nd band are H-polarized (in cyan), as was evidenced in chapter 3.

In **(c)**, the part related to the dispersions of the two coupled PhC waveguides, in which the electric field is essentially confined in each waveguide, are very similar to the band structure of a single PhC waveguide as they are formed by two overlapping bands. Indeed, omitting the cavity, the two elements are separated by 7 rows, and based on the conclusions of Fig. 5:5, the coupling between the two waveguides is negligible. In the figure, the cavity modes of (a) are overlaid, and the four points where $\#0_M^{(0)}$, $\#1_M^{(0)}$, $\#0_\Gamma^{(1)}$, $\#0_M^{(1)}$, $\#1_\Gamma^{(1)}$ cross the waveguide bands are labelled A, B, C, D and E. These points represent resonant coupling, where the cavity bridges the two PhC waveguides. This is similar to [262], [297] albeit with a different coupled system. In fact, due to the in-plane coupling, the optical resonances of the cavity are broadened (i.e. $\hbar\kappa$ is increased), becoming loss channels, the bandwidths of which can be adjusted by the number of rows separating the cavity and the waveguides. The photonic dispersion appears as a limit case of a system of three coupled PhC waveguides separated by 3 rows of holes (cf Fig. 5:4(c)) where the center part of the waveguide mode is laterally confined to conform to the $L_{n=3}$ cavity. In particular, coupling rates value corresponding to mode widths $[\sim 200\mu\text{eV}, \sim 1\text{meV}]$ and up to $\sim 6.1\text{meV}$ s have been extracted in [144] for the fundamental cavity mode $\#0_M^{(0)}$ coupled to a single waveguide over a photon energy range $[\sim 1.276\text{eV}, \sim 1.313\text{eV}]$. These coupling rates were also associated with cavity-waveguide coupling efficiencies ranging within $[50\%, 90\%]$. The coupling rates are related to the coupling geometry [282], [307], but also to the local density of states. Coupling rates are naturally larger for slow light regions near the band-edges where the LDOS diverges, than for the fast-light regions where the dispersion is steep, quasi linear and the LDOS is low. Flat cavity-like dispersions are observed; they belong to channels A, B, C, D and E, as peculiar manifestations in which the electric field is strongly confined within the center cavity. Modes belonging to B and D are slightly red-shifted in energy, whereas modes related to A and C are significantly red-shifted and are labelled A_0 and C_0 . Locally, due to the coupling, these modes are pulled down by the photonic potential dip, which is reminiscent of the defect-potential of chapter 3. However, it differs since this dip is generated by the coupling of several optical elements, contrary to the tailored-potential case, where it is induced by local tailoring of the dispersion of a single element by change of structural parameters.

Fig. 5:7 displays the intensity spatial distributions of optical modes nearby the resonant coupling points A, B and D, compared with those of the isolated, relevant L_3 cavity modes. Part **(a)** focuses on channel A, at the mode energy 1.292eV . This energy is detuned from the energy of the unloaded cavity mode at $\sim 1.2886\text{eV}$, a discrepancy of $\sim 3.4\text{meV}$ s, due to the large coupling rate provided in this part of the dispersion (see Fig. 5:6(c)). The mode pattern of the loaded cavity is barely modified with respect to the unloaded cavity mode $\#0_M^{(0)}$: the maxima still occur at the same lattice sites, which is ideal for interaction with an integrated QD. The tails reach a little bit further away across y . However, the coupled mode well spreads into the waveguide channels. From the lower panel, it is clear that coupling to the waveguide channels occurs preferentially along the diagonal directions of the triangular lattice, naturally compatible with the mode pattern, and known to provide the largest coupling [282], [307], [308]. The intensity is stronger in the region of the cavity than it is in the waveguides, and this situation is ideal to still provide strong interaction with the dipole of the QD r for single photon extraction and routing via the extended

waveguide tails. An optimal working point exists with balanced parameters [144] ensuring the leakage of the single photons into the waveguides a rate faster than the vertical scattering rate of the cavity. As seen from Fig. 5:6(c), few components intersect with the light cone, modes of this channel A thus constitute a target of choice for a QIP device relying on a QD integrated at position (0,0).

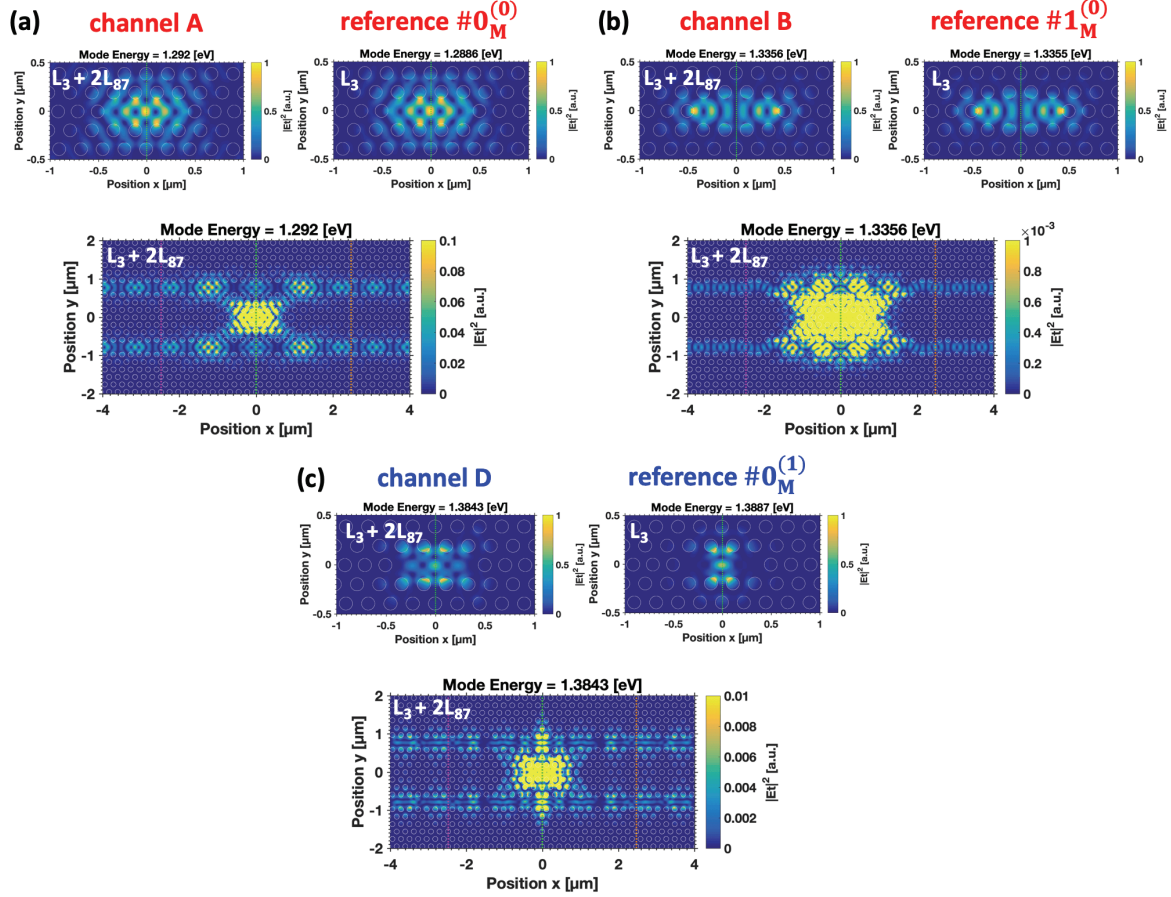


Fig. 5:7 – 2D FDM simulations of the intensity spatial distributions of resonant coupled modes of an $L_3 + 2L_{87}$ structure (3 holes structure) belonging to: (a) channel A, (b) channel B, (c) channel D as indicated in Fig. 5:6. Larger graphs: components extending in the waveguides, saturated color scale. Smaller panels: zoom-in and comparison with the intensity spatial distributions of modes of the single $L_{n=3}$. Numerical parameters: radius $r = 66.6\text{nm}$, pitch $a = 225\text{nm}$, thickness $t = 250\text{nm}$, $n_{\text{eff}}^{\text{slab}} = 3.167, 3.201, 3.241$.

Part (b) shows a mode of channel B, associated with the unloaded cavity mode $\#1_M^{(0)}$, with a mode energy of $\sim 1.3356\text{eV}$ as compared to the unloaded cavity mode at $\sim 1.336\text{eV}$, a discrepancy of $\sim 0.4\text{meV}$. From the two graphs of the upper panel, the spatial pattern is again practically not modified. From the bottom larger panel, the intensity color scale has to be saturated dramatically to evidence the components spreading into the waveguides which appear rather dark as compared to the cavity region, consistent with the weak cavity-waveguide coupling in this case. Coupling also occurs essentially thanks to the diagonals. Importantly, this mode presents a node at the center of the cavity, thus it is not expected to interact with the dipole of a QD integrated at position (0,0).

Fig. 5:8 illustrates the features of mode C_0 from channel C, related to the reference cavity mode $\#0_\Gamma^{(1)}$. This mode looks very similar to mode $\#1_\Gamma^{(1)}$ appearing at a higher mode energy, but the latter possesses a node in $x=0$, while the former has a weak but non-zero field there. Mode C_0 is the mode that appears below the band-edges of the 2nd band of the two coupled PhC waveguides, cf Fig. 5:6(c). It can be seen from part (a), which displays the spatial distribution of intensity, that the supermode, despite leaking from the cavity into the two PhC waveguides, cannot propagate due to exponentially decaying tails along x and stays locally confined. The coupling occurs essentially along y ; since $\#0_\Gamma^{(1)}$ is related to the Γ side, k_x is small but k_y is large in compensation so the components

propagate mainly along the transverse direction y . This scenario is very similar to the confined defect mode $\#0_{\Gamma}^{(1)}$ of the defect-potential of chapter 3. Despite co-existing with the quasi-continuum of fast-light modes of the 1st band, in the disorder-free case mode C_0 cannot couple to them due to orthogonality. However, as can be appreciated from **(b)**, supermode C_0 can hybridize with a fast-light mode of the 1st band, in the same fashion as discussed chapter 3, due to the occurrence of fabrication disorder, here with holes sizes variation defined by $\sigma_r = 1\text{nm}$ standard deviation. The effect occurs even for such a small disorder compatible with state-of-the-art fabricated device, so the phenomenon should be observable in μPL experiments of real devices. Here in particular, due to the peculiar effect of disorder, the coupling is unbalanced, asymmetric, favoring the upper PhC waveguide over the lower PhC waveguide, in which there are propagating components but much weaker.

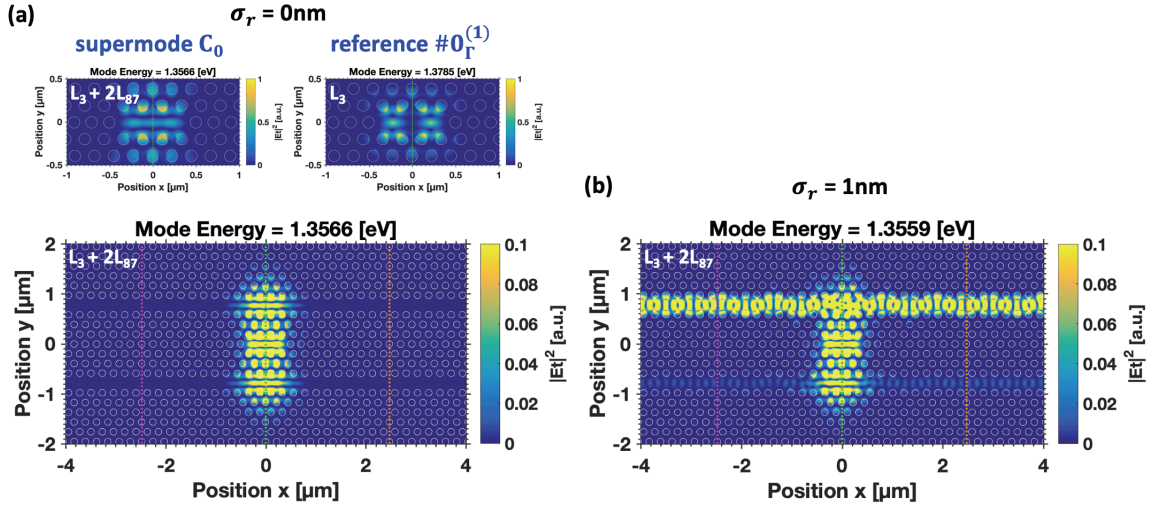


Fig. 5:8 – 2D FDM simulations of the intensity spatial distributions for mode C_0 of channel C in a L_3+2L_{87} (3 hole separation) see Fig. 5:6. **(a)** confined mode in the reference disorder-free case, **(b)** mode hybridized and asymmetric leakage in the case of holes size disorder, $\sigma_r = 1\text{nm}$. Inset in **(a)** compares supermode C_0 with the reference mode of the isolated cavity. Numerical parameters: radius $r = 66.6\text{nm}$, pitch $a = 225\text{nm}$, thickness $t = 250\text{nm}$, $n_{\text{eff,slab}} = 3.218$.

Fig. 5:9 details the optical mode structure of the coupled L_3+2L_{87} system with a focus on the resonant coupling region of channel A, by highlighting of some supermodes and their symmetries. Part **(a)** shows the energy-position intensity map of an isolated L_{87} , showing four “waveguide” modes and their reflection symmetries with regard to x , 1 ($\Pi_x = -1$), 2 ($\Pi_x = +1$), 3 ($\Pi_x = -1$) and 4 ($\Pi_x = +1$). With the addition of another parallel L_{87} structure separated by 7 rows, these four modes are duplicated and split by few hundreds μeV s. Part **(b)** reproduces the energy-position intensity of an isolated modified L_3 structure showing mode $\#0_M^{(0)}$ with its even symmetry ($\Pi_x = +1$). Its energy is almost resonant with waveguide mode 1 and detuned with modes 2, 3 and 4 of part (a). When the $L_{n=3}$ is inserted in between the two L_{87} with 3 rows separation, new eigen-supermodes are generated and the mode energies are adjusted in a non-trivial manner as depicted in **(c)**. The white and red dotted lines are visual cues of the reference mode energies from (a) and (b). In this energy range, nine supermodes are identified and labelled from 1A to 9A by increasing mode energy. Supermode 7A corresponds to the one depicted in Fig. 5:7(a). These supermodes have the following symmetries: 1A [$\Pi_x = -1, (+ 0 -)$], 2A [$\Pi_x = -1, (+ - +)$], 3A [$\Pi_x = +1, (+ - +)$], 4A [$\Pi_x = +1, (+ 0 -)$], 5A [$\Pi_x = -1, (+ 0 -)$], 6A [$\Pi_x = -1, (+ - +)$], 7A [$\Pi_x = +1, (+ + +)$], 8A [$\Pi_x = +1, (+ 0 -)$], 9A [$\Pi_x = +1, (+ + +)$]. Supermodes 3A, 7A and 9A appear significantly brighter in the $L_{n=3}$ cavity region as compared to the other supermodes. The 2D spatial patterns of three of these supermodes are reproduced in **(d)** (3A), **(e)** (7A) and **(f)** (8A).

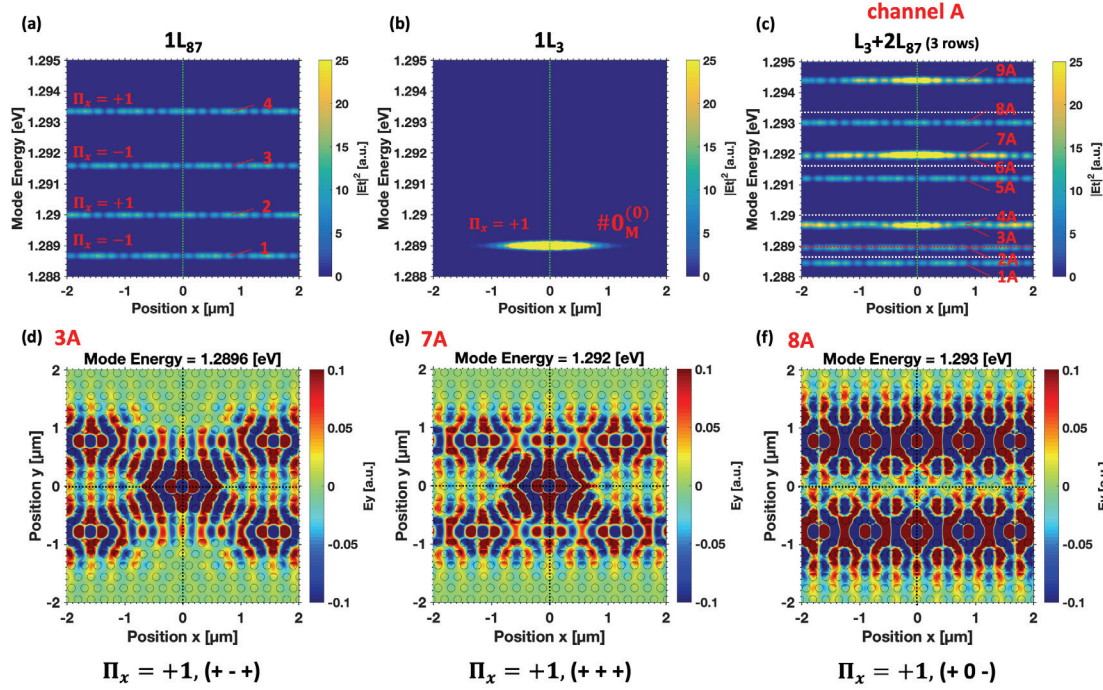


Fig. 5:9 – 2D FDM simulations of the optical mode structure of the L_3+2L_{87} , with focus on channel A, see Fig. 5:6. Energy-position intensity maps of (a) the L_{87} and (b) modified L_3 references. (c) Energy-position intensity map identifying 9 supermodes of channel A, in particular: (d) supermode 3A, component E_y , odd symmetry (+ - +); (e) supermode 7A, component E_y , even symmetry (+ + +); (f) supermode 8A, component E_y , even symmetry (+ 0 -). These three supermodes are even with respect to x . White dotted lines refer to the mode energies from (a), red dotted line refer to the mode energy from (b). Numerical parameters: radius $r = 66.6\text{nm}$, pitch $a = 225\text{nm}$, thickness $t = 250\text{nm}$, $n_{\text{eff}}^{\text{slab}} = 3.167$.

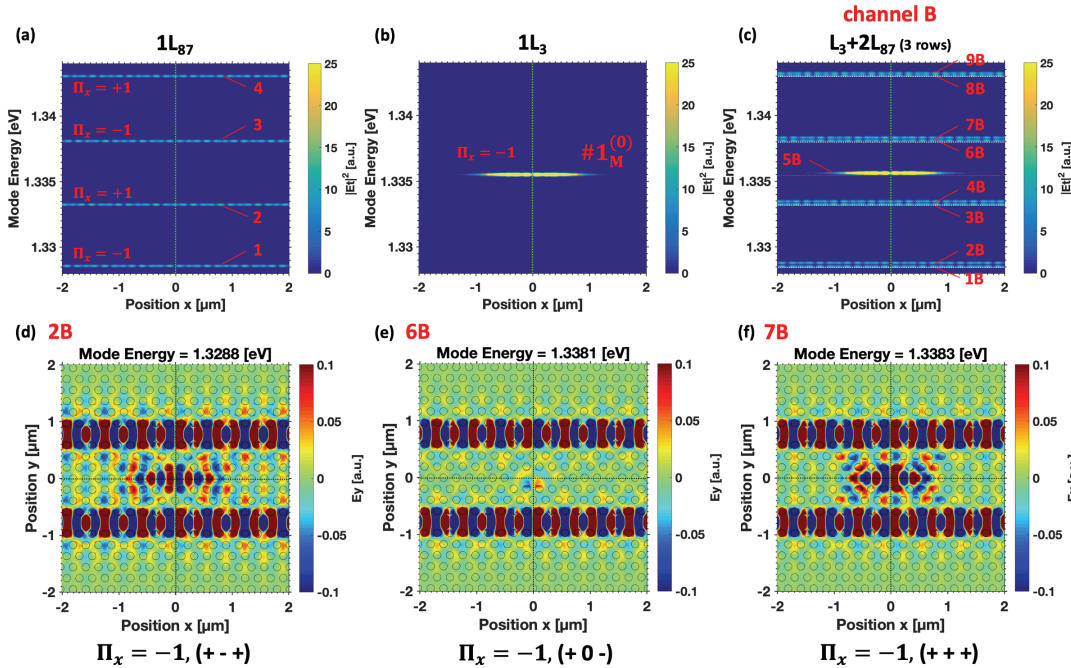


Fig. 5:10 – 2D FDM simulations of the optical mode structure of the L_3+2L_{87} (3 hole separations), with focus on channel B, see Fig. 5:6. Energy-position intensity maps of (a) the L_{87} and (b) L_3 references. (c) Energy-position intensity map identifying 9 supermodes of channel B, in particular: (d) supermode 2B, component E_y , odd symmetry (+ - +); (e) supermode 6B, component E_y , even symmetry (+ 0 -); (f) supermode 7B, component E_y , even symmetry (+ + +). These three supermodes are odd with respect to x . White dotted lines indicate the mode energies from (a), the red dotted line points to the mode energy from (b). Numerical parameters: radius $r = 66.6\text{nm}$, pitch $a = 225\text{nm}$, thickness $t = 250\text{nm}$, $n_{\text{eff}}^{\text{slab}} = 3.201$.

Fig. 5:10 is a repeat of the study above, focusing on channel B. Part **(a)** displays the energy-position intensity map of an isolated L_{87} , with again four “waveguide” modes (in a different energy range) 1 ($\Pi_x = -1$), 2 ($\Pi_x = +1$), 3 ($\Pi_x = -1$) and 4 ($\Pi_x = +1$). Part **(b)** depicts the same energy range with mode #1_M⁽⁰⁾ supporting an odd symmetry ($\Pi_x = +1$). Its mode energy is in between waveguide modes 2 and 3 with approximately equal detunings. The resulting new coupled optical mode structure is illustrated in **(c)**. The white and red dotted lines are once more visual cues of the reference mode energies from (a) and (b). Nine supermodes are observed and labelled from 1B to 9B by increasing mode energy. Supermode 5B corresponds to the one depicted in Fig. 5:7(b). These supermodes have the following symmetries: 1B [$\Pi_x = -1, (+ 0 -)$], 2B [$\Pi_x = -1, (+ - +)$], 3B [$\Pi_x = +1, (+ 0 -)$], 4B [$\Pi_x = +1, (+ - +)$], 5B [$\Pi_x = -1, (+ + +)$], 6B [$\Pi_x = -1, (+ 0 -)$], 7B [$\Pi_x = +1, (+ + +)$], 8B [$\Pi_x = +1, (+ 0 -)$], 9B [$\Pi_x = +1, (+ - +)$]. The 2D spatial patterns of three supermodes among these are reproduced in **(d)** (2B), **(e)** (6B), and **(f)** (7B). Properly weighted superpositions of these three supermodes result in electromagnetic modes where the electric field is dominant in either one of the $L_{n=87}$ “waveguides” or the $L_{n=3}$ cavity. Only 5B appears significantly brighter in the $L_{n=3}$ cavity region as compared to the other supermodes and Fig. 5:9(c), but as seen here, some of these (+ - +) supermodes do have components occupying the $L_{n=3}$ cavity. On the contrary, some other (+ - +) supermodes do not show such a pattern, and are not suitable for coupling. Note also that the odd x-symmetry of the cavity mode considered here results in a field null at the center of the cavity.

5.1.2.3 Detection: input/output couplers

Following processing, single photons must be guided to detection regions. Currently, the on-chip detection of single photons is still very challenging, as it relies on the integration of superconducting nanowires single-photon detectors (SNSPDs) fabricated on top of wide ridge waveguides [79], [99], [100]. Although some of these can even resolve the number of photons (PNR-SNSPDs) [99], which is a very anticipated feature, they yield detection efficiencies of typically $\sim 10^{-2}$ - 10^{-1} [309], [310], $\sim 24\%$ reported in [99], far from unity. In addition, they show important dark count rates of $\sim 10^0$ - 10^4 counts per second [79], which can result in errors in the registration of trusted detection events, preventing the realization of reliable QIP applications. Despite the stringent requirements, early proof-of-principle devices have been demonstrated with such integrated detectors [311], [312]. To circumvent this shortcoming, a functional device can be radiatively connected to the outside world by means of grating couplers [216], [291] that re-direct the photons out of the chip for monitoring of the generated and processed single photons. Since the propagation of light can be reversed, these grating couplers are also useful for light injection into the chip, either to (quasi-) resonantly pump the quantum emitters [217], or to conduct resonance transmission experiments to test non-linear effects generated by a QD’s dipole [204]. To couple the light at $\theta \approx 90^\circ$, the fabricated first order Bragg gratings are based on the design of [144]. They support a large bandwidth of ~ 127 meV (~ 100 nm) and provide a collection efficiency of $\sim 25\%$ using a numerical aperture $NA = 0.55$, but also introduce large reflections of ~ 30 - 50% . The target wavelength $\lambda_0 = 980$ nm required a period of $\Lambda = 490$ nm (~ 450 nm = $2a$) of the GaAs/air grating. Another possible design involves an adiabatic tip better suited to reduce the reflections and facilitate the collection of extracted photons [144]; however, it is not well adapted for efficient injection. For a first prototype, here only one flexible design was favored, but balancing the two, or other designs [214] could very well be envisioned. In the model system of Fig. 5:2, the gratings are distanced from the PhC region and connected by suspended nanobeams because the extent of the grating coupler is rather large, a few micrometers, and therefore they cannot be put side-by-side without overlapping each other. The nanobeams could have been replaced by bent waveguides in PhCs, but these must comply with the triangular lattice, which usually introduces important guiding losses unless very demanding and non-trivial designs are employed [313]–[316]. The introduction of suspended nanobeams was further motivated by the important need to interface hybrid platforms [81]. PhC waveguides are adequate for short distance transport of photons, but not suited for mid- to long-range propagation, where ridge/rib waveguides are typically preferred [317], [318]. These nanobeams thus provide a solution for eventual monolithic fully on-chip planar integration. In general, the optimization of optical interfaces is important, otherwise they can introduce strong reflections and scattering losses, which prevent any realistic QIP application. Even if a single photon source produced a deterministic stream of single photons, unpredictable losses at any point during processing or detection render the device probabilistic and unreliable. The nanobeams support an index guided photonic dispersion fairly different from the gap guided photonic dispersion of PhC waveguides,

adiabatic tapering between the two elements can solve this issue of compatibility [97], [318]. Highly efficient hybrid optical interconnects [319]–[321] from PhC to suspended nanobeam/ridge [318] and optical fibers [167] have been demonstrated.

5.2 Fabrication of the model structure

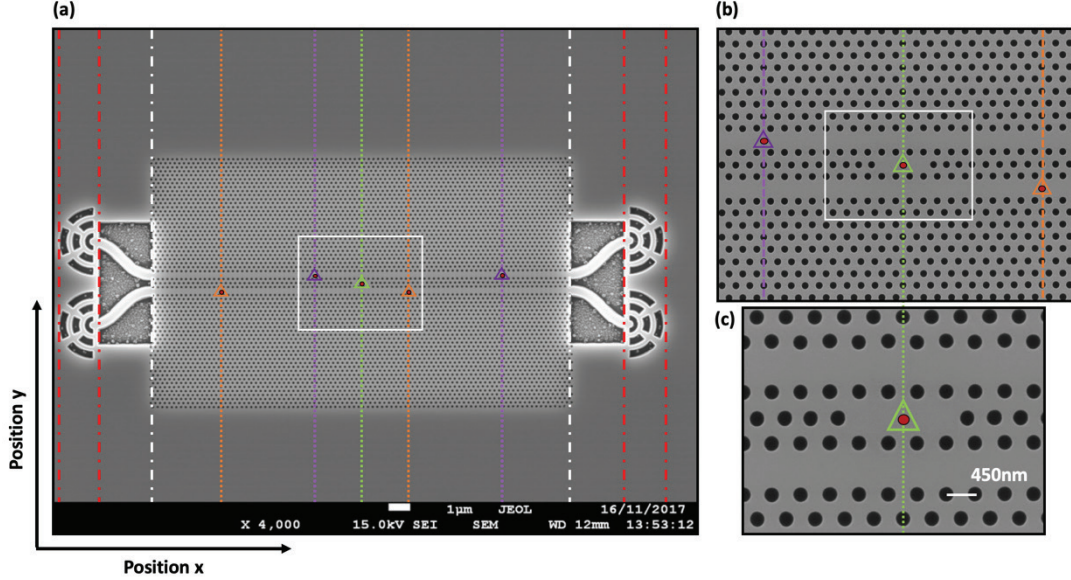


Fig. 5:11 – SEM top-view image of (a) the model device with two waveguides ($\sim L_{87}$) coupled by a mediating L_3 cavity, with one row separation between elements. The two waveguides connect to four input/output grating ports by suspended curved nanobeams. Five site-controlled pyramidal QDs are embedded at the specified locations, two (magenta) in the upper WG, one (green) in the center cavity, two (orange) in the lower WG. The colored vertical lines specify important locations for reference (see text). (b) Nested magnification of the center region. (c) Zoom-in at the cavity area.

Fig. 5:11 shows SEM images of one of the PhC structures fabricated on the same sample hosting the structures of Chapters 3 & 4. It is made of an $L_{n=3}$ cavity sandwiched in between two PhC W_1 waveguides implemented in the form of $L_{n=87}$ ($\sim 19.8\mu\text{m}$) long cavities opened at both ends. The $L_{n=3}$ cavity has an optimized design, discussed with respect to Fig. 5:6 earlier. The resulting four ports are linked to grating couplers by suspended s-bend nanobeams. These compact nanobeams have a width of $w \sim 390\text{nm}$ ($\approx \sqrt{3}a$) and the thickness of the slab is $t \sim 250\text{--}260\text{nm}$. They cover a lateral distance of $\sim 2.7\mu\text{m}$ ($12a$) along x , and a transverse distance of $\sim 1.56\mu\text{m}$ ($8\frac{\sqrt{3}}{2}a$) along y estimated from center to center, with a radius of curvature $R \approx 1.56\mu\text{m}$. The curvature was chosen to be rather smooth, so as to not introduce too important radiative losses by the inflexion [292]. Two configurations were realized, with one row (1r) separation, depicted in Fig. 5:7, and with three rows (3r) symmetric separations between cavity and waveguides. Once again, the fabricated PhC holes cover a wide range of $r_{\text{fab.}} \approx 47\text{--}74\text{nm}$ for coarse r/a tuning of the mode energies that are expected to appear in the $\sim 1.240\text{--}1.378\text{eV}$ photon energy range (900–1000nm) at $T \approx 10\text{K}$.

The structures are arranged in 6 series, repeated 4 times. Each series is comprised of 2×13 structures with radius $r_{\text{fab.}}$ ranging from ~ 47 to $\sim 63\text{nm}$ and from ~ 58 to $\sim 74\text{nm}$. Due to space constraints with the other fabricated structures, PhC structures with only few QDs were favoured over structures with QD arrays. Five pyramidal site-controlled QDs are embedded as indicated schematically in Fig. 5:7(b). Focusing on the 3r configuration, the QD locations are specified using the x - y system of Fig. 5:10, with origin at the green QD. Two pyramidal site-controlled QDs (in magenta) are located in the upper waveguide, at $(-2.475\mu\text{m} (-11a), +0.779\mu\text{m} (+4\frac{\sqrt{3}}{2}a))$ and $(+6.525\mu\text{m} (+29a), +0.779\mu\text{m} (+4\frac{\sqrt{3}}{2}a))$ respectively. Two more QDs (orange) in the lower waveguide, following inversion symmetry they are located respectively at $(-6.525\mu\text{m} (-29a), -0.779\mu\text{m} (-4\frac{\sqrt{3}}{2}a))$ and $(+2.475\mu\text{m} (+11a), -0.779\mu\text{m} (-4\frac{\sqrt{3}}{2}a))$ [(0.0) denotes the center of the coupling cavity]. Since the DIT effect

eventually depends on the resonant coupling of a QD transition with an optical mode itself coupling the center $L_{n=3}$ cavity to the PhC waveguides, half the structures have a fifth QD (green) embedded at the center of the $L_{n=3}$ at (0,0) whereas the other half contains an empty cavity. These PhC structures are located in the big square region, where QDs emit in the $\sim 1.264\text{-}1.279\text{eV}$ ($\lambda_{\text{QD}} \sim 970\text{-}980\text{nm}$) photon energy range at $T \approx 10\text{K}$. The spacing between the QDs is sufficient to prevent the pumping of more than one QD at a time when using diffraction limited spot excitation.

For the detailed layout of the sample and locations of investigated structures, we invite the reader to consult appendix C.

5.3 Observation of the optical mode structure

This part is devoted to experimental observations of the optical mode structures of the model device using our micro-photoluminescence imaging technique. In particular, we identify spectral channels through which light can scatter from the center cavity via the waveguides. Numerical simulations further confirm signatures of cavity coupling to the waveguides.

Fig. 5:12 reports the comparison between the numerically simulated and experimentally measured optical mode structures of the C+2WG (3 rows) functional device. The 2D FDM numerical simulation approximates the waveguides by long $L_{n=87}$ cavities of the same length. Part **(a)** reproduces the usual energy-position intensity map, which is in fact the 1D real space projection of the photonic dispersion of Fig. 5:6(b). The band-edge of the 1st band of supermodes $\text{BE}_M^{(0)}$ appears at $\sim 1.278\text{eV}$ (red solid line), and displays a potential dip dropping down to $\sim 1.2732\text{eV}$ ($\sim 4.8\text{meV}$ s depth) corresponding to the value of the bottom band-edge from the limit case of 3 coupled PhC waveguides, as in Fig. 5:4(c). Right above this dip, the supermode A_0 can be noticed, the spatial extent of which is reduced as it is being pulled down into the potential well, see **(a')**. The effective potential well is too shallow to completely confine the supermode within it, contrary to the defect mode $\#0_M^{(0)}$ of chapter 3, but deep enough to prevent the mode from reaching both ends of the $L_{n=87}$ structures. Around $\sim 1.2886\text{eV}$, corresponding to the spectral center of channel A, supermodes with an intensity brighter at the location of the $L_{n=3}$ cavity can be seen. The supermode at ~ 1.292 corresponds to the example displayed earlier in Fig. 5:7(a). At higher mode energy, one can recognize the part of Channel B displayed in Fig. 5:9(a), with the noticeable supermode at $\sim 1.3356\text{eV}$. At even higher energies, one can distinguish the two band-edges of the 2nd band, $\text{BE}_M^{(1)}$ at $\sim 1.36\text{eV}$ and $\text{BE}_\Gamma^{(1)}$ at $\sim 1.369\text{eV}$ with, analogous to the 1st band, a dip in the photonic potential, from the Γ side, down to $\sim 1.3489\text{eV}$ ($\sim 20.1\text{meV}$ s depth). A zoom in **(a'')**, shows this potential well and the supermode C_0 bound within it at $\sim 1.3566\text{eV}$ (see also again Fig. 5:8(a)). Due to the large background density of modes in the 2nd band, it is more difficult to appreciate the effects of channels C, D and E.

Part **(b)** shows the corresponding experimental mode structure. The open waveguide configuration, with reduced reflectivity at the extremities, prevents the manifestation of discrete optical modes, contrary to the cases of chapter 3 and 4, and therefore it is more difficult to establish a 1:1 correspondence with the numerical simulations. Despite this shortcoming, several features are noticeable due to scattered light from the center $L_{n=3}$ cavity, which also appears to extend towards the left and right. The features between $\sim 1.29\text{-}1.30\text{eV}$ are a manifestation of a part of channel A, showing light partly localized at the cavity and partly extended at the waveguides. The one near $\sim 1.333\text{-}1.337\text{eV}$ is related to channel B, and near $\sim 1.357\text{eV}$ the extended feature is likely the disorder-induced hybridized C_0 mode of Fig. 5:8(b). The long trail of light in the cavity region between $\sim 1.37\text{-}1.40\text{eV}$ is associated with the overlap of the leaky channels C, D and E.

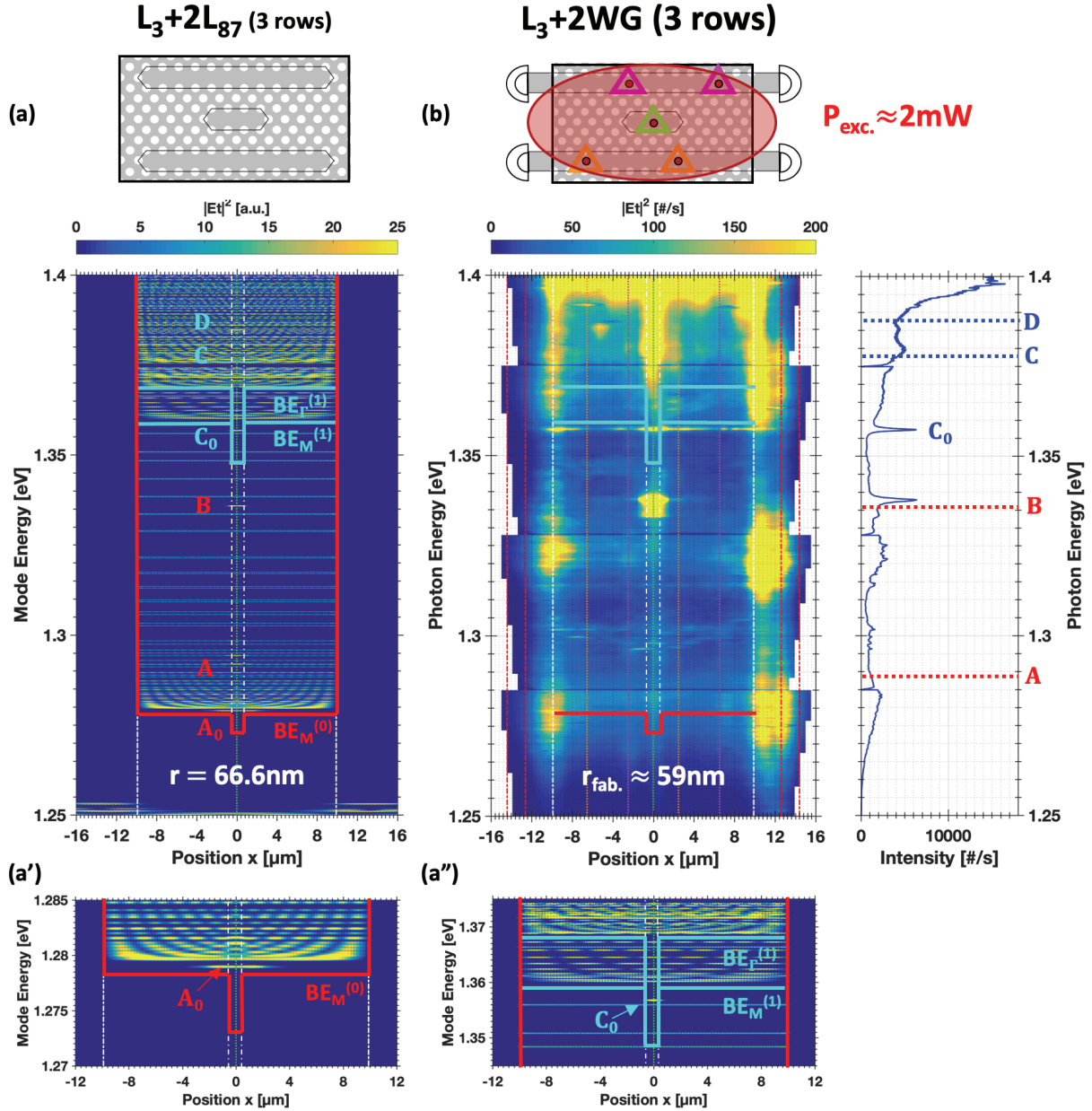


Fig. 5:12 – Mode structure of the cavity+2 waveguide test system (3r configuration). (a) 2D FDM numerical simulations of the optical modes of the L_3+2L_{87} with 3 rows of holes separation. Band-edges of the single waveguide and photonic potential dips are indicated (see Fig. 5:6). (a') and (a'') show magnified views of the coupled modes of interest. (b) Experimental energy-position map and spectrum integrated across x, with identification of the four escape channels A, B, C, D. $r_{fab.} \approx 59nm$. Upper panels depict the structures, the QD positions and experimental pumping scheme. Numerical parameters: radius $r = 66.6nm$, pitch $a = 225nm$, thickness $t = 250nm$. Above barrier excitation, laser wavelength $\lambda_{exc.} \approx 730nm$. Temperature $T \approx 10K$.

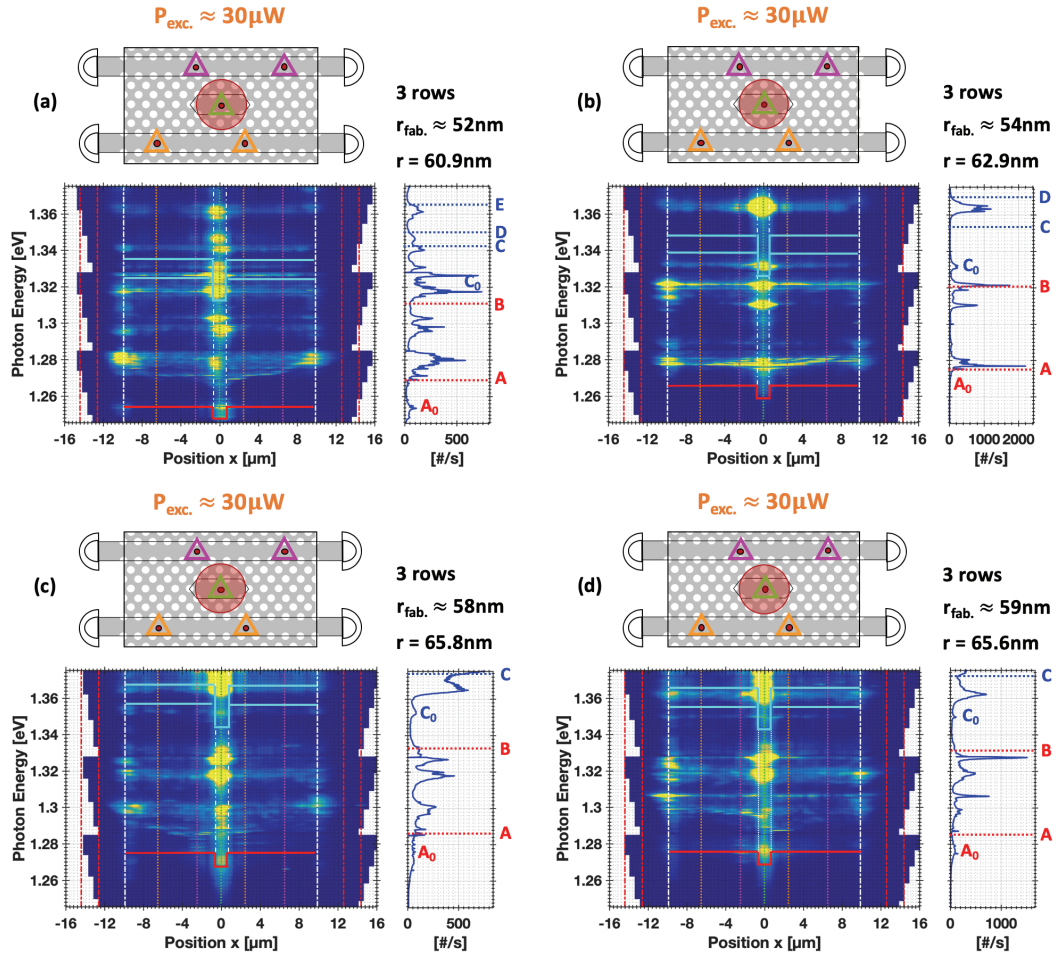


Fig. 5:13 – Energy-position maps and μ PL spectra integrated across x , acquired from high-power excitation $P_{\text{exc.}} \approx 30 \mu\text{W}$ of the configuration of Fig. 5:11 with different hole radii. Upper panels: schematic pumping arrangement. (a) $r_{\text{fab.}} \approx 52 \text{ nm}$; (b) $r_{\text{fab.}} \approx 54 \text{ nm}$; (c) $r_{\text{fab.}} \approx 58 \text{ nm}$; (d) $r_{\text{fab.}} \approx 59 \text{ nm}$. Red and cyan lines specify band-edges from numerical simulations. White dot-dash lines indicate the boundaries of the cavity. Dotted lines indicate the predicted mode energies of the isolated $L_{n=3}$, corresponding to the spectral centers of the various channels, red for 1st band, blue for 2nd band. Numerical parameters: radius $r = 60.9 \text{ nm}$, 62.9 nm , 65.8 nm and 65.6 nm , pitch $a = 225 \text{ nm}$, thickness $t = 250 \text{ nm}$. Above barrier excitation, laser wavelength $\lambda_{\text{exc.}} \approx 730 \text{ nm}$. Temperature $T \approx 10 \text{ K}$.

Fig. 5:13 displays a more consistent method for identifying the various spectral channels A-D of the C+2WG (3 rows) structures. Parts (a-d) report the measured energy-position maps of structures with different fabricated holes radii $r_{\text{fab.}}$ (i.e., r/a ratio), with which the spectral positions of channels A-D can be systematically tuned. The above barrier, spot excitation of the center QD embedded in the $L_{n=3}$ cavity at $P_{\text{exc.}} \approx 30 \mu\text{W}$ saturates the s-, p- and d- QD transitions. Following recombination of the charge carriers, the extracted photons propagate through the many resonant coupled supermodes. Observation of a center bright intensity spot indicates scattering from the center cavity, and connected extended components reaching to the vertical white dot-dashed lines indicate propagation up to the suspended nanobeams, which proves the optical coupling of the three PhC elements. From the side-by-side comparison of (a-d) it is seen that resonant coupling regions occur at different energies: the optical mode structure shifts accordingly to the variation of $r_{\text{fab.}}$. The intersection points A, B, C, D and E are extracted and reported as red and blue dotted lines from numerical modeling. The simulation holes radii are first estimated from attempts to match the experimental supermode energy of the observed C_0 signature with the predicted supermode energy from the equivalent L_3+2L_{87} structure. The band-edges are retrieved from simulations of L_{87} structures, and centers of channels A, B, C, D and E are retrieved from the cavity mode energies of the corresponding isolated L_3 cavities. Experimental signatures of the various channels are indeed observed on the energy-position maps,

close to the predicted intersection points. In the case of A, the resonantly coupled supermodes manifest with a large detuning. This is not surprising considering the bandwidth of the channel due to possibly few meVs coupling constants, as mentioned previously in the description of Fig. 5:6. Supporting this evidence, the bright spot occurring in the vicinity of the photonic dip of the 1st band, for instance at $\sim 1.272\text{eV}$ in (c) and $\sim 1.276\text{eV}$ in (d), might be the manifestation of supermode A_0 . According to the drawn photonic potentials, supermode C_0 appears within the potential dips of the 2nd band and appears hybridized at least in three instances: (a), (b) and (d). Independent tuning of the L_3 cavity resonances with respect to the waveguides photonic dispersions may be possible by shifts or size variations of the side-holes surrounding the L_3 cavity, following the results with the defect-potential in chapter 3.

For the eventual processing of single photons, supermodes from channel A must first be brought into resonance with the s-shell transitions of the various QDs, especially the center QD. Furthermore, resonances of the higher excited p- or d-shells with spectral channels B or C (especially hybridized mode C_0) could provide an interesting means to attempt the in-plane quasi-resonant excitation of these QDs by injection through a grating coupler.

5.4 Quasi-resonant pumping of integrated single site-controlled QDs

A true integration will also require on-chip pumping of the QDs. In this section, we explore the prospects of in-plane optical pumping using the spectral channel B previously identified. The laser pump light is injected through the grating couplers, and the spatially resolved micro-photoluminescence is analyzed. The cases of quasi-resonant excitation at normal incidence and above barrier pumping are also compared.

5.4.1 Strategy of excitation

Ideally, the excitation should be resonant with the QD ground state transition, to reduce the effects of dephasing and achieve the highest purity single photon emission [137]. In our experiments we were limited by the longest lasing wavelength of the Ti:Sapphire laser ($\sim 940\text{nm}$, $\sim 1.34\text{eV}$), which does not allow resonant excitation of the QD s-shells coupled to channel A. We thus opted for the quasi-resonant excitation of the p-shell states coupled to channel B. This is a reasonable trade-off, also employed by the authors of [212] where the p-shell states of a SKQD embedded in a suspended bare nanobeam are pumped at normal incidence and subsequent spectral filtering is applied to purify the extracted single photons with a free-space notch filter.

Fig. 5:14 shows a detailed investigation of the optical mode structure and QDs transitions for the device of Fig. 5:12, with a specific focus on the photon energy range spanning both channel A and B from the 1st band (above barrier excitation). In part **(a)**, moderate power line-excitation of $P_{\text{exc.}} \approx 100\mu\text{W}$ is used to reveal both QDs spectral lines and mode features. The band-edge delimitation and the spectral centers of channel A and B are estimated from simulations, and reported as the red solid line in the energy-position map and two red dotted lines plotted in the side spectrum integrated across position x. Extended features, bright at the center and the edges of the PhC region, manifest at $\sim 1.336\text{eV}$ (highlighted by the white rectangle) in agreement with the expected spectral center of channel B. These are supermodes where light is scattered by the center L_3 cavity and at the interfaces with the nanobeams. The groups of spectral lines seen around $\sim 1.265\text{eV}$ and $\sim 1.28\text{eV}$ at the locations of both magenta QDs and $\sim 1.285\text{eV}$ at the position of the green center QD are QDs transitions of the s-shells. In particular, the spectral lines of the latter appear nearby the $\sim 1.289\text{eV}$ spectral center of channel A. This is an optimal configuration to attempt the quasi-resonant excitation of the center QD in the coupled $L_{n=3}$ cavity by injection through channel B. Part **(a')** zooms on the white rectangle region of interest; the expectations from Fig. 5:10(c) (disorder-free) are overlaid as the red and white dotted-lines and the intensity saturation has been reduced. The spectral features observed result from the overlap of at least seven identifiable lines at ~ 1.3348 , 1.3355 , 1.3358 , 1.3372 , 1.3377 , 1.3381 and 1.3387eV . Two of these are attributed to supermodes, the $\sim 1.3355\text{eV}$ line belongs to the 5B (+ + +) supermode, the other at $\sim 1.3377\text{eV}$ to the 7B (+ + +) supermode, where light is seen to be scattered from the L_3 region. On the other hand, supermode 6B (+ 0 -) has a suppressed component inside the cavity and is thus unlikely to interact with the center QD. Discrepancies with the predicted supermode energies can be attributed to variations induced by disorder and slightly different holes sizes. The five remaining spectral lines, pointed by green arrows, and bright at the location of the L_3 cavity, are attributed to p-shell transitions from this center QD and are distributed quite symmetrically around $\sim 1.3364\text{eV}$. The two lines at $\sim 1.3381\text{eV}$ and $\sim 1.3372\text{eV}$ are interacting

with supermode 7B, and the latter extends all the way to the nanobeams. The spectral lines at $\sim 1.3358\text{eV}$ and at $\sim 1.3348\text{eV}$ interact with supermode 5B and also extend in the same fashion. Due to partial resonance with these two supermodes, the photons emitted by the center QD are extracted by the $L_{n=3}$ cavity and transferred to the PhC waveguides and thus can propagate to the left and right.

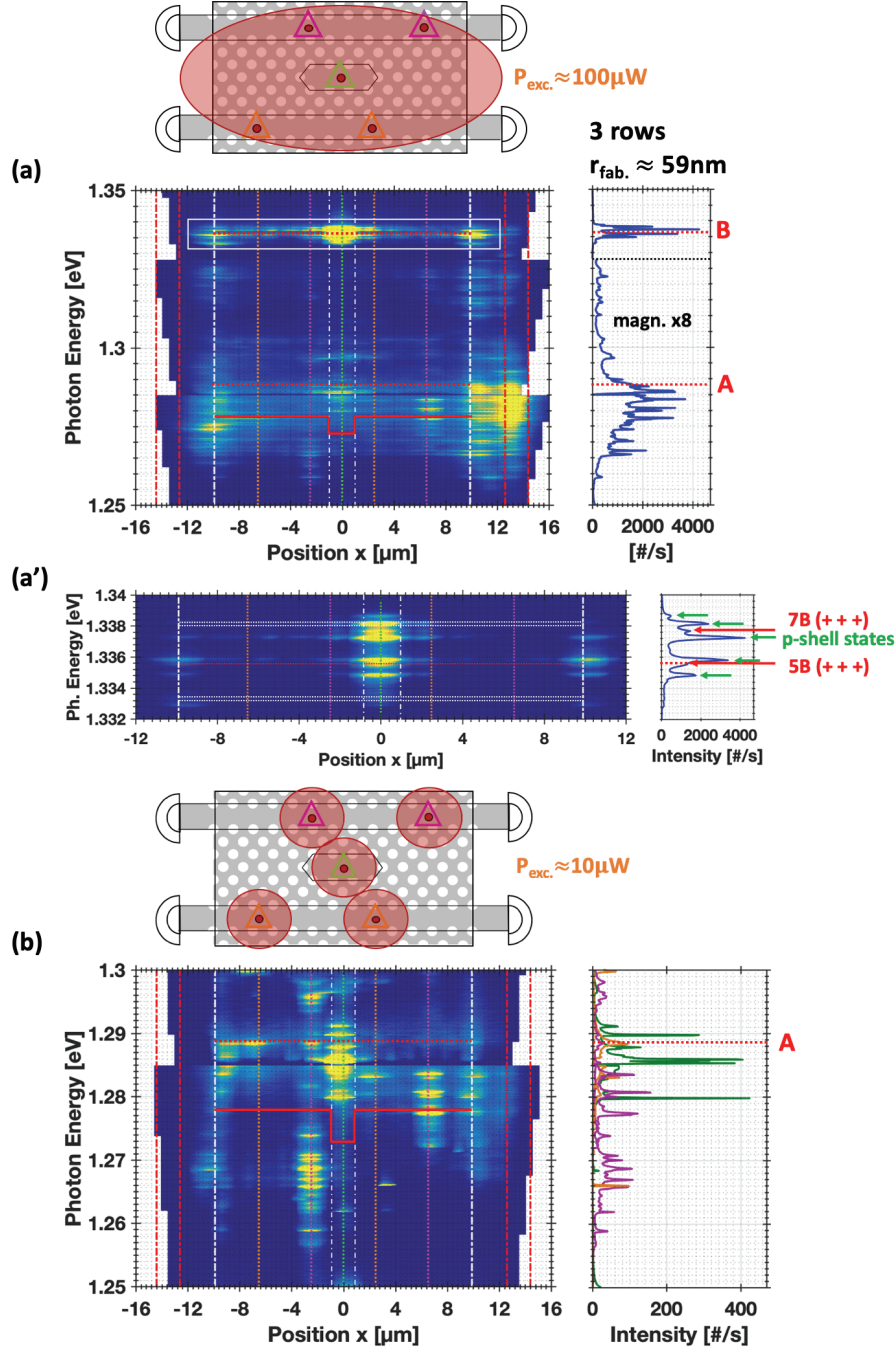


Fig. 5:14 – Detailed characterization of the C+2WG (3 rows) PhC device from Fig. 5:11, in which 5 QDs are embedded. Upper panels show schematically the experimental pumping arrangement. Side panels show spectra integrated along x , the part below the black dotted line is magnified by a factor 8. (a) Intermediate-power ($P_{\text{exc}} \approx 100 \mu\text{W}$) line excitation. Supermodes resonantly coupled via channel B and p-shell states are highlighted (white rectangle) and zoomed in (a'). (b) Intermediate power ($P_{\text{exc}} \approx 10 \mu\text{W}$) spot excitation at five QDs, with corresponding maps stitched together. Band-edge (red solid line), spectral centers of channel A and B (red dotted-lines) and some supermodes (white dotted-lines) predicted by numerical simulations are indicated. Radius $r_{\text{fab.}} \approx 59\text{nm}$. Numerical parameters: radius $r = 66.6\text{nm}$, pitch $a = 225\text{nm}$, thickness $t = 250\text{nm}$. Above barrier excitation, laser wavelength $\lambda_{\text{exc.}} \approx 730\text{nm}$. Temperature $T \approx 10\text{K}$.

In part **(b)**, the five embedded QDs are individually pumped by above-barrier spot excitation. The five spatial images are stitched together into a single energy-position image, and each energy-position image was integrated across x to produce the spectra displayed on the side, colour coded accordingly to their parent QD. Many discrete spectral transitions from the s-shell emissions are visible, appearing at the locations where the five QDs have been integrated by design. Out of the five QDs, the two orange QD are of lesser quality, with very few well-defined optical transitions. Some transitions of the QDs in the two different PhC waveguides and the cavity are almost resonant at $\sim 1.28\text{eV}$, $\sim 1.281\text{eV}$ and $\sim 1.283\text{eV}$, and fall in the region between the photonic band-edge and the predicted spectral center of channel A, especially the green center QD. This is a wanted scenario to attempt the resonant excitation through channel A of s-shell transitions of the center QD using either directly the laser pump, or indirectly, using single photons generated by the orange or magenta QD resonant transitions. As an illustration of the persistent challenge of inhomogeneous broadening, one can see that most s-shell transitions from the high quality left magenta QD are unfortunately below the predicted 1st band-edge of the structure and are thus unusable as they require a blue-shift of their energies by $\sim 15\text{--}20\text{ meV}$ s. But interestingly, the photons emitted by these transitions still propagate by radiation through the bandgap, up to the left nanobeam where they can be noticed due to out-of-plane scattering, as was also evidenced in Fig. 5:3.

5.4.2 Quasi-resonant excitations

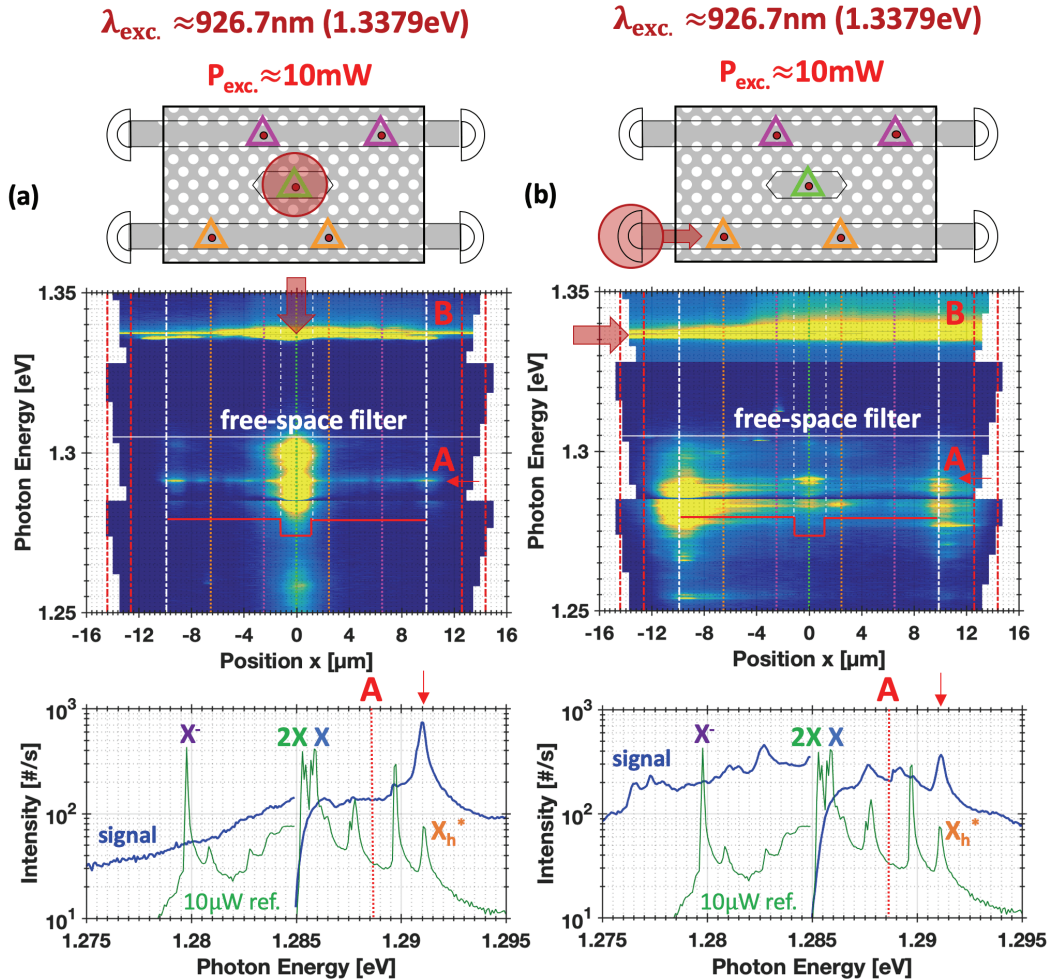


Fig. 5:15 – Quasi-resonant excitation of the center QD via excited p-shell states in the structure of Fig. 5:15 ($\lambda_{\text{exc.}} \approx 926.7\text{nm}$, 1.3379eV). Upper panels: pumping arrangement. (a) Vertical injection above the center QD and L_3 cavity. (b) Lower left grating injection into the lower waveguide. Center panels: energy-position maps. Lower panels: spectra integrated across x (blue) and $P_{\text{exc.}} \approx 10\mu\text{W}$ above barrier excitation (green). Horizontal red solid curve indicates the band-edge of 1st band. White line: 950nm cut-off of the free-space filter. Spectral center of channel A is indicated. Radius $r_{\text{fab.}} \approx 59\text{nm}$. Temperature $T \approx 10\text{K}$

Fig. 5:15 illustrates the photonic connectivity of all the elements: grating couplers, nanobeams, PhC waveguides, L_3 cavity and QDs transitions. In particular the s-shell transitions from the center QD integrated in the center L_3 cavity are spectrally overlapping with channel A, and the p-shell transitions with channel B. Channel B can be a useful intermediate track to guide light from the grating couplers up to the L_3 cavity for the quasi-resonant pumping of the center QD's p-shell. Channel A, however, is targeted for either: extraction of single photons from the center QD and funneling into coupled cavity-waveguide supermodes of this channel (i.e. the inverse operation of channel B), or for the switching of single photons propagating through coupled cavity-waveguide supermodes thanks to the dipole induced transparency effect arising from the coupling interaction of the center QD with such supermodes. In both sub figures, the laser photon energy is tuned to $\sim 1.3379\text{eV}$, practically in resonance with supermode 7B (+ + +) indicated in Fig. 5:14(a').

In part **(a)**, the laser spot impinges at normal incidence on the $L_{n=3}$ cavity and the center QD integrated within it as shown by the schematics in the upper panel. The energy-position map is acquired with a free space filter inserted in the path to the spectrometer (cf. Fig. 2:11 in chapter 2), such that it attenuates light with energy $> 1.305\text{eV}$, masking the high brightness of the pump laser at 1.3379eV . From this map, it is evident that light is propagating both left and right, which is the sign of the successful excitation of p-shell states, the emission of which is funneled into supermodes where the cavity is coupled to the PhC waveguides. This coupling is further supported by the clear evidence of a similar extraction with a supermode of channel A. At $\sim 1.2911\text{eV}$, a single feature extends to the left and right signaling again the propagation of photons through the waveguide channels. This feature stems from a bright spot of light seen in between $\sim 1.28-1.305\text{eV}$ corresponding to scattering from the $L_{n=3}$ cavity, and indicating the spectral extent of channel A (cf Fig. 5:6(b)) thanks to the overlapping s-shell transitions, as evidenced in Fig. 5:14(b). Part of the bright spot above $\sim 1.305\text{eV}$ may be cut by the free-space filter. The bottom panel displays the intensity spectrum integrated across position x of the device and focusing on a reduced range of photon energies. The reference signal from Fig. 5:14(c), acquired by above barrier excitation, is plotted in green; the s-shell transitions from the center QD are isolated and evidenced. The spectral line appearing at $\sim 1.2798\text{eV}$ is identified as the X- transition, which is bound by $\sim 6\text{meV}$ s to the X line recognized at $\sim 1.2858\text{eV}$, thanks to the 2X line bound to it by $\sim 0.3\text{meV}$ and the apparent $\sim 200\mu\text{eV}$ FSS split. The spectral line at $\sim 1.2911\text{eV}$, blue shifted to X by $\sim 5.3\text{meV}$ s, is attributed to the X_h^* same as in chapter 3 and 4. Plotted in blue is the spectrum extracted from the energy-position map. All transitions are merged in a continuum apart from the one line coinciding with the X_h^* . This can be explained by the spectral selectivity of quasi-resonant excitation: a specific excited p-shell state is preferentially connected to specific s-shell states either by radiative recombination of the charge carriers in a multi-excitonic state, or by non-radiative de-excitation of the trapped carriers. The single photons from the X_h^* are resonant with a coupled cavity-waveguide supermode of channel A, which is why light is seen propagating both to the left and right ends of the device.

The reverse scenario of propagation is demonstrated in part **(b)**, where the pump light is guided into the L_3 cavity to feed the center QD via the waveguides. The laser pump beam is shone onto one of the grating coupler which diffracts the light into the plane of the device, as shown in the upper panel. In the middle panel, the intense laser signal is seen propagating through the structure from left to right. Contrary to part (a), no bright spot is observed in the L_3 region, but instead a few discrete lines are evident. In particular, the feature at $\sim 1.2911\text{eV}$ photon energy is reproduced, the green center QD is excited and the photons generated from the X_h^* line are transported, as can be understood from the spectra in the bottom panel. A circular bright spot is seen between $\sim 1.275-1.295\text{eV}$ towards the left PhC-nanobeam interface, with components that extend towards the right. In particular, a QD transition from the orange QD located in the bottom waveguide, to the right, consistent with the characterization of Fig. 5:14(b), is apparently excited and emits at $\sim 1.283\text{eV}$. There are at least two possible explanations to these observations. Either the propagating pump signal in channel B along the bottom PhC waveguide intercepts a p-shell transition from the orange QD that is eventually connected to this s-shell transition, although it was not observed in Fig. 5:14(a'). Or, alternatively, the orange QD could be excited indirectly, not by the laser light but by the photons originating from parasitic QDs in the grating and nanobeams which could not be removed due to design constraints. These QDs can be pumped directly and emit photons at lower energies due to carrier relaxation. Subsequently, photons funneled into supermodes of channel A can propagate all the way through the structure. In fact, scattering from discrete lines can be seen at the opposite right edge of the PhC region, as opposed to the single

feature of part (a). All along the path, these photons can excite various resonant QDs, which then, are deterministically integrated, such as the green QD and the orange QD. The inhomogeneous broadening of the emission from the parasitic QDs could explain the large bright spot observed at lower photon energy. Even if these secondary sources are dimmer than the pump laser, the broadband character is intrinsically more suited for the incoherent quasi-resonant excitation of the other quantum emitters.

The driven transition at $\sim 1.2911\text{eV}$ produces ~ 750 counts/s at normal incidence compared to ~ 400 counts/s with grating injection despite the same level of pump power. This suggests that there is $\sim 47\%$ loss of the pumping efficiency between normal incidence and grating injection. This value can be expected since these grating couplers provide $\sim 25\%$ outcoupling efficiency to the space above [144] but also below the membrane. To reach readable PL intensities under quasi-resonant excitation the pump power had to be set to 10 milliWatts, which is related to the reduction of the absorption cross-section of the active medium. Above barrier, the bulk material is absorbing, and the density of generated charge carriers is ultimately dependent on the laser spot area (here $\sim 4\mu\text{m}^2$). A fraction of the drifting charge carriers is eventually trapped by the QD. Below barrier, outside of some trapping impurities, the material is mostly transparent apart from the QD discrete transitions, in which case the charge carriers are generated directly inside the QD. What is then relevant is the cross section of the QD ($\sim 100\text{nm}^2$, or $\sim 1.10^{-4}\mu\text{m}^2$) orthogonal to the laser beam photon flux. The ~ 750 counts/s of the X_h^* with 10mW spot below bandgap must be compared to the ~ 50 counts/s with 10 μW spot above barrier. This is a factor of 10^3 in excitation power and ~ 15 in intensity, which results in an overall factor $\sim 10^2$ - 10^3 which is rather consistent with the ratio of QD cross-section area to laser spot area.

As the experimental technique employed is intrinsically limited to the imaging along a single dimension, the two parallel waveguides cannot be resolved. **Fig. 5:16** supports the observations of Fig. 5:15, by displaying the numerically calculated field patterns generated by continuous sources of various energies located at different locations. These patterns approximate the excitation path of the incoherent CW laser pump in channel B and emission path of the emitted photons in channel A. The PhC waveguides have a length $L = 88a = 19.8\mu\text{m}$. In part (a), a supermode of channel B is stimulated by an H_z current source (or E_y dipole) located at position (0,0). The supermode pattern is illustrated for the source energy $E = 1.3379\text{eV}$, as an approximation of the quasi resonant excitation at normal incidence of the p-shell states from the center QD inside the L_3 cavity, as in Fig. 5:15(a). The pattern is identical to the 5B (+ + +) supermode from Fig. 5:7(b) and in good agreement with the observations of Fig. 5:14(a') and 5:15(a). The L_3 cavity appears bright and the two PhC waveguides appear rather dark in comparison, requiring a severe saturation of the intensity colour scale to be appreciated. The cavity-waveguide coupling efficiency is thus likely relatively low. This would be an issue for a dim stream single of photons, but not for the very intense stream of photons from the laser pump, hence it is seen experimentally without difficulty.

In part (b), a supermode of channel B is stimulated by a source located in the lower PhC waveguide, in order to approximate the stream of light injected through the lower left grating with a source energy $E = 1.3379\text{eV}$. The center L_3 cavity is indeed illuminated as supposed from Fig. 5:14(a') and Fig. 5:15(b) but the flow does not reach the upper PhC waveguide. This is due to the simultaneous activation of at least two supermodes: 6B (+ 0 -) and 7B (+ + +), and possibly 5B (+ + +) too, due to the $\sim 0.5\text{meV}$ bandwidth and far reaching tails of the source (cf Fig. 5:10(c)) and subsequent beating of these supermodes. Although the pump energy is the same as in part (a), the mode pattern differs because the source was launched inside the waveguide instead of the cavity, which represents a different superposition of eigen-states of the coupled system. P-shell states of the two magenta QDs would not be excited due to a missing spatial overlap with non-zero electric-field components even if their transitions were resonant in energy with supermodes of channel B.

Finally, in part (c), a source located in the center L_3 cavity, at the location of the center QD, stimulates a supermode of channel A with a source energy of $E = 1.2911\text{eV}$. This mode optically fully connects the two waveguides and the cavity regions. The coupling efficiency is much better than part (a) since a less severe (by two orders of magnitude) saturation of the intensity colour scale is required to appreciate the spatial distribution of intensity.

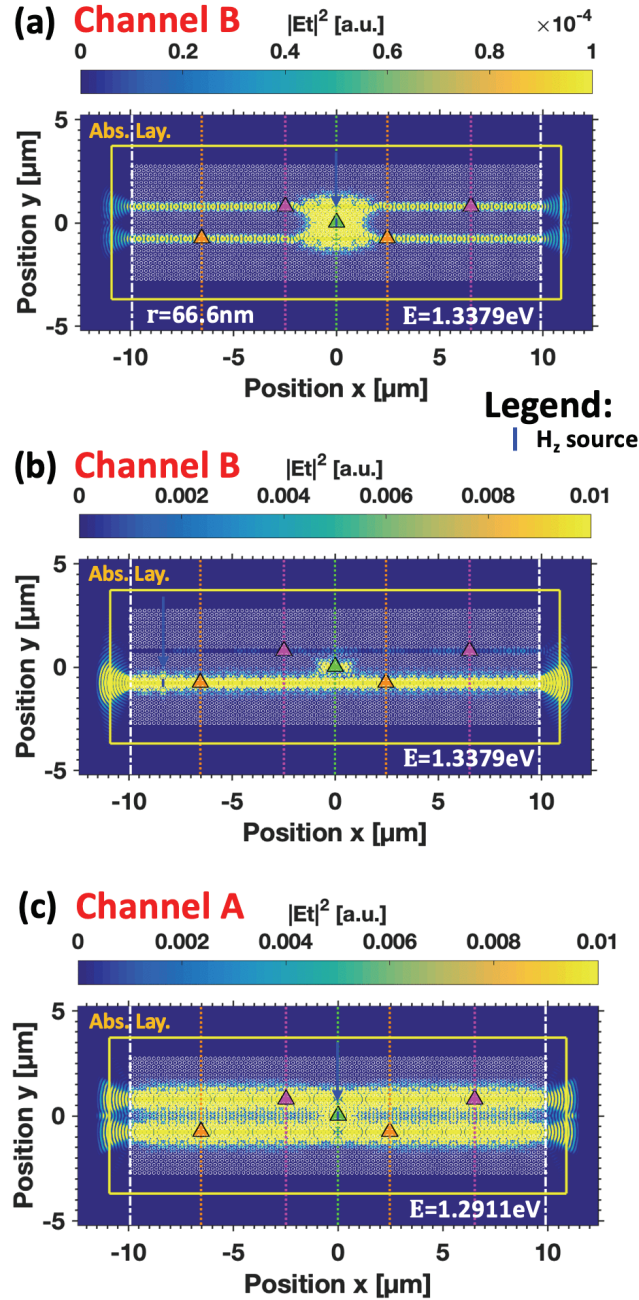


Fig. 5:16 – Numerical 2D FDTD simulations supporting the observations of Fig. 5:15, with sources located at different positions as indicated by the blue arrows. (a) Source at the green QD, source energy $E = 1.3379\text{eV}$. (b) Source at the lower waveguide, source energy $E = 1.3379\text{eV}$. (c) Source at the green QD, source energy $E = 1.2911\text{eV}$. Continuous wave sources, $\sim 0.5\text{meV}$ FWHM bandwidths. Surrounding absorbing layer, delimited by the yellow rectangle, prevents parasitic reflections. White dash-dotted contour delimits the PhC region. Contrast is enhanced by strong saturation of the colour scales. Numerical parameters: radius $r = 66.6\text{nm}$, pitch $a = 225\text{nm}$, thickness $t = 250\text{nm}$, by row $n_{\text{eff}}^{\text{slab}} = 3.203; 3.166$.

In Fig. 5:17, we schematize the various scenarios of the quasi-resonant excitation of p-shells transitions from QDs embedded in a transparent structure, which were evoked in the interpretation of Fig. 5:15(b). The green QD₁ depicted illustrates the center QD embedded in the L₃ cavity, the blue QD₂ represents a parasitic QD, such as the ones that likely remain in the lower-left grating coupler or suspended nanobeam, and the orange QD₃ corresponds to the one in the lower waveguide, to the right. The pump is injected with a photon energy corresponding to that of the mode energy of a single considered supermode of channel B.

In part (a), for QD₁, depicted in green, the recombination energy of the p-shells electron and holes are resonant with this input supermode of channel B. Once generated inside the QD, they can recombine, emitting photons coupled again into the path of the supermode of channel B with a coupling efficiency $\beta_1^{(B)} = \frac{\Gamma_{\text{path},1}^{(B)}}{\Gamma_{\text{path},1}^{(B)} + \Gamma_{\text{uc},1}^{(B)}}$, or emitting photons of the same energy that are not coupled to this same supermode of channel B or that are lost due to non-radiative effects, with a probability $1 - \beta_1^{(B)}$. Through phonon de-excitation, the confined charge carriers may also lose energy to occupy the s-shells. The resulting charge carriers can ultimately recombine and produce photons coupled to a single considered supermode of channel A, with a coupling efficiency $\beta_1^{(A)}$. This is the ideal targeted scenario and what was apparently observed with the X_h* emission in Fig. 5:15(a,b).

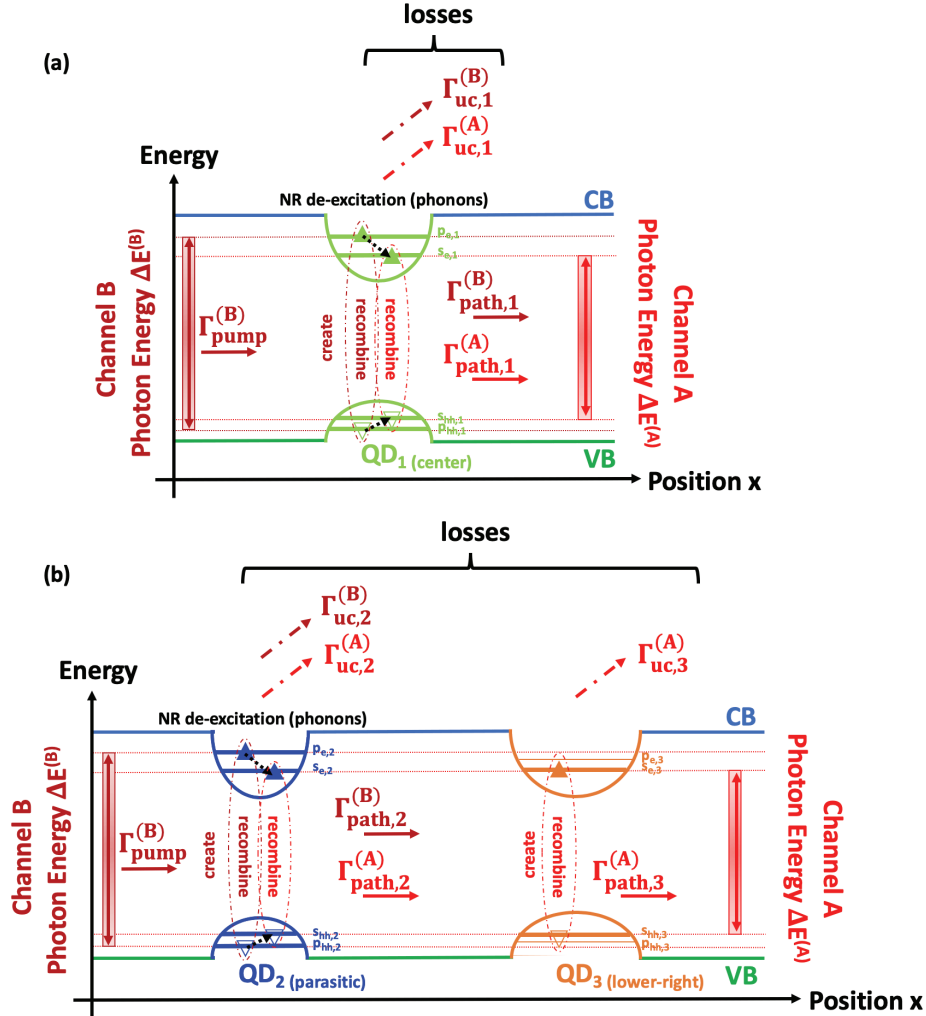


Fig. 5:17 – Schematics of quasi resonant excitation of QDs p-shell states coupled to a supermode of channel B with a target output of s-shell states into a supermode of channel A. (a) Targeted operation with direct pumping of a QD₁ (green), (b) Fortuitous operation, photons of a QD₃ (orange) are emitted into the supermode of channel A due to resonant pumping via a parasitic QD₂ (blue), in the excitation path, operating as in (a). Symbol Γ refers to photon rates. $\Gamma_{\text{path},i}^{(X)}$ refer to photons originating from QD_i, radiatively coupled into channel X flowing in the intended path of channel X (cavity out-of-plane radiation channel or waveguide in-plane radiation channel). $\Gamma_{\text{uc},i}^{(X)}$ refer to photons generated by QD_i, at the energy of channel X, but uncoupled to the intended emission path of the channel. Solid arrows point to pure radiative processes, dot arrows indicate a non-radiative process, dot-dash arrows are a mixture of the two.

In part **(b)**, a second QD₂ (blue) behaves the same way as in part (a), with the difference being that this QD₂ is not introduced by design. It corresponds to one of the QDs that may not have been removed in the grating couplers or nanobeams and can be coupled to both the supermodes of channel B and A. Here the two considered supermodes are not necessarily the same as in part (a). In the case of the third orange QD₃ charge carriers cannot be generated into the p-shells via the considered supermode of channel B. In this scenario, the QD would remain dark; it should not emit photons, especially not into the supermode of channel A despite the resonance of its s-shell states, unless it is pumped by the intermediate parasitic QD₂ to which it is radiatively coupled via the supermode of channel A transmitting s-shell states photons. This is a coincidental mode of operation and could explain what was apparently observed in Fig. 5:15(b) with the emission at $\sim 1.283\text{eV}$ of the lower-right orange QD.

5.5 Conclusion of chapter and perspectives

This chapter presented the first steps towards the realization of a functional photonic element incorporating QDs within a coupled PhC cavity-waveguide system, in views of on-chip processing of single photons generated within the same device. The selected model system is composed of an L₃ cavity inserted symmetrically in between two PhC waveguides. The photonic dispersion consists of the waveguide bands of the two coupled waveguides, the coupling of which is controlled by the number of rows separating them from the coupling cavity, and the resonantly coupled channels labelled here A, B, C..., opened around the energies of the L₃ cavity modes. Due to the opening of these channels, the optical supermode structure projected in energy-position space supports local photonic potential dips at the location of the L₃ cavity, reminiscent of the defect-potential of chapter 3. In the same fashion, these can trap and localize each supermodes of the 1st (named A₀) and 2nd band (C₀). Supermode C₀ again exists within the quasi-continuum of the 1st band, and modelling predicts disorder-enabled mode hybridization and delocalization.

In the fabricated devices, five site-controlled QDs are incorporated, in particular one within the center cavity. The waveguides are connected to four grating coupler ports, by intermediate suspended nanobeams, to allow both the extraction of optical signal and the injection of laser light. The characterization of the optical mode structure by near-field imaging indeed revealed manifestation of resonantly coupled channels by the observation of bright scattering spots originating from the cavity region, connected to extended components. At lower pump power, finer spectral features signatures of coupling between the optical elements can be seen, and the various QDs transitions were observed individually by selective spot excitation. One such feature of the B channel was brought into resonance with p-shell states of the center QD by lithographic tuning of the PhC hole radius, which allowed the below barrier, quasi-resonant excitation of these states at normal pump incidence. The s-shell states of this center QD were populated by de-excitation of the p-shell confined charge carriers. These subsequently recombined to produce photons from the excited hole state X_h* which were funneled into a supermode of channel A. The reverse process was reproduced by injection of the tuned laser pump into the plane of the structure via the grating coupler, which completed a demonstration of the complete connectivity of the QD, cavity, waveguides and grating couplers.

The study constituted the first investigation of a complex 2D PhC structure incorporating several site-controlled QDs with identifiable spectral features. More specific structures, discussed at the beginning of this chapter, could be explored to implement other quantum processing functionality. For instance, two cavity side-coupled to a same PhC waveguide, each cavity containing a QD in resonance with a single supermode connecting both cavities would be useful for demonstrating N0-0N states [288]. Finally, the in-plane optical quasi-resonant excitation may prove useful for reducing pure dephasing contributions, and the QD emission could be driven by on-chip coherent pulsed excitation.

Chapter 6 Conclusions of thesis and outlooks

6.1 Conclusions of thesis

This thesis targeted the development of monolithic functional devices for on-chip quantum-dot (QD)-based single photon manipulation in views of future integrated quantum photonics applications. The extraction and processing of single photons in a solid-state platform faces many hurdles, among which is the necessity to reproducibly and precisely control the locations of more than one quantum emitter's dipole for deterministic local interactions with the engineered density of states of electromagnetic modes. This work addresses this issue using the MOCVD-grown pyramidal site-controlled quantum dot technology using highly unconventional [111]B-oriented GaAs substrates. The approach provides a mean for systematic and precise positioning (within $<50\text{nm}$) of an arbitrary number of QDs inside specifically tailored or coupled photonic crystal (PhC) structures that can be integrated on a chip. The three main core chapters of the thesis use the tools introduced in chapter 2 in order to design, fabricate and analyze the integrated QD-PhC devices. The focus is set on photonic modes presenting both localized features overlapping with the QD emitters and having extended parts reaching to remote regions on the chip. The fabrication techniques involved in the integration of the site-controlled QD systems and the tailored PhC cavities and waveguides were briefly recalled. To identify the photonic modes, a broadband imaging technique is used to record the optical mode structures excited by dense embedded QDs arrays acting as internal broadband light emitters. The optical set up described is also useful for acquiring polarization-resolved and time-resolved photoluminescence spectra. The deterministic coupling of the integrated quantum emitters is targeted in views of the generation, extraction and funneling of single photons into resonantly coupled modes. Several aspects of the physics and technology involved in reaching this target are presented in detail in the three core chapters.

Chapter 3 reports the case study of a first tailored-potential photonic heterostructure: the defect-potential PhC cavity, consisting of a deterministic defect made by shifting a few selected holes of an $L_{n=61}$ cavity. The photonic potential generated by the defect locally traps defect modes, pulled down in energy from waveguide bands and naturally co-polarized to them. The local defect-potential is adjustable by structural parameters: the hole shifts and the number of rows. Whereas similar structures were considered previously by others, here we concentrated on effects of mode polarization and coupling between localized and extended photonic states. Due to disorder effects, defect modes from the 2nd band (H-polarized) can hybridize with nearby extended fast-light modes from the 1st band (V-polarized), which allows the defect modes to delocalize. The experimental optical mode structures measured by polarization-resolved near-field spatial imaging agrees to a good extent with the calculated optical properties and binding energies of the various defect modes. The estimated Q-factors of the extended modes from the 1st band follow a trend that is reproduced by a borrowed model, showing the strong limiting contributions of the Urbach tail from the semiconductor band-edge and scattering losses near the PhC structure's band-edge. The V-polarized fundamental defect mode displays promising high Q values up to 9'300 in the $\sim 1.26\text{-}1.27\text{eV}$ photon energy range. The deterministic weak coupling of the excited hole state X_h^* transition from a single pyramidal site-controlled QD to one such defect mode ($Q \approx 6'900$, $\hbar\kappa \approx 185\mu\text{eV}$) was achieved by temperature tuning. Several manifestations of the Purcell effect were demonstrated when approaching QD-cavity resonance: intensity increase, linewidth decrease, co-polarization, and decay time reduction of the QD emission. An effective enhancement factor $Enh. \approx 8.5 \pm 2.7$ was retrieved, associated with a minimum $\beta^{cav.} \approx 0.87 \pm 0.04$ coupling efficiency.

The Q-factor is design-sensitive and could be further increased by optimizing the defect configuration [160], [161], [238]. A deeper understanding of the hybridization phenomenon may be interesting for the extraction of single photons from highly symmetric QDs to fully exploit the two orthogonal dipoles.

Chapter 4 presented another case study of a more elaborate tailored-potential photonic heterostructure: the tilted-potential PhC cavity, defined by the staggered shifts of the side holes, from one end of the cavity to the other. The adiabatic widening produces a triangular potential the gradient of which can be adjusted by a structural parameter: the maximum hole shift. The confined Airy-Bloch modes possess a main lobe where the field is strongest, allowing for efficient local interaction with a well-positioned QD, connected to a trailing tail of lesser lobes. The fabricated devices faithfully reproduced the predicted optical mode structure as they provided large enough potential gradients to partially quench the effects of fabrication disorder, in particular Anderson localization. Q-factors in the range of $\sim 5'000$ - $10'000$ were observed. The deterministic weak coupling of the negative trion X^- to one such mode ($Q \approx 5'900$, $\hbar\kappa \approx 217\mu\text{eV}$) was evidenced, once more by thermal tuning, with clear evidences of a Purcell effect: QD intensity increase, mode linewidth decrease, co-polarization and decay time reduction of the QD emission. A modest enhancement factor $Enh. \approx 1.3 \pm 0.1$ was extracted, caused by the large mode volume and likely by unfavorable spatial overlap of the QD with the mode peak. The latter issue could in principle be rectified with a tuning technique for selecting another more appropriate Airy-Bloch mode, since the location of the main lobes shifts linearly with the mode energy. A minimum coupling efficiency factor $\beta^{cav.} \approx 0.24 \pm 0.06$ was estimated, as well as a coupling constant $\hbar g \approx 50\mu\text{eV}$ close to that observed in GaAs QD systems.

Airy-Bloch photonic wavefunctions resonantly coupled to a waveguide channel, similarly to $L_{n=3}$ cavity side-coupled to a semi-waveguide system, can provide a solution for efficient unidirectional single photon injection into an integrated quantum photonic circuit.

Chapter 5 explored the potential of site-controlled QDs towards functional QIP devices using a test platform consisting of two PhC waveguides coupled via a PhC cavity, with four ports connected by suspended nanobeams to grating free-space couplers. The optical mode structure is predicted, especially the coupled cavity-waveguide modes, and various supermodes are analyzed in detail. Resonant coupled channels are identified around the intersection points of the cavity mode energies with the band structure of the two coupled PhC waveguides. In the fabricated structures, five site-controlled QDs are integrated at locations set by design within both waveguides and cavity. The QDs were individually characterized by selective spatial excitation. In particular, the various resonant channels were evidenced by the spot excitation of the QD integrated within the center cavity. By selection of the PhC hole radius, two such channels were brought into resonance with both the p-shell states and s-shell states of the center QD. The quasi-resonant excitation at normal incidence of the p-shell states evidenced generation of photons from the X_h^* s-shell transition and their transfer into the PhC waveguides. Reproduction of the experiment with in-plane injection through a grating coupler demonstrated the complete optical connectivity of the various elements: QD coupled to the cavity, cavity coupled to waveguides, waveguides coupled to suspended nanobeams, themselves coupled to grating couplers.

This preliminary study displayed the reproducible integration of $N=5$ trackable quantum emitters in a 2D photonic structure and the possibility to analyze such a device with our spatially-resolved imaging technique. It verified the necessary requirements for potential processing of single photons. Exploration of the QD dipole-induced transparency phenomenon will require the wavelength scanning of the laser pump to estimate the reflection/transmission of the device with and without the X_h^* in resonance with the supermode of the resonantly coupled channel. Other, closely related functional elements could be envisioned, relying for instance on the engineering of a 50/50 directional coupling to use the HOM effect.

In conclusion, the results presented in this thesis are encouraging for future developments of quantum-dot-based QIP applications: they show that the PhC fabrication and the site-controlled QD technology have passed a number of milestones. Advanced photonic crystal structures can be designed, modelled to make prediction over the modes' properties and fabricated to a high degree of fidelity. These structures can exploit photonic potential tailoring or coupling of several PhC elements to provide optical modes possessing both cavity and waveguide components for local interaction with a QD's dipole and connectivity to remote locations. The optical mode structures measured using QDs as internal light emitters and an image technique are in good agreement with the predictions, despite currently unavoidable fabrication disorder levels. The various spectral contributions, between electromagnetic modes (1st or 2nd band) and QDs can be distinguished with little ambiguity. An arbitrary number of QDs can be integrated by design at specific locations within $<50\text{nm}$, deterministically and reproducibly across a chip.

The spectral linewidths of pyramidal QDs are reasonably narrow, down to $20\mu\text{eV}$, mostly broadened by pure dephasing, but inhomogeneous broadening, although much smaller than that of self-assembled QDs, is still an essential issue to tackle. The site-controlled QDs can be brought into resonance with prescribed electromagnetic modes, by selection of an adequate structure with a first lithographic coarse tuning and further external (here, thermal) fine tuning, to achieve a deterministic weak coupling interaction. The results are consistent with previous works on pyramidal site-controlled QDs.

The presented work verified several requirements to fabricate functional elements for quantum-dot-based QIP applications relying on weak coupling, such as on-chip single photon sources (SPS). The principles of achieving directional coupling and switching using coupled cavity-waveguide systems were also demonstrated. An on-chip nonlinear processing of these single photons, for instance by dipole induced transparency, is yet to be demonstrated, but constitutes a realistic future goal. Similarly, the strong coupling threshold is within reach, and may lead to promising polariton-based functional elements. In this perspective, more efforts should be oriented toward the increase of Q factors and QDs oscillator strengths, and toward the integration of means to tune individually the various resonances.

6.2 Future directions

The future directions proposed here are classified from short-term to more long-term projects.

First, we propose to shift the focus to the various issues linked to single-photons. The very first is to ensure that the QD emission into the tailored photonic modes is truly characteristic of a stream of single photons. To do this, the setup must be modified into a Hanbury-Brown and Twiss configuration to record the photon correlation characteristics. Preliminary auto-correlations results from the light-hole X_h^* resonance at $T \approx 27.5\text{K}$ with the fundamental mode $\#0_M^{(0)}$ of the defect-potential cavity (chapter 3) yielded a raw $\tilde{g}^{(2)}(0) = 0.64 \pm 0.07$, eventually deconvolved with the instrumental transfer function to give $g^{(2)}(0) = 0.48 \pm 0.10$. As for the X resonance at $T \approx 41.5\text{K}$ and the Airy-Bloch mode $\#8$ of the tilted-potential cavity (chapter 4), a raw $\tilde{g}^{(2)}(0) = 0.68 \pm 0.10$ was estimated, deconvolved to $g^{(2)}(0) = 0.25 \pm 0.13$ after taking into account the finite time response of the photodetectors. Thus, the integrated QDs qualify as single photon emitters. Next, to estimate the indistinguishability of the single photons, a Hong-Ou-Mandel interferometer could be used to characterize the single photon interference features [68]. Eventually, these qualities should be preserved all along the propagation through a highly dispersive photonic device, that can alter the shape of single photons wavepackets. Spatially resolved photon correlations can be done by coupling fiber optics over the various implemented grating couplers, or by the spatial filtering of the magnified collected signal propagating in free-space up to a spectrometer to precisely select various regions of interest.

The work could be pushed further by adapting the tailored-potential cavity structures into waveguides and grating couplers in views of in-plane integration rather than out-of-plane interfacing. This will also allow the estimation of the waveguide beta factor by separation of the currently ambiguous top emissions of both the QD and CM components.

The defect-potential could be upgraded with two grating couplers for the extraction of single photons from the $\#0_F^{(1)}$ or $\#0_M^{(1)}$ hybridized modes, the latter will require smaller PhC hole sizes to spectrally overlap with the QD s-shell emission. Alternatively, the defect-potential could be side-coupled to a waveguide or two semi-waveguides as in [253], to simply extract the generated photons from a QD resonantly coupled to the fundamental mode $\#0_M^{(0)}$, or more interestingly, to use dipole induced transparency for all-optical switching [284][291]. The generation of other non-classical states could be pursued, such as the generation of two-photon states using the leapfrog process, which was demonstrated in [258] using a defect-mode of cavity analogous to the defect-potential cavity. The Xenon deposition technique could be used on a structure similar to that of chapter 3 to shift only the defect mode $\#0_M^{(0)}$ in resonance with the middle point of the X-2X couple. As it stands, the cavity mode is too broad and would likely interact with both X-2X split linewidths preventing a clear manifestation of the effect. Further optimization of the design could help to increase the Q-factor of this defect mode to circumvent this issue, and also to eventually achieve the strong coupling of a pyramidal site-controlling QD to a cavity mode.

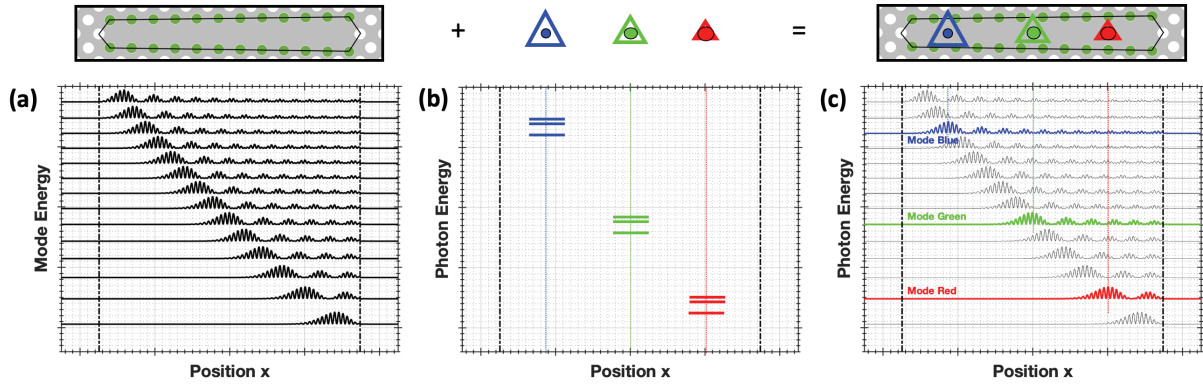


Fig. 6:1 – Blueprint for the making of a wavelength-multiplexed “RGB” Single Photon Source based on a tilted-potential structure for QIP applications. (a) Energy-Position map of a Tilted-Potential PhC cavity of the Airy-Bloch modes; (b) Energy-Position of three site-controlled quantum dots with their respective s-shell emissions, which are tailored by the sizes of the pyramids $s_B > s_G > s_R$ ($\lambda_B < \lambda_G < \lambda_R$); (c) Energy-Position of the device resulting of the combination of (a) & (b) with fine tuning of the appropriate single QD lines to their respective single Airy-Bloch mode. Injection of single photons would occur by optically interconnecting/interfacing the right end of the waveguide.

In Fig. 6:1, we present a blue-print for a tilted-potential wavelength-multiplexed single-photon injector, an “RGB” SPS. Such device would provide streams of single photons at rates beyond the ones achievable with bare single QD emitters. The concept of the device revolves around the spatial multiplexing of wavelength-shifted pyramidal QDs [143][322] making use of the slanted photonic energy-position dispersion of the optical mode structure. From part (a), the tilted-potential PhC L_n cavity is designed with a gradient dE/dx (i.e. length of cavity and s_{max}) selected so that the Airy-Bloch modes energy dispersion covers the span in photon energy of the intended wavelength-shifted QDs’ s-shell transitions seen in part (b). The locations of these quantum emitters must be selected to precisely interact with the maxima of the main lobes of selected Airy-Bloch modes, as seen in (c), and the selected excitonic species of each QD must be brought in resonance with the modes by individual fine energy tuning. The generation of single photons could be done by vertical pulsed resonant excitation of each site-controlled QD by as many wavelength-tuned laser beams, or by in-plane coherent quasi-resonant excitation of higher-energy excited states through the narrower end interfaced to an input waveguide (as in chapter 5). To retain the triangle potential part, necessary to form the Airy-Bloch modes, the broader end of the cavity can be interfaced to a waveguide channel with a partially transparent element, a few holes for instance, serving as a thin vertical potential barrier at the broader end, to allow eventual leakage of the single photons extracted into the Airy-Bloch modes by optical tunneling into travelling modes, or with a cavity filter to enable resonant coupling, for instance via a $L_n=3$ and channel A of chapter 5.

More generally, the present tailored-potential cavities could be improved following the inverse design methodology of [240] and other types could also be investigated. For instance, it could be interesting to introduce chirality [156] in a tilted-potential where the upper side of the cavity is widened towards the right, shifted by half a lattice constant with respect to the bottom side, widened towards the left, to see if the left and right circularly polarized components propagate in two opposite directions.

The completion of the work initiated in chapter 5 requires two developments. First, the evaluation of the coupling strength of the center QD to the $L3$ cavity is needed. This would require a pump laser sources that can be tuned to reach the s-shell emission and the resonant channel A in order to probe very small spectral variations in the reflection/transmission characteristics. To resolve the most interesting effects, the μ PL setup should be upgraded to $\sim 4\mu\text{eV}$ spectral resolution using a Fabry-Pérot scanning cavity [323]. Second, an optimization of the suspended nanobeam/PhC interfaces to increase the transmission and reduce optical losses by scattering would be useful. Several adiabatic tapering designs already exist, and FEM or FDTD simulations combined with genetic algorithms [319]–[321] could be used to find optimal structural parameters. It is also worth extending the size of the suspended nanobeams to increase the radius of curvature of the bends and thus decrease related radiative losses. The setup could be further modified to give the possibility to control multiple beams, for instance to realize

pump probe experiments, in order to generate single photons from a QD as probes while pumping another processing QD.

Overall, efforts in increasing the quality of fabrication of the PhC structures, and optimization of the growth of the pyramidal QDs is beneficial at all levels. Deterministic resonant coupling from spatial and spectral overlap is more easily achieved with reduced disorder effects, highly symmetric QDs with a reduced inhomogeneous broadening, narrower linewidths and stronger dipole oscillator strengths. As the important interactions are based on the resonant coupling of electromagnetic modes of optical elements and QDs transitions, efforts must be directed towards the integration of tuning knobs to finely adjust independently each and every component. Strain tuning with a thin layer of phase change material deposited on top of structures [209] and Stark effect with p-i-n junctions [70], [207], [213], [324], [325] are particularly promising for the QDs spectral lines. This is unavoidable in order to proceed further and achieve deterministic interactions with an arbitrary number ($N > 1$) of quantum emitters. A long-term goal consists in having several QDs resonant with a single optical channel, composed for instance of multiple L_3 cavities side-coupled to a single PhC waveguide [326] to enable mutual dipole-dipole radiative coupling [294], for coherent absorption [327], [328], superradiant correlated emission [329], [206], [209] and entanglement distribution [22], [330].

Appendix A

Supplementary equations

The extracted lifetimes can then be plotted versus detuning. Data points are fit with a function, extension of **(Eq. 1:20)**, having two or three free parameters: F_P^{\max} , $\tau_{sp.}^{\text{homog.}}$ and possibly $\tau_{\text{leak.}}$.

$$\tau_{sp.}^c(\Delta) = \frac{\tau_{sp.}^{\text{homog.}}}{\left\{ F_P^{\max} \cdot \zeta^2 \cdot \mathcal{L}(\hbar\omega_c, \hbar\kappa, \hbar\omega_{QD}, \hbar\gamma_{QD}) \cdot \chi(\Delta, T) + \frac{\tau_{sp.}^{\text{homog.}}}{\tau_{\text{leak.}}} \right\}} \quad \textbf{(Eq. A:1)}$$

The effective Purcell enhancement factor is defined as:

$$\text{Enh.} = \frac{\tau_{sp.}^{\text{homog.}}}{\tau_X(\Delta = 0)} \geq 1 \quad \textbf{(Eq. A:2)}$$

and the Anti-Purcell inhibition factor as:

$$\text{Inh.} = \frac{\tau_{\text{leak.}}}{\tau_{sp.}^{\text{homog.}}} \geq 1 \quad \textbf{(Eq. A:3)}$$

which would be unity if the bandgap effect does not impact the intrinsic lifetime $\tau_{sp.}^{\text{homog.}}$.

With these two factors, the $\beta^{cav.}$ coupling efficiency is expressed as [195], [196]:

$$\beta^{cav.} = \frac{\Gamma_{sp.}^c}{\Gamma_{sp.}^c + (\Gamma_{sp.}^{nc} + \Gamma_{nr})} = 1 - \frac{\tau_X(\Delta=0)}{\tau_{\text{leak.}}} = 1 - \left(\frac{1}{\text{Enh.}} \cdot \frac{1}{\text{Inh.}} \right) \quad \textbf{(Eq. A:4)}$$

Appendix B

Supplementary fabrication details

Alignment marks (AMs) fabrication procedure:

Four 300 x 300 μm^2 large squares AMs are needed to surround the future regions of EBL writing with sufficient redundancy to ensure alignment capability in case of accident. To increase the AMs reliability, nine 10 x 10 μm^2 squares are written in a 3 x 3 configuration with a pitch of 100 μm . The AMs are etched to $\sim 1\mu\text{m}$ depth into the GaAs substrate which is first exposed by local removal of the GaAs membrane and AlGaAs sacrificial layer. The alignment procedure consists in the detection of the etched squares' edges with a scanning algorithm during the EBL writing.

Plasma Enhanced Chemical Vapour Deposition (PECVD) SiO_2 mask recipe:

- Temperature $T=300^\circ\text{C}$; flux rates $\text{SiH}_4=400\text{cm}^3/\text{s}$, $\text{N}_2\text{O}=710\text{cm}^3/\text{s}$; pressure $P=1\text{Bar}$, RF power 20W.
- The chamber should be conditioned by a first unloaded coating run.

Reactive Ion Etching (RIE) recipes:

- Plasma ashing: $\text{O}_2=100\text{cm}^3/\text{min}$, $P=100\text{mTorr}$, 50W 5'
- Etching: flux rates $\text{CHF}_3=25\text{cm}^3/\text{min}$, $\text{Ar}=25\text{cm}^3/\text{min}$; pressure $P=15\text{mTorr}$, RF power 50W.
- The chamber should be purged with the plasma ashing recipe and then conditioned by a 12 minutes unloaded etching run.

Inductively Coupled Plasma (ICP) recipes:

- Cleaning: Temperature $T=29^\circ\text{C}$, flux rates $\text{O}_2=20\text{cm}^3/\text{min}$, pressure $P=3\text{Pa}$, coil power 400W, RF power 150W RF.
- Etching: $T=29^\circ\text{C}$, flux rates $\text{BCl}_3=8.5\text{cm}^3/\text{min}$ (etchant), $\text{N}_2=11.5\text{cm}^3/\text{min}$ (passivation), pressure $P=0.18\text{Pa}$, coil power 600W, RF power 20W RF.
- The chamber should be cleaned for 11 or 30 minutes using the cleaning recipe and then conditioned by a first unloaded etching run.
- The sample is held in position by a quickstick piece melt at 120°C pasted on the back on top of a support wafer that was initially cleaned with acetone + IPA + water.

Substrate exposure for the AMs:

- PECVD of 150nm SiO_2 mask
- 1' PMMA A8 electron-resist spin coating at 6000rpm and soft baking at $T=160^\circ\text{C}$ degrees for 5'.
- EBL writing of big square openings in PMMA to define the AMs regions
- 1' MIBK:IPA (1:3) development of PMMA
- 20' RIE transfer of openings into SiO_2 mask
- 5' acetone bath in ultrasound (US) 60kHz + IPA + water + 5' RIE plasma ashing to fully remove PMMA
- Optical Microscope quality check
- 400'' ICP GaAs membrane dry etching
- 4' 10% HF $\text{Al}_x\text{Ga}_{1-x}\text{As}$ sacrificial layer wet etching + 5' water rinsing, SiO_2 mask is stripped
- Optical Microscope quality check

Appendix B

AMs fabrication:

- PECVD of 300nm SiO₂ mask
- 1' PMMA A8 electron-resist spin coating at 6000rpm and soft baking at T=160C degrees for 5'.
- EBL writing of square openings in PMMA to define AMs
- 1' MIBK:IPA (1:3) development of PMMA
- 40' RIE transfer of square openings into SiO₂ mask
- 5' Acetone bath in US 60kHz + IPA + water + 5' RIE plasma ashing to fully remove PMMA
- Optical Microscope quality check
- 1200" ICP GaAs substrate dry etching
- Optical Microscope + SEM quality check
- 4' BHF removal of SiO₂ mask + 5' water rinsing + 5' RIE plasma ashing

Pyramidal recesses patterning procedure:

- PECVD of 40nm SiO₂ mask
- PMMA A4 spin-coating at 6000rpm and baking at T=160C
- EBL of triangle openings into PMMA using AMs to define regions to be patterned (+ big triangles at edges and other visual cues to define regions)
- 1' MIBK:IPA(1:3) development of PMMA
- 5'RIE transfer of openings into SiO₂ mask
- Wafer cleaved in 1/6th pieces, continues with piece #4 (A177-3-4A & 4B)
- Optical Microscope check
- 10' Acetone bath in US 60kHz + IPA + water + 2' RIE plasma ashing to fully remove PMMA
- SEM quality check
- 30" water + 30" Methanol + 10" Bromine-Methanol (Br₂-CH₃OH) 0.06% prepared few hours earlier wet etching of a dummy (111)B sample + 10" Methanol rinsing + 2' water rinsing + SEM quality check
- 30" water + 30" Methanol + 10" Bromine-Methanol (Br₂-CH₃OH) 0.06% wet etching on real (111)B sample+ 10" Methanol rinsing + 2' water rinsing, on real sample
- SEM quality check
- 4' HF removal of SiO₂ mask+ 4' water rinsing + 5' RIE plasma ashing
- SEM quality check
- Cleaning: 5' plasma ashing + 5' 10% BHF + 2' Water + N₂ blow drying
- Inserted in a box placed into a glove filled with N₂ for transfer to MOCVD

MOCVD pyramidal QDs Growth:

- Temperature of sample stabilized at T=600C, carrier gas N₂, pressure P=20mBar
- 4' deoxidation with maximal V in the V/III ratio
- 1000" growth of the 5nm GaAs buffer: TEGa + AsH₃ (growth rate of 0.005nm/s, V/III=260)
- 68.8" growth of the 0.75nm In_xGa_{1-x}As core, x=0.25: TEGa + TMIn + AsH₃ (growth rate of 0.011nm/s, V/III=246)
- 400" growth of the 2nm GaAs spacer: TEGa + AsH₃ (growth rate of 0.005nm/s, V/III=260)
- 919.5" growth of the 8nm GaAs cap: TMGa + AsH₃ (growth rate of 0.009nm/s, V/III=942)

Photonic Crystals fabrication and membrane release:

- Cleaning: 5' HF 40% + water rinsing
- PECVD of 80nm SiO₂ mask
- PMMA spin-coating A4 at 2000rpm and baking at T=160C
- EBL of PhC holes openings using AMs to overlap precisely PhCs pattern with pre-existing QDs pattern
- 1' MIBK:IPA(1:3) development of PMMA
- 12' RIE mask transfer of holes openings into SiO₂ mask
- 10' Acetone bath in US 60kHz + IPA + water + 5' RIE plasma ashing
- Optical Microscope + SEM quality check
- 1/6th piece cleaved in two, to separate A and B parts, continues with piece #4B (A177-3-4B)
- 400" ICP (300nm depth) dry etching of a dummy (100) membrane + cleaved for SEM cross-section quality check

- 400" ICP (300nm depth) dry etching of real sample
- 2' RIE plasma ashing
- 50" 10% BHF heated 10'@T=40C , large droplet prepared aside and rolled over for wet etching of AlGaAs sacrificial layer to release the membrane of a dummy (100) membrane sample + cleaved for SEM cross-section quality check
- 50" 10% BHF heated 10'@T=40C , large droplet prepared aside and rolled over for wet etching of AlGaAs sacrificial layer to release the membrane of the real sample
- 25" Water rinsing @T=40C
- 15' citric acid bath
- 1 night drying in N₂ box
- inserted in cryostat

Appendix C

Investigated sample's layout

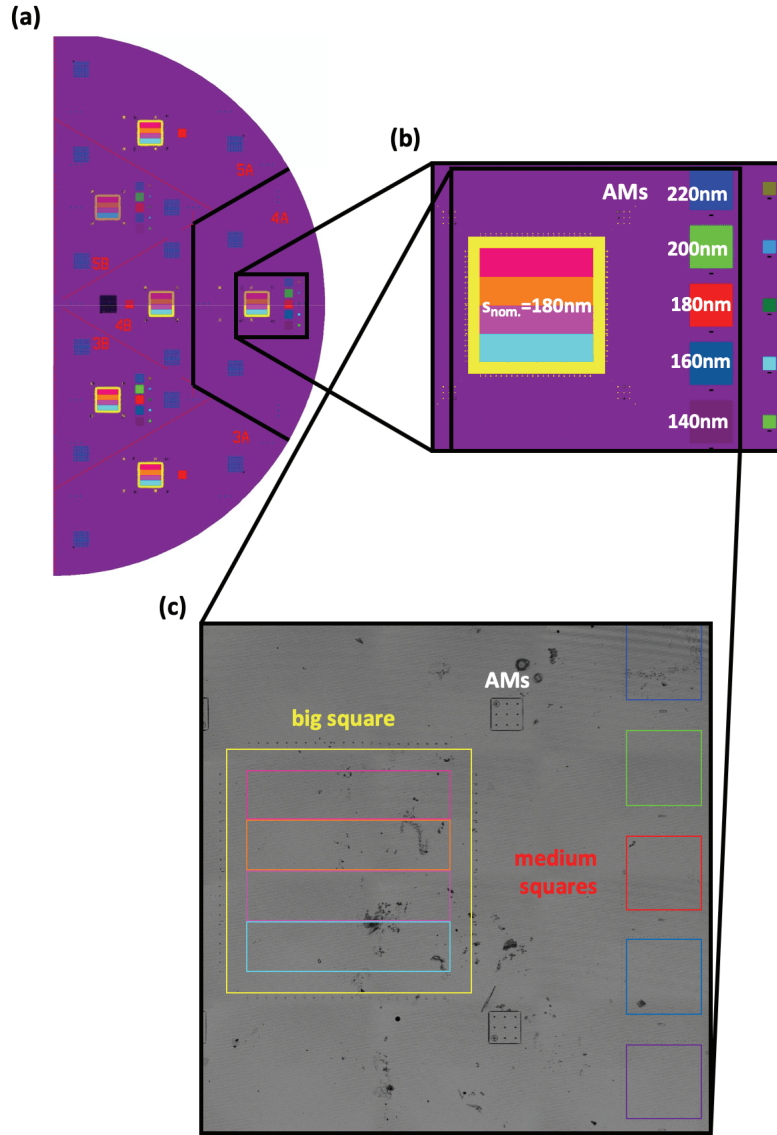


Fig. C:1 – Design of the processed sample in views of QD patterning and eventual integration with PhC structures. (a) QD pattern design for one half of a 2'' GaAs wafer. It is composed of three sixths further subdivided in A and B pieces (3A, 3B), (4A, 4B) and (5A, 5B). The sample investigated in this thesis corresponds to piece 4A. **(b)** Focus on the QD pattern of piece 4A. Four alignment marks (AMs) surround a big $2.4 \times 2.4mm^2$ square region planned to incorporate $s_{nom.}=180nm$ inverted pyramids. The big square is subdivided in four strips with specific patterns to accommodate the integration of single QDs in PhC structures. Four $720 \times 720\mu m^2$ medium squares and four $216 \times 216\mu m^2$ are also visible and planned to incorporate $s_{nom.}=140, 160, 180, 200$ and $220nm$ inverted pyramids, and periodically arranged smaller inverted pyramids of size $s'_{nom.}=s_{nom.} - 80, 60, 40, 20nm$ to fill PhC structures with complete arrays. **(c)** Confocal image of 4A's surface after QD growth and optical characterization and before PhC fabrication.

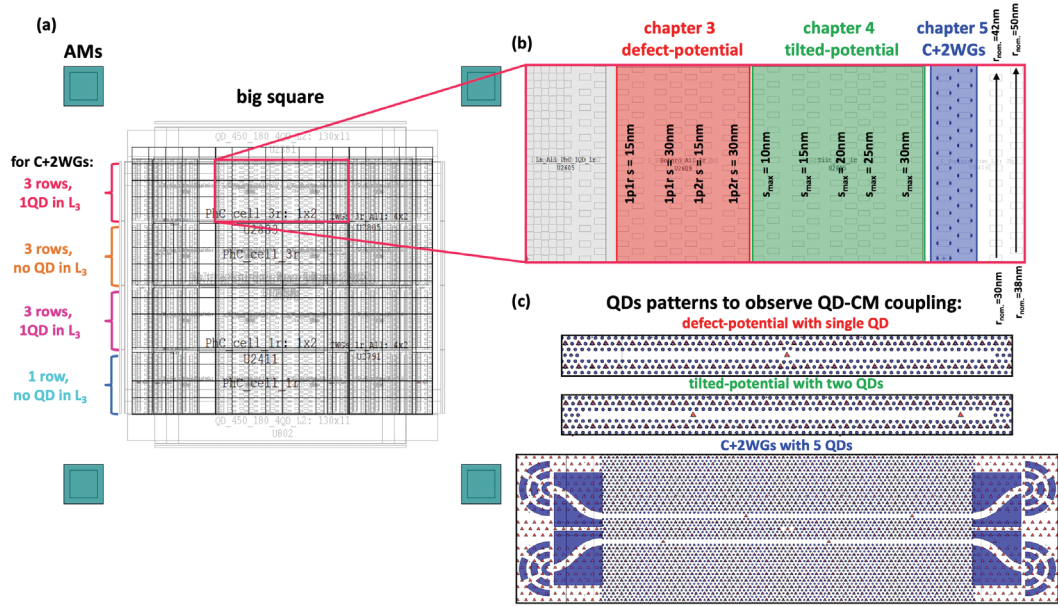


Fig. C:2 – Details of the PhC patterning of the big square region. (a) Broad view. (b) Zoom of a cell including in particular the tailored-potential L_{61} cavities and coupled cavity-waveguides. The latter are highlighted with colours. The defect-potential (red, chapter 3) series include the 1p1r and 1p2r variants with $s=15, 30\text{nm}$. The tilted-potential (green, chapter 4) series include $s_{\text{max}}=10, 15, 20, 25$ and 30nm . On a given stripe, the C+2WGs (blue, chapter 5) repetitions are identical. There are four variants of the C+2WGs depending on the choice of the stripe: 1 row of holes separation, with or without a single QD integrated inside the modified L_3 cavity, and same with 3 rows of holes separation. (c) The defect-potential cavities possess a single QD at the center, the tilted-potential cavities incorporate two QDs, while the C+2WGs structure have up to 5 QDs integrated by design. Parasitic QDs likely remain in the grating couplers and the suspended nanobeams. Within a series, the PhC structures are reproduced to enable lithographic tuning of the mode energies with variation of the nominal radius $r_{\text{nom}}=30, 31, \dots, 50\text{nm}$.

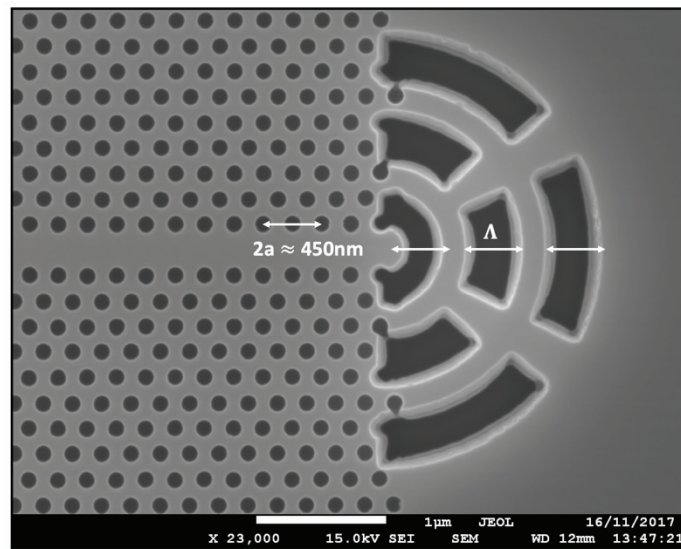


Fig. C:3 – SEM image of a Bragg grating coupler terminating a straight PhC w_1 WG, useful for single-photon extraction or laser light injection. The period Λ is approximately equal to $2a \approx 450\text{nm}$.

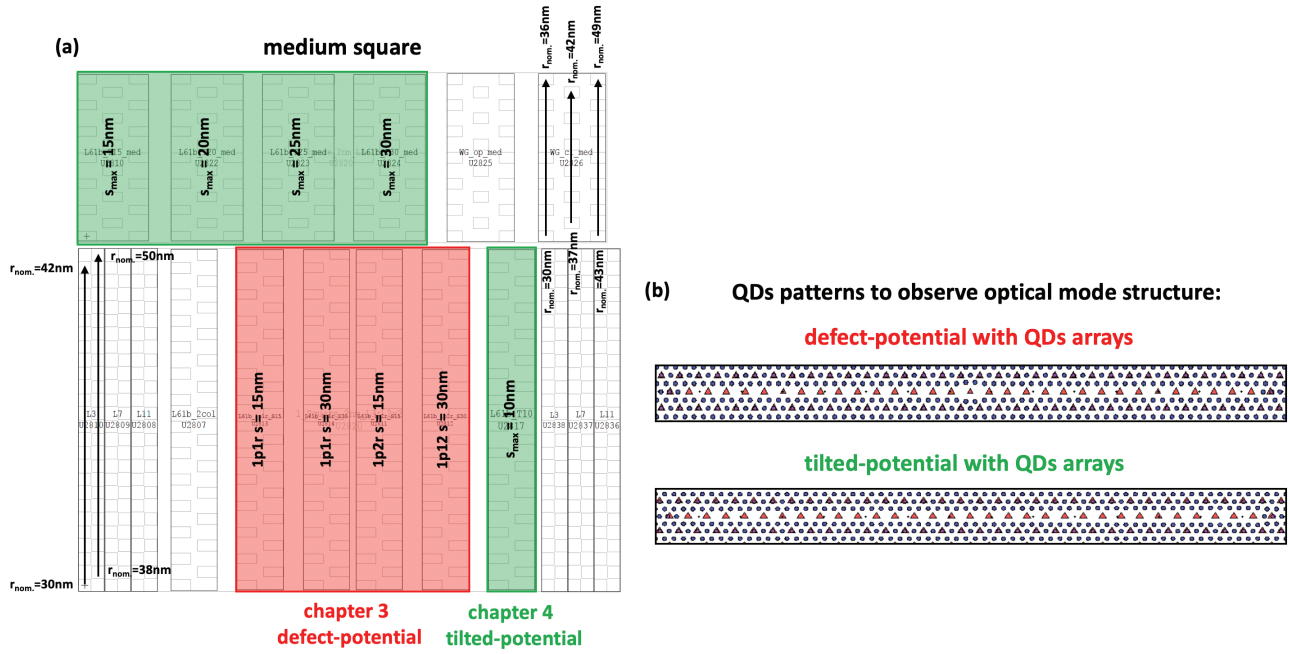


Fig. C:4 – Details of the PhC patterning of a medium square region. (a) Broad view showing the various series for all variants of the defect-potential (red, chapter 3) and the tilted-potential (green, chapter 4) cavities. (b) For the observation of the optical mode structure, both the defect-potential and tilted-potential cavities are embedded with QDs arrays. The few wavelength-shifted QDs incorporated are not important here. Within a series, the PhC structures are reproduced to enable lithographic tuning of the mode energies with variation of the nominal radius $r_{\text{nom.}}=30, 31, \dots$, up to 49nm for the upper part, and up to 50nm for the bottom part.

Contributions

The author performed all numerical modelling, optical experiments and interpretation of data presented in the core chapters 3, 4 and 5. The 2D FDM Matlab script was originally written by Dr. F. Karlsson. Preliminary 2D FDM simulations of the tilted-potential structures were performed by M. Zimmermann, in the framework of a summer project. The optical experiments were performed using optical setups developed in previous theses and refined by Dr. B. Dwir and the author during this thesis work. Preliminary data leading to some of the presented results in chapters 3 and 5 were provided by F. Gremion, G. Terrasanta and F. Persoud in the framework of semester projects supervised by the author.

The MBE-grown (111)B GaAs/AlGaAs membrane wafer was provided by Dr. A. Arnoult of the French RENATECH network. The MOCVD growth of the InGaAs/GaAs QDs was implemented by Dr. A. Rudra. The nanofabrication of the QD and PhC structures was carried out by Dr. B. Dwir and Dr. A. Miranda, with the participation of B. Rigal, A. Lyasota, J. Delaloye and the author. The work was supported by the Swiss National Science Foundation (SNSF).

Bibliography

- [1] Y. Makhlin, G. Schön, and A. Shnirman, “Quantum-state engineering with Josephson-junction devices,” *Rev. Mod. Phys.*, vol. 73, no. 2, pp. 357–400, May 2001.
- [2] J. M. Martinis, S. Nam, J. Aumentado, and C. Urbina, “Rabi Oscillations in a Large Josephson-Junction Qubit,” *Phys. Rev. Lett.*, vol. 89, no. 11, p. 117901, Aug. 2002.
- [3] J. I. Cirac and P. Zoller, “Quantum Computations with Cold Trapped Ions,” *Phys. Rev. Lett.*, vol. 74, no. 20, pp. 4091–4094, May 1995.
- [4] R. Blatt and D. Wineland, “Entangled states of trapped atomic ions,” *Nature*, vol. 453, no. 7198, pp. 1008–1015, Jun. 2008.
- [5] A. Kiraz, M. Atatüre, and A. Imamoglu, “Quantum-dot single-photon sources: Prospects for applications in linear optics quantum-information processing,” *Phys. Rev. A*, vol. 69, no. 3, p. 032305, Mar. 2004.
- [6] J. L. O’Brien, M. J. Cryan, J. G. Rarity, S. Yu, and J. L. O’Brien, “Optical Quantum Computing,” *Science*, vol. 318, no. 5856, Dec. 2007.
- [7] B. E. Kane, “Silicon-based Quantum Computation,” *Fortschritte der Phys.*, vol. 48, no. 9–11, pp. 1023–1041, Sep. 2000.
- [8] M. Veldhorst, H. G. J. Eenink, C. H. Yang, and A. S. Dzurak, “Silicon CMOS architecture for a spin-based quantum computer,” *Nat. Commun.*, vol. 8, no. 1, p. 1766, Dec. 2017.
- [9] R. Maurand *et al.*, “A CMOS silicon spin qubit,” *Nat. Commun.*, vol. 7, no. 1, p. 13575, Dec. 2016.
- [10] S. Das Sarma, M. Freedman, and C. Nayak, “Topological quantum computation,” *Phys. Today*, vol. 59, no. 7, pp. 32–38, Jul. 2006.
- [11] C. Nayak, S. H. Simon, A. Stern, M. Freedman, and S. Das Sarma, “Non-Abelian anyons and topological quantum computation,” *Rev. Mod. Phys.*, vol. 80, no. 3, pp. 1083–1159, Sep. 2008.
- [12] D. Jaksch, C. Bruder, J. I. Cirac, C. W. Gardiner, and P. Zoller, “Cold Bosonic Atoms in Optical Lattices,” *Phys. Rev. Lett.*, vol. 81, no. 15, pp. 3108–3111, Oct. 1998.
- [13] A. Potočník *et al.*, “Studying light-harvesting models with superconducting circuits,” *Nat. Commun.*, vol. 9, no. 1, p. 904, Dec. 2018.
- [14] P. J. J. O’Malley *et al.*, “Scalable Quantum Simulation of Molecular Energies,” *Phys. Rev. X*, vol. 6, no. 3, p. 031007, Jul. 2016.
- [15] D. Castelvecchi, “Quantum computers ready to leap out of the lab in 2017,” *Nature*, vol. 541, no. 7635, pp. 9–10, Jan. 2017.
- [16] N. Gisin and R. Thew, “Quantum communication,” *Nat. Photonics*, vol. 1, no. 3, pp. 165–171, Mar. 2007.
- [17] B. Hensen *et al.*, “Loophole-free Bell inequality violation using electron spins separated by 1.3 kilometres,” *Nature*, vol. 526, no. 7575, pp. 682–686, Oct. 2015.
- [18] J. Yin *et al.*, “Satellite-based entanglement distribution over 1200 kilometers,” *Science*, vol. 356, no. 6343, pp. 1140–1144, Jun. 2017.
- [19] J.-G. Ren *et al.*, “Ground-to-satellite quantum teleportation,” *Nature*, vol. 549, no. 7670, pp. 70–73, Sep. 2017.
- [20] S.-K. Liao *et al.*, “Satellite-Relayed Intercontinental Quantum Network,” *Phys. Rev. Lett.*, vol. 120, no. 3, p. 030501, Jan. 2018.

- [21] D. Bouwmeester, J.-W. Pan, K. Mattle, M. Eibl, H. Weinfurter, and A. Zeilinger, "Experimental quantum teleportation," *Nature*, vol. 390, no. 6660, pp. 575–579, Dec. 1997.
- [22] J. I. Cirac, P. Zoller, H. J. Kimble, and H. Mabuchi, "Quantum State Transfer and Entanglement Distribution among Distant Nodes in a Quantum Network," *Phys. Rev. Lett.*, vol. 78, no. 16, pp. 3221–3224, Apr. 1997.
- [23] H.-J. Briegel, W. Dür, J. I. Cirac, and P. Zoller, "Quantum Repeaters: The Role of Imperfect Local Operations in Quantum Communication," *Phys. Rev. Lett.*, vol. 81, no. 26, pp. 5932–5935, Dec. 1998.
- [24] H. J. Kimble, "The quantum internet," *Nature*, vol. 453, no. 7198, pp. 1023–1030, Jun. 2008.
- [25] V. Giovannetti, S. Lloyd, and L. Maccone, "Quantum-enhanced measurements: beating the standard quantum limit," *Science*, vol. 306, no. 5700, pp. 1330–6, Nov. 2004.
- [26] S. Pirandola, B. R. Bardhan, T. Gehring, C. Weedbrook, and S. Lloyd, "Advances in photonic quantum sensing," *Nat. Photonics*, vol. 12, no. 12, pp. 724–733, Dec. 2018.
- [27] J. R. Maze *et al.*, "Nanoscale magnetic sensing with an individual electronic spin in diamond," *Nature*, vol. 455, no. 7213, pp. 644–647, Oct. 2008.
- [28] V. G. Lucivero, P. Anielski, W. Gawlik, and M. W. Mitchell, "Shot-noise-limited magnetometer with sub-picotesla sensitivity at room temperature," *Rev. Sci. Instrum.*, vol. 85, no. 11, p. 113108, Nov. 2014.
- [29] P. Berg *et al.*, "Composite-Light-Pulse Technique for High-Precision Atom Interferometry," *Phys. Rev. Lett.*, vol. 114, no. 6, p. 063002, Feb. 2015.
- [30] J. P. Dakin, D. J. Pratt, G. W. Bibby, and J. N. Ross, "Distributed optical fibre Raman temperature sensor using a semiconductor light source and detector," *Electron. Lett.*, vol. 21, no. 13, p. 569, 1985.
- [31] T. L. S. Collaboration, "A gravitational wave observatory operating beyond the quantum shot-noise limit," *Nat. Phys.*, vol. 7, no. 12, pp. 962–965, Dec. 2011.
- [32] T. B. Pittman, Y. H. Shih, D. V. Strekalov, and A. V. Sergienko, "Optical imaging by means of two-photon quantum entanglement," *Phys. Rev. A*, vol. 52, no. 5, pp. R3429–R3432, Nov. 1995.
- [33] A. F. Abouraddy, B. E. A. Saleh, A. V. Sergienko, and M. C. Teich, "Role of Entanglement in Two-Photon Imaging," *Phys. Rev. Lett.*, vol. 87, no. 12, p. 123602, Aug. 2001.
- [34] A. Kellerer, "Quantum telescopes," *Astron. Geophys.*, vol. 55, no. 3, pp. 3.28–3.32, Jun. 2014.
- [35] A. R. Kurek, T. Pięta, T. Stebel, A. Pollo, and A. Popowicz, "Quantum telescope: feasibility and constraints," *Opt. Lett.*, vol. 41, no. 6, p. 1094, Mar. 2016.
- [36] A. N. Boto, P. Kok, D. S. Abrams, S. L. Braunstein, C. P. Williams, and J. P. Dowling, "Quantum Interferometric Optical Lithography: Exploiting Entanglement to Beat the Diffraction Limit," *Phys. Rev. Lett.*, vol. 85, no. 13, pp. 2733–2736, Sep. 2000.
- [37] D. Sridharan, R. Bose, H. K. G. S. Solomon, and E. Waks, "Attojoule all-optical switching with a single quantum dot," *arXiv:1107.3751 [cond-mat, physics:physics, physics:quant-ph]*, Aug. 2011.
- [38] G. Jaliel *et al.*, "Experimental Realization of a Quantum Dot Energy Harvester," *Phys. Rev. Lett.*, vol. 123, no. 11, p. 117701, Sep. 2019.
- [39] J. L. O'Brien, A. Furusawa, and J. Vučković, "Photonic quantum technologies," *Nat. Photonics*, vol. 3, no. 12, pp. 687–695, Aug. 2009.
- [40] S. J. Freedman and J. F. Clauser, "Experimental Test of Local Hidden-Variable Theories," *Phys. Rev. Lett.*, vol. 28, no. 14, pp. 938–941, Apr. 1972.
- [41] A. Aspect, P. Grangier, and G. Roger, "Experimental Tests of Realistic Local Theories via Bell's Theorem," *Phys. Rev. Lett.*, vol. 47, no. 7, pp. 460–463, Aug. 1981.
- [42] P. G. Kwiat, K. Mattle, H. Weinfurter, A. Zeilinger, A. V. Sergienko, and Y. Shih, "New High-Intensity Source of Polarization-Entangled Photon Pairs," *Phys. Rev. Lett.*, vol. 75, no. 24, pp. 4337–4341, Dec. 1995.

-
- [43] H. Takesue, K. Inoue, O. Tadanaga, Y. Nishida, and M. Asobe, "Generation of pulsed polarization-entangled photon pairs in a 155- μm band with a periodically poled lithium niobate waveguide and an orthogonal polarization delay circuit," *Opt. Lett.*, vol. 30, no. 3, p. 293, Feb. 2005.
 - [44] T. Kim, M. Fiorentino, and F. N. C. Wong, "Phase-stable source of polarization-entangled photons using a polarization Sagnac interferometer," *Phys. Rev. A*, vol. 73, no. 1, p. 012316, Jan. 2006.
 - [45] A. Kuhn, M. Hennrich, and G. Rempe, "Deterministic Single-Photon Source for Distributed Quantum Networking," *Phys. Rev. Lett.*, vol. 89, no. 6, p. 067901, Jul. 2002.
 - [46] J. McKeever *et al.*, "Deterministic generation of single photons from one atom trapped in a cavity," *Science*, vol. 303, no. 5666, pp. 1992–4, Mar. 2004.
 - [47] M. Keller, B. Lange, K. Hayasaka, W. Lange, and H. Walther, "Continuous generation of single photons with controlled waveform in an ion-trap cavity system," *Nature*, vol. 431, no. 7012, pp. 1075–1078, Oct. 2004.
 - [48] S. Brattke, B. T. H. Varcoe, and H. Walther, "Generation of Photon Number States on Demand via Cavity Quantum Electrodynamics," *Phys. Rev. Lett.*, vol. 86, no. 16, pp. 3534–3537, Apr. 2001.
 - [49] M. Hijlkema, B. Weber, H. P. Specht, S. C. Webster, A. Kuhn, and G. Rempe, "A single-photon server with just one atom," *Nat. Phys.*, vol. 3, no. 4, pp. 253–255, Apr. 2007.
 - [50] T. Wilk, S. C. Webster, A. Kuhn, and G. Rempe, "Single-atom single-photon quantum interface," *Science*, vol. 317, no. 5837, pp. 488–90, Jul. 2007.
 - [51] I. Marcikic, H. de Riedmatten, W. Tittel, V. Scarani, H. Zbinden, and N. Gisin, "Time-bin entangled qubits for quantum communication created by femtosecond pulses," *Phys. Rev. A*, vol. 66, no. 6, p. 062308, Dec. 2002.
 - [52] L. Olislager *et al.*, "Frequency-bin entangled photons," *Phys. Rev. A*, vol. 82, no. 1, p. 013804, Jul. 2010.
 - [53] A. Mair, A. Vaziri, G. Weihs, and A. Zeilinger, "Entanglement of the orbital angular momentum states of photons," *Nature*, vol. 412, no. 6844, pp. 313–316, Jul. 2001.
 - [54] A. S. Solntsev *et al.*, "Generation of Nonclassical Biphoton States through Cascaded Quantum Walks on a Nonlinear Chip," *Phys. Rev. X*, vol. 4, no. 3, p. 031007, Jul. 2014.
 - [55] J. W. Silverstone *et al.*, "On-chip quantum interference between silicon photon-pair sources," *Nat. Photonics*, vol. 8, no. 2, pp. 104–108, Feb. 2014.
 - [56] H. Jin *et al.*, "On-Chip Generation and Manipulation of Entangled Photons Based on Reconfigurable Lithium-Niobate Waveguide Circuits," *Phys. Rev. Lett.*, vol. 113, no. 10, p. 103601, Sep. 2014.
 - [57] F. Setzpfandt *et al.*, "Tunable generation of entangled photons in a nonlinear directional coupler," *Laser Photon. Rev.*, vol. 10, no. 1, pp. 131–136, Jan. 2016.
 - [58] A. S. Solntsev and A. A. Sukhorukov, "Path-entangled photon sources on nonlinear chips," *Rev. Phys.*, vol. 2, pp. 19–31, Nov. 2017.
 - [59] R. H. Brown and R. Q. Twiss, "Correlation between Photons in two Coherent Beams of Light," *Nature*, vol. 177, no. 4497, pp. 27–29, Jan. 1956.
 - [60] C. K. Hong, Z. Y. Ou, and L. Mandel, "Measurement of subpicosecond time intervals between two photons by interference," *Phys. Rev. Lett.*, vol. 59, no. 18, pp. 2044–2046, Nov. 1987.
 - [61] A. Divochiy *et al.*, "Superconducting nanowire photon-number-resolving detector at telecommunication wavelengths," *Nat. Photonics*, vol. 2, no. 5, pp. 302–306, May 2008.
 - [62] T. Thomay *et al.*, "Simultaneous, Full Characterization of a Single-Photon State," *Phys. Rev. X*, vol. 7, no. 4, p. 41036, Feb. 2017.
 - [63] R. J. Glauber, "The Quantum Theory of Optical Coherence," *Phys. Rev.*, vol. 130, no. 6, pp. 2529–2539, Jun. 1963.
 - [64] U. M. Titulaer and R. J. Glauber, "Correlation Functions for Coherent Fields," *Phys. Rev.*, vol. 140, no. 3B, pp. B676–B682, Nov. 1965.
-

- [65] J. Beugnon *et al.*, “Quantum interference between two single photons emitted by independently trapped atoms,” *Nature*, vol. 440, no. 7085, pp. 779–782, Apr. 2006.
- [66] R. Kaltenbaek, B. Blauensteiner, M. Żukowski, M. Aspelmeyer, and A. Zeilinger, “Experimental Interference of Independent Photons,” *Phys. Rev. Lett.*, vol. 96, no. 24, p. 240502, Jun. 2006.
- [67] K. Sanaka, A. Pawlis, T. D. Ladd, K. Lischka, and Y. Yamamoto, “Indistinguishable Photons from Independent Semiconductor Nanostructures,” *Phys. Rev. Lett.*, vol. 103, no. 5, p. 053601, Jul. 2009.
- [68] C. Santori, D. Fattal, J. Vučković, G. S. Solomon, and Y. Yamamoto, “Indistinguishable photons from a single-photon device,” *Nature*, vol. 419, no. 6907, pp. 594–597, Oct. 2002.
- [69] A. J. Bennett *et al.*, “Indistinguishable photons from a diode,” *Appl. Phys. Lett.*, vol. 92, no. 19, p. 193503, May 2008.
- [70] R. B. Patel, A. J. Bennett, I. Farrer, C. A. Nicoll, D. A. Ritchie, and A. J. Shields, “Two-photon interference of the emission from electrically tunable remote quantum dots,” *Nat. Photonics*, vol. 4, no. 9, pp. 632–635, Aug. 2010.
- [71] S. Krapick, H. Herrmann, V. Quiring, B. Brecht, H. Suche, and C. Silberhorn, “An efficient integrated two-color source for heralded single photons,” *New J. Phys.*, vol. 15, no. 3, p. 033010, Mar. 2013.
- [72] C. Reimer *et al.*, “Integrated frequency comb source of heralded single photons,” *Opt. Express*, vol. 22, no. 6, p. 6535, Mar. 2014.
- [73] M. J. Collins *et al.*, “Integrated spatial multiplexing of heralded single-photon sources,” *Nat. Commun.*, vol. 4, p. 2582, Apr. 2013.
- [74] D. Liang and J. E. Bowers, “Recent progress in lasers on silicon,” *Nat. Photonics*, vol. 4, no. 8, pp. 511–517, Aug. 2010.
- [75] G. Roelkens *et al.*, “III-V/silicon photonics for on-chip and intra-chip optical interconnects,” *Laser Photon. Rev.*, vol. 4, no. 6, pp. 751–779, Nov. 2010.
- [76] A. Politi, M. J. Cryan, J. G. Rarity, S. Yu, and J. L. O’Brien, “Silica-on-Silicon Waveguide Quantum Circuits,” *Science*, vol. 320, no. 5876, pp. 646–649, Apr. 2008.
- [77] G. D. Marshall *et al.*, “Laser written waveguide photonic quantum circuits,” *Opt. Express*, vol. 17, no. 15, p. 12546, Jul. 2009.
- [78] A. Melloni *et al.*, “Tunable Delay Lines in Silicon Photonics: Coupled Resonators and Photonic Crystals, a Comparison,” *IEEE Photonics J.*, vol. 2, no. 2, pp. 181–194, Apr. 2010.
- [79] J. P. Sprengers *et al.*, “Waveguide superconducting single-photon detectors for integrated quantum photonic circuits,” *Appl. Phys. Lett.*, vol. 99, no. 18, p. 181110, Oct. 2011.
- [80] P. Lodahl, S. Mahmoodian, and S. Stobbe, “Interfacing single photons and single quantum dots with photonic nanostructures,” *Rev. Mod. Phys.*, vol. 87, no. 2, pp. 347–400, May 2015.
- [81] C. P. Dietrich, A. Fiore, M. G. Thompson, M. Kamp, and S. Höfling, “GaAs integrated quantum photonics: Towards compact and multi-functional quantum photonic integrated circuits,” *Laser Photon. Rev.*, vol. 10, no. 6, pp. 870–894, Aug. 2016.
- [82] N. Somaschi *et al.*, “Near-optimal single-photon sources in the solid state,” *Nat. Photonics*, vol. 10, no. 5, pp. 340–345, Aug. 2016.
- [83] A. Schwagmann *et al.*, “In-plane single-photon emission from a L3 cavity coupled to a photonic crystal waveguide,” *Opt. Express*, vol. 20, no. 27, pp. 28614–28624, Oct. 2012.
- [84] A. Jamil *et al.*, “On-chip generation and guiding of quantum light from a site-controlled quantum dot,” *Appl. Phys. Lett.*, vol. 104, no. 10, p. 101108, Aug. 2014.
- [85] M. H. Baier, C. Constantin, E. Pelucchi, and E. Kapon, “Electroluminescence from a single pyramidal quantum dot in a light-emitting diode,” *Appl. Phys. Lett.*, vol. 84, no. 11, pp. 1967–1969, Mar. 2004.
- [86] M. Francardi *et al.*, “Enhanced spontaneous emission in a photonic-crystal light-emitting diode,” *Appl. Phys. Lett.*, vol. 93, no. 14, p. 143102, Aug. 2008.
- [87] B. Ellis *et al.*, “Ultralow-threshold electrically pumped quantum-dot photonic-crystal nanocavity laser,” *Nat. Photonics*, vol. 5, no. 5, pp. 297–300, Aug. 2011.

-
- [88] T. Baba, "Slow light in photonic crystals," *Nat. Photonics*, vol. 2, no. 8, pp. 465–473, Aug. 2008.
 - [89] P. W. Anderson, "Absence of Diffusion in Certain Random Lattices," *Phys. Rev.*, vol. 109, no. 5, pp. 1492–1505, Mar. 1958.
 - [90] S. John, "Strong localization of photons in certain disordered dielectric superlattices," *Phys. Rev. Lett.*, vol. 58, no. 23, pp. 2486–2489, Jul. 1987.
 - [91] M. Segev, Y. Silberberg, and D. N. Christodoulides, "Anderson localization of light," *Nat. Photonics*, vol. 7, no. 3, pp. 197–204, Mar. 2013.
 - [92] L. Sapienza, H. Thyrrestrup, S. Stobbe, P. D. Garcia, S. Smolka, and P. Lodahl, "Cavity Quantum Electrodynamics with Anderson-Localized Modes," *Science*, vol. 327, no. 5971, pp. 1352–1355, Sep. 2010.
 - [93] T. Crane, O. J. Trojak, J. P. Vasco, S. Hughes, and L. Sapienza, "Anderson Localization of Visible Light on a Nanophotonic Chip," *ACS Photonics*, vol. 4, no. 9, pp. 2274–2280, 2017.
 - [94] R. Faggiani *et al.*, "Lower bound for the spatial extent of localized modes in photonic-crystal waveguides with small random imperfections," *Sci. Rep.*, vol. 6, pp. 27037, Jun. 2016.
 - [95] D. Gerace and L. C. Andreani, "Effects of disorder on propagation losses and cavity Q-factors in photonic crystal slabs," *Photonics Nanostructures - Fundam. Appl.*, vol. 3, no. 2–3, pp. 120–128, Dec. 2005.
 - [96] S. Hughes, L. Ramunno, J. F. Young, and J. E. Sipe, "Extrinsic Optical Scattering Loss in Photonic Crystal Waveguides: Role of Fabrication Disorder and Photon Group Velocity," *Phys. Rev. Lett.*, vol. 94, no. 3, p. 033903, Jan. 2005.
 - [97] H. S. Dutta, A. K. Goyal, V. Srivastava, and S. Pal, "Coupling light in photonic crystal waveguides: A review," *Photonics Nanostructures - Fundam. Appl.*, vol. 20, pp. 41–58, Nov. 2016.
 - [98] N. Prtljaga *et al.*, "On-chip interference of single photons from an embedded quantum dot and an external laser," *Appl. Phys. Lett.*, vol. 108, no. 25, p. 251101, Jun. 2016.
 - [99] D. Sahin *et al.*, "Waveguide photon-number-resolving detectors for quantum photonic integrated circuits," *Appl. Phys. Lett.*, vol. 103, no. 11, p. 111116, Sep. 2013.
 - [100] D. Sahin *et al.*, "Waveguide Nanowire Superconducting Single-Photon Detectors Fabricated on GaAs and the Study of Their Optical Properties," *IEEE J. Sel. Top. Quantum Electron.*, vol. 21, no. 2, pp. 1–10, 2015.
 - [101] M. Davanco *et al.*, "Heterogeneous integration for on-chip quantum photonic circuits with single quantum dot devices," *Nat. Commun.*, vol. 8, no. 1, p. 889, Nov. 2017.
 - [102] E. Murray *et al.*, "Quantum photonics hybrid integration platform," *Appl. Phys. Lett.*, vol. 107, no. 17, p. 171108, Aug. 2015.
 - [103] D. J. P. Ellis *et al.*, "Independent indistinguishable quantum light sources on a reconfigurable photonic integrated circuit," *Appl. Phys. Lett.*, vol. 112, no. 21, p. 211104, May 2018.
 - [104] M. Levinshtein, S. Rumyantsev, and M. Shur, *Handbook Series on Semiconductor Parameters*, vol. 2. WORLD SCIENTIFIC, 1996.
 - [105] B. Saleh, M. Teich, and R. E. Slusher, "Fundamentals of Photonics," *Phys. Today*, vol. 45, no. 11, pp. 87–88, Nov. 1992.
 - [106] B. Tian, T. J. Kempa, and C. M. Lieber, "Single nanowire photovoltaics," *Chem. Soc. Rev.*, vol. 38, no. 1, pp. 16–24, Dec. 2009.
 - [107] A. J. Williamson and A. Zunger, "InAs quantum dots: Predicted electronic structure of free-standing versus GaAs-embedded structures," *Phys. Rev. B*, vol. 59, no. 24, pp. 15819–15824, Jun. 1999.
 - [108] Y. H. Huo *et al.*, "A light-hole exciton in a quantum dot," *Nat. Phys.*, vol. 10, no. 1, pp. 46–51, Jan. 2014.
 - [109] O. Gywat, H. J. Krenner, and J. Berezovsky, *Spins in optically active quantum dots : concepts and methods*. Wiley-VCH, 2010.
 - [110] K. F. Karlsson *et al.*, "Spectral signatures of high-symmetry quantum dots and effects of symmetry breaking," *New J. Phys.*, vol. 17, no. 10, p. 103017, May 2015.
-

- [111] S. Rodt, R. Heitz, A. Schliwa, R. L. Sellin, F. Guffarth, and D. Bimberg, "Repulsive exciton-exciton interaction in quantum dots," *Phys. Rev. B*, vol. 68, no. 3, p. 035331, Jul. 2003.
- [112] M. Abbarchi *et al.*, "Fine structure splitting of quantum dot excitons: Role of geometry and environment," *Phys. E Low-dimensional Syst. Nanostructures*, vol. 42, no. 4, pp. 881–883, Feb. 2010.
- [113] I. Schwartz *et al.*, "Deterministic Writing and Control of the Dark Exciton Spin Using Single Short Optical Pulses," *Phys. Rev. X*, vol. 5, no. 1, p. 011009, Jan. 2015.
- [114] E. del Valle, "Distilling one, two and entangled pairs of photons from a quantum dot with cavity QED effects and spectral filtering," *New J. Phys.*, vol. 15, no. 2, p. 25019, Apr. 2013.
- [115] L. Cohen, "Generalization of the Wiener-Khinchin theorem," *IEEE Signal Process. Lett.*, vol. 5, no. 11, pp. 292–294, Nov. 1998.
- [116] T. Itakura and Y. Tokura, "Dephasing due to background charge fluctuations," *Phys. Rev. B*, vol. 67, no. 19, p. 195320, May 2003.
- [117] A. L. Efros and D. J. Nesbitt, "Origin and control of blinking in quantum dots," *Nat. Nanotechnol.*, vol. 11, no. 8, pp. 661–671, Aug. 2016.
- [118] A. Auffèves, J.-M. Gérard, and J.-P. Poizat, "Pure emitter dephasing: A resource for advanced solid-state single-photon sources," *Phys. Rev. A*, vol. 79, no. 5, p. 53838, Apr. 2009.
- [119] A. Auffèves, D. Gerace, J.-M. Gérard, M. F. Santos, L. C. Andreani, and J.-P. Poizat, "Controlling the dynamics of a coupled atom-cavity system by pure dephasing," *Phys. Rev. B*, vol. 81, no. 24, p. 245419, 2010.
- [120] M. K. Yakes *et al.*, "Leveraging Crystal Anisotropy for Deterministic Growth of InAs Quantum Dots with Narrow Optical Linewidths," *Nano Lett.*, vol. 13, no. 10, pp. 4870–4875, Oct. 2013.
- [121] J. R. Arthur, "Molecular beam epitaxy," *Surf. Sci.*, vol. 500, no. 1–3, pp. 189–217, Mar. 2002.
- [122] M. Behet, R. Hövel, A. Kohl, A. M. Küsters, B. Opitz, and K. Heime, "MOVPE growth of III–V compounds for optoelectronic and electronic applications," *Microelectronics J.*, vol. 27, no. 4–5, pp. 297–334, Jul. 1996.
- [123] C. N. Allen, P. Finnie, S. Raymond, Z. R. Wasilewski, and S. Fafard, "Inhomogeneous broadening in quantum dots with ternary aluminum alloys," *Appl. Phys. Lett.*, vol. 79, no. 17, pp. 2701–2703, Oct. 2001.
- [124] S. Sanguinetti *et al.*, "Role of the wetting layer in the carrier relaxation in quantum dots," *Appl. Phys. Lett.*, vol. 81, no. 4, pp. 613–615, Jul. 2002.
- [125] S. Lee, O. L. Lazarenkova, P. von Allmen, F. Oyafuso, and G. Klimeck, "Effect of wetting layers on the strain and electronic structure of InAs self-assembled quantum dots," *Phys. Rev. B*, vol. 70, no. 12, p. 125307, Sep. 2004.
- [126] M. Markiewicz and H. Voss, "Electronic States in Three Dimensional Quantum Dot/Wetting Layer Structures," Springer, Berlin, Heidelberg, 2006, pp. 684–693.
- [127] M. Eichelmann and J. Wiersig, "Morphology of wetting-layer states in a simple quantum-dot wetting-layer model," *J. Phys. Condens. Matter*, Oct. 2019.
- [128] E. Peter *et al.*, "Exciton-Photon Strong-Coupling Regime for a Single Quantum Dot Embedded in a Microcavity," *Phys. Rev. Lett.*, vol. 95, no. 6, p. 067401, Aug. 2005.
- [129] S. Sanguinetti and N. Koguchi, "Droplet epitaxy of nanostructures," *Mol. Beam Ep.*, pp. 95–111, Jan. 2013.
- [130] M. Gurioli, Z. Wang, A. Rastelli, T. Kuroda, and S. Sanguinetti, "Droplet epitaxy of semiconductor nanostructures for quantum photonic devices," *Nat. Mater.*, vol. 18, no. 8, pp. 799–810, Aug. 2019.
- [131] T. Mano *et al.*, "Ultra-narrow emission from single GaAs self-assembled quantum dots grown by droplet epitaxy," *Nanotechnology*, vol. 20, no. 39, p. 395601, Sep. 2009.
- [132] B. Mahler, P. Spinicelli, S. Buil, X. Quelin, J.-P. Hermier, and B. Dubertret, "Towards non-blinking colloidal quantum dots," *Nat. Mater.*, vol. 7, no. 8, pp. 659–664, Aug. 2008.
- [133] J.-H. Kim, S. Aghaeimeibodi, C. J. K. Richardson, R. P. Leavitt, D. Englund, and E. Waks, "Hybrid Integration of Solid-State Quantum Emitters on a Silicon Photonic Chip," *Nano Lett.*, vol. 17, no. 12, pp. 7394–7400, Jan. 2017.

-
- [134] K. Kuruma, Y. Ota, M. Kakuda, D. Takamiya, S. Iwamoto, and Y. Arakawa, "Position dependent optical coupling between single quantum dots and photonic crystal nanocavities," *Appl. Phys. Lett.*, vol. 109, no. 7, p. 071110, Aug. 2016.
 - [135] J. Liu *et al.*, "A solid-state source of strongly entangled photon pairs with high brightness and indistinguishability," *Nat. Nanotechnol.*, vol. 14, no. 6, pp. 586–593, Jun. 2019.
 - [136] V. Giesz *et al.*, "Coherent manipulation of a solid-state artificial atom with few photons," *Nat. Commun.*, vol. 7, no. 1, p. 11986, Sep. 2016.
 - [137] H. Thyrrestrup *et al.*, "Quantum Optics with Near-Lifetime-Limited Quantum-Dot Transitions in a Nanophotonic Waveguide," *Nano Lett.*, vol. 18, no. 3, pp. 1801–1806, Mar. 2018.
 - [138] A. Hartmann, Y. Ducommun, L. Loubies, K. Leifer, and E. Kapon, "Structure and photoluminescence of single AlGaAs/GaAs quantum dots grown in inverted tetrahedral pyramids," *Appl. Phys. Lett.*, vol. 73, no. 16, pp. 2322–2324, Oct. 1998.
 - [139] A. Hartmann, Y. Ducommun, K. Leifer, and E. Kapon, "Structure and optical properties of semiconductor quantum nanostructures self-formed in inverted tetrahedral pyramids," *J. Phys. Condens. Matter*, vol. 11, no. 31, p. 5901, Nov. 1999.
 - [140] G. Biasiol and E. Kapon, "Mechanism of self-limiting epitaxial growth on nonplanar substrates," *J. Cryst. Growth*, vol. 201–202, pp. 62–66, May 1999.
 - [141] A. Surrente *et al.*, "Ordered systems of site-controlled pyramidal quantum dots incorporated in photonic crystal cavities," *Nanotechnology*, vol. 22, no. 46, p. 465203, Apr. 2011.
 - [142] A. Mohan *et al.*, "Record-Low Inhomogeneous Broadening of Site-Controlled Quantum Dots for Nanophotonics," *Small*, vol. 6, no. 12, pp. 1268–1272, Jun. 2010.
 - [143] I. V. Kulkova *et al.*, "Emission wavelength control of ordered arrays of InGaAs/GaAs quantum dots," *J. Cryst. Growth*, vol. 464, pp. 69–74, Apr. 2017.
 - [144] B. M. D. Rigal, "Site-controlled quantum dots integrated with photonic crystal waveguides and cavities," *EPFL Thesis*, 2018.
 - [145] M. Felici, P. Gallo, A. Mohan, B. Dwir, A. Rudra, and E. Kapon, "Site-Controlled InGaAs Quantum Dots with Tunable Emission Energy," *Small*, vol. 5, no. 8, pp. 938–943, Apr. 2009.
 - [146] M. H. Baier *et al.*, "Single photon emission from site-controlled pyramidal quantum dots," *Appl. Phys. Lett.*, vol. 84, no. 5, pp. 648–650, Aug. 2004.
 - [147] L. O. Mereni, V. Dimastrodonato, G. Juska, and E. Pelucchi, "Physical properties of highly uniform InGaAs pyramidal quantum dots with GaAs barriers: Fine structure splitting in pre-patterned substrates," *Superlattices Microstruct.*, vol. 49, no. 3, pp. 279–282, Feb. 2011.
 - [148] A. Mohan *et al.*, "Entangled photons produced with high-symmetry site-controlled quantum dots," in *2009 IEEE International Conference on Indium Phosphide & Related Materials*, 2009, pp. 410–411.
 - [149] T. H. Chung, G. Juska, S. T. Moroni, A. Pescaglini, A. Gocalinska, and E. Pelucchi, "Selective carrier injection into patterned arrays of pyramidal quantum dots for entangled photon light-emitting diodes," *Nat. Photonics*, vol. advance on, Nov. 2016.
 - [150] E. Yablonovitch, "Inhibited Spontaneous Emission in Solid-State Physics and Electronics," *Phys. Rev. Lett.*, vol. 58, no. 20, pp. 2059–2062, May 1987.
 - [151] J. D. Joannopoulos, S. G. Johnson, J. N. Winn, and R. D. Meade, *Photonic Crystals: Molding the Flow of Light (Second Edition)*. Princeton University Press, 2008.
 - [152] S. Noda, M. Fujita, and T. Asano, "Spontaneous-emission control by photonic crystals and nanocavities," *Nat. Photonics*, vol. 1, no. 8, pp. 449–458, Nov. 2007.
 - [153] K. Ishizaki, M. Koumura, K. Suzuki, K. Gondaira, and S. Noda, "Realization of three-dimensional guiding of photons in photonic crystals," *Nat. Photonics*, vol. 7, no. 2, pp. 133–137, Feb. 2013.
 - [154] M. Notomi, K. Yamada, A. Shinya, J. Takahashi, C. Takahashi, and I. Yokohama, "Extremely Large Group-Velocity Dispersion of Line-Defect Waveguides in Photonic Crystal Slabs," *Phys. Rev. Lett.*, vol. 87, no. 25, p. 253902, Nov. 2001.
-

- [155] I. Söllner *et al.*, “Deterministic photon-emitter coupling in chiral photonic circuits,” *Nat. Nanotechnol.*, vol. 10, no. 9, pp. 775–778, Sep. 2015.
- [156] P. Lodahl *et al.*, “Chiral quantum optics,” *Nature*, vol. 541, no. 7638, pp. 473–480, Jan. 2017.
- [157] S. R. Huisman *et al.*, “Measurement of a band-edge tail in the density of states of a photonic-crystal waveguide,” *Phys. Rev. B*, vol. 86, no. 15, p. 155154, 2012.
- [158] K. A. Atlasov *et al.*, “1D photonic band formation and photon localization in finite-size photonic-crystal waveguides,” *Opt. Express*, vol. 18, no. 1, pp. 117–122, Feb. 2010.
- [159] Y. Akahane, T. Asano, B.-S. Song, and S. Noda, “High- Q photonic nanocavity in a two-dimensional photonic crystal,” *Nature*, vol. 425, no. 6961, pp. 944–947, Jun. 2003.
- [160] Y. Lai *et al.*, “Genetically designed L3 photonic crystal nanocavities with measured quality factor exceeding one million,” *Appl. Phys. Lett.*, vol. 104, no. 24, p. 241101, Jun. 2014.
- [161] M. Minkov and V. Savona, “Automated optimization of photonic crystal slab cavities,” *Sci. Rep.*, vol. 4, no. 1, p. 5124, May 2015.
- [162] B. Rigal *et al.*, “Propagation losses in photonic crystal waveguides: effects of band tail absorption and waveguide dispersion,” *Opt. Express*, vol. 25, no. 23, p. 28908, Nov. 2017.
- [163] Y. Ota *et al.*, “Large vacuum Rabi splitting between a single quantum dot and an H0 photonic crystal nanocavity,” *Appl. Phys. Lett.*, vol. 112, no. 9, p. 093101, Feb. 2018.
- [164] B.-S. Song, S. Noda, T. Asano, and Y. Akahane, “Ultra-high- Q photonic double-heterostructure nanocavity,” *Nat. Mater.*, vol. 4, no. 3, pp. 207–210, Jun. 2005.
- [165] S. Combrié *et al.*, “GaAs photonic crystal cavity with ultrahigh Q : microwatt nonlinearity at 1.55 μm ,” *Opt. Lett.*, vol. 33, no. 16, pp. 1908–1910, Oct. 2008.
- [166] A. Yariv, Y. Xu, R. K. Lee, and A. Scherer, “Coupled-resonator optical waveguide: a proposal and analysis,” *Opt. Lett.*, vol. 24, no. 11, p. 711, Jun. 1999.
- [167] R. S. Daveau *et al.*, “Efficient fiber-coupled single-photon source based on quantum dots in a photonic-crystal waveguide,” *Optica*, vol. 4, no. 2, pp. 178–184, Jan. 2017.
- [168] A. Schlehahn *et al.*, “A stand-alone fiber-coupled single-photon source,” *Sci. Rep.*, vol. 8, no. 1, Dec. 2018.
- [169] S. Unsleber *et al.*, “Observation of resonance fluorescence and the Mollow triplet from a coherently driven site-controlled quantum dot,” *Optica*, vol. 2, no. 12, p. 1072, Dec. 2015.
- [170] P. Senellart, G. Solomon, and A. White, “High-performance semiconductor quantum-dot single-photon sources,” *Nat. Nanotechnol.*, vol. 12, no. 11, p. 1026, Dec. 2017.
- [171] K. Hennessy *et al.*, “Tuning photonic crystal nanocavity modes by wet chemical digital etching,” *Appl. Phys. Lett.*, vol. 87, no. 2, p. 021108, Jul. 2005.
- [172] A. Faraon, D. Englund, I. Fushman, J. Vučković, N. Stoltz, and P. Petroff, “Local quantum dot tuning on photonic crystal chips,” *Appl. Phys. Lett.*, vol. 90, no. 21, p. 213110, Aug. 2007.
- [173] S. Sokolov, J. Lian, E. Yüce, S. Combrié, A. De Rossi, and A. P. Mosk, “Tuning out disorder-induced localization in nanophotonic cavity arrays,” *Opt. Express*, vol. 25, no. 5, pp. 4598–4606, Sep. 2017.
- [174] A. Faraon and J. Vučković, “Local temperature control of photonic crystal devices via micron-scale electrical heaters,” *Appl. Phys. Lett.*, vol. 95, no. 4, p. 43102, May 2009.
- [175] S. Mosor *et al.*, “Scanning a photonic crystal slab nanocavity by condensation of xenon,” *Appl. Phys. Lett.*, vol. 87, no. 14, p. 141105, Oct. 2005.
- [176] E. T. Jaynes and F. W. Cummings, “Comparison of quantum and semiclassical radiation theories with application to the beam maser,” *Proc. IEEE*, vol. 51, no. 1, pp. 89–109, 1963.
- [177] F. P. Laussy, E. del Valle, and C. Tejedor, “Strong Coupling of Quantum Dots in Microcavities,” *Phys. Rev. Lett.*, vol. 101, no. 8, p. 083601, Aug. 2008.

-
- [178] K. Roy-Choudhury and S. Hughes, "Spontaneous emission from a quantum dot in a structured photonic reservoir: phonon-mediated breakdown of Fermi's golden rule," *Optica*, vol. 2, no. 5, pp. 434–437, Dec. 2015.
- [179] K. Roy-Choudhury and S. Hughes, "Quantum theory of the emission spectrum from quantum dots coupled to structured photonic reservoirs and acoustic phonons," *Phys. Rev. B*, vol. 92, no. 20, p. 205406, May 2015.
- [180] C. Jarlov *et al.*, "Effect of Pure Dephasing and Phonon Scattering on the Coupling of Semiconductor Quantum Dots to Optical Cavities," *Phys. Rev. Lett.*, vol. 117, no. 7, p. 76801, Apr. 2016.
- [181] M. Calic *et al.*, "Phonon-Mediated Coupling of InGaAs/GaAs Quantum-Dot Excitons to Photonic Crystal Cavities," *Phys. Rev. Lett.*, vol. 106, no. 22, p. 227402, Apr. 2011.
- [182] K. Hennessy *et al.*, "Quantum nature of a strongly coupled single quantum dot-cavity system," *Nature*, vol. 445, no. 7130, pp. 896–899, Feb. 2007.
- [183] S. Münch *et al.*, "The role of optical excitation power on the emission spectra of a strongly coupled quantum dot-micropillar system," *Opt. Express*, vol. 17, no. 15, p. 12821, Jul. 2009.
- [184] Y. Ota *et al.*, "Investigation of the Spectral Triplet in Strongly Coupled Quantum Dot-Nanocavity System," *Appl. Phys. Express*, vol. 2, no. 12, p. 122301, Nov. 2009.
- [185] H. Takagi, Y. Ota, N. Kumagai, S. Ishida, S. Iwamoto, and Y. Arakawa, "Enhanced optical Stark shifts in a single quantum dot embedded in an H1 photonic crystal nanocavity," *Appl. Phys. Express*, vol. 10, no. 6, p. 062002, Jun. 2017.
- [186] R. Ohta *et al.*, "Strong coupling between a photonic crystal nanobeam cavity and a single quantum dot," *Appl. Phys. Lett.*, vol. 98, no. 17, p. 173104, Apr. 2011.
- [187] P. T. Kristensen, C. Van Vlack, and S. Hughes, "Effective mode volumes and Purcell factors for leaky optical cavities," *Opt. Lett.*, vol. 37, no. 10, p. 1649, Dec. 2012.
- [188] T. Yoshie *et al.*, "Vacuum Rabi splitting with a single quantum dot in a photonic crystal nanocavity," *Nature*, vol. 432, no. 7014, pp. 200–203, Nov. 2004.
- [189] T. Aoki *et al.*, "Observation of strong coupling between one atom and a monolithic microresonator," *Nature*, vol. 443, no. 7112, pp. 671–674, Oct. 2006.
- [190] S. Reitzenstein *et al.*, "Coherent photonic coupling of semiconductor quantum dots," *Opt. Lett.*, vol. 31, no. 11, pp. 1738–1740, Apr. 2006.
- [191] E. M. Purcell, "Spontaneous Emission Probabilities at Radio Frequencies," Springer, Boston, MA, 1995, pp. 839–839.
- [192] D. G. Gevaux *et al.*, "Enhancement and suppression of spontaneous emission by temperature tuning InAs quantum dots to photonic crystal cavities," *Appl. Phys. Lett.*, vol. 88, no. 13, p. 131101, Mar. 2006.
- [193] H. Y. Ryu and M. Notomi, "Enhancement of spontaneous emission from the resonant modes of a photonic crystal slab single-defect cavity," *Opt. Lett.*, vol. 28, no. 23, p. 2390, Dec. 2003.
- [194] C. Jarlov *et al.*, "Exciton dynamics in a site-controlled quantum dot coupled to a photonic crystal cavity," *Appl. Phys. Lett.*, vol. 107, no. 19, p. 191101, Apr. 2015.
- [195] W.-H. Chang, W.-Y. Chen, H.-S. Chang, T.-P. Hsieh, J.-I. Chyi, and T.-M. Hsu, "Efficient Single-Photon Sources Based on Low-Density Quantum Dots in Photonic-Crystal Nanocavities," *Phys. Rev. Lett.*, vol. 96, no. 11, p. 117401, Mar. 2006.
- [196] L. Balet *et al.*, "Enhanced spontaneous emission rate from single InAs quantum dots in a photonic crystal nanocavity at telecom wavelengths," *Appl. Phys. Lett.*, vol. 91, no. 12, p. 123115, Sep. 2007.
- [197] J. Iles-Smith, D. P. S. McCutcheon, A. Nazir, and J. Mørk, "Phonon scattering inhibits simultaneous near-unity efficiency and indistinguishability in semiconductor single-photon sources," *Nat. Photonics*, vol. advance on, no. 8, pp. 521–526, Jul. 2017.
- [198] S. Ates, S. M. Ulrich, S. Reitzenstein, A. Löffler, A. Forchel, and P. Michler, "Post-Selected Indistinguishable Photons from the Resonance Fluorescence of a Single Quantum Dot in a Microcavity," *Phys. Rev. Lett.*, vol. 103, no. 16, p. 167402, Oct. 2009.
- [199] I. J. Luxmoore *et al.*, "III-V quantum light source and cavity-QED on Silicon," *Sci. Rep.*, vol. 3, no. 1, p. 1239, Dec. 2013.
-

- [200] H. Thyrrestrup, L. Sapienza, and P. Lodahl, "Extraction of the β -factor for single quantum dots coupled to a photonic crystal waveguide," *Appl. Phys. Lett.*, vol. 96, no. 23, p. 231106, Jul. 2010.
- [201] M. Arcari *et al.*, "Near-Unity Coupling Efficiency of a Quantum Emitter to a Photonic Crystal Waveguide," *Phys. Rev. Lett.*, vol. 113, no. 9, p. 93603, Jul. 2014.
- [202] L. Scarpelli *et al.*, "99% beta factor and directional coupling of quantum dots to fast light in photonic crystal waveguides determined by spectral imaging," *Phys. Rev. B*, vol. 100, no. 3, p. 035311, Jul. 2019.
- [203] B. Rigal, B. Dwir, A. Rudra, I. Kulkova, A. Lyasota, and E. Kapon, "Single photon extraction and propagation in photonic crystal waveguides incorporating site-controlled quantum dots," *Appl. Phys. Lett.*, vol. 112, no. 5, p. 51105, Jul. 2018.
- [204] P. Türschmann *et al.*, "Coherent nonlinear optics of quantum emitters in nanophotonic waveguides," *Nanophotonics*, vol. 8, no. 10, pp. 1641–1657, Sep. 2019.
- [205] N. Chauvin *et al.*, "Controlling the charge environment of single quantum dots in a photonic-crystal cavity," *Phys. Rev. B*, vol. 80, no. 24, p. 241306, Dec. 2009.
- [206] J.-H. Kim, S. Aghaeimeibodi, C. J. K. Richardson, R. P. Leavitt, and E. Waks, "Super-Radiant Emission from Quantum Dots in a Nanophotonic Waveguide," *Nano Lett.*, vol. 18, no. 8, pp. 4734–4740, Aug. 2018.
- [207] A. Laucht *et al.*, "Electrical control of spontaneous emission and strong coupling for a single quantum dot," *New J. Phys.*, vol. 11, no. 2, p. 23034, Aug. 2009.
- [208] S. Sun, H. Kim, G. S. Solomon, and E. Waks, "Strain tuning of a quantum dot strongly coupled to a photonic crystal cavity," *Appl. Phys. Lett.*, vol. 103, no. 15, p. 151102, Aug. 2013.
- [209] J. Q. Grim *et al.*, "Scalable in operando strain tuning in nanophotonic waveguides enabling three-quantum-dot superradiance," *Nat. Mater.*, vol. 18, no. 9, 2019.
- [210] H. Kim, T. C. Shen, D. Sridharan, G. S. Solomon, and E. Waks, "Magnetic field tuning of a quantum dot strongly coupled to a photonic crystal cavity," *Appl. Phys. Lett.*, vol. 98, no. 9, p. 91102, Aug. 2011.
- [211] H. Kim, D. Sridharan, T. C. Shen, G. S. Solomon, and E. Waks, "Strong coupling between two quantum dots and a photonic crystal cavity using magnetic field tuning," *Opt. Express*, vol. 19, no. 3, pp. 2589–2598, Apr. 2011.
- [212] G. Kiršanskė *et al.*, "Indistinguishable and efficient single photons from a quantum dot in a planar nanobeam waveguide," *Phys. Rev. B*, vol. 96, no. 16, p. 165306, Oct. 2017.
- [213] T. B. Hoang *et al.*, "Widely tunable, efficient on-chip single photon sources at telecommunication wavelengths," *Opt. Express*, vol. 20, no. 19, pp. 21758–21765, Aug. 2012.
- [214] C. Papon *et al.*, "Nanomechanical single-photon routing," *Optica*, vol. 6, no. 4, p. 524, Apr. 2019.
- [215] T. Kojima, K. Kojima, T. Asano, and S. Noda, "Accurate alignment of a photonic crystal nanocavity with an embedded quantum dot based on optical microscopic photoluminescence imaging," *Appl. Phys. Lett.*, vol. 102, no. 1, p. 011110, Jan. 2013.
- [216] A. Javadi *et al.*, "Single-photon non-linear optics with a quantum dot in a waveguide," *Nat. Commun.*, vol. 6, p. 8655, Aug. 2015.
- [217] R. Bose, D. Sridharan, H. Kim, G. S. Solomon, and E. Waks, "Low-Photon-Number Optical Switching with a Single Quantum Dot Coupled to a Photonic Crystal Cavity," *Phys. Rev. Lett.*, vol. 108, no. 22, p. 227402, Aug. 2012.
- [218] P. Gallo *et al.*, "Integration of site-controlled pyramidal quantum dots and photonic crystal membrane cavities," *Appl. Phys. Lett.*, vol. 92, no. 26, p. 263101, Aug. 2008.
- [219] M. Čalić and M. Calic, "Cavity Quantum Electrodynamics with Site-Controlled Pyramidal Quantum Dots in Photonic Crystal Cavities," *EPFL Thesis*, 2013.
- [220] C. W. T. Jarlov, "Cavity quantum electrodynamics with systems of site-controlled quantum dots and photonic crystal cavities," *EPFL Thesis*, 2016.
- [221] A. Lyasota, "Interaction between site-controlled quantum dot systems and photonic cavity structures," *EPFL Thesis*, 2017.

-
- [222] M. Calic, C. Jarlov, P. Gallo, B. Dwir, A. Rudra, and E. Kapon, "Deterministic radiative coupling of two semiconductor quantum dots to the optical mode of a photonic crystal nanocavity," *Sci. Rep.*, vol. 7, no. 1, p. 4100, Dec. 2017.
 - [223] A. Lyasota *et al.*, *Integration of multiple site-controlled pyramidal quantum dot systems with photonic-crystal membrane cavities*, vol. 414. North-Holland, 2016, pp. 192–195.
 - [224] M. J. Holmes, K. Choi, S. Kako, M. Arita, and Y. Arakawa, "Room-Temperature Triggered Single Photon Emission from a III-Nitride Site-Controlled Nanowire Quantum Dot," *Nano Lett.*, vol. 14, no. 2, pp. 982–986, Feb. 2014.
 - [225] A. Surrente, "Epitaxial Growth and Optical Properties of Dense Arrays of Pyramidal Quantum Dots," *EPFL Thesis*, 2013.
 - [226] A. D. Rakić and M. L. Majewski, "Modeling the optical dielectric function of GaAs and AlAs: Extension of Adachi's model," *J. Appl. Phys.*, vol. 80, no. 10, pp. 5909–5914, Nov. 1996.
 - [227] C. C. Cheng, A. Scherer, V. Arbet-Engels, and E. Yablonovitch, "Lithographic band gap tuning in photonic band gap crystals," *J. Vac. Sci. Technol. B Microelectron. Nanom. Struct.*, vol. 14, no. 6, p. 4110, Nov. 1996.
 - [228] O. Painter *et al.*, "Lithographic tuning of a two-dimensional photonic crystal laser array," *IEEE Photonics Technol. Lett.*, vol. 12, no. 9, pp. 1126–1128, Sep. 2000.
 - [229] Y.-S. Choi *et al.*, "Lithographic tuning of photonic-crystal unit-cell resonators with InGaAsGaAs quantum dots emitting at 1.2 μm ," *J. Vac. Sci. Technol. B Microelectron. Nanom. Struct.*, vol. 23, no. 1, p. 252, Jan. 2005.
 - [230] Kane Yee, "Numerical solution of initial boundary value problems involving maxwell's equations in isotropic media," *IEEE Trans. Antennas Propag.*, vol. 14, no. 3, pp. 302–307, May 1966.
 - [231] A. Christ and H. L. Hartnagel, "Three-Dimensional Finite-Difference Method for the Analysis of Microwave-Device Embedding," *IEEE Trans. Microw. Theory Tech.*, vol. 35, no. 8, pp. 688–696, Aug. 1987.
 - [232] A. Taflove, S. C. Hagness, and M. Piket-May, "Computational Electromagnetics: The Finite-Difference Time-Domain Method," *Electr. Eng. Handb.*, pp. 629–670, Jan. 2005.
 - [233] A. Taflove, A. Oskooi, and S. G. Johnson, *Advances in FDTD computational electrodynamics: photonics and nanotechnology*.
 - [234] A. F. Oskooi, D. Roundy, M. Ibanescu, P. Bermel, J. D. Joannopoulos, and S. G. Johnson, "Meep: A flexible free-software package for electromagnetic simulations by the FDTD method," *Comput. Phys. Commun.*, vol. 181, no. 3, pp. 687–702, Mar. 2010.
 - [235] S. Ozaki and S. Adachi, "Spectroscopic ellipsometry and thermorefectance of GaAs," *J. Appl. Phys.*, vol. 78, no. 5, pp. 3380–3386, Sep. 1995.
 - [236] S. Gehrsitz, F. K. Reinhart, C. Gourgon, N. Herres, A. Vonlanthen, and H. Sigg, "The refractive index of $\text{Al}_x\text{Ga}_{1-x}\text{As}$ below the band gap: Accurate determination and empirical modeling," *J. Appl. Phys.*, vol. 87, no. 11, pp. 7825–7837, Feb. 2000.
 - [237] G. Guerrero, D. L. Boiko, and E. Kapon, "Photonic crystal heterostructures implemented with vertical-cavity surface-emitting lasers," *Opt. Express*, vol. 12, no. 20, p. 4922, Oct. 2004.
 - [238] E. Kuramochi, M. Notomi, S. Mitsugi, A. Shinya, T. Tanabe, and T. Watanabe, "Ultrahigh-Q photonic crystal nanocavities realized by the local width modulation of a line defect," *Appl. Phys. Lett.*, vol. 88, no. 4, p. 41112, Aug. 2006.
 - [239] M. Charbonneau-Lefort, E. Istrate, M. Allard, J. Poon, and E. H. Sargent, "Photonic crystal heterostructures: Waveguiding phenomena and methods of solution in an envelope function picture," *Phys. Rev. B*, vol. 65, no. 12, p. 125318, Mar. 2002.
 - [240] M. Felici, K. A. Atlasov, A. Surrente, and E. Kapon, "Semianalytical approach to the design of photonic crystal cavities," *Phys. Rev. B*, vol. 82, no. 11, p. 115118, Aug. 2010.
 - [241] S. Tomljenovic-Hanic, C. M. de Sterke, and M. J. Steel, "High-Q Cavities in Photonic Crystal Slab Heterostructures Formed by Variation in the Refractive Index," in *2007 9th International Conference on Transparent Optical Networks*, 2007, vol. 2, pp. 2–5.
 - [242] A. Arnoult, French RENATECH.
 - [243] T. La Grange, IPHYS LUMES LPN.
-

- [244] A. Surrente, R. Carron, P. Gallo, A. Rudra, B. Dwir, and E. Kapon, "Self-formation of hexagonal nanotemplates for growth of pyramidal quantum dots by metalorganic vapor phase epitaxy on patterned substrates," *Nano Res.*, vol. 9, no. 11, pp. 3279–3290, Nov. 2016.
- [245] E. Pelucchi *et al.*, "Decomposition, diffusion, and growth rate anisotropies in self-limited profiles during metalorganic vapor-phase epitaxy of seeded nanostructures," *Phys. Rev. B*, vol. 83, no. 20, p. 205409, May 2011.
- [246] G. Biasiol, A. Gustafsson, K. Leifer, and E. Kapon, "Mechanisms of self-ordering in nonplanar epitaxy of semiconductor nanostructures," *Phys. Rev. B*, vol. 65, no. 20, p. 205306, Apr. 2002.
- [247] B. Rigal *et al.*, "Site-controlled InGaAs/GaAs pyramidal quantum dots grown by MOVPE on patterned substrates using triethylgallium," *J. Cryst. Growth*, vol. 414, pp. 187–191, Apr. 2015.
- [248] K. Leifer, A. Hartmann, Y. Ducommun, and E. Kapon, "Carrier transport and luminescence in inverted-pyramid quantum structures," *Appl. Phys. Lett.*, vol. 77, no. 24, pp. 3923–3925, Dec. 2000.
- [249] K. F. Karlsson *et al.*, "Fine structure of exciton complexes in high-symmetry quantum dots: Effects of symmetry breaking and symmetry elevation," *Phys. Rev. B*, vol. 81, no. 16, p. 161307, Apr. 2010.
- [250] M. A. Dupertuis *et al.*, "Symmetries and the Polarized Optical Spectra of Exciton Complexes in Quantum Dots," *Phys. Rev. Lett.*, vol. 107, no. 12, p. 127403, Apr. 2011.
- [251] D. W. Scott, "Scott's rule," *Wiley Interdiscip. Rev. Comput. Stat.*, vol. 2, no. 4, pp. 497–502, Jul. 2010.
- [252] B. Rigal *et al.*, "Probing disorder and mode localization in photonic crystal cavities using site-controlled quantum dots," *J. Appl. Phys.*, vol. 123, no. 4, p. 43109, May 2018.
- [253] T. Tanabe, M. Notomi, E. Kuramochi, A. Shinya, and H. Taniyama, "Trapping and delaying photons for one nanosecond in an ultrasmall high- Q photonic-crystal nanocavity," *Nat. Photonics*, vol. 1, no. 1, pp. 49–52, Aug. 2007.
- [254] Y. Tanaka, T. Asano, and S. Noda, "Design of Photonic Crystal Nanocavity With $-Q$ -Factor of," *J. Light. Technol.*, vol. 26, no. 11, pp. 1532–1539, 2008.
- [255] M. Notomi, E. Kuramochi, and T. Tanabe, "Large-scale arrays of ultrahigh- Q coupled nanocavities," *Nat. Photonics*, vol. 2, no. 12, pp. 741–747, Dec. 2008.
- [256] D. Sam-Giao *et al.*, "High quality factor AlN nanocavities embedded in a photonic crystal waveguide," *Appl. Phys. Lett.*, vol. 100, no. 19, p. 191104, May 2012.
- [257] C. Brimont *et al.*, "Imaging of photonic modes in an AlN-based photonic crystal probed by an ultra-violet internal light source," *Opt. Lett.*, vol. 38, no. 23, p. 5059, Dec. 2013.
- [258] Y. Ota, S. Iwamoto, N. Kumagai, and Y. Arakawa, "Spontaneous Two-Photon Emission from a Single Quantum Dot," *Phys. Rev. Lett.*, vol. 107, no. 23, p. 233602, Nov. 2011.
- [259] Y. Ooka, T. Tetsumoto, A. Fushimi, W. Yoshiki, and T. Tanabe, "CMOS compatible high- Q photonic crystal nanocavity fabricated with photolithography on silicon photonic platform," *Sci. Rep.*, vol. 5, p. 11312, Aug. 2015.
- [260] B. Dwir, IPHYS LPN EPFL.
- [261] G. Ghosh, "Dispersion-equation coefficients for the refractive index and birefringence of calcite and quartz crystals," *Opt. Commun.*, vol. 163, no. 1–3, pp. 95–102, May 1999.
- [262] D. Englund, A. Faraon, B. Zhang, Y. Yamamoto, and J. Vučković, "Generation and transfer of single photons on a photonic crystal chip," *Opt. Express*, vol. 15, no. 9, pp. 5550–5558, Aug. 2007.
- [263] J. P. Vasco and S. Hughes, "Anderson Localization in Disordered LN Photonic Crystal Slab Cavities," *ACS Photonics*, vol. 5, no. 4, pp. 1262–1272, May 2018.
- [264] P. Lalanne, C. Sauvan, and J. P. Hugonin, "Photon confinement in photonic crystal nanocavities," *Laser Photonics Rev.*, vol. 2, no. 6, pp. 514–526, Aug. 2008.
- [265] F. Urbach, "The Long-Wavelength Edge of Photographic Sensitivity and of the Electronic Absorption of Solids," *Phys. Rev.*, vol. 92, no. 5, pp. 1324–1324, Dec. 1953.
- [266] S. John, C. Soukoulis, M. H. Cohen, and E. N. Economou, "Theory of Electron Band Tails and the Urbach Optical-Absorption Edge," *Phys. Rev. Lett.*, vol. 57, no. 14, pp. 1777–1780, Oct. 1986.

-
- [267] C. W. Greeff and H. R. Glyde, "Anomalous Urbach tail in GaAs," *Phys. Rev. B*, vol. 51, no. 3, pp. 1778–1783, Jan. 1995.
 - [268] A. Hartmann, Y. Ducommun, E. Kapon, U. Hohenester, and E. Molinari, "Few-Particle Effects in Semiconductor Quantum Dots: Observation of Multicharged Excitons," *Phys. Rev. Lett.*, vol. 84, no. 24, pp. 5648–5651, Jun. 2000.
 - [269] M. H. Baier, S. Watanabe, E. Pelucchi, and E. Kapon, "High uniformity of site-controlled pyramidal quantum dots grown on prepatterned substrates," *Appl. Phys. Lett.*, vol. 84, no. 11, pp. 1943–1945, Mar. 2004.
 - [270] C. Jarlov, P. Gallo, M. Calic, B. Dwir, A. Rudra, and E. Kapon, "Bound and anti-bound biexciton in site-controlled pyramidal GaInAs/GaAs quantum dots," *Appl. Phys. Lett.*, vol. 101, no. 19, p. 191101, Apr. 2012.
 - [271] K. F. Karlsson *et al.*, "Optical polarization anisotropy and hole states in pyramidal quantum dots," *Appl. Phys. Lett.*, vol. 89, no. 25, p. 251113, Apr. 2006.
 - [272] J. S. Blakemore, "Semiconducting and other major properties of gallium arsenide," *J. Appl. Phys.*, vol. 53, no. 10, pp. R123–R181, Oct. 1982.
 - [273] J. Yu, Y. Chen, S. Cheng, and Y. Lai, "Temperature dependence of anisotropic mode splitting induced by birefringence in an InGaAs/GaAs/AlGaAs vertical-cavity surface-emitting laser studied by reflectance difference spectroscopy," *Appl. Opt.*, vol. 52, no. 5, p. 1035, Feb. 2013.
 - [274] K. H. Madsen *et al.*, "Measuring the effective phonon density of states of a quantum dot in cavity quantum electrodynamics," *Phys. Rev. B*, vol. 88, no. 4, p. 045316, Jul. 2013.
 - [275] L. D. Landau and E. M. Lifshitz, *Quantum mechanics : non-relativistic theory*. Pergamon Press, 1977.
 - [276] J. H. Davies, *The Physics of Low-dimensional Semiconductors*. Cambridge University Press, 1997.
 - [277] O. Vallée and M. Soares, *Airy functions and applications to physics*. Imperial College Press, 2010.
 - [278] A. Delgoffe *et al.*, "Tilted-potential photonic crystal cavities for integrated quantum photonics," *Opt. Express*, vol. 27, no. 15, p. 21822, Jul. 2019.
 - [279] M. Kaniber *et al.*, "Investigation of the nonresonant dot-cavity coupling in two-dimensional photonic crystal nanocavities," *Phys. Rev. B*, vol. 77, no. 16, p. 161303, Apr. 2008.
 - [280] M. Winger *et al.*, "Explanation of Photon Correlations in the Far-Off-Resonance Optical Emission from a Quantum-Dot-Cavity System," *Phys. Rev. Lett.*, vol. 103, no. 20, p. 207403, Nov. 2009.
 - [281] A. Laucht, M. Kaniber, A. Mohtashami, N. Hauke, M. Bichler, and J. J. Finley, "Temporal monitoring of nonresonant feeding of semiconductor nanocavity modes by quantum dot multiexciton transitions," *Phys. Rev. B*, vol. 81, no. 24, p. 241302, Jun. 2010.
 - [282] A. Faraon, E. Waks, D. Englund, I. Fushman, and J. Vučković, "Efficient photonic crystal cavity-waveguide couplers," *Appl. Phys. Lett.*, vol. 90, no. 7, p. 73102, Jan. 2007.
 - [283] P. Yao and S. Hughes, "Controlled cavity QED and single-photon emission using a photonic-crystal waveguide cavity system," *Phys. Rev. B*, vol. 80, no. 16, p. 165128, Oct. 2009.
 - [284] E. Waks and J. Vuckovic, "Dipole Induced Transparency in Drop-Filter Cavity-Waveguide Systems," *Phys. Rev. Lett.*, vol. 96, no. 15, p. 153601, Aug. 2006.
 - [285] S. Schumacher *et al.*, "Cavity-assisted emission of polarization-entangled photons from biexcitons in quantum dots with fine-structure splitting," *Opt. Express*, vol. 20, no. 5, pp. 5335–5342, Apr. 2012.
 - [286] J.-H. Kim, C. J. K. Richardson, R. P. Leavitt, and E. Waks, "Two-Photon Interference from the Far-Field Emission of Chip-Integrated Cavity-Coupled Emitters," *Nano Lett.*, vol. 16, no. 11, pp. 7061–7066, Jan. 2016.
 - [287] J.-T. Shen and S. Fan, "Strongly Correlated Two-Photon Transport in a One-Dimensional Waveguide Coupled to a Two-Level System," *Phys. Rev. Lett.*, vol. 98, no. 15, p. 153003, Apr. 2007.
 - [288] and Y. A. Kenji Kamide, Yasutomo Ota, Satoshi Iwamoto, "Phys. Rev. A 96, 013853 (2017) - Method for generating a photonic NOON state with quantum dots in coupled nanocavities." 06-Apr-2018.
 - [289] J. T. Shen and S. Fan, "Coherent photon transport from spontaneous emission in one-dimensional waveguides," *Opt. Lett.*, vol. 30, no. 15, pp. 2001–2003, Jan. 2005.
-

- [290] J.-T. Shen and S. Fan, "Theory of single-photon transport in a single-mode waveguide. I. Coupling to a cavity containing a two-level atom," *Phys. Rev. A*, vol. 79, no. 2, p. 23837, Aug. 2009.
- [291] A. Faraon, I. Fushman, D. Englund, N. Stoltz, P. Petroff, and J. Vuckovic, "Dipole induced transparency in waveguide coupled photonic crystal cavities," *Opt. Express*, vol. 16, no. 16, p. 12154, Aug. 2008.
- [292] N. Prtljaga *et al.*, "Monolithic integration of a quantum emitter with a compact on-chip beam-splitter," *Appl. Phys. Lett.*, vol. 104, no. 23, p. 231107, Aug. 2014.
- [293] M. J. Hartmann, F. G. S. L. Brandão, and M. B. Plenio, "Quantum many-body phenomena in coupled cavity arrays," *Laser Photonics Rev.*, vol. 2, no. 6, pp. 527–556, Dec. 2008.
- [294] M. Minkov and V. Savona, "Radiative coupling of quantum dots in photonic crystal structures," *Phys. Rev. B*, vol. 87, no. 12, Nov. 2013.
- [295] Y. Sato, Y. Tanaka, J. Upham, Y. Takahashi, T. Asano, and S. Noda, "Strong coupling between distant photonic nanocavities and its dynamic control," *Nat. Photonics*, vol. 6, no. 1, pp. 56–61, Aug. 2012.
- [296] R. Konoike, Y. Sato, Y. Tanaka, T. Asano, and S. Noda, "Adiabatic transfer scheme of light between strongly coupled photonic crystal nanocavities," *Phys. Rev. B*, vol. 87, no. 16, p. 165138, Apr. 2013.
- [297] R. Konoike, H. Nakagawa, M. Nakadai, T. Asano, Y. Tanaka, and S. Noda, "On-demand transfer of trapped photons on a chip," *Sci. Adv.*, vol. 2, no. 5, p. e1501690, Aug. 2016.
- [298] H. Takano, B.-S. Song, T. Asano, and S. Noda, "Highly efficient in-plane channel drop filter in a two-dimensional heterophotonic crystal," *Appl. Phys. Lett.*, vol. 86, no. 24, p. 241101, Jun. 2005.
- [299] C. Manolatou, M. J. Khan, S. Fan, P. R. Villeneuve, H. A. Haus, and J. D. Joannopoulos, "Coupling of modes analysis of resonant channel add-drop filters," *IEEE J. Quantum Electron.*, vol. 35, no. 9, pp. 1322–1331, 1999.
- [300] J. C. F. Matthews, A. Politi, A. Stefanov, and J. L. O'Brien, "Manipulation of multiphoton entanglement in waveguide quantum circuits," *Nat. Photonics*, vol. 3, no. 6, pp. 346–350, Oct. 2009.
- [301] A. Peruzzo *et al.*, "Quantum Walks of Correlated Photons," *Science*, vol. 329, no. 5998, pp. 1500–1503, Oct. 2010.
- [302] J. C. F. Matthews and M. G. Thompson, "Quantum optics: An entangled walk of photons," *Nature*, vol. 484, no. 7392, pp. 47–48, Oct. 2012.
- [303] J. C. Laredo *et al.*, "Boson Sampling with Single-Photon Fock States from a Bright Solid-State Source," *Phys. Rev. Lett.*, vol. 118, no. 13, p. 130503, 2017.
- [304] H. A. Haus and W. Huang, "Coupled-mode theory," *Proc. IEEE*, vol. 79, no. 10, pp. 1505–1518, 1991.
- [305] A. Yariv, "Coupled-mode theory for guided-wave optics," *IEEE J. Quantum Electron.*, vol. 9, no. 9, pp. 919–933, Sep. 1973.
- [306] A. R. A. Chalcraft *et al.*, "Mode structure of the L3 photonic crystal cavity," *Appl. Phys. Lett.*, vol. 90, no. 24, p. 241117, Apr. 2007.
- [307] K. A. Atlasov, K. F. Karlsson, A. Rudra, B. Dwir, and E. Kapon, "Wavelength and loss splitting in directly coupled photonic-crystal defect microcavities," *Opt. Express*, vol. 16, no. 20, p. 16255, Sep. 2008.
- [308] C. Jarlov *et al.*, "1D and 2D arrays of coupled photonic crystal cavities with a site-controlled quantum wire light source," *Opt. Express*, vol. 21, no. 25, p. 31082, Dec. 2013.
- [309] C. M. Natarajan, M. G. Tanner, and R. H. Hadfield, "Superconducting nanowire single-photon detectors: physics and applications," *Supercond. Sci. Technol.*, vol. 25, no. 6, p. 063001, Jun. 2012.
- [310] O. Kahl, S. Ferrari, V. Kovalyuk, G. N. Goltsman, A. Korneev, and W. H. P. Pernice, "Waveguide integrated superconducting single-photon detectors with high internal quantum efficiency at telecom wavelengths," *Sci. Rep.*, vol. 5, no. 1, p. 10941, Sep. 2015.
- [311] R. H. Hadfield, J. L. Habif, J. Schlafer, R. E. Schwall, and S. W. Nam, "Quantum key distribution at 1550nm with twin superconducting single-photon detectors," *Appl. Phys. Lett.*, vol. 89, no. 24, p. 241129, Dec. 2006.
- [312] C. M. Natarajan *et al.*, "Operating quantum waveguide circuits with superconducting single-photon detectors," *Appl. Phys. Lett.*, vol. 96, no. 21, p. 211101, May 2010.

-
- [313] A. Chutinan and S. Noda, "Waveguides and waveguide bends in two-dimensional photonic crystal slabs," *Phys. Rev. B*, vol. 62, no. 7, pp. 4488–4492, Aug. 2000.
 - [314] E. Chow, S. Y. Lin, J. R. Wendt, S. G. Johnson, and J. D. Joannopoulos, "Quantitative analysis of bending efficiency in photonic-crystal waveguide bends at $\lambda = 155\text{ }\mu\text{m}$ wavelengths," *Opt. Lett.*, vol. 26, no. 5, p. 286, Mar. 2001.
 - [315] M. Dinu, R. L. Willett, K. Baldwin, L. N. Pfeiffer, and K. W. West, "Waveguide tapers and waveguide bends in AlGaAs-based two-dimensional photonic crystals," *Appl. Phys. Lett.*, vol. 83, no. 22, pp. 4471–4473, Dec. 2003.
 - [316] L. H. Frandsen, A. Harpøth, P. I. Borel, M. Kristensen, J. S. Jensen, and O. Sigmund, "Broadband photonic crystal waveguide 60° bend obtained utilizing topology optimization," *Opt. Express*, vol. 12, no. 24, p. 5916, Nov. 2004.
 - [317] H. Inoue, K. Hiruma, K. Ishida, T. Asai, and H. Matsumura, "Low loss GaAs optical waveguides," *IEEE Trans. Electron Devices*, vol. 32, no. 12, pp. 2662–2668, Dec. 1985.
 - [318] S. Fattah poor *et al.*, "Efficient coupling of single photons to ridge-waveguide photonic integrated circuits," *Appl. Phys. Lett.*, vol. 102, no. 13, p. 131105, Apr. 2013.
 - [319] J. Lu and J. Vučković, "Nanophotonic computational design," *Opt. Express*, vol. 21, no. 11, p. 13351, Jun. 2013.
 - [320] A. Y. Piggott, J. Petykiewicz, L. Su, and J. Vučković, "Fabrication-constrained nanophotonic inverse design," *Sci. Rep.*, vol. 7, no. 1, p. 1786, Dec. 2017.
 - [321] S. Molesky, Z. Lin, A. Y. Piggott, W. Jin, J. Vucković, and A. W. Rodriguez, "Inverse design in nanophotonics," *Nat. Photonics*, vol. 12, no. 11, pp. 659–670, Nov. 2018.
 - [322] E. Pelucchi *et al.*, "Mechanisms of Quantum Dot Energy Engineering by Metalorganic Vapor Phase Epitaxy on Patterned Nonplanar Substrates," 2007.
 - [323] M. Abbarchi, T. Kuroda, R. Duval, T. Mano, and K. Sakoda, "Scanning Fabry-Pérot interferometer with largely tuneable free spectral range for high resolution spectroscopy of single quantum dots," *Rev. Sci. Instrum.*, vol. 82, no. 7, p. 073103, Jul. 2011.
 - [324] A. J. Bennett *et al.*, "Electric-field-induced coherent coupling of the exciton states in a single quantum dot," *Nat. Phys.*, vol. 6, no. 12, pp. 947–950, Aug. 2010.
 - [325] C. Bentham *et al.*, "On-chip electrically controlled routing of photons from a single quantum dot," *Appl. Phys. Lett.*, vol. 106, no. 22, p. 221101, Aug. 2015.
 - [326] X. Yang, M. Yu, D.-L. Kwong, and C. W. Wong, "All-Optical Analog to Electromagnetically Induced Transparency in Multiple Coupled Photonic Crystal Cavities," *Phys. Rev. Lett.*, vol. 102, no. 17, p. 173902, Jul. 2009.
 - [327] Y. Chen, M. Wubs, J. Mørk, and A. F. Koenderink, "Coherent single-photon absorption by single emitters coupled to one-dimensional nanophotonic waveguides," *New J. Phys.*, vol. 13, no. 10, p. 103010, Dec. 2011.
 - [328] L. Garziano, V. Macrì, R. Stassi, O. Di Stefano, F. Nori, and S. Savasta, "One Photon Can Simultaneously Excite Two or More Atoms," *Phys. Rev. Lett.*, vol. 117, no. 4, p. 43601, Aug. 2016.
 - [329] N. E. Rehler and J. H. Eberly, "Superradiance," *Phys. Rev. A*, vol. 3, no. 5, pp. 1735–1751, May 1971.
 - [330] S. J. Devitt, A. D. Greentree, R. Ionicioiu, J. L. O'Brien, W. J. Munro, and L. C. L. Hollenberg, "Photonic module: An on-demand resource for photonic entanglement," *Phys. Rev. A*, vol. 76, no. 5, p. 52312, Aug. 2007.
-

Publications and conferences

Journal publications

- A. Delgoffe, A. Miranda, B. Rigal, A. Lyasota, A. Rudra, B. Dwir, and E. Kapon, "Tilted-potential photonic crystal cavities for integrated quantum photonics," *Opt. Express*, vol. 27, issue 15, pp. 21822-21833, Jul. 2019.

Conference presentations

- A. Delgoffe, A. Miranda, A. Lyasota, A. Rudra, B. Dwir, Y. Yu and E. Kapon, "Integrated Quantum Photonics with Tailored Potential Quantum Dots and Photonic Crystal Structures," *ICTON*, Angers, Jul. 2019 (talk)
- A. Delgoffe, A. Miranda, A. Lyasota, A. Rudra, B. Dwir, Y. Yu, and E. Kapon, "Integrated Quantum Photonics using Site-Controlled Quantum Dots and Tailored-Potential Photonic Crystals," *CLEO*, San José, May 2019 (talk)
- A. Delgoffe, F. Gremion, A. Miranda, B. Rigal, A. Lyasota, B. Dwir, A. Rudra, Y. Yu, and E. Kapon, "Tailoring of Photonic Confinement in Photonic Crystal Cavities for Integrated Quantum Nanophotonics," *Nanometa*, Seefeld, Jan. 2019 (poster)
- A. Delgoffe, A. Miranda, B. Rigal, A. Lyasota, A. Rudra, B. Dwir, and E. Kapon, "Tilted-Potential Photonic Crystal Cavities for Integrated Quantum Photonics," *ECIO*, Valencia, May 2018 (talk)

Curriculum-Vitae

Antoine Delgoffe

3 Chemin de la Grosse-Pierre,
appartement 61
1110 Morges
☎ +41 79 617 69 61
✉ a.delgoffe@gmail.com
born on 27.01.1990 • single • french



Profile

Diligent, meticulous, responsible and dutiful. Curiosity-driven, passionate about developing cutting-edge technologies in view of philanthropic endeavors : health, quality of life improvement, space exploration. Trained as an EPFL Engineer and Applied Physicist in the fields of general physics, specialized in photonics and quantum information science & technologies. Interests in cryptography, sensing, artificial intelligence, IoT, augmented reality.

Diplomas

- 2015–2020 **PhD in Physics**,
Swiss Federal Institute of Technologies (EPFL), Lausanne, Switzerland,
Integrated Quantum Photonics.
- 2013–2015 **MSc in Applied Physics**,
Swiss Federal Institute of Technologies (EPFL), Lausanne, Switzerland,
Major in Optics, Optoelectronics, Condensed Matter and Quantum Physics.
- 2010–2013 **BSc in Physics**,
Swiss Federal Institute of Technologies (EPFL), Lausanne, Switzerland.
- 2008–2010 **Classes Préparatoires aux Grandes Ecoles (CPGE), MPSI - MP**,
Lycée Henri Poincaré, Nancy, France,
Admissible to Sup'Optique Paris-Palaiseau in Centrale-Supélec Concours.

Academics

- PhD Thesis ***Functional Elements for Quantum-Dot-Based Integrated Quantum Photonics***,
Supervised by Pr. Elyahou Kapon and Pr. Nicolas Grandjean,
Laboratory of Physics of Nanostructures (LPN).
- MSc Thesis ***Investigation of Purcell effect in site-controlled quantum dots incorporated in a photonic crystal cavity by time-resolved photoluminescence spectroscopy***,
Supervised by Pr. Elyahou Kapon and his PhD student Clément Jarlov,
Laboratory of Physics of Nanostructures (LPN).
- Publications ***Tilted-potential photonic crystal cavities for integrated quantum photonics***, A. Delgoffe, et al., OSA, Optics Express, Vol. 27, Issue 15, pp. 21822-21833 (2019), <https://doi.org/10.1364/OE.27.021822>.
- Conferences **CLEO : Laser Science to Photonic Applications 2019**, San Jose, United States of America, "Integrated Quantum Photonics using Site-Controlled Quantum Dots and Tailored-Potential Photonic Crystals", PhD student talk.
Hello Tomorrow 2018 : The Future of Quantum Business, Geneva, Switzerland, volunteer staff member.

European Conference on Integrated Optics (ECIO) 2018, *Valencia*, Spain,
"Tilted-Potential Photonic Crystal Cavities for Integrated Quantum Photonics",
PhD student talk.

Summer Schools **Recent Trends on Light-Matter Interaction 2017**, *Lausanne*, Switzerland.

Workshops **IBM Quantum Experience**, *Zurich*, Switzerland.

Swiss Photonics, *Lausanne*, Switzerland.

Tutoring **Optics I-II**, *main assistant for Physics Bachelor 3rd year (2018-19)*.

General Physics III-IV, *main assistant for Physics Bachelor Sophomores (2015-18)*.

Professional/Industry

August 2014 - **Engineering Internship - Solid-State Flash Imaging LiDAR (Indirect**
January 2015 **Time-of-Flight) : Phase Unwrapping**, *for potential European Space Agency (ESA) missions*, supervised by Alexandre Pollini, Centre Suisse d'Electronique et de Microtechnique (CSEM), *Neuchâtel*, Switzerland.

Computer Skills

Numerical Modelling, Image Processing, Computer Vision, Data Analysis

General : \LaTeX , Microsoft Office

Tools : Jupyter Notebook, Matlab, Mathematica

Programming : Python, C++

Methods : 2D-3D FDTD (PyMeep) and FDFD

Technical Skills

Laboratory : Design of optical setup, cryogenic cooling, micro-photoluminescence spectroscopy, time-resolved PL, HBT single-photons correlations

Micro/Nano-fabrication : spin-coating, PECVD, RIE dry-etching, wet-etching, photo-lithography, e-beam evaporation, lift-off, SEM, AFM, confocal microscopy

Languages

French Mother tongue

English Comprehension : C1, Expression : C1

Spanish Comprehension : B1, Expression : B1

Japanese Comprehension : B1, Expression : A2

Miscellaneous

Student Life.

2011-2014 **Member of PolyJapan Board of Direction, in charge of anime projections**, *EPFL*, Lausanne.

2010-2011 **Member of AGEPoly Board of Direction, in charge of services to EPFL students**, *EPFL*, Lausanne.

Sports.

Golf, *unranked license*, Club de Pulnoy, Pulnoy, France.

Sailing, *D license*, Club Nautique Morgien, Morges, Suisse.

Hobbies.

Astronomy, *Sky-Watcher Explorer-130P EQ2*.

Raspberry Pi, *beginner*.

Hiking.